EXPERIMENTAL TESTING OF CAST-IN-PLACE SEISMIC RESISTANT UNBONDED POST-TENSIONED SPECIAL REINFORCED CONCRETE WALLS

Report to
Charles Pankow Foundation
RGA#3-10

by

Leary Pakiding

Stephen Pessiki

Richard Sause

Moises Rivera

ATLSS Report No. 14-07

December 2014

ATLSS is a National Center for Engineering Research on Advanced Technology for Large Structural Systems

117 ATLSS Drive
Bethlehem, PA 18015-4729

Phone: (610)758-3525
Fax: (610)758-5902

www.atlss.lehigh.edu
Email:inatl@lehigh.edu

EXPERIMENTAL TESTING OF CAST-IN-PLACE SEISMIC RESISTANT UNBONDED POST-TENSIONED SPECIAL REINFORCED CONCRETE WALLS

Report to
Charles Pankow Foundation
RGA#3-10

by

Leary Pakiding
Graduate Research Assistant

Stephen Pessiki
Professor of Structural Engineering
pessiki@lehigh.edu

Richard Sause
Professor of Structural Engineering
rs0c@lehigh.edu

Moises Rivera
Former Graduate Research Assistant

ATLSS Report No. 14-07

December 2014

ATLSS is a National Center for Engineering Research on Advanced Technology for Large Structural Systems

117 ATLSS Drive
Bethlehem, PA 18015-4729

Phone: (610)758-3525
Fax: (610)758-5902

www.atlss.lehigh.edu
Email:inatl@lehigh.edu

ACKNOWLEDGEMENTS

This research project was supported by the Charles Pankow Foundation and conducted at the Center for Advanced Technology for Large Structural Systems (ATLSS) at Lehigh University, Bethlehem, PA.

The following organizations are acknowledged for their support and contributions to this research project: Tipping Mar for their collaboration in designing the candidate test walls, DSI America for donating the prestressing system utilized in this research project, NUCOR Steel Connecticut for donating the necessary rebar to complete the project, A.H. Harris Construction Supplies for the formwork panels for the duration of the project, and VSL for the technical expertise that they provided.

In addition, the following individuals are recognized for their involvement and assistance during the course of the project. First, thanks are given to the ATLSS staff, including Darrick Fritchman, Roger Moyer, Carl Bowman, Edward Tomlinson, Adam Kline, Peter Bryan, and Thomas Marullo for their assistance with the construction and instrumentation of the test walls. Second, thanks are expressed to former students and visiting student involved in the project, including Sonam Srivastava, Christian Stephan, Mujahid Noor, and Hao Wu. Finally, thanks are extended to Dr. Wesley Keller, Rosalyn Mendez, and Norzaireen Mohd Azmee for their help during the test.

The opinions, findings, and conclusions expressed in this report are those of the authors and do not necessarily reflect the views of the organizations and individuals acknowledged above.

TABLE OF CONTENTS

LIST OF FIGURES

LIST OF TABLES

ABSTRACT

The work described in this report is part of a project at Lehigh University to develop experimental test data to confirm and codify a design protocol cast-in-place concrete shear walls that incorporate unbonded vertical post-tensioning. The defining feature of the wall system sought by this research is the rocking/flexural response and self-centering capability provided by unbounded vertical post-tensioned tendons coupled with the energy dissipation provided by the reinforcing bars. The research performed to date focused on three tasks: Task 1 - Development of closed form expression to describe the monotonic lateral load behavior of unbonded post-tensioned cast-in-place special structural walls with bonded or debonded longitudinal mild steel reinforcement; Task 2 - Experimental evaluation the effects of inelastic tensile cyclic loading of the longitudinal mild steel reinforcement embedded in a confined concrete core on the behavior, strength, and ductility of the confined concrete under compression loading; Task 3 - Experimental evaluation of large-scale of unbonded post-tensioned cast-in-place special structural walls with bonded or debonded longitudinal mild steel reinforcement. The objectives of this experimental work was to study the behavior of unbonded post-tensioned cast-in-place special concrete walls, and to evaluate different wall details intended to control the response of each test wall. The focus of this report is Task 3. The following is a summary of findings.

Test Wall 1 represented a wall with low ratio of post-tensioned steel to mild steel reinforcement ratio. The wall showed a very good energy dissipation capacity; however, the self-centering capacity of the wall was low which was indicated by the high residual drift in the wall. Failure of Wall 1 was characterized by the formation of shallow diagonal cracks in the web. These cracks corresponded to high shear demand in the wall. The wall eventually failed along these cracks by sliding.

Test Wall 2 represented a wall with higher ratio of post-tensioned steel to mild steel reinforcement ratio as compared to Wall 1. Wall 2 showed a very good response in terms of self-centering as well as energy dissipation capabilities. The wall failed by fracture of longitudinal steel reinforcement at the boundaries and the web. The behavior of Wall 2 was more similar to the anticipated behavior of a rocking wall. The energy dissipation in this wall was quite good which is shown by large hysteresis loop of load deformation response. The self-centering capacity of the wall was improved by the used of higher post-tensioned steel to steel reinforcement ratio.

Test Wall 3 included modified details at the boundary elements. Some of the longitudinal bars were terminated at the wall-foundation interface, and the other bars were debonded over 48 inch above top of foundation block. Wall 3 showed less cracking and no fracture of longitudinal steel reinforcement. However, failure mode of Wall 3 was sudden and occurred at drift level which was lower than those of the other test walls experienced. This failure was suspected to be precipitated by the formation of a splitting plane along the vertical web reinforcement, followed by buckling of this reinforcement and failure of the wall in shear.

CHAPTER 1
INTRODUCTION

1.1 INTRODUCTION

Structural damage observed in past earthquakes has shown that, in general, buildings with structural walls performed better than those without any walls. Two inherent limitations found in commonly used structural walls are: (1) the required nonlinearity or softening of the wall is caused by damage (i.e., yielding of reinforcing steel and softening of concrete in compression); and (2) residual lateral drift after a major seismic event. Both of these limitations can be addressed through the use of post-tensioning as addressed in this report.

Figure 1-1 is an illustration of a typical cast-in-place ACI-complaint wall, an unbonded post-tensioned precast concrete wall, and an unbonded post-tensioned hybrid cast-in-place concrete wall. Included in this figure is an idealization of the base moment-lateral drift response of each wall. The unbonded post-tensioned precast concrete wall (Figure 1-1(b)) represents construction similar to the precast wall with post-tensioning for self-centering studied by Kurama et al. (1996), Kurama (1997), Perez (2004), and Perez et al. (2007). The unbonded post-tensioned hybrid cast-in-place concrete wall (Figure 1-1(c)) represents construction similar the cast-in-place wall with post-tensioning for self-centering studied in the work described in this report and related studies at Lehigh University (Srivastava et al. (2013); Rivera et al. (2013); Noor et al. (2013).

The structural wall in Figure 1-1(a) is a cast-in-place concrete wall with longitudinal mild steel reinforcement extending into the foundation (as per ACI 318), but without post-tensioning. As lateral force is applied, concrete cracking occurs, and the wall softens due to yielding of the steel reinforcement and non-linear stress-strain concrete response in compression. After the seismic event, the wall is likely to have some residual lateral drift due to the absence of a restoring force. However, it can be seen in the expected base moment-lateral drift curve that the yielding of the longitudinal steel reinforcement provided energy dissipation, which could translate into the reduction of overall drift, but ultimately extensive damage to the wall is expected.

Figure 1-1(b) is an unbonded post-tensioned precast wall with post-tensioning for self-centering that extends from the top of the wall to the foundation, but without longitudinal mild steel reinforcement extending into the foundation. Under earthquake loading, larger drifts may be expected, compared to a cast-in-place wall. After the seismic event, restoring forces are provided by the post-tensioning and therefore residual lateral drift is virtually zero. However, the expected moment-lateral drift curve shows no energy dissipation. This is due to the lack of longitudinal mild steel reinforcement crossing the horizontal joint between the stacked precast panels and the foundation. Nonetheless, with adequate concrete confinement, minimum damage of the wall is expected.

Figure 1-1(c) is an unbonded post-tensioned hybrid cast-in-place concrete wall with post-tensioning that extends from the top of the wall to the foundation with longitudinal mild steel reinforcement extending into the foundation as per ACI 318. As the lateral force is applied, drifts are reduced by the energy dissipation provided by the longitudinal mild steel

reinforcement and residual lateral drift is reduced by the post-tensioning. After a seismic event, residual drift is virtually zero and damage to the wall is minimal. As shown in the expected moment-lateral drift curve, this hybrid system provides for life safety through ductility, and energy dissipation, and the reduction of residual drift allows for immediate occupancy after the seismic event.

1.2 OBJECTIVE

The work described in this report is part of a project at Lehigh University to develop experimental test data to confirm and codify a design protocol cast-in-place concrete shear walls that incorporate unbonded vertical post-tensioning. The ultimate aim of the research is to deliver a complete design procedure ready to be employed on actual commercial building construction projects in all seismic zones. The defining feature of the wall system sought by this research is the rocking/flexural response and self-centering capability provided by unbounded vertical post-tensioned tendons coupled with the energy dissipation provided by the reinforcing bars. The system has the potential to significantly reduce the cost of building seismically safe concrete structures using currently available construction methods and materials. Structural engineers would use the final work product to design buildings for the ultimate benefit of the general public.

1.3 OVERVIEW OF PANKOW FOUNDATION RESEARCH AT LEHIGH UNIVERSITY

The research performed to date, and supported by the Charles Pankow Foundation at Lehigh University, focused on three tasks:

Task 1 - Development of closed form expression to describe the monotonic lateral load behavior of unbonded post-tensioned cast-in-place special structural walls with bonded or debonded longitudinal mild steel reinforcement.

Task 2 - Experimental evaluation the effects of inelastic tensile cyclic loading of the longitudinal mild steel reinforcement embedded in a confined concrete core on the behavior, strength, and ductility of the confined concrete under compression loading.

Task 3 - Experimental evaluation of large-scale of unbonded post-tensioned cast-in-place special structural walls with bonded or debonded longitudinal mild steel reinforcement.

1.3.1 TASK 1 - DEVELOPMENT OF CLOSED-FORM EXPRESSIONS

The objective of this part of the study was to derive closed-form expressions to describe monotonic lateral load behavior of an unbonded post-tensioned cast-in-place special structural wall with bonded or debonded longitudinal mild steel reinforcement. Once developed, the closed-form expressions were then used as tools in the design studies to develop the wall test specimens (Task 3).

Two sets of generalized closed-form expressions were derived for estimating the lateral load responses, base moment and lateral drift, of the walls for critical limit states. The first set of equations is for cast-in-place special structural walls with bonded longitudinal

reinforcement, and the second for cast-in-place special structural walls with predetermined length of debonded longitudinal reinforcement at the base of the wall.

The analytical models and the closed-form expressions were to investigate the effects of six design parameters in the lateral load response of the walls. The parameters considered were area of post-tensioning steel with constant initial prestress; initial prestress in post-tensioning steel with constant area of post-tensioning steel; constant initial prestress force with varying area and initial prestress; area of boundary longitudinal reinforcement; area of web longitudinal reinforcement; and spacing of web longitudinal reinforcement.

It was found that debonding the longitudinal reinforcement over a predetermined height at the base of the wall significantly increased the lateral drift value with minimal effect on base moment. This additional deformation capacity of the walls was achieved by delaying the yielding of longitudinal reinforcement without any change in the restoring action of unbonded post-tensioning steel. With increase in the area or initial prestress of post-tensioning steel base moment value increases and drift value decreases for all the limit states. Increasing the area of boundary or web longitudinal reinforcement also increases the lateral load response values of the walls, whereas, spacing of web longitudinal reinforcement with constant longitudinal reinforcement area does not have any significant effect.

Complete details of this part of the work performed at Lehigh are given in Srivastava et al. (2013).

1.3.2 TASK 2 - EFFECT OF INELASTIC TENSILE CYCLIC LOADING ON THE CONCRETE BEHAVIOR

The objective of this part of the study was to experimentally evaluate the effects of inelastic tensile cyclic loading of the longitudinal mild steel reinforcement embedded in a confined concrete core on the behavior, strength, and ductility of the confined concrete under compression loading. The investigation focused on the critical confined concrete crushing height of the boundary zone confined concrete in a well-detailed reinforced concrete lateral-load-resisting wall where the longitudinal mild steel reinforcement inside the confined core yields and develops a plastic hinge at the base of the wall.

The test specimens treated in this part of the work represented the confined concrete boundary zone of the walls tested in Task 3. Two identical 10 in. x 15 in. cross-section confined concrete specimens were studied to observe the effects of two different ranges of quasi-static inelastic tensile cyclic loading of the longitudinal mild steel reinforcement bars on the behavior, strength, and ductility of the confined concrete under compression loading. The first specimen was tested under increasing tensile cyclic loading up to 4 times the tensile yielding strain limit of the longitudinal mild steel reinforcement bars of the confined concrete core. The specimen was then loaded to failure in compression. The second specimen was tested under increasing tensile cyclic loading up to 16 times the tensile yielding strain limit of the longitudinal mild steel reinforcement bars of the confined concrete core. Then, the specimen was loaded to failure in compression.

The test results for the two test specimens were compared to observe the effects of different levels of inelastic tensile cyclic loading of the longitudinal mild steel reinforcement bars inside the confined concrete. The test results were also compared with the theoretical results from previously developed confined concrete models under monotonic compression loading. These comparisons focused on the effects of tensile loading on the compression behavior, strength, and ductility of confined concrete under compression loading.

It was found that after inelastic tensile deformation of the longitudinal mild steel reinforcement inside the confined concrete core, a compression load greater than the prior tensile load was required to close the cracks. In the inelastic tensile deformation load steps, the reversing compression strain in the reinforcement was small compared to the tensile strain. The compression stiffness and ductility of the confined concrete were not affected by inelastic tensile cyclic loading of the longitudinal mild steel reinforcement of the confined concrete core. There was a noticeable reduction in the compression strength of confined concrete. The peak compression strength of the confined concrete was smaller than the results of any of the theoretical confined concrete models that were considered.

Complete details of this part of the work performed at Lehigh are given in Noor et al. (2013).

1.3.3 TASK 3 - EXPERIMENTAL EVALUATION OF LARGE-SCALE UNBONDED POST-TENSIONED CAST-IN-PLACE SPECIAL STRUCTURAL WALLS

The third part of the work at Lehigh University, and the subject of this report, was the experimental evaluation of large-scale of unbonded post-tensioned cast-in-place special structural walls with bonded or debonded longitudinal mild steel reinforcement.

The objectives of this experimental work was to study the behavior of unbonded post-tensioned cast-in-place special concrete walls, and to evaluate different wall details intended to control the response of each test wall.

Details of the design of the experimental program, and results of the first wall test (referred to in this report as Wall 1), are given in Rivera et al. (2013). The results of Wall 1 are summarized in the current report along with the detailed presentation of results from Wall 2 and Wall 3.

1.4 REPORT ORGANIZATION

The remainder of this report is divided into four chapters. Chapter 2 describes the development of potential test walls and the development of analytical model for prediction of wall responses. Chapter 3 explains the experimental program which includes experimental setup, materials testing, and instrumentation arrangement. Chapter 4 presents the experimental results of three test walls including discussions as well as comparisons to the analytical predictions. Finally, Chapter 5 presents the summary and conclusions of the experimental results.

1.5 NOTATION

For consistency, similar notations as those in Rivera et al. (2013) and Srivastava et al. (2013) are used in this report. The notations are as follows:

CCC = crushing of confined conrete
E_d = normalized cumulative hysteretic energy dissipation
$ELL1$ = effective linear limit when neutral axis depth is 25% of L_w
$ELL2$ = effective linear limit with non-linear behavior of unconfined concrete
$ELL3$ = effective linear limit when the moment at the base of the wall is $2.5M_{dec}$
$ELL4$ = effective linear limit when furthest bonded longitudinal reinforcement bar(s) begin to yield in tension
F = lateral force acting on wall
FMS = farthest longitudinal mild steel reinforcement bar(s) reaches its ultimate strength
f'_c = compressive strength of unconfined concrete
f'_{cce} = compressive strength of confined concrete
f_{pi} = initial stress in the post-tensioning steel after elastic shortening
f_{pu} = ultimate strength of the post-tensioning steel
f_{py} = yield strength of the post-tensioning steel
f_{ue} = actual ultimate strength of the steel reinforcement ($1.5f_{ye}$)
f_y = yield strength of the steel reinforcement
f_{ye} = yield strength of the steel reinforcement ($1.1f_y$)
H_f = height of the applied lateral force from the base of the wall
H_w = total height of wall
LLP = farthest post-tensioned steel begins to yield in tension
L_w = length of the wall cross-section
P_{pi} = initial post-tensioning tension force
P_{py_n} = nominal yielding force of post-tensioning steel
t_w = thickness of the wall cross-section
Δ = displacement due to lateral force acting on wall
Δ_r = residual displacement after a seismic event
ε_c = measured concrete strain
ε_{sy_n} = nominal yield strains of longitudinal mild steel
ε_{r_n} = nominal modulus of rupture of concrete strain at f'_c
Θ_{CCC} = drift of the wall at CCC
Θ_{ELL1} = drift of the wall at $ELL1$
Θ_{ELL2} = drift of the wall at $ELL2$
Θ_{ELL3} = drift of the wall at $ELL3$
Θ_{ELL4} = drift of the wall at $ELL4$
Θ_{FMS} = drift of the wall at FMS
Θ_{LLP} = drift of the wall at LLP
Θ_{bms_o} = drift of the wall at observed buckling of longitudinal mild steel
Θ_{ccr_o} = drift of the wall at observed flexural concrete cracking
Θ_{fms_o} = drift of the wall at observed fracture of longitudinal mild steel reinforcement
Θ_{llp_n} = drift of the wall at nominal yielding of post-tensioning steel
Θ_{spl_o} = drift of the wall at observed concrete spalling
Θ_{yms_n} = drift of the wall at nominal yielding of longitudinal mild steel reinforcement

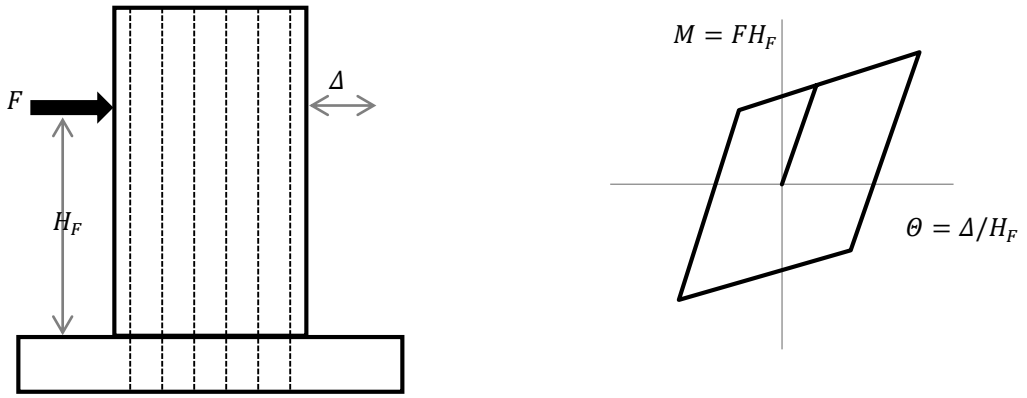

(a) ACI compliant cast-in-place wall and base moment-lateral drift curve

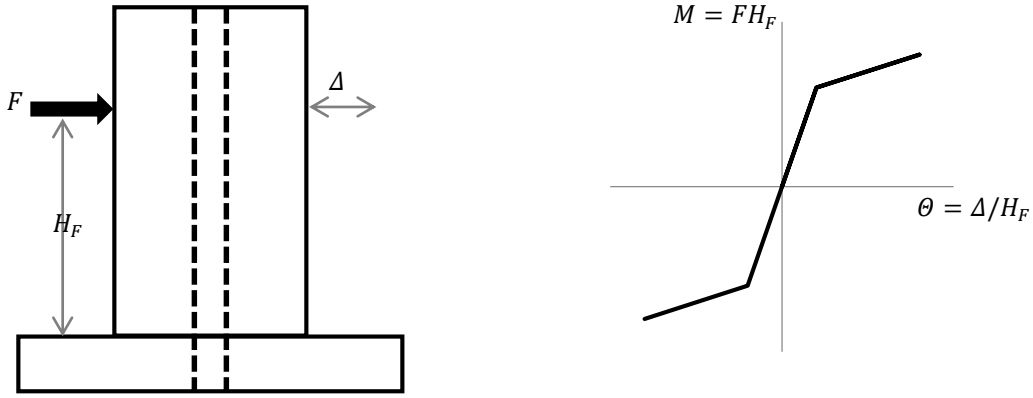

(b) Unbonded post-tensioned precast concrete wall and base moment-lateral drift curve

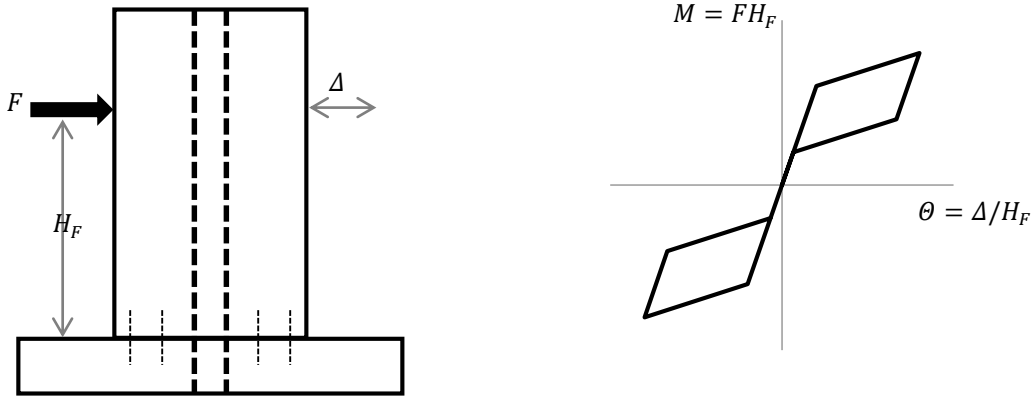

(c) Unbonded post-tensioned hybrid precast concrete wall and base moment-lateral drift curve

Figure 1-1: Base moment-lateral drift behavior of cast-in-place wall, unbonded post-tensioned wall and unbonded post-tensioned hybrid precast wall

CHAPTER 2
TEST WALL DEVELOPMENT

2.1 INTRODUCTION

The experimental program consisted of tests of three walls, identified as Wall 1, Wall 2, and Wall 3. This chapter describes the design development of Walls 1 and 2. The details of Wall 3 were not determined in the design study, but instead were determined based on the test results from Wall 1 and Wall 2. The experimental program (Chapter 3) and experimental results (Chapter 4) include all three test walls.

2.2 DEVELOPMENT OF CANDIDATE TEST WALLS

In this project, collaborative work was done with Ti$_{pp}$ing Mar (a structural engineering company based in San Francisco, CA) at the stage of designing the candidate test walls. Tipping Mar performed analytical studies on cast-in-place UPT special RC walls and results of their studies can be found in Tipping Mar (2011).

Figure 2-1 shows the geometry of the test walls. The test walls represented 40% scale of actual wall in building practice. Following the common wall thickness/width used in practice, thickness of 10 inch was chosen. To achieve certain unbonded length of the post-tensioned steel, the wall was made taller than the height of the applied load as shown in Figure 2-1. The idea of having longer unbonded length was to assure that tensile strain in post-tensioned steel can be redistributed over a long length which in turn delayed early yielding of the post-tensioned steel.

Figure 2-2 shows a generic cross section of a candidate test wall including mild steel boundary reinforcement, PT bundles, transverse boundary and web reinforcement, and longitudinal web reinforcement. Analytical studies in Tipping Mar (2011) involved six walls which have proportions of steel reinforcement and post-tensioned steel as tabulated in Table 2-1. Responses of each wall under monotonic and cyclic static loads are shown in Figure 2-3. Based on these results, two test wall specimens were selected and subjected to further design development.

The goal during the iterative design process was to design wall specimens which have ultimate strengths very close to the maximum lateral force demand that can be provided by the actuator. Wall 1 (Wall 01) and Wall 3 (Wall 03) in Tipping Mar (2011) were chosen from Table 2-1. These walls represented two different design goals. Wall 1 was to represent the design of a strong wall with a low ratio of post-tensioned steel to mild steel, while Wall 3 was to represent the design of a more self-centering wall with a high ratio of post-tensioned steel to mild steel. In addition, for the same ultimate strength, Wall 1 is expected to be more economical than Wall 3.

Material properties of concrete, steel reinforcement, post-tensioned steel used in the design iteration process are given in Table 2-3. During the design iteration process for each wall, the parameters that were changed were amount of mild steel, amount of post-tensioned steel, locations of mild steel, and locations of post-tensioned steel. Ratios of post-tensioned steel to mild steel are shown in Table 2-3 for each test walls.

Table 2-2 shows the geometry of each potential test wall at the start and at the end of design iterations. For each test specimens, two different strand diameters were proposed, 0.5-inch diameter and 0.6-inch diameter. The final iterated test walls incorporated 0.6 inch-diameter strands since it is mostly used in practice and no special details were needed in order to be used in the experiment.

Figure 2-4 shows the final cross sections of each test walls. Detailing of each specimen was in compliance to ACI 318-11 (ACI 2011) specifically chapter 21. Each test wall consisted of two parts, boundary element and web element as shown in Figure 2-5. Table 2-4 shows all detailing requirements according to ACI 318-11 (ACI 2011) and the corresponding details for each wall.

Although these walls were 40% scaled, not all dimensions were scaled. Spacing of steel hoops at the boundary was not scaled since the actual spacing was quite small already which could give problem during concrete casting. In addition, size of the steel reinforcement was not scaled because the scaling will result in required reinforcement size that might not be available in practice.

Table 2-5 summarizes the nominal shear capacity for each wall. The reduced nominal shear capacity $\varphi_v V_n$ for the two specimens was larger than the reduced shear demand $\varphi_f V_{dMn}$.

2.3 ANALYTICAL MODEL

An analytical model was developed for predicting the lateral load responses of the two test walls. The results of the analyses will be used later for comparison to the experimental results. The following highlights the analytical model.

2.3.1 GEOMETRY AND BOUNDARY CONDITIONS

Figure 2-6(a) shows the geometry of test wall that was modeled. Since the foundation block was assumed to be rigid then it was possible to idealize the model as shown in Figure 2-6(b).

The modeling was done using nonlinear finite element analysis software DRAIN-2DX (Prakash et al. 1993). The modeling was started by defining the geometry and boundary conditions of the wall as shown in Figure 2-6(c). The geometry was represented by nodes and elements. Two different types of elements were used in this modeling, fiber element (Taucer et al. 1991) and nonlinear truss element. Fiber element represented the concrete as well as the steel reinforcement as shown in Figure 2-7 while truss element was assigned for the post-tensioned steel. Details and advantages of using a fiber model to model this particular type of wall are explained in Kurama et al. (1996), Kurama (1997), and El-Sheikh (1997).

The first fiber element from the base represented the plastic hinge length of the wall or the critical height. The critical height H_{cr} was determined to be twice of the width of the boundary element which is based on Perez (2004). To model the application of post-tensioned anchorage at the top of the wall, kinematic constraints were applied to the top

nodes of the truss elements. As for the boundary conditions, the base node of the fiber element was fixed and the base nodes of the truss elements were pinned.

2.3.2 MATERIAL MODELS

The same material properties as in Tipping Mar (2011) were used in the modeling of the test walls and they are summarized in Table 2-3. The nominal values as well as the expected values are given regarding the strength of the materials. Nominal compressive strength of concrete was 6 ksi, nominal yield strength of reinforcement steel was 60 ksi with modulus of elasticity of 29000 ksi, and the ultimate strength of post-tensioned steel was 270 ksi with modulus of elasticity of 27500 ksi.

There were two types of concrete modeled in the fiber element, confined concrete model and unconfined concrete model. Confined concrete model represented the concrete in the boundary elements while unconfined concrete model represented concrete cover as well as concrete in the web element. The assignment of each concrete types in the cross section level is shown in Figure 2-7.

The confined concrete and unconfined concrete models were developed using Mander model (Mander et al. 1988b). As the input in DRAIN-2DX, a maximum 5 points were used to represent these material models. These concrete models are shown in Figure 2-8. The strain at which the concrete crushed is estimated to be 0.06 which was based on Mander et al. (1988b). Tensile capacity of the concrete was set to be zero and linear shear capacity of concrete was included in the assignment of fiber elements.

The material models for steel reinforcement and post-tensioned steel were represented by bilinear material model which was defined by two points. Each point denoted the combination of strain and stress at yield and at ultimate conditions respectively. These material models are shown in Figure 2-9 and Figure 2-10 separately for steel reinforcement and post-tensioned steel.

2.3.3 ANALYSIS AND RESULTS

Before beginning the lateral load analysis, the gravity analysis was performed first by applying the self-weight of the wall and the post-tensioned forces of the post-tensioned steel. This must be done in order to avoid zero stiffness in the wall.

Following the gravity analysis, the wall models were analyzed by applying monotonically and cyclically displacement at the height of 150 inch from the base. The loading protocol for the monotonic and cyclic analysis is given in Figure 2-11. Monotonic analysis was done by increasing the applied displacement gradually until it reached the prescribed displacement. For cyclic analysis, the wall was pushed back and forth one full cycle for each displacement level (drift level). The effect of multiple cycles on the same drift level was not taken into account in the cyclic analysis.

Figure 2-12 shows the result of pushover (monotonic) analysis as well as cyclic analysis for each test walls. It is clear that Wall 1 dissipated more energy and reached more maximum strength than Wall 2. In contrast, for the same drift level, residual drift of Wall

2 was less compared to that of Wall 1. These results became the predictions of the test walls responses and they will be compared later with the test results.

Table 2-1 Matrix of candidate wall specimens (adapted from Tipping Mar 2011)

WALL ID	Field Reinforcement		Boundary Reinforcement		PT Strand Quantity (0.5" dia.)	Shear Reinforcement	
	Bar size	Spacing (in)	Quantity	Bar Size		Bar size	Spacing (in)
W01	#5	6	4	#8	30	#6	6
W02	#3	6	4	#5	11	#4	6
W03	#3	24	4	#3	19	#4	6
W04	#4	6	4	#6	18	#5	6
W05	#5	6	6	#10	0	#6	6
W06	#3	12	4	#3	30	#5	6

Table 2-2 Wall geometry

Wall ID			Specimen 1		Specimen 2	
			Wall 1 (start)	Wall 1 (final)	Wall 3 (start)	Wall 3 (final)
Dimension (in)	H_w		300	300	300	300
	H_f		150	150	150	150
	L_w		72	72	72	72
	t_w		10	10	10	10
Aspect Ratio	H_f/L_w		2.08	2.08	2.08	2.08
	L_w/t_w		7.2	7.2	7.2	7.2
Reinforcement	Bound.	Long.	4 - #8	16 - #7 and 4 - #3	4 - #3	16 - #5 and 4 - #3
		Trans.	#3 @ 3"	#3 @ 2.25"	#3 @ 3"	#3 @ 2.25"
	Web	Long.	18 - #5	12 - #3	6 - #3	12 - #3
		Trans.	#6 @ 6"	#4 @ 4.5"	#4 @ 6"	#4 @ 4.5"
#PT Strand			30-0.5"dia.	10-0.6"dia.	19-0.5"dia.	19-0.6"dia.

Table 2-3 Material properties and PT ratio

Wall ID			Specimen 1		Specimen 2	
			Wall 1 (start)	Wall 1 (final)	Wall 3 (start)	Wall 3 (final)
Concrete (ksi)	$f_c^{'}$		6	6	6	6
	$f_{ce}^{'}$		7.8	7.8	7.8	7.8
	$f_{cce}^{'}$		9.8	9.8	9.8	9.8
Steel Reinforcement (ksi)	f_y		60	60	60	60
	f_{ye}		66	66	66	66
	f_{ue}		99	99	99	99
PT Strand (ksi)	f_{py}		220	220	220	220
	f_{pu}		270	270	270	270
	$f_{pi} = 0.61 f_{pu}$		164.7	164.7	164.7	164.7
Axial Force Ratio	Initial PT Force	$P_{pi}/(A_g f_c^{'})$	0.18	0.08	0.11	0.16
		$P_{pi}/(A_g f_{ce}^{'})$	0.13	0.06	0.09	0.12
	Yield PT Force Ratio	$P_{py}/(A_g f_c^{'})$	0.23	0.11	0.15	0.21
		$P_{py}/(A_g f_{ce}^{'})$	0.18	0.08	0.11	0.16
PT Ratio			0.49	0.34	0.84	0.63

Table 2-4 Wall detailing based on ACI 318-11 (ACI 2011)

	ACI 318-11		Wall 1	Wall 2
	Section	Requirement		
Minimum web reinforcement ratio	21.9.2.1	$\rho_l = 0.0025$	0.003	0.003
		$\rho_t = 0.0025$	0.00889	0.00889
Maximum reinforcement spacing	21.9.2.1	7.2 in*	7.0 in*	7.0 in*
Maximum nominal shear strength	21.9.4.4	$10\sqrt{f'_c}$	$6.4\sqrt{f'_c}$	$6.4\sqrt{f'_c}$
Nominal moment	In accordance to 10.2 and 10.3	Mn	32397 kip-in	31473 kip-in
Neutral axis	In accordance to 10.2 and 10.3	c	12.7 in	18.1 in
Horizontal length of boundary element from end of the wall	21.9.6.4 (a)	Not less than the larger of $c-0.1L_w$ and $c/2$	14.5 in	14.5 in
Vertical length of boundary element	21.9.6.2 (b)	Minimum 72 in	90 in	90 in
Spacing of boundary element transverse reinforcement	21.6.4.3	Minimum of: 3.33 in 2.25 in 6 in	2.25 in#	2.25 in#
Minimum amount of boundary transverse reinforcement	21.6.4.4 (b) Eq. (21-5)	x direction=0.167 in^2	0.22 in^2	0.22 in^2
		y direction=0.268 in^2	0.44 in^2	0.44 in^2
Web horizontal reinforcement extension to the boundary element	21.9.6.4 (e)	Maximum 6 in from the end of wall	3.5 in	3.5 in

*This is a 40% scaled value
#This is not scaled

Table 2-5 Shear capacity according to ACI 318-11 (ACI 2011)

Wall ID	Wall 1	Wall 2
Mn (kip-in)	32397	31473
V_{dMn} ($\sqrt{f'_c}$)	3.87	3.77
V_n ($\sqrt{f'_c}$)	6.4	6.4
$\varphi_f V_{dMn}$ ($\sqrt{f'_c}$)	3.48	3.48
$\varphi_v V_n$ ($\sqrt{f'_c}$)	4.8	4.8
$\varphi_v V_c$ ($\sqrt{f'_c}$)	1.5	1.5
$\varphi_v V_s$ ($\sqrt{f'_c}$)	3.3	3.3

Note:
V_s is determined based on the assumption that the crack makes 45 degree angle with the vertical direction of the wall.
φ_f=0.9 and φ_v=0.75 (ACI. 2011)

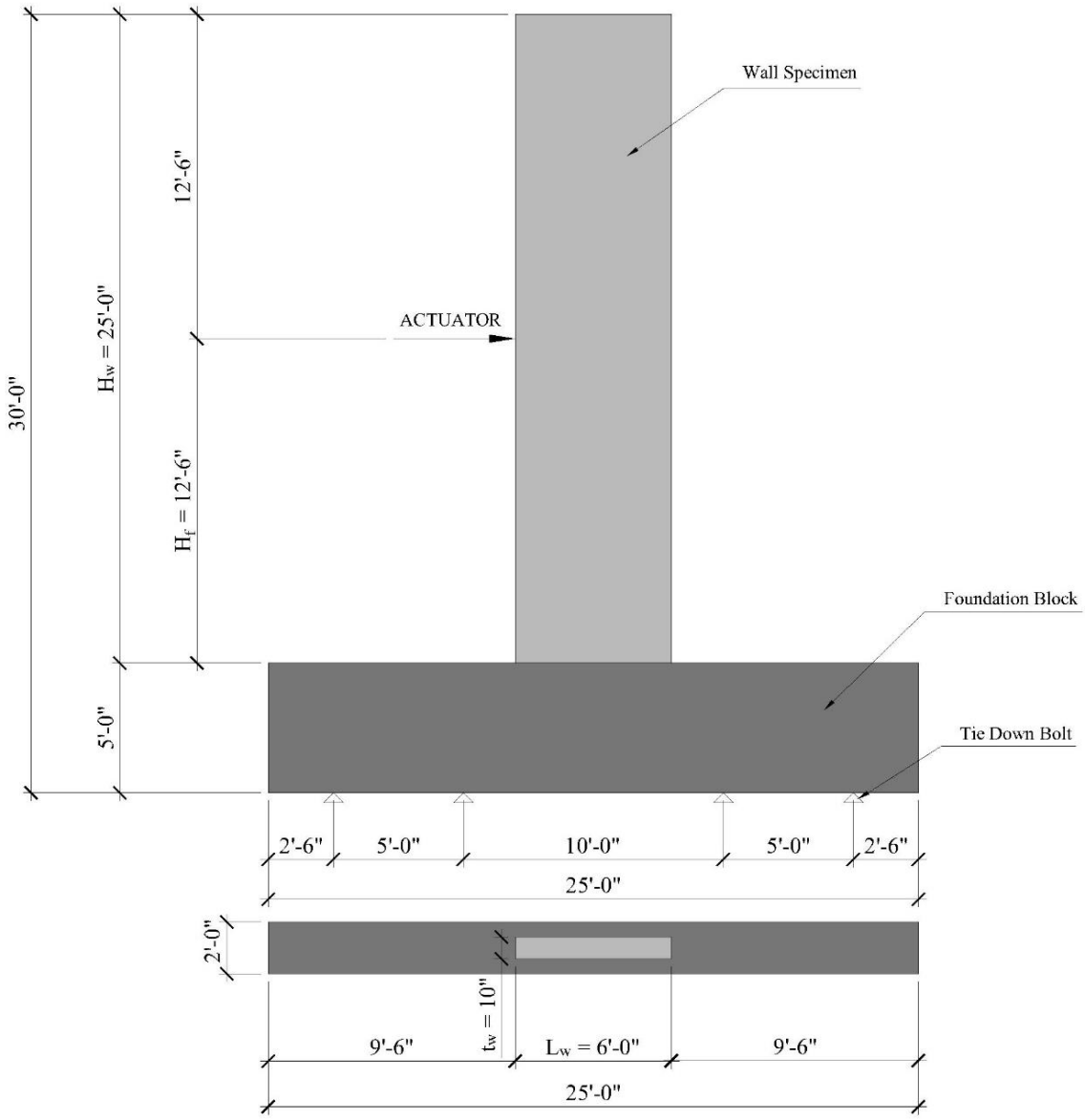

Figure 2-1Geometry of test specimen

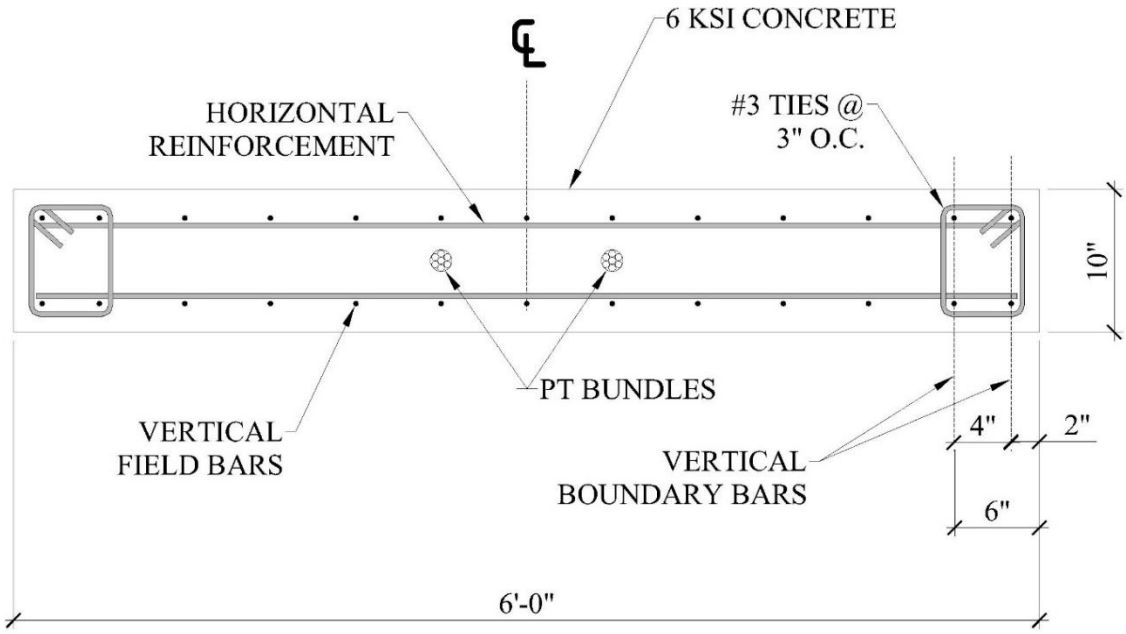

Figure 2-2 Typical cross section of studied walls (adapted from Tipping Mar 2011)

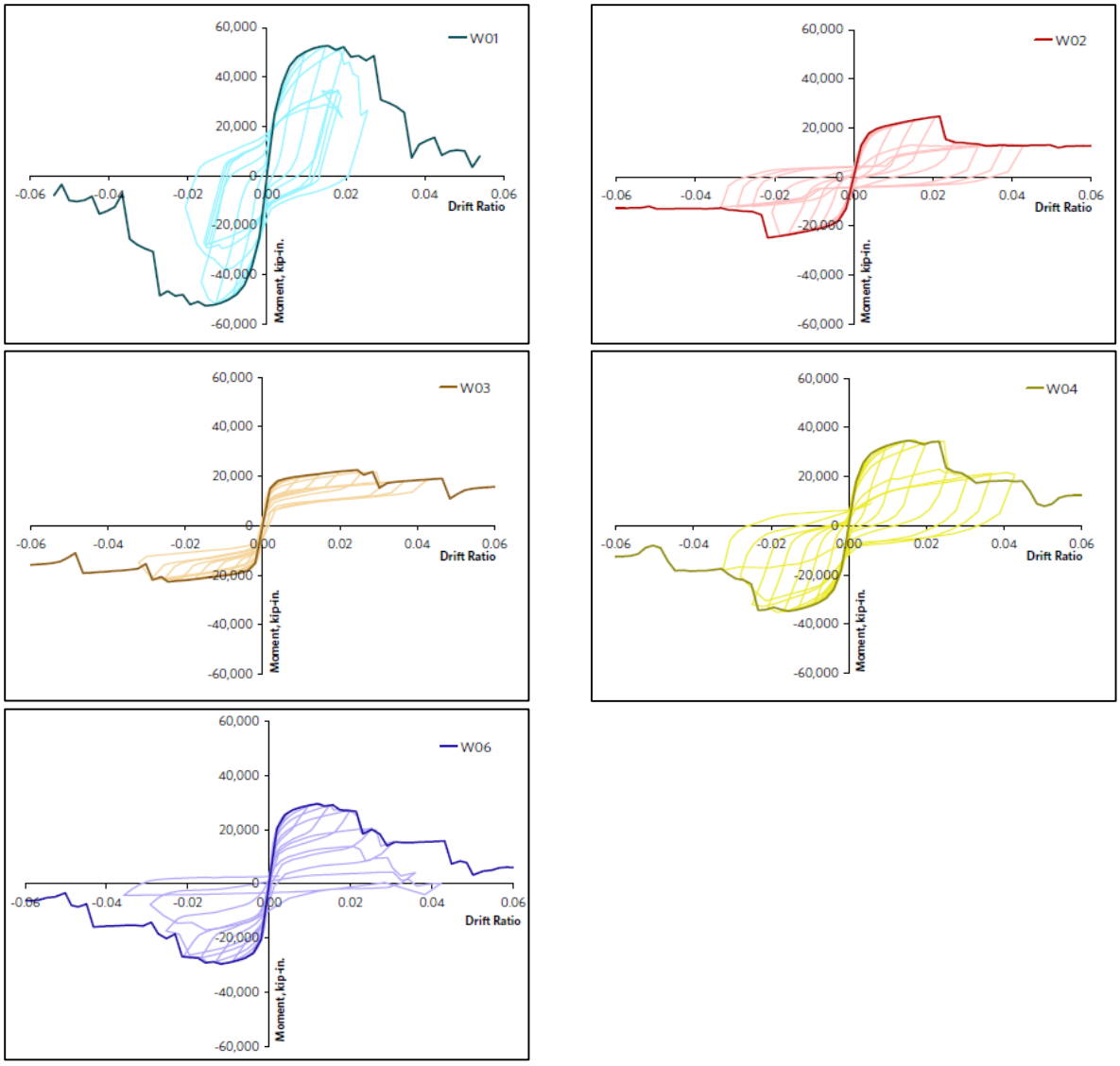

Figure 2-3 Wall responses (adapted from Tipping Mar 2011)

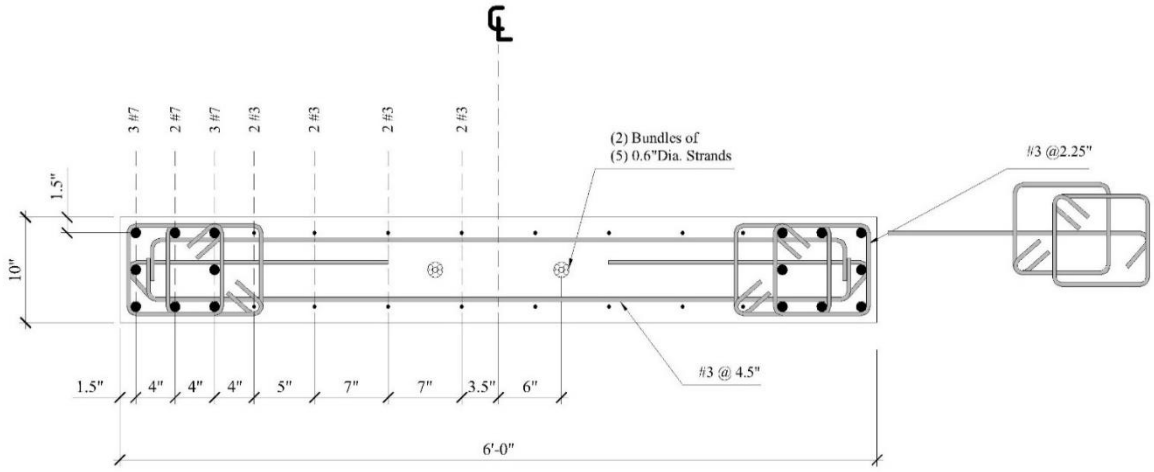

(a)

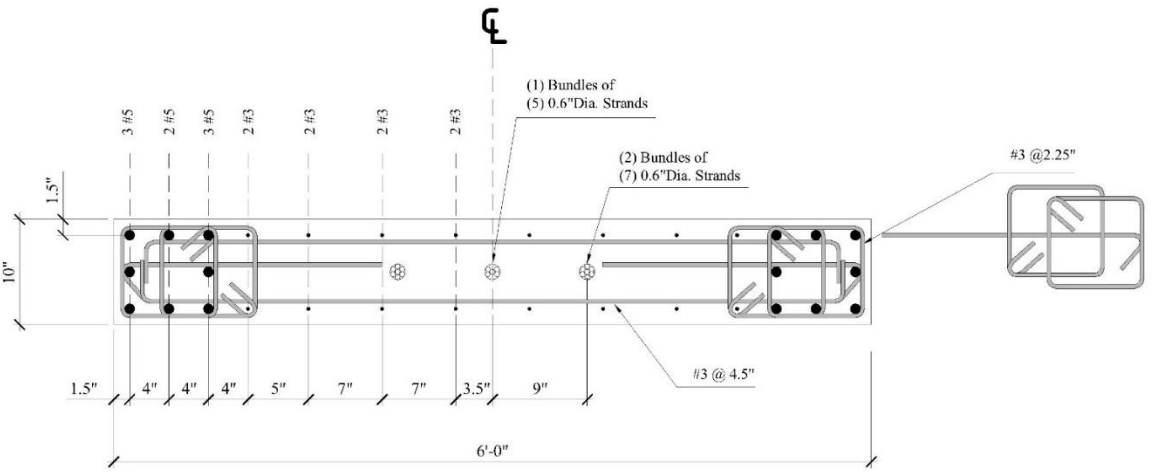

(b)

Figure 2-4 Wall cross sections at final iteration: (a) Wall 1, (b) Wall 2

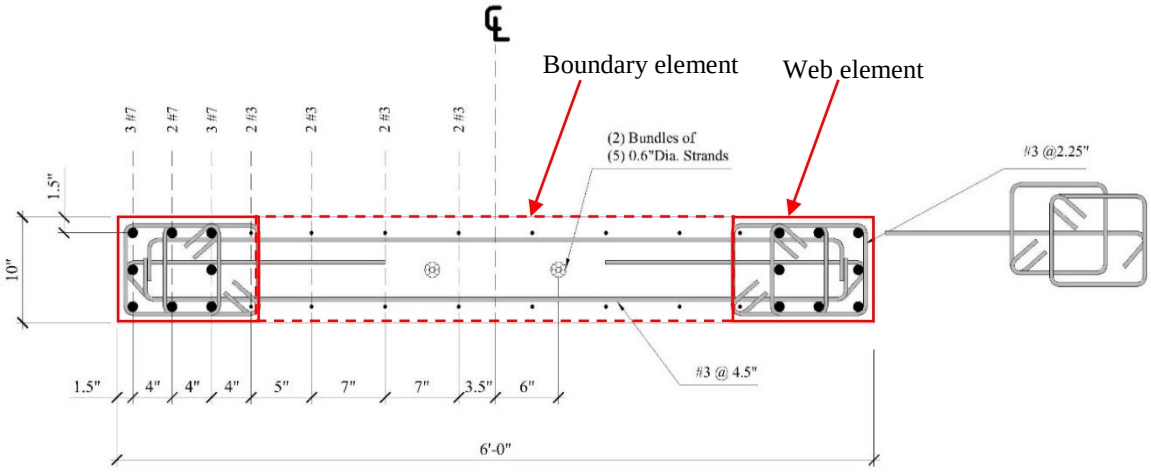

Figure 2-5 Parts of wall

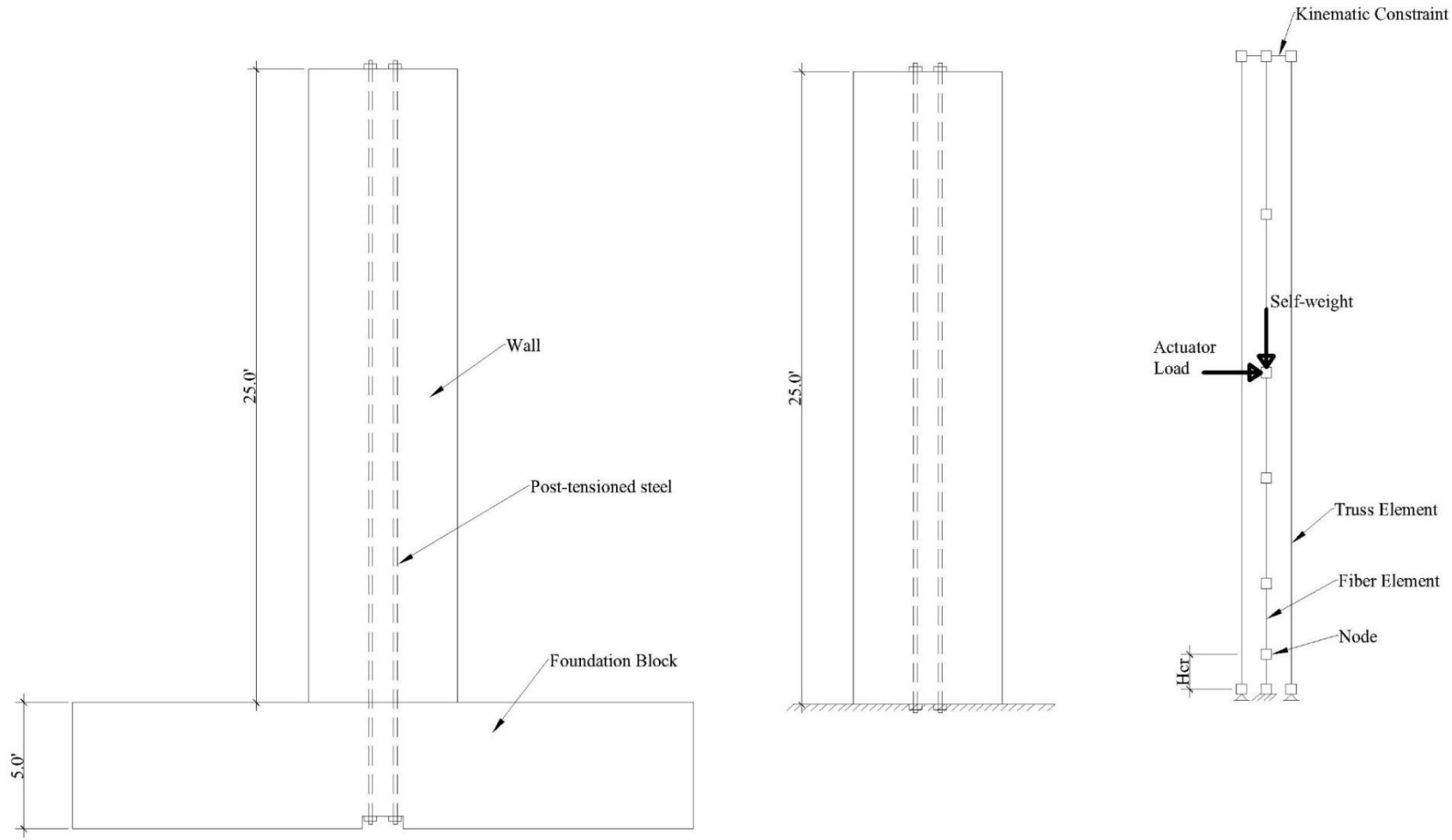

Figure 2-6 Wall idealization: (a) actual geometry, (b) simplified geometry, (c) idealized geometry in DRAIN-2DX

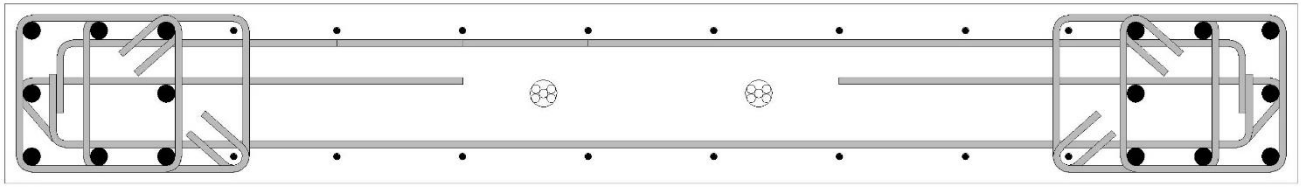

(a)

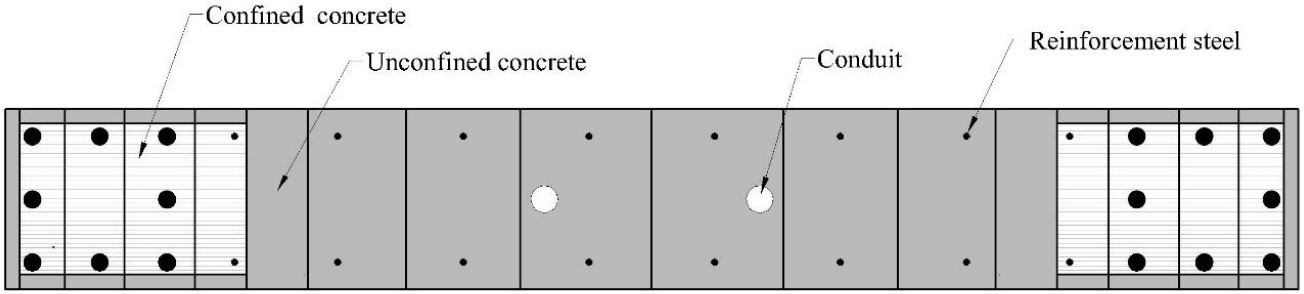

(b)

Figure 2-7 Cross section idealization: (a) actual cross section, (b) idealized cross section in DRAIN-2DX

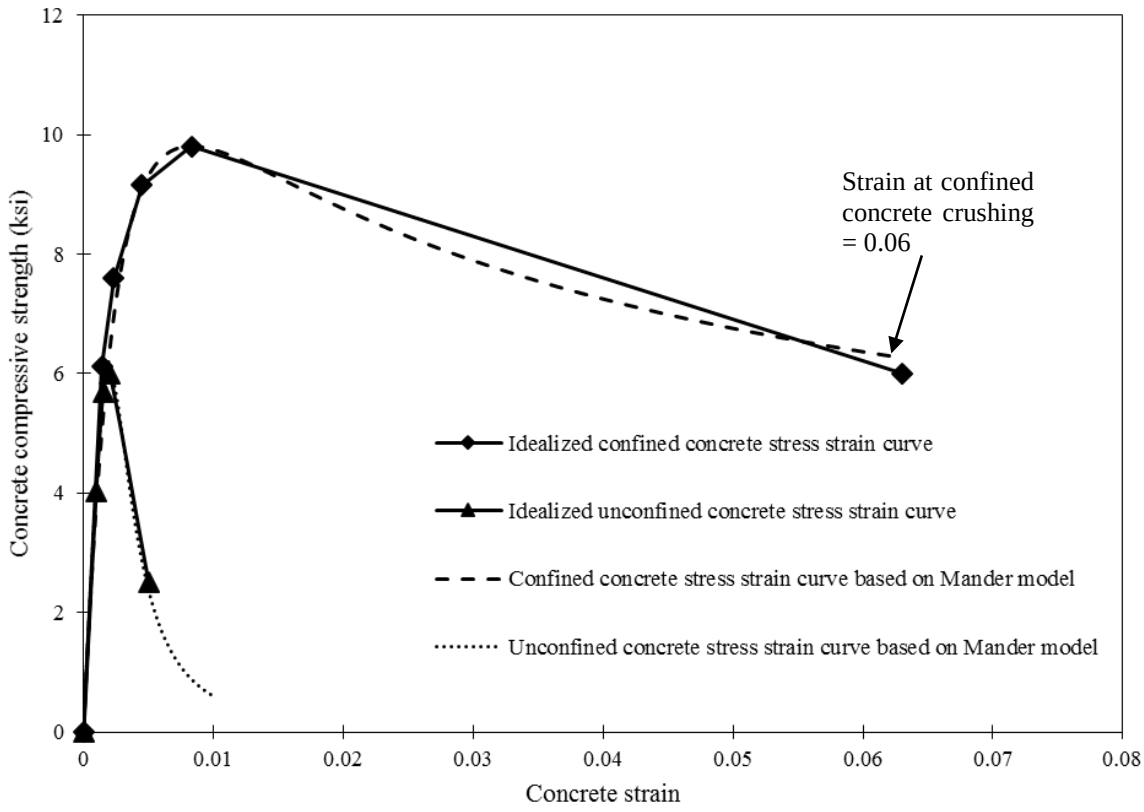

Figure 2-8 Concrete models

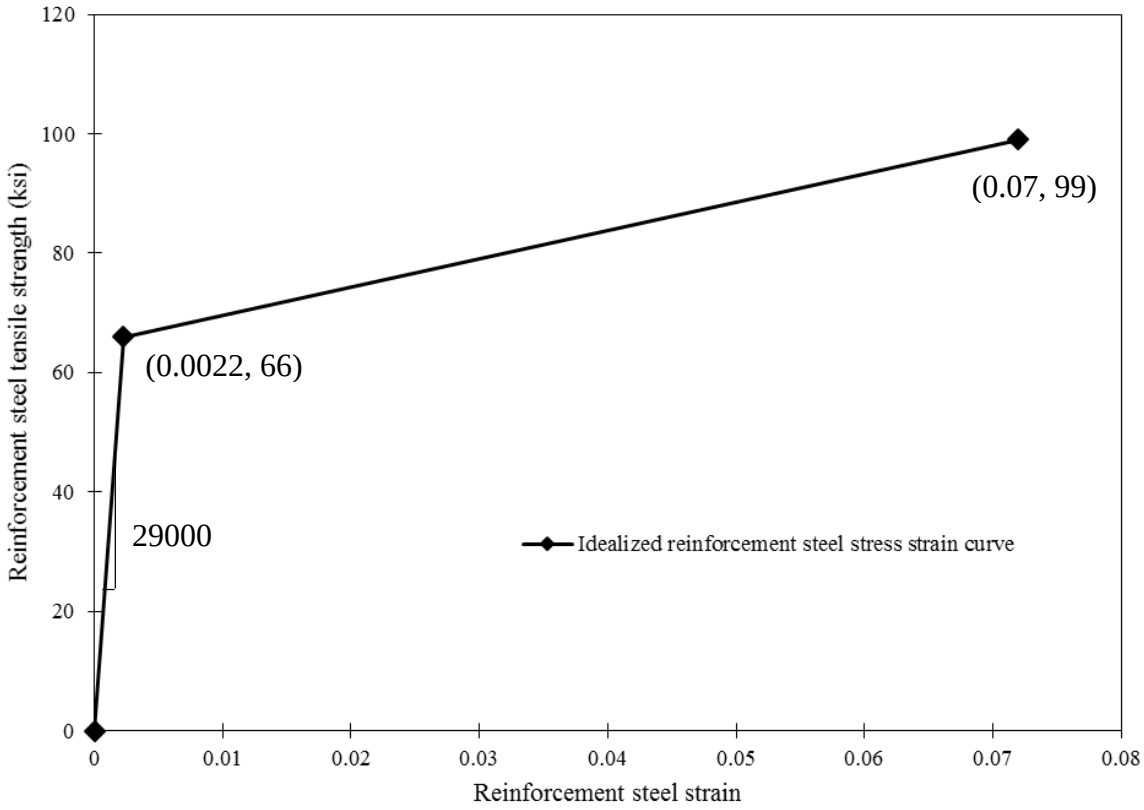

Figure 2-9 Steel reinforcement model

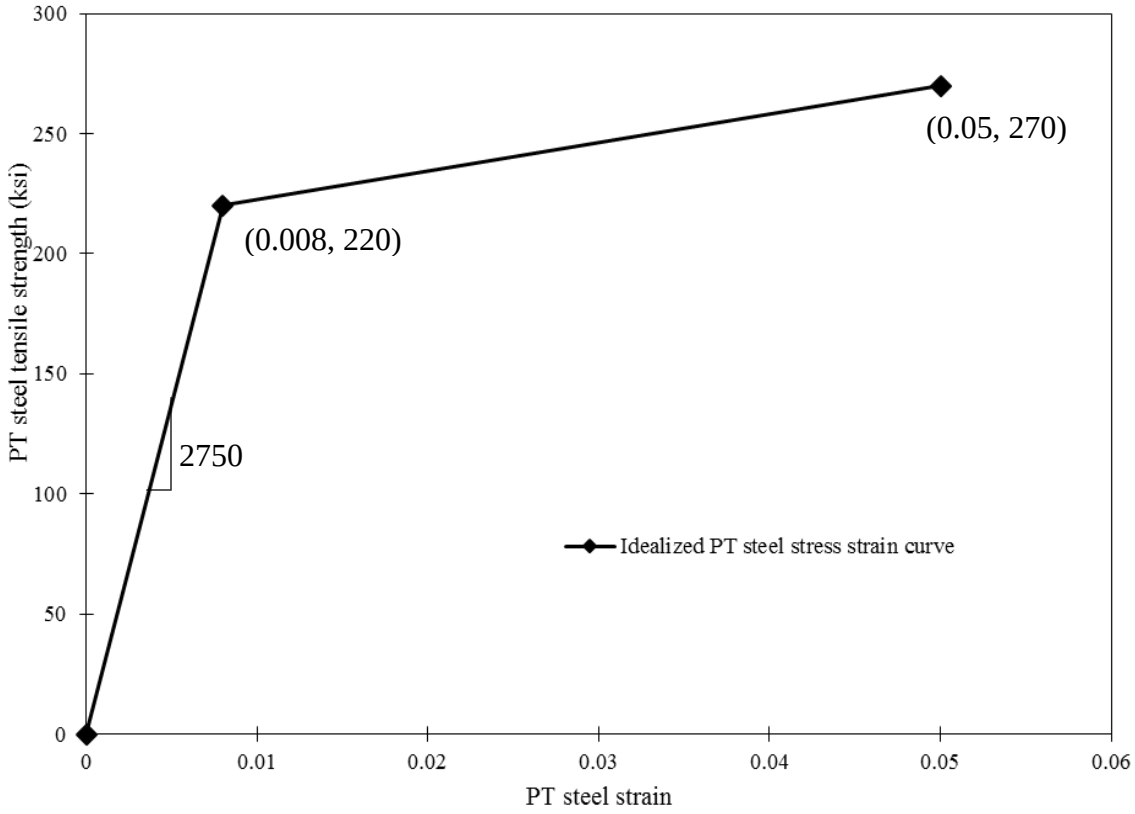

Figure 2-10 Post-tensioned steel model

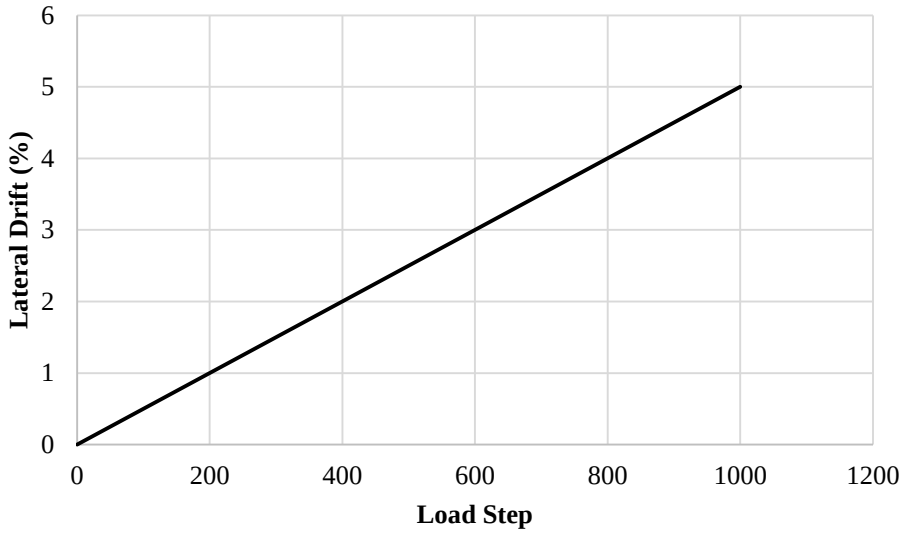

(a)

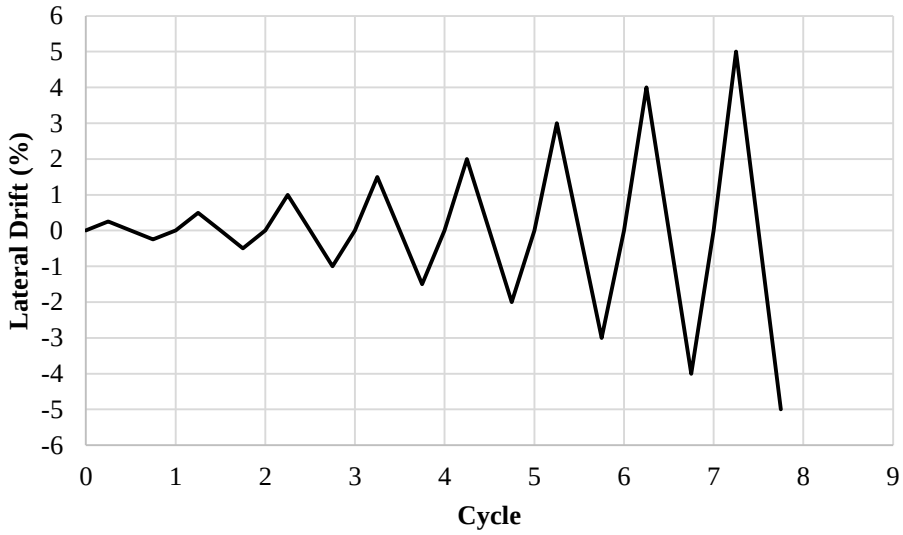

(b)

Figure 2-11 Loading protocol: (a) monotonic load, (b) cyclic load

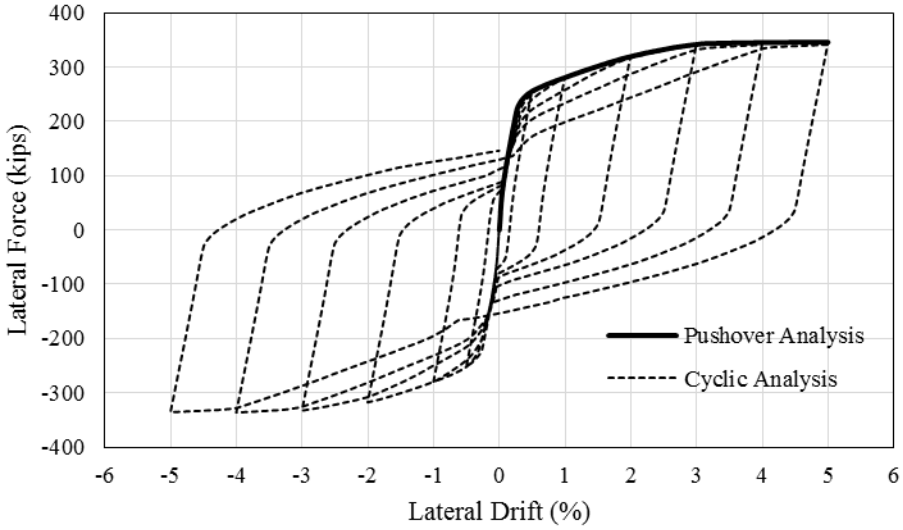

(a)

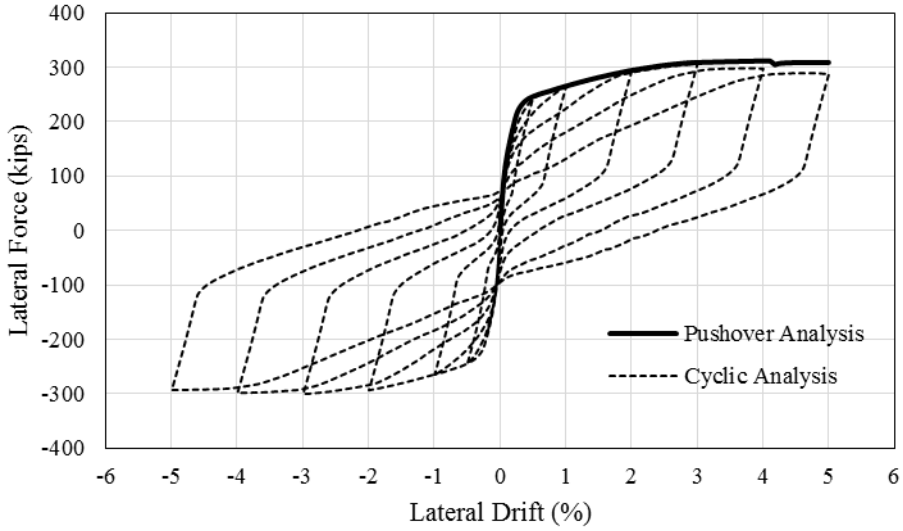

(b)

Figure 2-12 Lateral load response: (a) Wall 1, (b) Wall 2

CHAPTER 3
EXPERIMENTAL PROGRAM

3.1 OVERVIEW

Detailed descriptions of the geometry and reinforcement in Wall 1 and Wall 2 were given in Rivera et al. (2013). In this chapter, revisions in the experimental set-up, instrumentation, and loading history of Wall 2 are given. In addition, a complete description of wall number three is presented.

3.2 WALL 1

3.2.1 OVERALL WALL GEOMETRY AND TEST SET UP

The description of Wall 1 is given in the companion report by Rivera et al. (2013).

3.2.2 INSTRUMENTATION AND DATA ACQUISITION

The instrumentation and data acquisition details for Wall 1 are given in the companion report by Rivera et al. (2013).

3.2.3 MATERIAL PROPERTIES

Material properties for Wall 1 were not included in Rivera et al. (2013). Table 3-1, Table 3-2, and Table 3-3 show the material properties of concrete, steel reinforcement, and post-tensioned steel, respectively.

Concrete compression test results shown in Table 3-1 are for the wall. Each wall was cast in four pours. No concrete cylinders tests were performed for the last pour for Wall 1. Pour 1 shown in Table 3-1 represents the base of the wall at the top of the foundation.

Two grades of steel reinforcement were used in the wall, namely ASTM A615 and ASTM A706. For #3 bars, ASTM A615 was used due to the limitation on the availability ASTM A706 at the time. According to ACI 318-11, this is allowed only if the minimum yield strength requirement as well as the ratio of tensile strength to yield strength is satisfied. These requirements were satisfied as can be seen in Table 3-2. The requirement regarding minimum elongation based on ASTM A706 was not satisfied for most of the steel reinforcement tension test specimens.

Material properties for post-tensioned steel were based on the data provided by the fabricator (Dywidag System International). No material tests were performed.

3.3 WALL 2

3.3.1 OVERALL WALL GEOMETRY AND TEST SET UP

The geometry of Wall 2 was the same as for Wall 1 as shown in Figure 3-1 and Figure 3-2. Wall length was 72 inch with a width of 10 inch. Total wall height measured from the top of foundation block was 265 inch. The wall had two main parts, the boundary element and web element. The boundary element consisted of 8 #7 and 2 #3 longitudinal steel reinforcements which were confined by #3 steel hoops with 2.25 inch spacing. The web element contained 12 #3 longitudinal steel reinforcements and #4 transverse steel reinforcements with 4.5 inch spacing. There were three groups of post-tensioned steel in

the wall, two groups of 7 strands and one group of 5 strand, as shown in Figure 3-1. The strand comprised of seven-wire steel and the diameter was 0.6 inch. Initial prestressing forces were 239.9 kips, 173.5 kips, and 241 kips in the first group, second group, and third group of post-tensioned steel respectively (refer to Figure 3-3 for the designation of post-tensioned groups).

In general, the same set up as for the first test wall was used in the test and it is shown in Figure 3-3. The foundation block was clamped to the strong floor to prevent sliding at the interface. Steel beams at two levels provided bracing the wall from out of plane movement during the test. Polytetrafluoroethylene (Teflon) was used to prevent friction between the steel beams and wall surfaces. The detail attachment of Teflon on the surface of the wall is slightly different than that of test wall one. Figure 3-4 (a) shows the attachment of Teflon on the wall. Instead of gluing the Teflon steel plates directly on the wall surfaces, they were first tact welded to steel angles (one steel angle has two Teflon steel plates on East and West ends) and then attached to the wall surfaces by clamping both angles on North and South face of the wall using threaded rods. Since the length from strong wall to the side of the wall was longer than actuator length, a steel bracket which attached to the strong wall was used for extension as in Rivera et al. (2013). One side of the actuator's clevis foot was clamped to the steel bracket and the other side was attached to the West side of the wall. To prevent sliding between the interface of actuator's clevis foot and the wall, a total of eight-one inch diameter threaded rods (four threaded rods were placed on each North and South sides of the wall) were used to clamp the wall on the direction of loading.

The location of Wall 2 with respect to the reaction wall was five feet further away compared to Wall 1 location as shown in Figure 3-5. Therefore, longer steel bracket was used as shown in Figure 3-6. In order to prevent lateral displacement of this bracket, it was braced horizontally to the strong wall using two diagonal parallel angles which were clamped at the top and bottom flanges of top chord of the steel bracket. These angles are also depicted in Figure 3-6.

3.3.2 INSTRUMENTATION AND DATA ACQUISITION

Several types of instrumentations were used in the experiment to collect data such as loads, displacements, rotations, strains and gap opening.

In addition to the load cells used for Wall 1 (two load cells) (Rivera et al. 2013), another load cell was added for measuring the post-tensioned force. Its capacity was the same as to the other two load cells, namely 450 kips. The three load cells are shown in Figure 3-7.

Two displacement transducers (Temposonic) were used to measure the horizontal displacement at the loading point, one at each side (East and West sides). The arrangement of these displacement transducers is depicted in Figure 3-3.

There were seven string potentiometers and four linear variable displacement transformers (LVDTs) used to measure vertical and horizontal displacements of the wall and to measure the horizontal and vertical movements of the foundation block respectively. The set-up of these instruments is shown in Figure 3-8.

Figure 3-9 shows a total of eight LVDTs and three rotation meters placed in the wall on the North face. The vertical and diagonal arrangements of these LVDTs on the wall surface were meant to measure shear deformation while the rotation meters were used for measuring the rotations of the base and of the wall.

There were in total sixty-nine strain gauges mounted in the wall to measure strain in the steel reinforcement. Thirty strain gauges were installed on the longitudinal reinforcements at the boundary elements as depicted in Figure 3-10; nineteen strain gauges were installed on the steel hoops at the boundary elements as can be seen in Figure 3-11; twenty strain gauges were placed on the transverse reinforcement at the web element as shown in Figure 3-12. Two strain gauges that were installed on #3 steel reinforcements with length of 16.5 inch were used for measuring strain in the confined concrete at the boundary elements. They were embedded in the center core of each boundary element as shown in Figure 3-13.

Displacement transducers (plastic slides) were used to measure the gap opening at the base of the wall. There were 5 plastic slides used in this experiment as shown in Figure 3-14.

A data logger was used for data acquisition and in total there were 104 data channels of instrumentation. Data was sampled and recorded at a frequency of 1 reading per second.

3.3.3 MATERIAL PROPERTIES

The following describes properties of the concrete, reinforcement steel, and post-tensioned steel used to construct the wall.

Concrete for the wall was poured in four pours as to that of Wall 1 (Rivera et al. 2013). The height of the first three pours was six feet each and for the final pour it was four feet and one inch. The nominal compressive strength of concrete was 6 ksi. The actual average compressive strength which was based on two cylinders tests for each pour at the test day is given in Table 3-4.

Two different types of steels were used in the wall, ASTM A706 steel and ASTM A615 steel. ASTM A706 steel was used for #5 longitudinal steel reinforcement, #3 steel hoops on the boundary element and #4 horizontal steel reinforcement on the web element while ASTM A615 steel was for #3 longitudinal steel reinforcement in the web. The nominal yield strength of the steel reinforcement was 60 ksi. Based on tensile tests of four specimens of #5 ASTM A706 longitudinal steel reinforcements, they have an average yield strength of 63.3 ksi and an average tensile strength of 87.7 ksi. As for #3 ASTM A615 longitudinal steel reinforcements (4 test specimens), the average yield strength and the average tensile strength were 68.8 ksi and 108.2 ksi respectively. Table 3-5 summarizes the results from tensile tests of #5 and #3 steel reinforcements. The ACI 318-11 requirements on the minimum yield strength and on the minimum ratio of yield strength to tensile strength were satisfied for ASTM A615 steel reinforcement used in this wall. The requirement of minimum elongation given by ASTM A706 was not satisfied.

As mentioned previously, the post-tensioned strands used in the wall were seven-wire 0.6-inch diameter strands. There were no specimen tests for these strands. Material properties of the strands were based on the manufacturer information and are shown in Table 3-3.

3.4 WALL 3

3.4.1 OVERALL WALL GEOMETRY AND TEST SET UP

The geometry of Wall 3 was similar to that of Walls 1 and 2 as can be seen in Figure 3-1 and Figure 3-2. The size and dimension of steel hoops at the boundary elements and of the longitudinal and transverse steel reinforcement in the web were the same as to those of the previous test walls. The main difference in Wall 3 was the detailing of longitudinal steel reinforcement in the boundary elements. In each boundary element there were 11 #7 bars. The first two rows of the longitudinal steel reinforcement (5 bars total) from outer edge of the wall at each boundaries were terminated at the interface of the foundation block and the wall which created discontinuity of these steel reinforcement while entering the foundation block. The subsequent two rows of the longitudinal steel reinforcement (6 bars total) were debonded using plastic sheet over 48 inch above the top of foundation block and over one inch below the top of foundation block.

The number and arrangement of the post-tensioned steel in Wall 3 were similar to Wall 2. Compared to Wall 2, the applied initial post-tensioning force in Wall 3 was different. The initial post-tensioning force for the first, second, and third post-tensioned groups were 247 kips, 198.9 kips, and 255.4 kips respectively.

The experimental setup for Wall 3 was similar to the experimental setup for Wall 2. This setup can be seen in Figure 3-3, Figure 3-5, and Figure 3-6. The only difference was in how the Teflon was attached on the wall surface compared to the first two test walls. The Teflon attachment is shown in Figure 3-4(b). For this wall, the steel plates (glued to the Teflon) were attached on the wall surfaces by screwing anchor bolts on the plates into the wall.

3.4.2 INSTRUMENTATION AND DATA ACQUISITION

Wall 3 instrumentation was the same as was used for Wall 1 and Wall 2. The locations of displacement transducers (Temposonic) at the height of loading point are depicted in Figure 3-3. Figure 3-8 shows the locations of the LVDTs and string potentiometers for measuring the horizontal and vertical movements of the wall and foundation block. There was an additional LVDT which has a range of ±1.0 inch placed on the East side of the wall (referred as ABS_DISPL in Figure 3-8) at the Temposonic level. This instrument was meant to capture better the displacement at low lateral drift level.

Figure 3-9 shows the arrangement of LVDTs and rotation meters that were placed on the North face of the wall. Figure 3-10 shows the strain gauges that were installed on the longitudinal bars in the boundary elements. In total there were 12 strain gauges placed on these longitudinal bars. 20 strain gauges were placed on the steel hoops on the boundary elements. The arrangement of these instruments is shown in Figure 3-11. Figure 3-12 shows the ten strain gauges that were installed on the transverse steel reinforcement on the

web of the wall. Figure 3-14 shows the arrangement of five plastic slides that were used to measure the gap opening at wall base.

3.4.3 MATERIAL PROPERTIES

Material properties of concrete, reinforcement steel, post-tensioned steel, and grout are shown in Table 3-6, Table 3-7, Table 3-3, and Table 3-8 respectively.

The average concrete compressive strengths for each wall pour and the corresponding ages at testing day are tabulated in Table 3-6. For the first six feet height of the wall (first pour), the average concrete compressive strength was 5.1 ksi. It is noted that this compressive strength was smaller than the nominal concrete compressive strength of 6 ksi.

The average yield strength and ultimate strength of #3 ASTM A615 steel were 70.1 ksi and 111.9 ksi respectively. For #7 ASTM A706 steel, the average yield strength was 75.9 ksi and the average tensile strength was 108.3 ksi. ACI 318-11 requirements on the minimum tensile strength and the minimum ratio of yield strength to tensile strength of these steel reinforcement were satisfied. For most of the steel bars specimens, the requirement of minimum elongation given by ASTM A706 was not satisfied.

Post-tensioned material properties were exactly the same to that of previous test walls have. The nominal yield strength and tensile strength of the strand were 243 ksi and 270 ksi respectively.

Non-shrinkage grout was used in the wall for patching the voids in the first pour of the wall. The grout has compressive strength of 6.4 ksi based on the test of 2 in x 2 in x 2 in grout cube during the test day of the wall.

Table 3-1 Measured concrete properties Wall 1

Concrete Pour	Height	Compressive Strength (f'_c) (ksi)	Age* (days)
1	6 ft	6.3 (28 day)	N/A
2	6 ft	5.7 (26 day)	N/A
3	6 ft	5.8 (15 day)	N/A

*These are the ages of each concrete segments counted from the day of the segments were poured to the day of the wall testing. N/A indicates that at the day of wall testing there were no concrete cylinders tests.

Table 3-2 Measured steel reinforcement properties Wall 1

Steel Size	Grade	Specimen	Yield Strength (f_y) (ksi)	Tensile Strength (f_t) (ksi)	Elongation (%)
#3	ASTM A615	1 (Heat 1)	68.6	110.1	11.6
		2 (Heat 1)	68.7	110	10.9
		3 (Heat 2)	70.8	111.6	14.4
		4 (Heat 2)	70.5	110.8	13.5
		5 (Heat 3)	67.8	106.2	11.2
		6 (Heat 3)	67.9	104.8	11.4
		7 (Heat 3)	67.9	102.9	13.1
		8 (Heat 3)	66.4	104.7	10.0
#4	ASTM A706	1	64.0	98.6	16.1
		2	61.4	99.1	15.8
		3	65.1	99.2	14.1
		4	64.8	99.3	16.4
		5	64.9	99.4	16.6
#7	ASTM A706	1	75.2	107.9	20.0

Note:

- ACI 318-11 Chapter 21.1.5.2(a) requires that for steel with nominal strength of 60 ksi, the actual yield strength should not exceed 78 ksi.
- ACI 318-11 Chapter 21.1.5.2(b) requires that ratio of actual yield strength to actual tensile strength should be more than or equal to 1.25.
- ASTM A706 requires that minimum elongation at fracture to be 14.0%.
- Yield strength (f_y) was determined based on 0.2% strain offset rule.

Table 3-3 Nominal post-tensioned steel properties Wall 1, Wall 2, and Wall 3

Strand Diameter (in)	Modulus of Elasticity (ksi)	Yield Strength (f_{py}) (ksi)	Tensile Strength (f_{pt}) (ksi)	Cross-sectional area (in^2)
0.6	28000	243	270	0.217

Table 3-4 Measured concrete properties Wall 2

Concrete Pour	Height	Compressive Strength (f'_c) (ksi)	Age* (days)
1	6 ft	6.9	65
2	6 ft	6.3	58
3	6 ft	6.3	49
4	4 ft – 1 in	7.0	39

*These are the ages of each concrete segments counted from the day of the segments were poured to the day of the wall testing.

Table 3-5 Measured steel reinforcement properties Wall 2

Steel Size	Grade	Specimen	Yield Strength (f_y) (ksi)	Tensile Strength (f_t) (ksi)	Elongation (%)
#3	ASTM A615	1	68.8	107.8	13.0
		2	68.0	106.2	9.0
		3	69.7	108.8	9.5
		4	68.8	109.9	11.3
#5	ASTM A706	1	64.1	88.2	13.5
		2	63.4	87.9	18.1
		3	63.0	87.4	18.8
		4	62.8	87.3	16.9

Note:

- ACI 318-11 Chapter 21.1.5.2(a) requires that for steel with nominal strength of 60 ksi, the actual yield strength should not exceed 78 ksi.
- ACI 318-11 Chapter 21.1.5.2(b) requires that ratio of actual yield strength to actual tensile strength should be more than or equal to 1.25.
- ASTM A706 requires that minimum elongation at fracture to be 14.0%.
- Yield strength (f_y) was determined based on 0.2% strain offset rule.

Table 3-6 Measured concrete properties Wall 3

Concrete Pour	Height	Compressive Strength (f'_c) (ksi)	Age* (days)
1	6 ft	5.1	46
2	6 ft	5.3	36
3	6 ft	7.9	32
4	4 ft – 1 in	5.7	25

*These are the ages of each concrete segments counted from the day of the segments were poured to the day of the wall testing.

Table 3-7 Measured steel reinforcement properties Wall 3

Steel Size	Grade	Specimen	Yield Strength (f_y) (ksi)	Tensile Strength (f_t) (ksi)	Elongation (%)
#3	ASTM A615	1	69.2	111.8	12.0
		2	71.1	111.5	9.8
		3	70.1	110.8	8.8
		4	70.1	113.4	10.6
#7	ASTM A706	1	74.8	108.0	10.1
		2	75.6	108.4	13.4
		3	77.1	108.1	11.1
		4	76.1	108.5	15.1

Note:

- ACI 318-11 Chapter 21.1.5.2(a) requires that for steel with nominal strength of 60 ksi, the actual yield strength should not exceed 78 ksi.
- ACI 318-11 Chapter 21.1.5.2(b) requires that ratio of actual yield strength to actual tensile strength should be more than or equal to 1.25.
- ASTM A706 requires that minimum elongation at fracture to be 14.0%.
- Yield strength (fy) was determined based on 0.2% strain offset rule.

Table 3-8 Measured Grout properties Wall 3

Compressive Strength (ksi)	Age* (days)
6.4	21

*These are the age of grout counted from the day of the grout was filled in the concrete voids to the day of the wall testing.

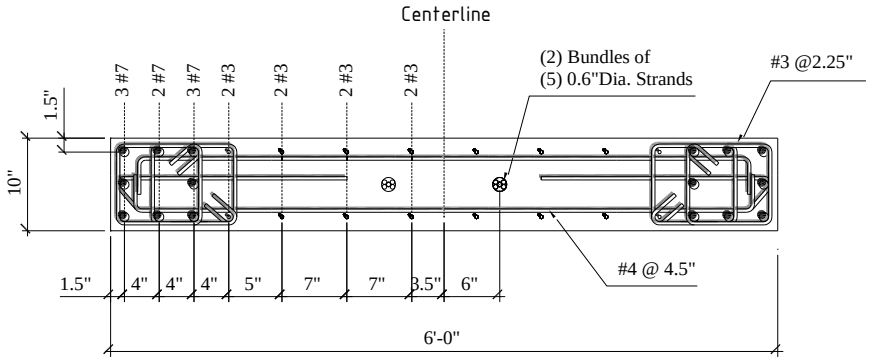

Wall 1

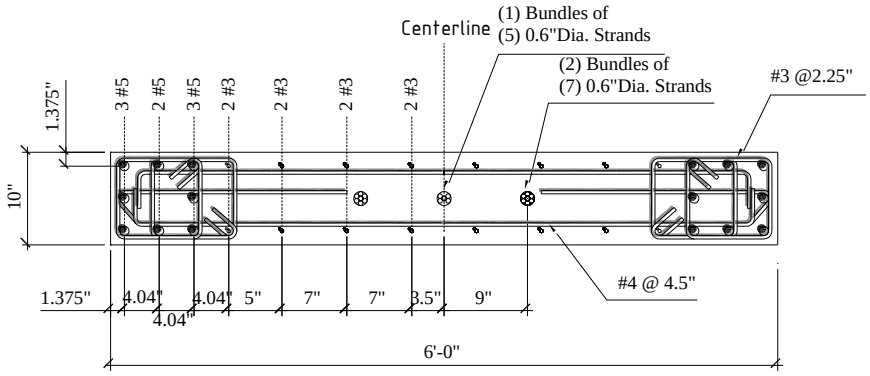

Wall 2

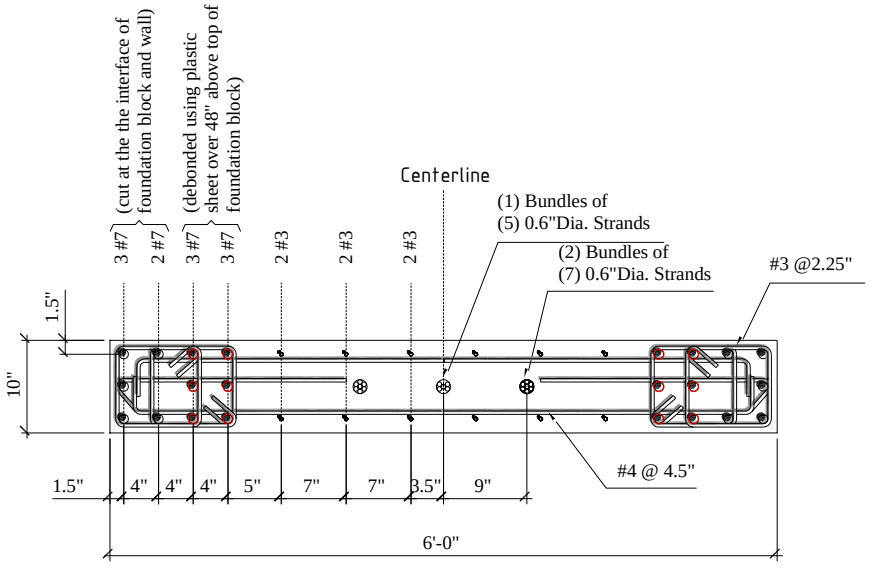

Wall 3

Figure 3-1 Cross sections of test walls

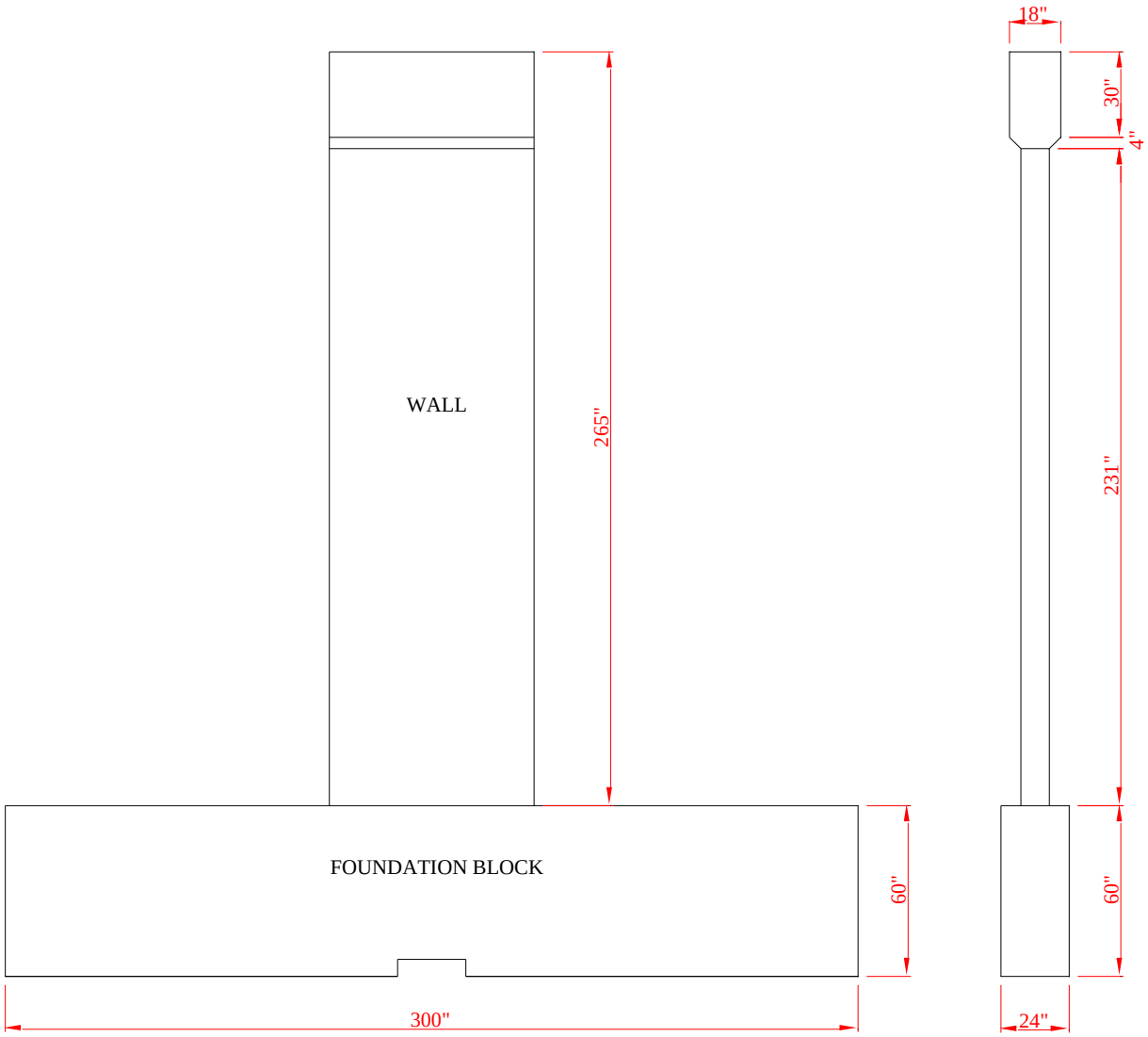

Figure 3-2 Elevation of test walls

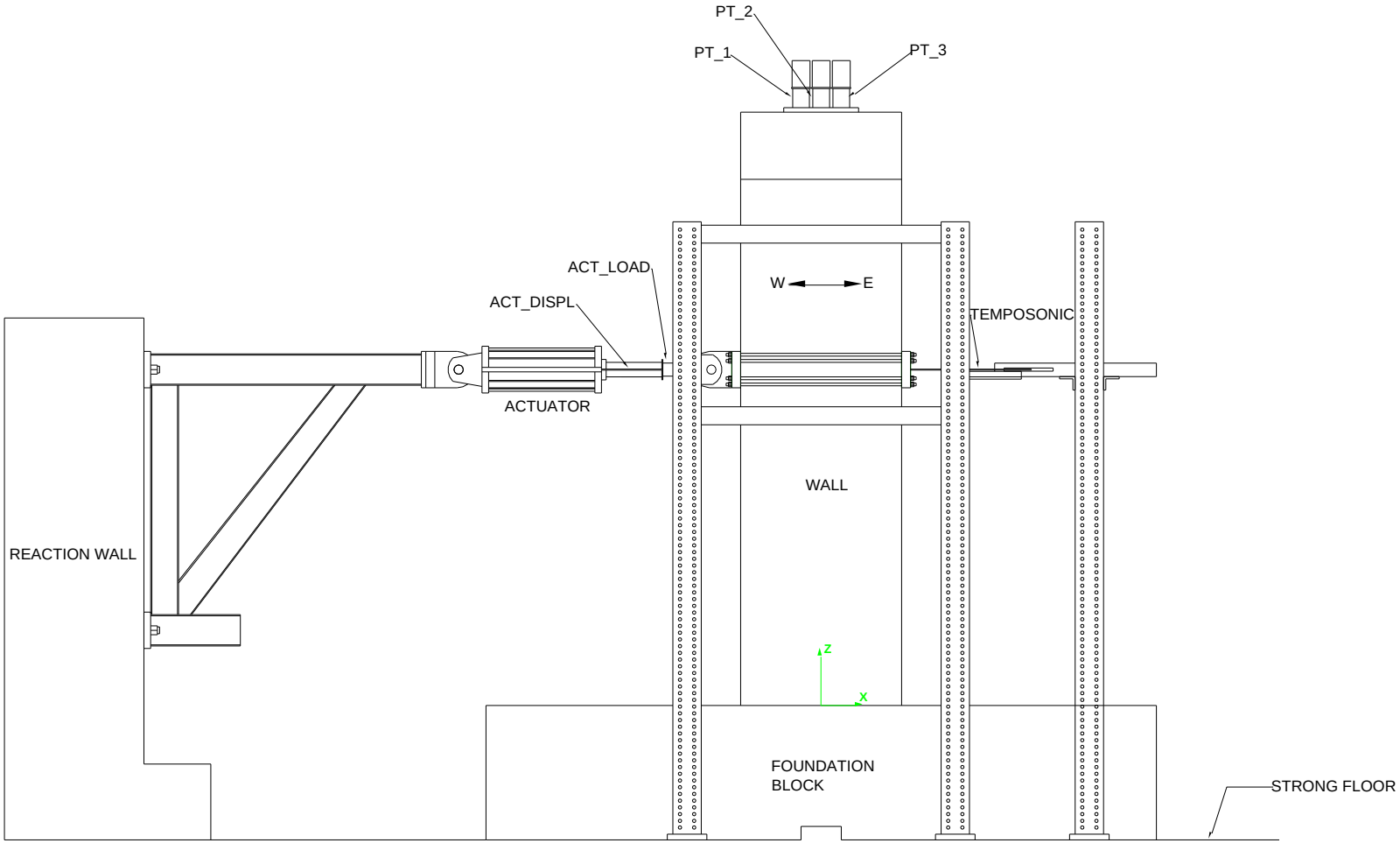

Figure 3-3 Test set up and locations of load cells and Temposonic transducers for Wall 2 and Wall 3

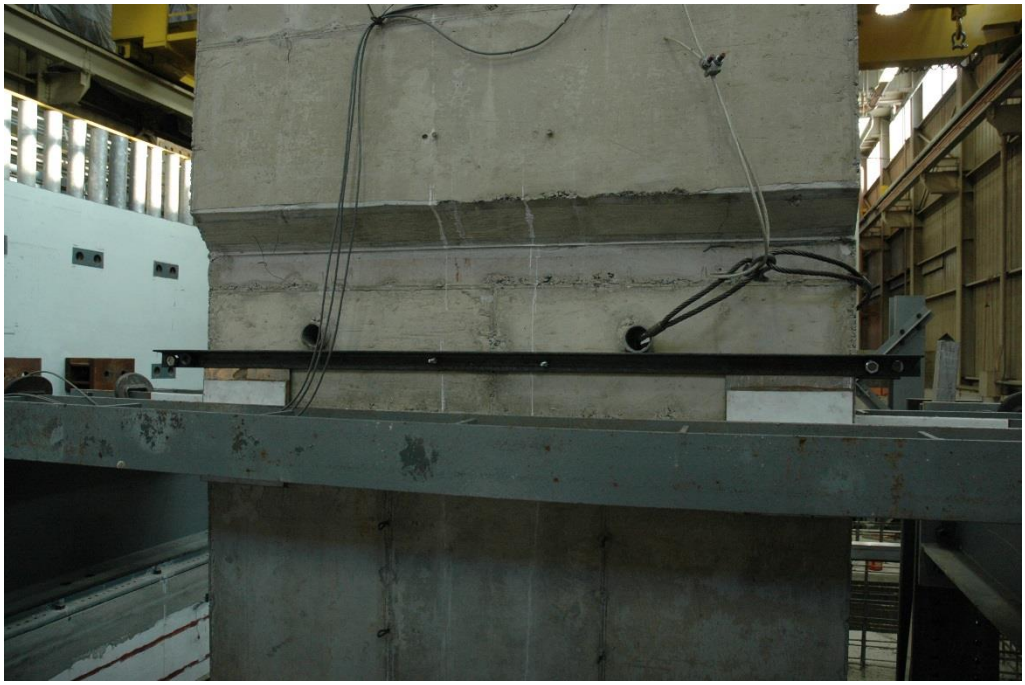

(a)

(b)

Figure 3-4 Teflon attachment: (a) Wall 2, (b) Wall 3

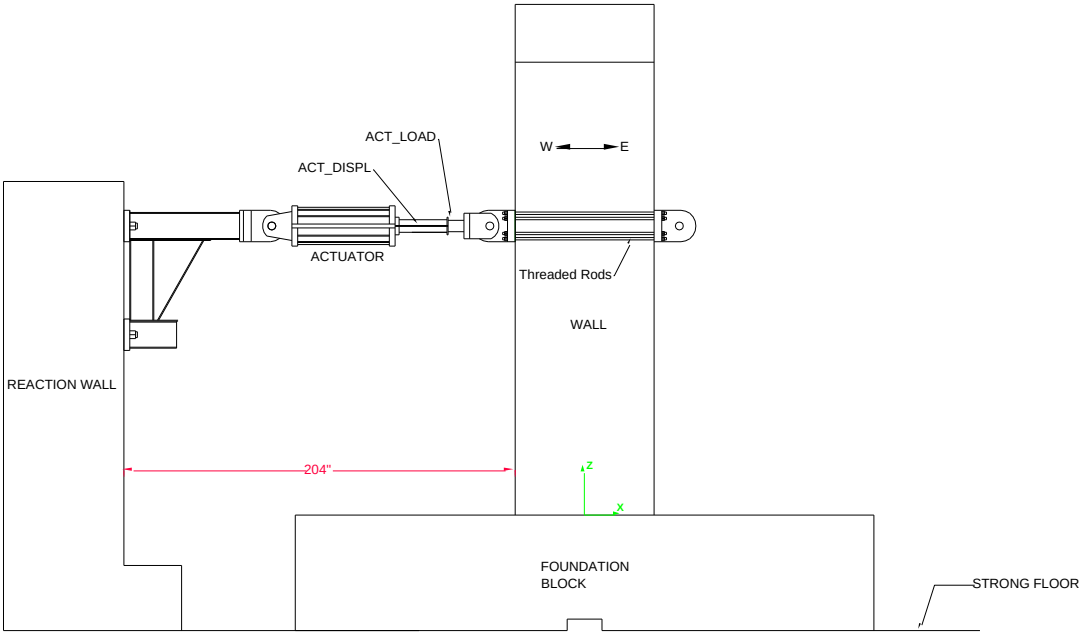

WALL 1

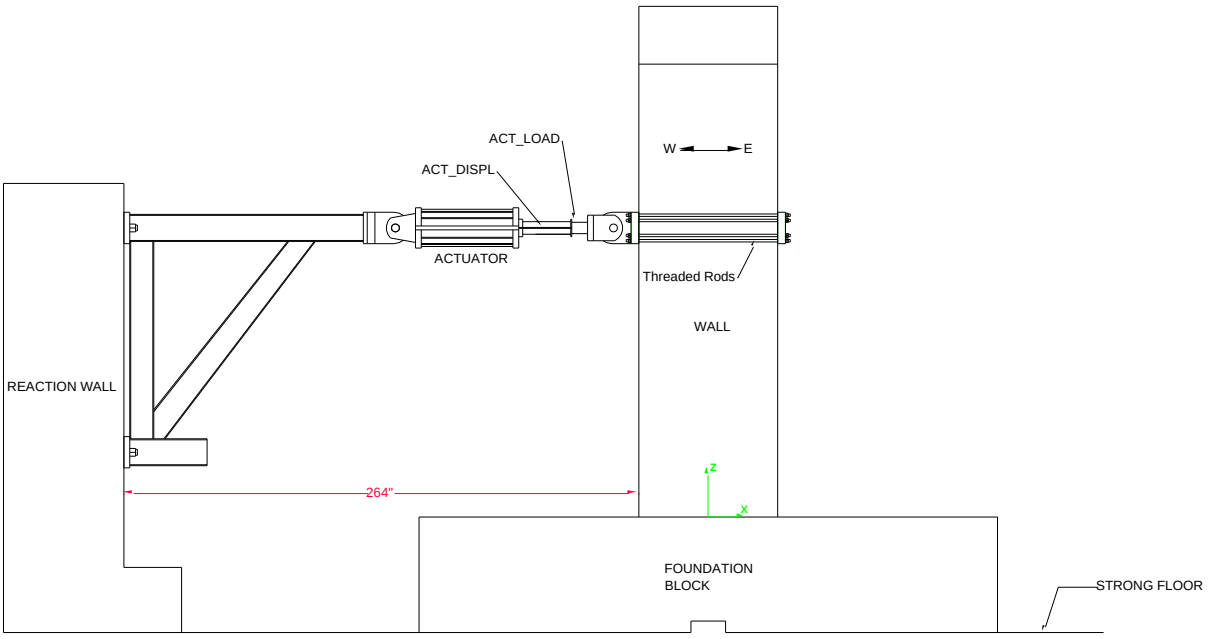

WALL 2 & WALL 3

Figure 3-5 Locations of Wall 1, Wall 2, and Wall 3 with respect to the reaction wall

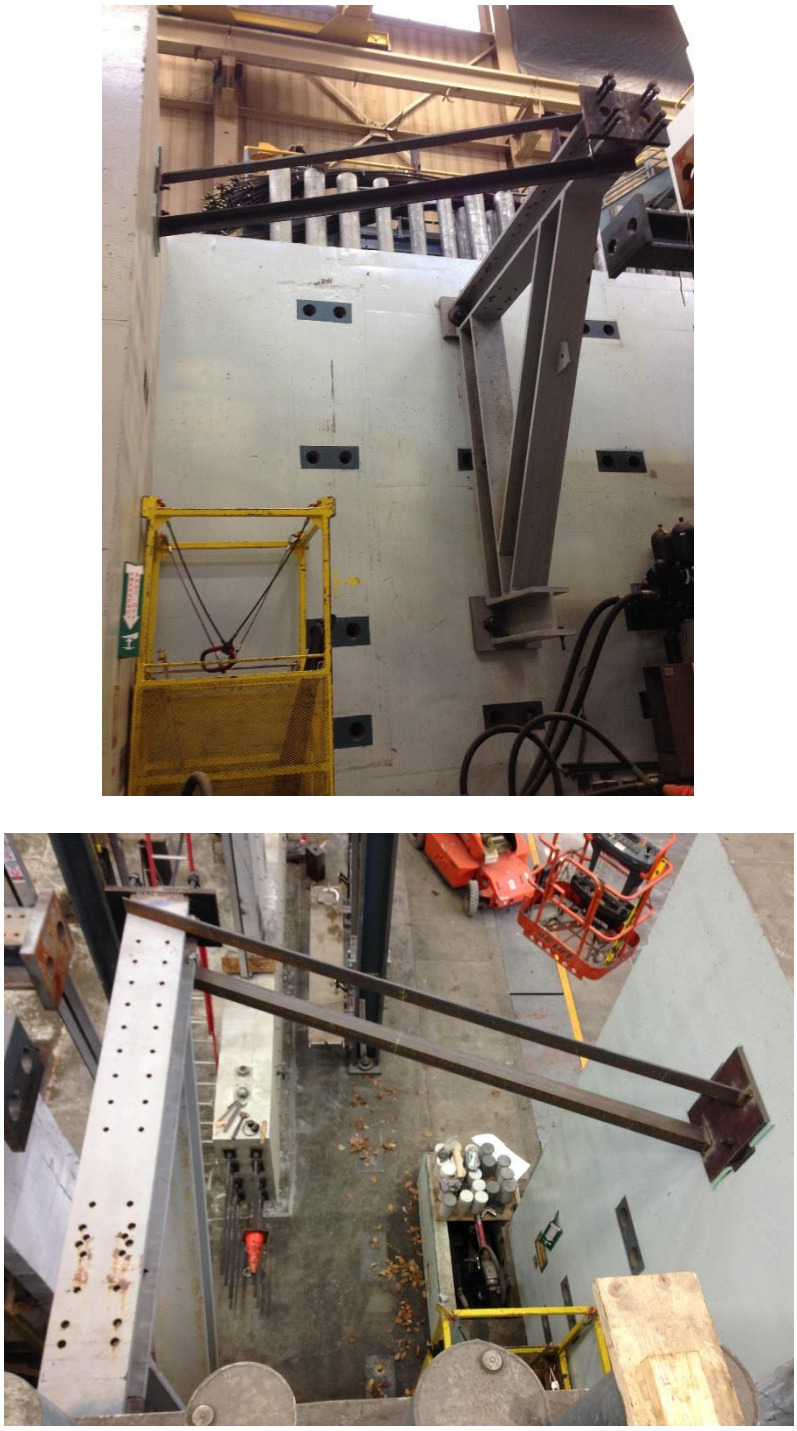

Figure 3-6 Steel bracket and steel angles used in the setup of Wall 2 and Wall 3

Figure 3-7 Load cells

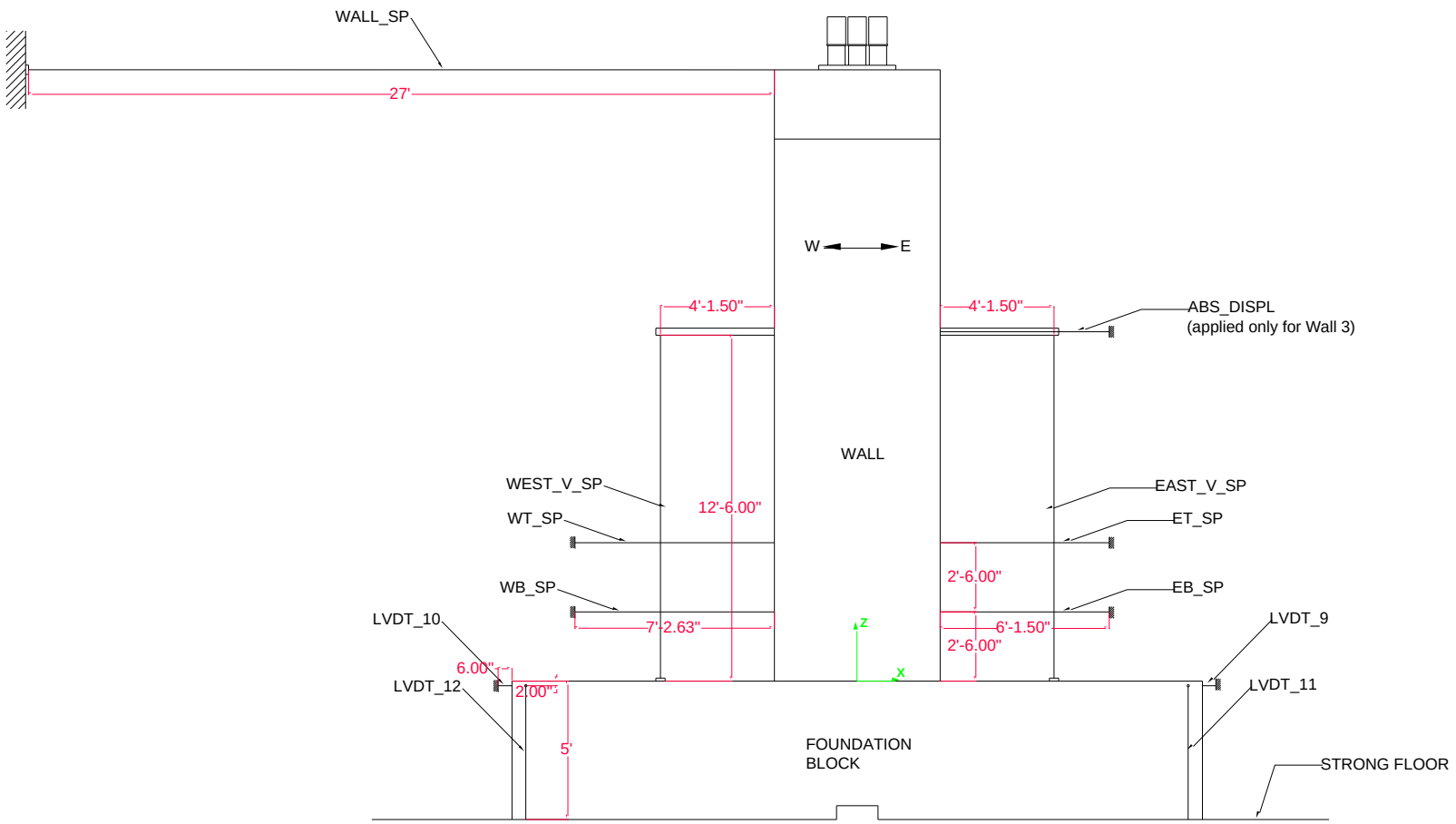

Figure 3-8 Vertical and horizontal displacements transducers on Wall 2 and Wall 3

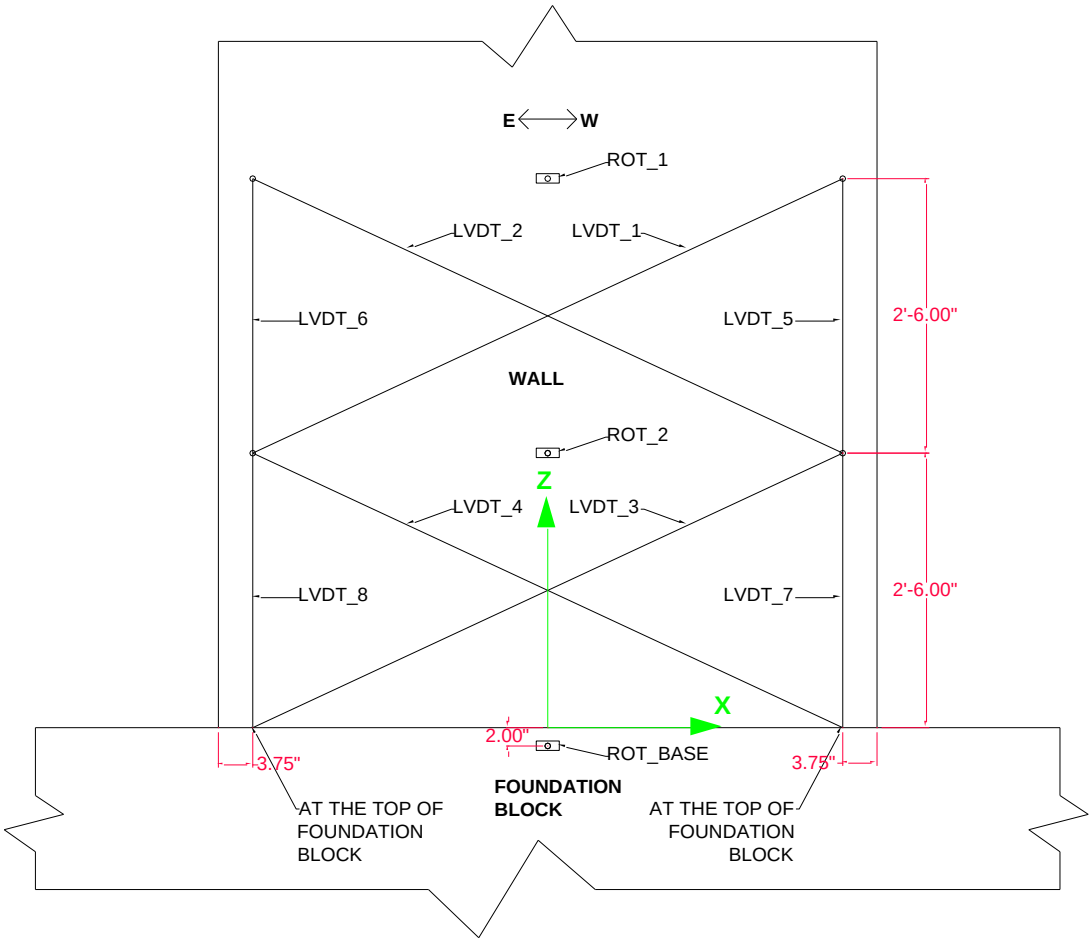

Figure 3-9 LVDTs and rotation meters on Wall 2 and Wall 3

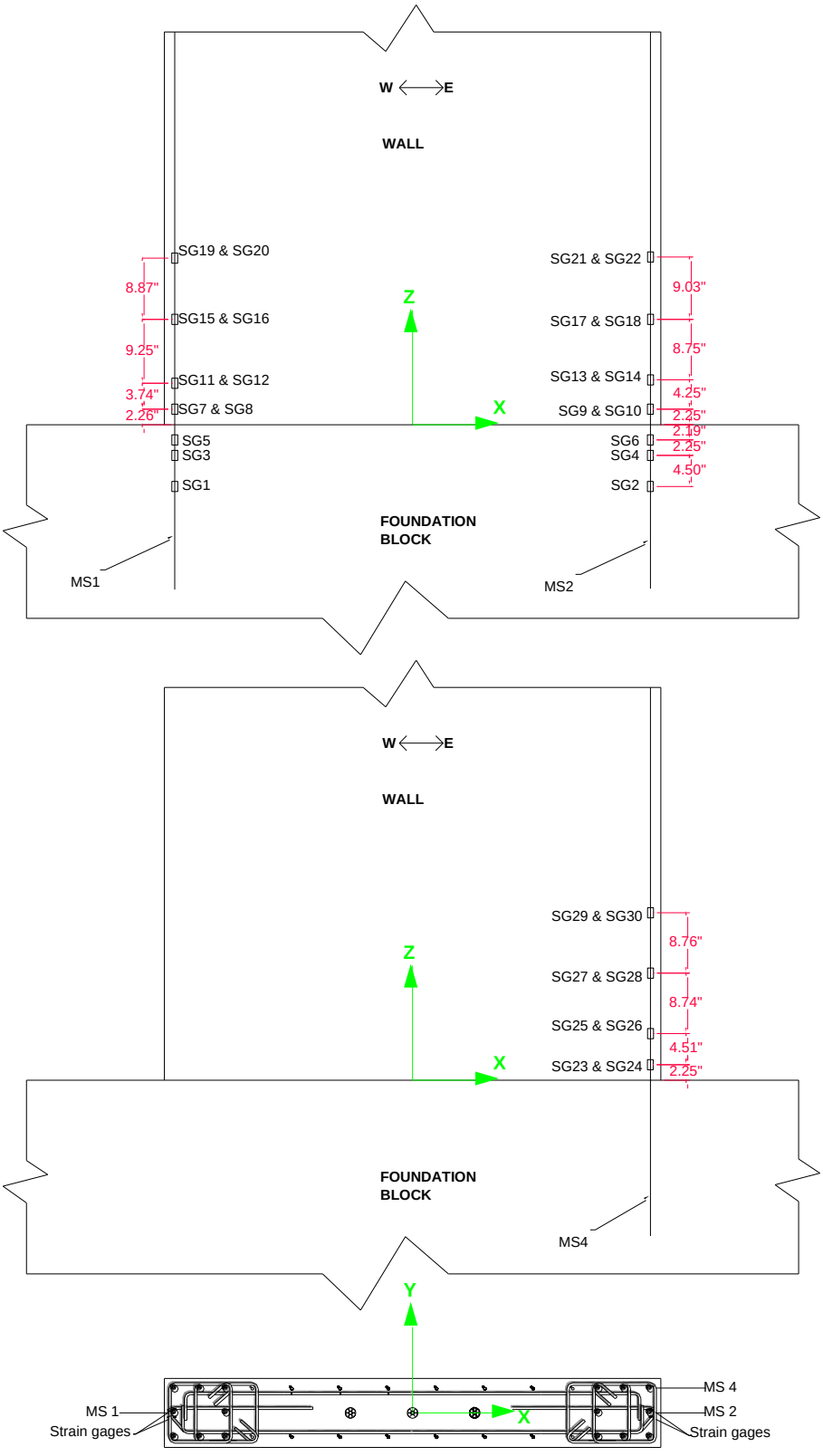

Figure 3-10 Strain gauges on longitudinal steel reinforcement on Wall 2

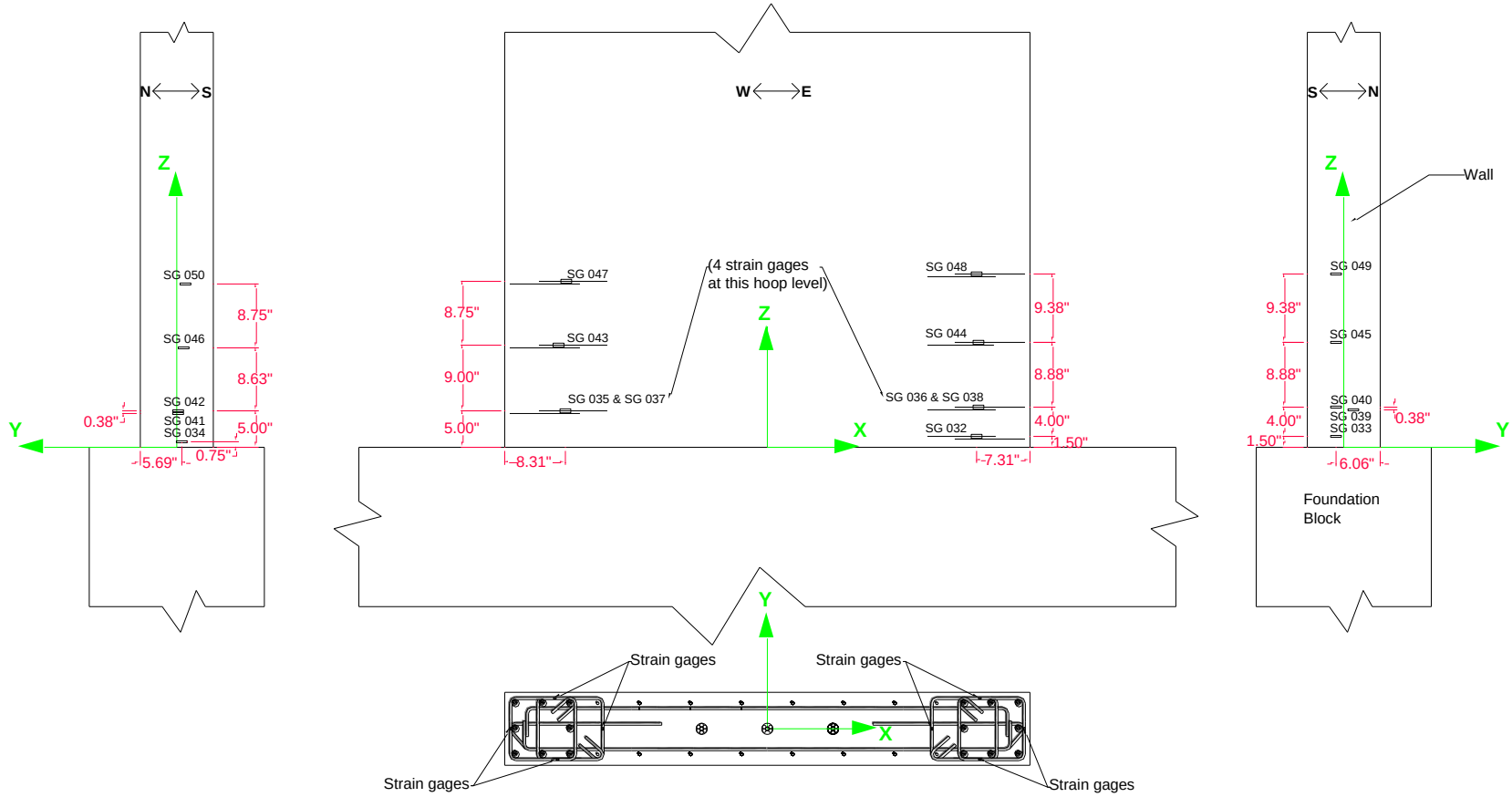

Figure 3-11 Strain gauges on steel hoops on Wall 2

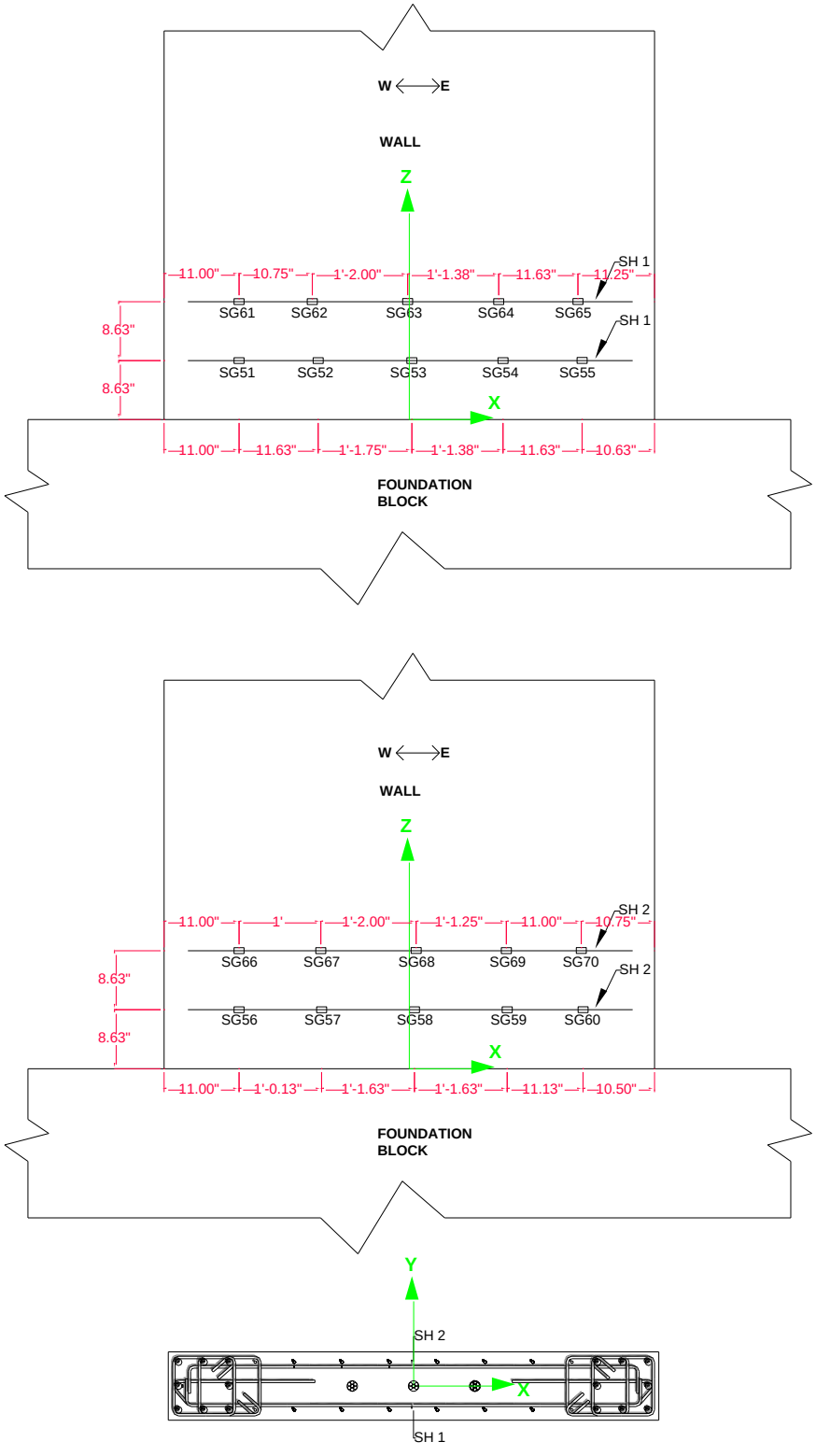

Figure 3-12 Strain gauges on web transverse steel reinforcement on Wall 2

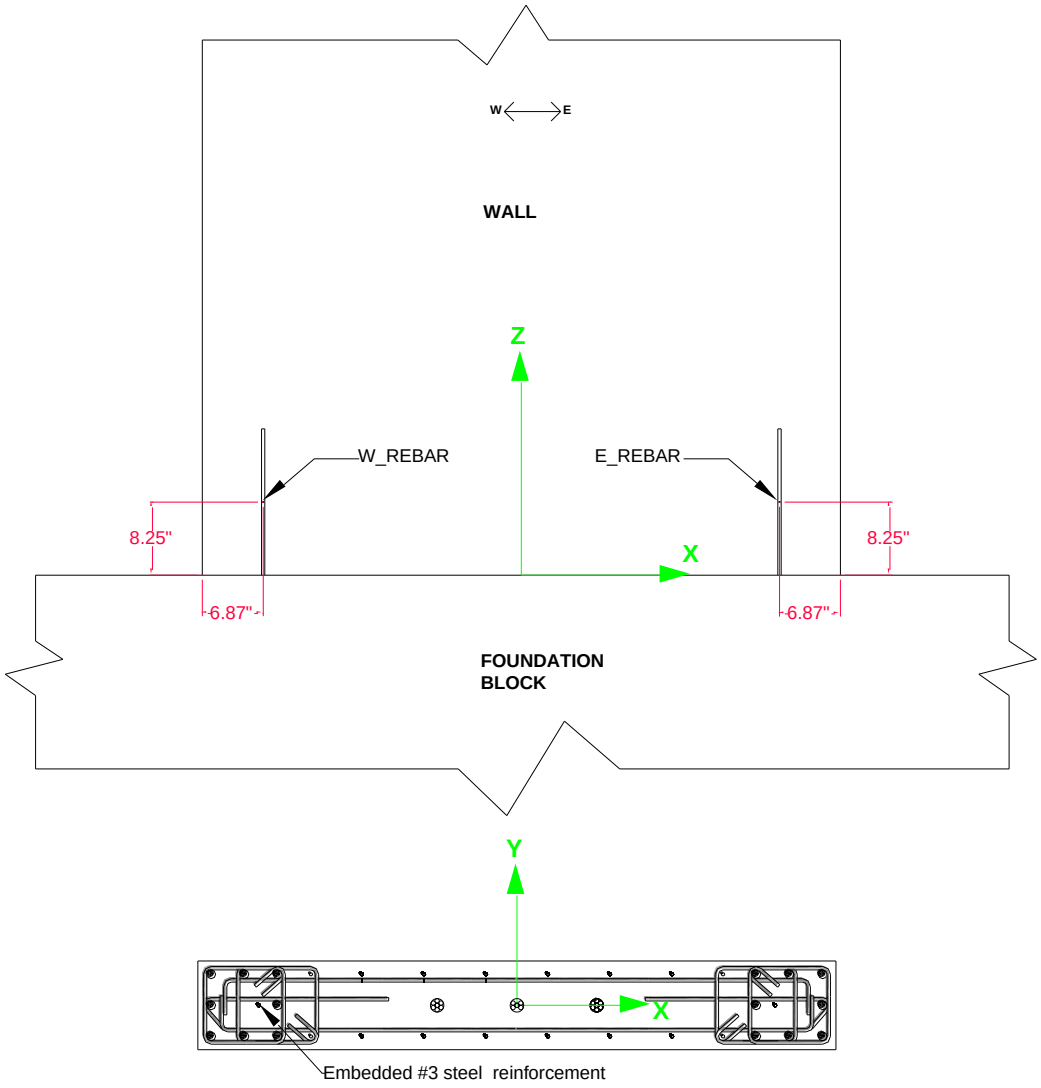

Figure 3-13 Embedded strain gauges in confned concrete on Wall 2

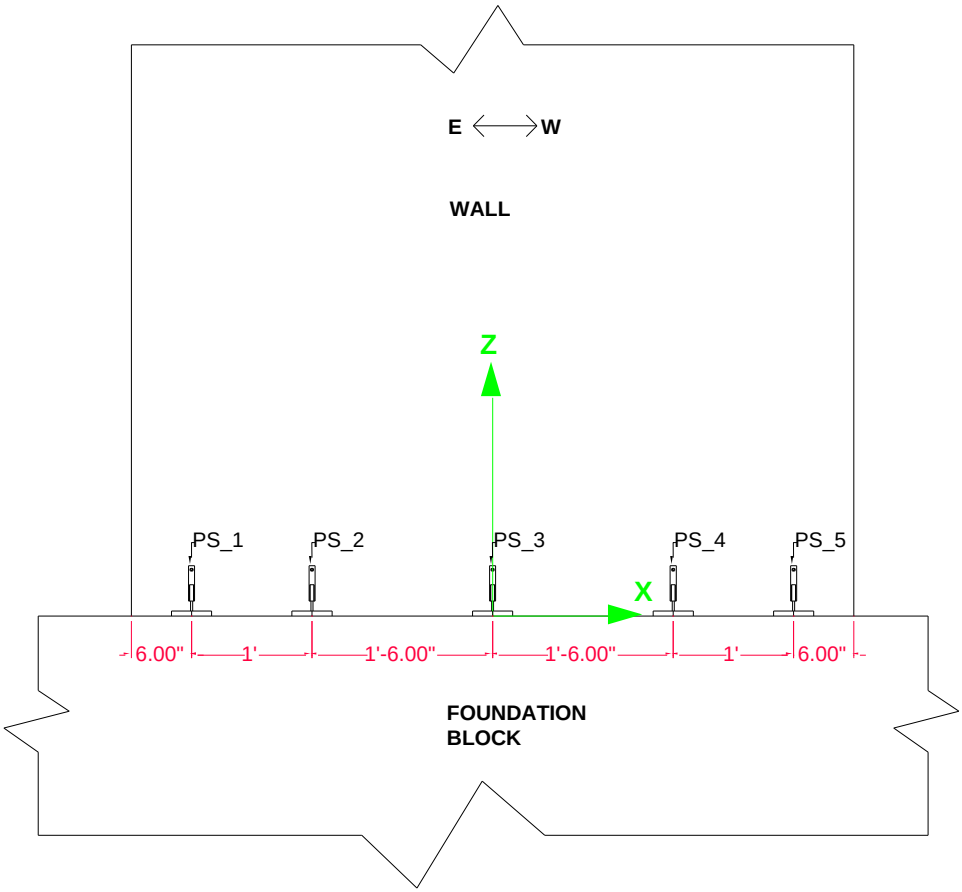

Figure 3-14 Plastic slides on Wall 2 and Wall 3

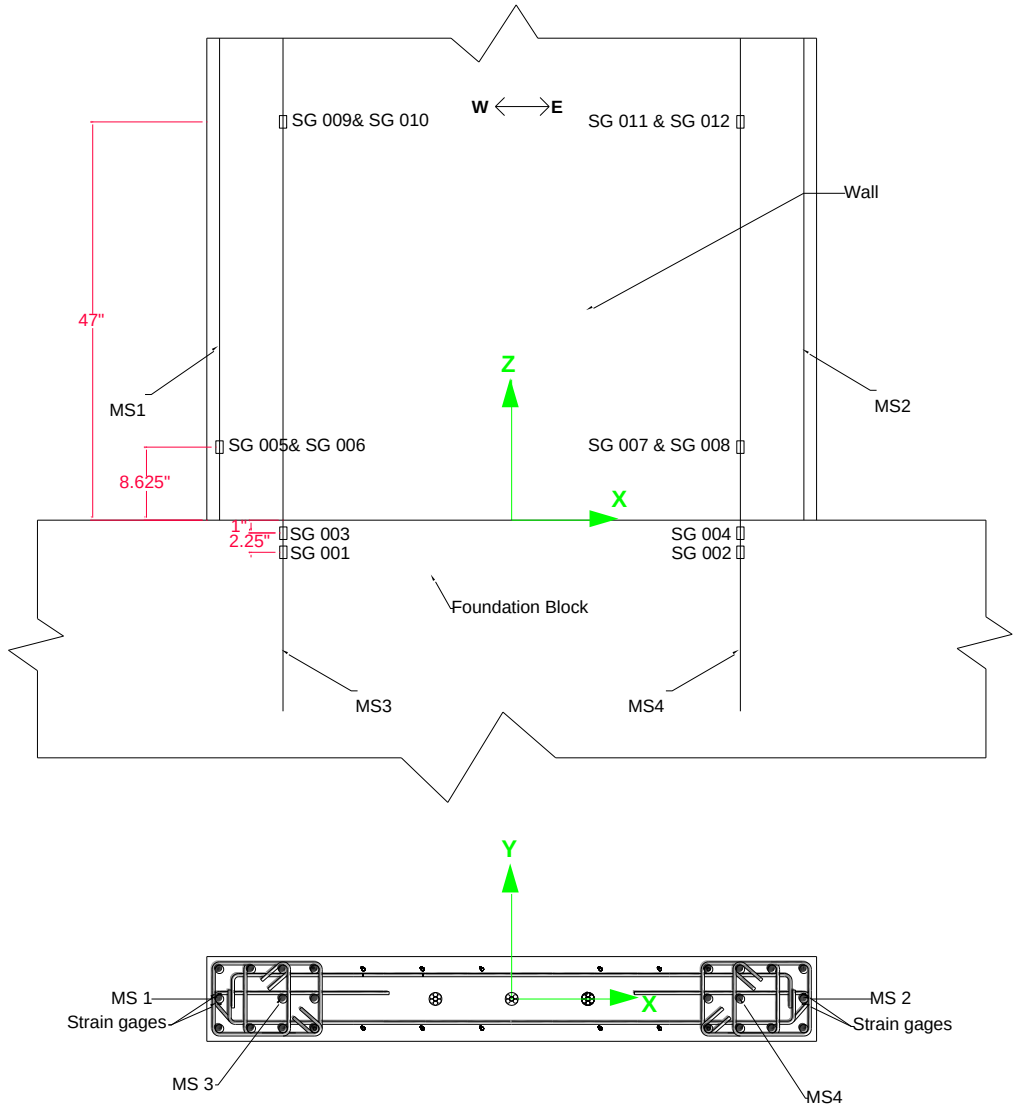

Figure 3-15 Strain gauges on longitudinal steel reinforcement on Wall 3

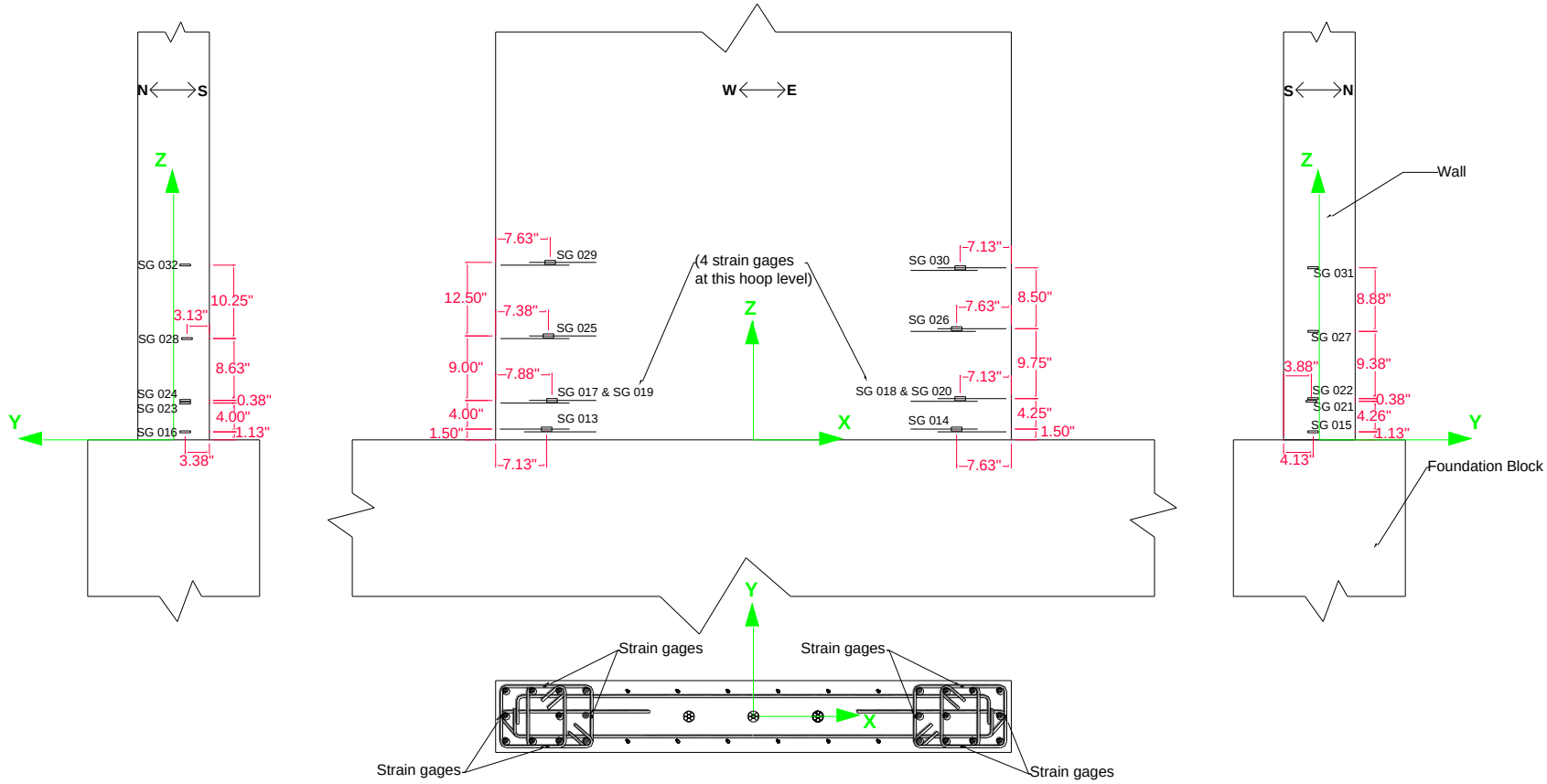

Figure 3-16 Strain gauges on steel hoops on Wall 3

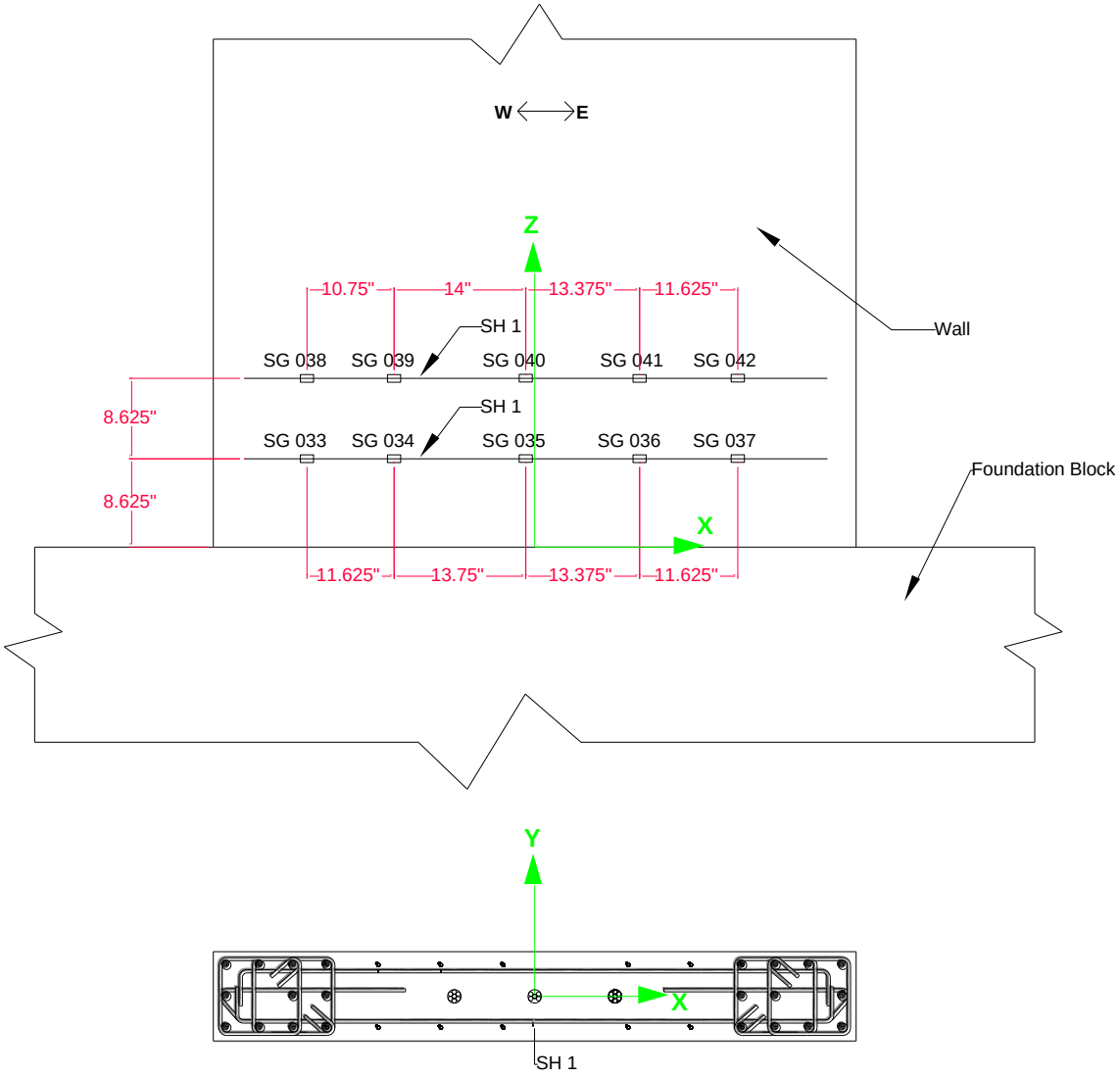

Figure 3-17 Strain gauges on web transverse steel reinforcement on Wall 3

CHAPTER 4
EXPERIMENTAL RESULTS

4.1 INTRODUCTION
This chapter presents the experimental results for Walls 1, 2, and 3.

4.2 AXIAL LOAD RATIO
Table 4-1 shows the axial load ratio for each test wall in terms of the nominal concrete compressive strength. For each wall, that stress represents a combination of gravity load and prestressing force.

4.3 WALL 1
The contents (text and figures) of this section are extracted from Rivera et al. (2013). This was done for the sake of completeness and to facilitate discussion and comparisons between walls. Additional information is included in this section on shear deformation which was not included in the report by Rivera et al. (2013).

4.3.1 LOADING HISTORY
Figure 4-1 and Figure 4-2 show the test wall in its displaced configuration when it is loaded Eastward and Westward, respectively. Also shown in Figure 4-1 and Figure 4-2 the lateral force actuator also applied a component of P-Δ moment. This added moment is small and is not included in the presentation of results in this report. Additionally in this report, actuator forces are positive in tension, loading Westward, and negative in compression, loading Eastward. Similarly, lateral displacements are also positive when loading Westward, and negative when loading Eastward. Lateral displacements were obtained at the actuator level from two LVDTs, one attached to the actuator, and another connected to an independent column as shown in Figure 3-3. Figure 4-3 shows the complete loading history planned for the test wall. The loading sequence was obtained from ACI ITG 5. The complete loading history was divided into 16 load steps and each load step has three full cycles. The wall was loaded up until Load Step 15, Cycle Number 1. At that point failure occurred and the test was ended.

At the start of the test, the first three loading steps are applied under load control, and the remaining 13 load steps are applied under displacement control. Figure 4-4 shows the portion of the load history under load control. Displacements collected during the load control portion of the load history were obtained from the LVDT connected to the independent column, and displacements collected during the displacement control portion of the load history were obtained from the LVDT attached to the actuator.

Figure 4-5 shows a plot that superposes the applied load over the experimental results for the load control portion of the load history. This figure shows the accuracy of the applied loads at every cycle. In this figure, load is plotted verses record number. The record number is increased by 1 each time data is saved. In this experiment data, was saved every 2 seconds. Figure 4-5 shows the accuracy of the applied loads at every cycle.

Figure 4-6 shows a plot that superposes the applied displacements over the experimental results for the displacement control portion of the load history. Again, the control parameter (displacement in this case) is plotted versus record number. This figure also shows the accuracy of the applied displacement at every cycle.

Figure 4-7 shows a plot of the base moment versus record number. Base moment is represented by the applied actuator force times the height of wall at the actuator level. Similarly, Figure 4-8 shows a plot of the base shear versus record number. Base shear is represented by the applied actuator force. These plots also show the overall uniformity of load and displacement applications during the test as well as the displacement increase every three cycles.

4.3.2 LATERAL LOAD RESPONSE

Figure 4-9 shows a plot of the complete experimental response of Wall 1. Failure occurred during Load Step 15, after 43 cycles of load. This plot represents the base moment versus the lateral drift. The lateral drift is represented by the ratio of lateral displacement at the actuator height divided by the height of the wall at the actuator level.

Figure 4-10 shows a plot presented by Srivastava (2013) that describes the limit states of an unbonded post-tensioned cast-in-place structural wall. These limits states are decompression (DEC), effective linear limit (ELL), yielding of mild steel (YMS), fracture of mild steel (FMS), yielding of PT (LLP), and crushing of confined concrete (CCC).

4.3.2.1 Stiffness Degradation

Figure 4-11 shows a plot of the experimental envelope curve using base moment versus lateral drift. This envelope curve shows key components of the structural response during the test. These components are concrete cracking, yielding of the mild steel, observed concrete spalling, yielding of PT, and observed fracture of the longitudinal bars.

Figure 4-12 and Figure 4-13 show the stiffness degradation versus the load steps and lateral drift, respectively. The lateral stiffness was obtained by taking the slope of the hysteresis curve for each load step. This was done by first, selecting data ranging from $\Theta = \pm 0.015$ to $\Theta = \pm 0.040$, and then obtaining the regression line slope from this data. This range was selected to avoid data close to zero drift due to excessive static noise and to avoid the nonlinear portion of the lateral force-lateral drift curve. The initial lateral stiffness at Load Step 1 was 1254 kip/in. At Load Step 2, the lateral stiffness decreased 4.03% to 1202 kip/in. This trend continued throughout the load steps. The stiffness at the final load step was 37 kip/in, a 97.1% reduction compared to the initial stiffness.

4.3.2.2 Strength Deterioration

Figure 4-14 describes a plot of the lateral strength deterioration exhibited during each load steps (loaded Eastward). In this plot, the second and third cycles are compared versus the first cycle of that load step. This plot also shows that during the elastic portion of the test, the strength deterioration at Cycles 2 and 3 is almost negligible. However, after the effective linear limit (ELL) state, the lateral strength deterioration ranges from 2.0% to 3.7% for the second cycle and from 2.4% to 16.7% for the third cycle.

4.3.2.3 Energy Dissipation

Figure 4-15 shows a plot of the normalized cumulative hysteretic energy dissipation ($E_d/E_{d,max}$). The energy dissipation values were obtained from the area enclosed by the cycle of the force-displacement curve. These values are plotted versus the lateral drift. From this plot, it is evident that cycles after the effective linear limit (ELL) found in Figure 4-10, dissipate larger amounts of energy. This dissipation, among other factors, is due to concrete cracking, yielding of longitudinal bars, shear sliding along cracks, yielding of PT, fracture of longitudinal bars, and nonlinear compression in concrete.

4.3.3 CONRETE CRACKING

Figure 4-16 shows a plot of the concrete strains versus the lateral drift. The concrete strain is normalized by the strain at which concrete cracks under tension. The strain at which the concrete cracks was obtained by dividing the concrete modulus of rupture (f_r) by the concrete modulus of elasticity (E_c). In this research, the predicted concrete cracking strain was 1316 με.

Using strain gauges embedded in the confined section of the wall, the concrete on the East end of the wall was found to crack during Cycle 13W. The measured drift at this point was recorded at Θ_{ccr} = 0.023%. Figure 4-17 shows a photograph at the end of Cycle 13W, where cracks can be observed on the East end of the wall.

Figure 4-18 shows a plot of the concrete strains versus the lateral drift. The concrete strain is normalized by the strain at which concrete cracks under tension. The strain at which the concrete cracks was obtained by dividing the concrete modulus of rupture (f_r) by the concrete modulus of elasticity (E_c). Using strain gauges embedded in the confined section of the wall, the concrete on the West end of the wall was found to crack during Cycle 13E. The measured drift at this point was recorded at Θ_{ccr} = -0.016%. Figure 4-19 shows a photograph at the end of Cycle 13E, where cracks can be observed on the West end of the wall.

4.3.4 LONGITUDINAL BAR YIELDING

Figure 4-20 shows the strains in the midface longitudinal bar in the extreme fiber of the East toe of the wall. The strain is normalized by the yield strain, and plotted versus the lateral drift. For clarity, the bar location is illustrated in the wall section and a photo included in the figure. The yield strain for the #7 reinforcing bar was obtained from a tensile test following ASTM A370 guidelines.

The #7 rebar tested was a cut-off section of the bar adjacent to where the strain gauge is located. The recorded strain from the strain gauge was then divided by the yield strain. From this figure, it can be shown that the middle bar reached its nominal yielding strain at about Θ_{msy_n} = 0.57%. This occurred during Cycle 28W. Figure 4-21 shows the again the steel bar strain normalized by the yield strain, but now versus the cycle numbers. In this figure, it is easier to appreciate the yielding of this middle bar during this cycle.

Figure 4-22 shows the strains in the North corner of the East toe of the wall. The strain is normalized by the yield strain, and plotted versus the lateral drift. For clarity, the bar location is illustrated in the wall section and a photo included in the figure. The yield strain for the #7 reinforcing bar was obtained from a tensile test following ASTM A370 guidelines.

From this figure, it can be shown that the corner bar reached its yielding strain at about Θ_{msy_n} = 0.43%. This also occurred during Cycle 28W. Figure 4-23 shows the again the steel bar strain normalized by the yield strain, but now versus the cycle numbers. In this figure, it is easier to appreciate the yielding of this corner bar during this cycle.

Other strain gauges were located on the West side of the wall. However, those strain gauges were either disturbed during the concrete placing or became inoperable after only a few cycles, never reaching the rebar nominal yielding strain.

4.3.5 CONCRETE SPALLING

Figure 4-24 shows photographs of both the West and East ends of the wall showing the initiation of concrete spalling. Concrete spalling was observed to occur at the end of Cycle 31, West and East respectively, during Load Step 11. Concrete spalling was observed to occur at a measured at drift of Θ_{spl} = 1.35%. Figure 4-25 shows the load step and cycle at which concrete spalling was observed.

4.3.6 POST-TENSIONING RESPONSE

Figure 4-26 shows the complete response of the unbonded post-tension (UPT) tendon on the East side identified as UPT 1 in the figure. The PT force is normalized by the PT yielding force. In this figure, it can be seen that only actuator Westward lateral forces bring the tendon to yielding, while Eastward lateral forces bring the tendon to only about 85% yielding. Figure 4-27 shows the UPT force and the normalized yielding peaks. In total there were four yielding peaks. These yielding peaks occurred at Cycles 37W, 40W, 41W, and 42W. Yielding peak during Cycle 37W was measured at Θ_{llp_n} = 3.04%, while the other three yielding peaks were measure at Θ_{llp_n} = 3.98%, Θ_{llp_n} = 4.00%, and Θ_{llp_n} = 4.00%, respectively.

Figure 4-27 also shows the loss of prestressing forces that occurred on the PT after its first yielding peak. As mentioned before, the first yielding of UPT 1 occurred at the end of Cycle 37W. At this applied drift (Θ = 3.0%), the PT force for UPT 1 at Cycle 37W was recorded at 239.6 kips. Subsequent cycles during this applied drift, 38W and 39W, show a loss in prestressing force recorded at 237.6 kips and 236.6 kips, respectively. This loss in prestressing force becomes more prominent during the following applied drift. During the three cycles at this next applied drift of Θ = 4.0%, the prestressing forces decrease from 252.6 kips at Cycle 40W, to 249.6 kips at Cycle 41W, to finally 241.9 kips at Cycle 42W. At the last applied drift of Θ = 5.0%, during Cycle 43W, the prestressing force was recorded at 227.5 kips. From this loss of prestressing forces due to the yielding of UPT 1, it is evident that self-centering capabilities are greatly diminished.

Figure 4-28 shows the complete response of the UPT tendon on the East side identified as UPT 2 in the figure. The PT force is normalized by the PT yielding force. In this figure, it can be seen that only actuator Eastward lateral forces bring the tendon to yielding, while Westward lateral forces bring the tendon to only about 95% yielding. Figure 4-29 shows the UPT force and the normalized yielding peaks. In total there were five yielding peaks. These yielding peaks occurred at Cycles 37E, 38E, 39E, 40E, and 41E. Yielding peak during Cycle 37E was measured at Θ_{llp_n} = -2.99%, while the other four yielding peaks were measure at Θ_{llp_n} = -2.99%, Θ_{llp_n} = -2.99%, Θ_{llp_n} = -3.99%, and Θ_{llp_n} = -3.98%, respectively.

Figure 4-29 also shows the loss of prestressing forces that occurred on the PT after its first yielding peak. As mentioned before, the first yielding of UPT 2 occurred at the end of Cycle 37E. At this applied drift (Θ = -3.0%), the PT force for UPT 2 at Cycle 37E was recorded at 243.1 kips. Subsequent cycles during this applied drift, 38E and 39E, show a loss in prestressing force recorded at 240.7 kips and 239.6 kips, respectively. This loss in prestressing force becomes more prominent during the following applied drift. During the three cycles at this next applied drift of Θ = -4.0%, the prestressing forces decrease from 256.6 kips at Cycle 40E, to 248.8 kips at Cycle 41E, to finally 208.7 kips at Cycle 42E. At the last applied drift of Θ = -5.0%, during Cycle 43E, the prestressing force was recorded at 194.2 kips. From this loss of prestressing forces due to the yielding of UPT 2, self-centering capabilities are greatly reduced.

4.3.7 LONGITUDINAL BAR FRACTURE

Figure 4-30 shows a plot of the last three load cycles in which the buckling and fracture of the extreme fiber longitudinal bars was observed. At the end of Cycle 41E, buckling of the longitudinal bars B1E and B3E was observed. Subsequently, before reaching the end of Cycle 42W, bars B1E, B2E, and B3E fractured (see Figure 4-31). The fracture of these bars was recorded at a drift of Θ = 3.56%. At the end of this cycle (42W), buckling of the longitudinal bars B1W and B3W was observed. Subsequently, before reaching the end of Cycle 42E, bars B1W, B2W, and B3W fractured (see Figure 4-31). The fracture of these bars was recorded at a drift of Θ = -3.35%.

A detail inspection of the test wall was performed at the conclusion of the test. It was found that no other rebar, longitudinal or otherwise, had fractured.

4.3.8 CONFINED CONCRETE RESPONSE

Figure 4-32 shows the response of the confined concrete under compression at the East end of the wall. The strain gauge is located in the center on this confined region, and gauge provided data until it failed at the end of Cycle 19. From this figure, stiffness degradation and energy dissipation can be obtained as the slope of the hysteretic loops becomes smaller and the unloading path differs from the loading path. Figure 4-33, the response of the confined concrete at the West end of the wall, shows a similar trend. This strain gauge provided data until it failed at the end of Cycle 16.

4.3.9 SHEAR DEFORMATIONS

Figure 4-34 shows total shear deformations in the wall. The shear deformation was calculated based on the diagonal and vertical arrangements of the LVDTs. The equations that were used for these calculations were in line with those equations in Massone et al. (2004). At early load steps, shear deformations were not significant and the ratio of the shear deformation to the flexure deformation was approximately 13%. This ratio was also relatively constant until Load Step 14 as shown in Figure 4-35. As the wall was pushed to lateral drift of 4%, the shear deformation increased and this change can be seen clearly during Cycle 43W in Figure 4-34. Significant shear deformations were observed during the last load step which indicated the sliding shear in the wall.

4.3.10 FAILURE MODE

From experimental observation, it was concluded that the failure mode of the test wall was shear. Figure 4-36 shows photographs of the progression of this failure mode. As shown in the photographs, shear cracks (those seen on the web portion of the wall) developed as early as Cycle 13 along with flexure cracks (those seen on the flange portion of the wall). During this cycle, at which shear cracks were first observed, drift was recorded at Θ = 0.14%. As larger displacements were applied at subsequent load steps, more and larger flexure cracks develop as well as shear cracks. Eventually, shear cracks dominated over flexure cracks crushing the concrete on the web portion of the wall and exposing the shear steel reinforcement. After this point (during Cycle 43), the test wall lost its shear strength and therefore its ability to resist any more applied lateral force.

Figure 4-37 shows a photograph of the test wall after the broken concrete was removed from the web portion of the wall. This photograph also shows the flange portion of the wall and validates the importance of the confined boundary elements of the wall.

4.4 WALL 2

4.4.1 LOADING HISTORY

The loading protocol for Wall 2 is shown in Figure 4-3. The loading protocol for the test was based on ACI ITG-5 (ACI 2007, ACI 2009) recommendation. For each drift level (load step), there were three full cycles. For the first three-drift levels, load control was applied (planned load control portion is shown in Figure 4-38) since the applied displacements were too small and difficult for precision control. For subsequent drift levels, displacement control was used.

Only 14 load steps with 41 load cycles of the load history were applied when the wall specimen failed. The sign convention of the loading was the same to that of the first test wall. West direction loading was positive and it was negative for the East direction loading.

Figure 4-39 compares the planned load control portion versus the actual load control portion. In general the actual load control portion matched the planned load control portion very well. As for the displacement portion of the loading history, there were discrepancies between the planned and actual displacement loading. First discrepancy, referring to Figure 4-40, at Load Step 4 and Load Step 5, the actual lateral drift were lower than the planned lateral drift. The planned lateral drifts were 0.1 % and 0.14% while the actual lateral drifts

were 0.06% and 0.09% for Load Step 4 and Load Step 5 respectively. Second discrepancy, during Load Step 9 Cycle 25W, the lateral drift was overshoot to 0.71% instead of 0.6%.

In order to inspect the condition of the wall during the test, the loading was held at the peak of the first and third cycles of each load step (applied both for positive and negative peaks). Figure 4-40, Figure 4-41, and Figure 4-42 indicates when these inspections were performed.

4.4.2 LATERAL LOAD RESPONSE

Figure 4-43 shows the lateral load response of the wall in terms of base moment versus lateral drift and accompanied with sign convention of the loading directions. Base moment and lateral drift were calculated as in Rivera et al. (2013). The maximum base moment was 43557 kip-in and maximum lateral drift was 4.08%. Nominal moment (M_n) of the wall was 31473 kip-in and it is plotted on the envelope curve. It can be observed that this moment is slightly larger than the moment at first yielding of the longitudinal steel reinforcement. Figure 4-43 also shows the superposition of the envelope curve with the hysteretic curve to show several different limit states (Srivastava. 2013) observed during the test. In each limit state, the corresponding cycle number and lateral drift are given and they are described in the subsequent sections.

Self-centering capacity of the wall was shown to be good especially until Load Step 14 Cycle 40. The residual drift at this cycle was less than 25% of the peak drift of 4%. The flag-shape hysteretic curve also can be seen clearly until the end of Cycle 40. Excessive residual drift can be observed at the subsequent cycles until the end of the test.

The following is an observation of wall responses regarding its stiffness, strength, and energy dissipation capacity.

4.4.2.1 Stiffness Degradation

Figure 4-44 shows the plot of stiffness degradation per load step increase. In this plot, Load Step 4 is omitted since the load level at this load step was approximately the same to that of the previous load step. Therefore, the number of points in the plot was 13 instead of 14. The same omission applied in Figure 4-45, Figure 4-46, and Figure 4-47.

Initial stiffness of this wall was 1185 kip/in as can be seen in Figure 4-44 and Figure 4-45. The same method for determining stiffness that used in Wall 1 was applied here. After the first observed concrete cracking in the wall, at Load Step 6, the stiffness in the wall was 766 kip/in. Significant stiffness degradation can be seen to occur right after concrete started to spall at Load Step 9 (Load Step 10) left the stiffness of 409 kip/in. Stiffness at the beginning of Load Step 13 (Load Step 14) was 151 kip/in.

4.4.2.2 Strength Deterioration

Figure 4-46 shows percentage of strength deterioration after the first cycle of each load steps. In general, for every second and third cycles at each load steps, there was deterioration of strength. Significant strength deterioration only occurred once several longitudinal reinforcements fractured. At 2.99% drift, for example, the reduction of

strength was 14.7% at the third cycle. Strength deterioration clearly pronounced at the last load step (4% drift) which shows 28.5% reduction in strength.

4.4.2.3 Energy Dissipation

Figure 4-47 shows normalized cumulative energy for each lateral drifts. Until lateral drift of 0.88%, the cumulative energy dissipation was just above 10%. As the lateral drift increased, the normalized energy dissipation became more significant due to yielding of mild steel. It is noticeable also in Figure 4-47 that the difference of energy dissipated for the second and third cycle was almost insignificant.

4.4.3 CONCRETE CRACKING

In this experimental program, the nominal fracture strain ε_{r_n} of the concrete was calculated to be 1316 με as explained in Rivera et al. (2013). Figure 4-48 shows the plot of lateral drift against the normalized concrete strain and the same normalization method as in Rivera et al. (2013) was used. Based on this figure, cracking in the wall was supposed to happen during Load Step 7 according to the above concrete strain assumption, however, Figure 4-49 and Figure 4-50 show that cracks already occurred during Load Step 6 Cycle 16W and Cycle 16E.

4.4.4 LONGITUDINAL BAR YIELDING

Figure 4-51 and Figure 4-53 show the plots of strain in the longitudinal reinforcement versus lateral drift. The strain in the reinforcement steel ε_{ms} was normalized with respect to the reinforcement steel nominal yield strain as in Rivera et al. (2013). The average nominal yielding strain of longitudinal steel reinforcement ε_{msy_n} was 0.0026. The dashed lines in Figure 4-51 and Figure 4-53 indicate the nominal yielding limit of the reinforcement steel. Yielding of longitudinal steel reinforcement in tension started during Load Step 7 Cycle 19W at lateral drift of 0.21% when the wall was loaded Westward. The corresponding longitudinal steel reinforcement is marked MS2 in Figure 3-10. The condition of the wall at this particular load cycle is shown in Figure 4-52.

As for Eastward loading, Figure 4-53 shows that yielding of longitudinal steel reinforcement at the boundary element occurred during Cycle 19E at drift level of -0.22%. The corresponding longitudinal steel reinforcement is marked MS1 in Figure 3-10. Figure 4-54 shows the conditions of the wall at Southeast and Southwest of the wall at the end of Cycle 19E.

4.4.5 CONCRETE SPALLING

Splitting cracks started to occur at Load Step 9 Cycle 25 (drift level of 0.6%) as shown in Figure 4-55 and during the subsequent cycles, the cracks lengthen and grew. Finally, at Load Step 10 Cycle 28E, concrete spalling occurred on the wall. Figure 4-56 shows concrete spalling at East and West side of the wall at Cycle 28E. The lateral drift corresponding with this limit state was 0.9%.

4.4.6 POST-TENSIONING RESPONSE

Figure 4-57, Figure 4-58, and Figure 4-59 show hysteretic plots of post-tensioned force versus lateral drift for three post-tensioned steel groups used in the wall. In addition, a

straight dashed line which represents the yielding limit of each group is also included in each figures. The yielding limit of 7-strands post-tensioned steel groups (referred as PT_1 and PT_3 in Figure 3-3) and 5-strands group of post-tensioned steel (PT_2 in Figure 3-3) is 334.2 kips and 238.7 kips respectively. Yielding of the first post-tensioned steel group was at Load Step 14 Cycle 40E at drift of 3.3% and for the third post-tensioned steel group, it happened at Load Step 14 Cycle 40W at drift 3.56%. For the second group, yielding of the post-tensioned steel did not occur.

During Cycle 41 (4% drift), significant loss of post-tensioning force occurred due to shortening of the post-tensioned steel which caused by fractured of longitudinal steel reinforcements and excessive deformations on the wall.

4.4.7 LONGITUDINAL BAR FRACTURE

Figure 4-60 shows hysteresis plot of base moment with lateral drift at Load Step 13 and Load Step 14. In the plot, the beginning of bar fracture was marked for both West and East side of the wall. During Cycle 39W, it was observed the fracture of two longitudinal steel reinforcement at the outer row of East side boundary element and they can be seen clearly in Figure 4-61. At the same time, it was also observed that the longitudinal steel reinforcement at the outer row of West side boundary element buckled and this is shown in Figure 4-62.

In the subsequent cycle, Cycle 39E, two longitudinal steel reinforcements of the outer edge of West side boundary element were fractured and they can be seen in Figure 4-63. Once the test was completed, the excavation was done in order to determine the number of longitudinal steel reinforcement that fractured. In total, there were 16 fractured longitudinal steel reinforcement by the end of the test and they can be seen in Figure 4-64.

4.4.8 CONFINED CONCRETE RESPONSE

Figure 4-65 shows the plot of confined concrete strain versus lateral drift. The strains measurements were based on strain gauges set up shown in Figure 3-13. This shows the strain of confined concrete at East side only since the strain gauge at West side failed during construction of the wall. The final recorded concrete compressive strain at confined concrete was -0.0137% at Cycle 31E before the strain gauge failed.

Figure 4-66 shows the conditioned of confined concrete at East and West boundary elements at the end of the test. It can be seen clearly that confined concrete at both boundary elements pulverized at the height where the longitudinal steel reinforcement fractured.

4.4.9 SHEAR DEFORMATIONS

Figure 4-67 shows total shear deformation in the wall. Throughout the test, shear deformations were relatively small compared to the total deformations. Significant shear deformations were observed at last cycle of the test due to sliding shear in the wall as a consequence of the fracture of the longitudinal steel reinforcement in the boundary and web elements.

4.4.10 FAILURE MODE

The test ended when the wall force capacity drop significantly during the last cycle of the test (as shown in Figure 4-60) due to fracture of longitudinal steel reinforcement. From this observation, the failure mode of the wall was fracture of longitudinal steel reinforcement.

4.5 WALL 3

4.5.1 LOADING HISTORY

The load history for Wall 3 was similar to the load history for Wall 1 and Wall 2, as shown in Figure 4-3. Figure 4-68 shows the loading history for the loading control portion. The first, second, and third Load Steps of the applied loads were 17.5 kips, 40.0 kips, and 75.0 kips respectively. Figure 4-69 shows very good agreement between the planned and the actual load control portion.

In general, the actual displacement control portion of the loading history also matched the planned one as shown in Figure 4-70. Very small differences can be observed if comparison is made to the planned displacement control portion in Figure 4-3.

The test of Wall 3 was completed in two days. For the first day, the test stopped at Load Step 7 and the load was set to 0 kips. The test was resumed the next day by first bringing the wall to zero displacement position. Figure 4-71 and Figure 4-72 show the location where the test was stopped and then resumed. It can be seen that there was no significant change in the loading history during this period.

4.5.2 LATERAL LOAD RESPONSE

Figure 4-73 shows the complete response of wall in terms of moment versus lateral drift. Hysteresis plot was superposed with the envelope plot. On these plots, three observed limit states on Westward and Eastward loadings are indicated, namely concrete cracking, yielding of longitudinal bars, and concrete spalling. Compared to Wall 1 and Wall 2, there was no fracture of longitudinal bars limit state observed during the test. For each limit state in Figure 4-73, the corresponding load cycle and the corresponding drift are shown on the envelope curve. In addition, the nominal moment is also presented on these plots. Based on the information of the hysteresis plot, stiffness, strength, and energy dissipation capacities of this wall are evaluated. The evaluations are given in the following section.

4.5.2.1 Stiffness Degradation

Initial stiffness of this wall was 1076 kip/in. Stiffness degradation occurred in gradual fashion as shown in Figure 4-74 and Figure 4-75. By Load Step 6, the wall stiffness was about 70% of the initial stiffness. At the beginning of the last step, Load Step 12, the stiffness of the wall was approximately one tenth of the initial stiffness. Stiffness degradation occurred mainly due to concrete cracking, concrete cover spalling, and longitudinal bar yielding.

4.5.2.2 Strength Deterioration

Figure 4-76 shows strength deterioration of the wall for every load step (lateral drift). This plot was based on the loading on the West direction only. In each load step, the differences in strength deterioration at the second and third cycles are indicated. In general as the lateral

drift increases, this discrepancy increases. Significant strength deterioration was observed at the last load step. The strength deterioration was about 14%.

4.5.2.3 Energy Dissipation

Figure 4-77 shows the plot of normalized cumulative energy versus lateral drift. The energy dissipates during each loading cycles was compared to the total energy dissipation. At early lateral drift until lateral drift of 0.59%, the energy dissipated in each cycle was less than 10% of the total dissipation. This was an indication that until this point during the test, damage in the wall was not significant. It also indicated that the self-centering capacity of the wall was good. In the subsequent lateral drifts, the energy dissipation became significant which indicates more damage in the wall.

4.5.3 CONCRETE CRACKING

Concrete cracking was observed for the first time at Cycle 16W. The type of concrete crack was a vertical splitting crack as shown in Figure 4-78. This crack started from the Southwest toe of the wall. Figure 4-79 shows similar concrete crack that formed in the East side of the wall during Cycle 18E. Flexure-shear crack and shear crack did not exist until Cycle 25W and Cycle 25E respectively for Southeast and Southwest sides of the wall. Figure 4-80 and Figure 4-83 show these concrete cracks on the wall surface.

4.5.4 LONGITUDINAL BAR YIELDING

Figure 4-81 shows plot of strain in the debonded longitudinal center bar of the East boundary element versus lateral drift. The corresponding strain gauge was SG_11 (refer to Figure 3-15). The strain was normalized with respect to the nominal yielding strain. Figure 4-82 displays the enlargement of Figure 4-81 to emphasize the occurrence of yielding. According to this plot, this longitudinal steel reinforcement yielded during Cycle 25W which was indicated by the normalized strain that passed unity.

Figure 4-84 shows comparable plot to that of Figure 4-81. The strain of debonded longitudinal center bar at West boundary element was plotted against lateral drift. The corresponding strain gauge was SG_9 (refer to Figure 3-15). Figure 4-85 shows that this bar yielded during Cycle 25E.

4.5.5 CONCRETE SPALLING

Figure 4-86 shows the condition of boundary element at West side of the wall. It can be seen that concrete cover slightly above the base spalled. This was the first occurrence of concrete spalling observed which happened during Cycle 28W. As for the East side of the wall, the occurrence of concrete spalling was observed during Cycle 28E as shown in Figure 4-87.

4.5.6 POST-TENSIONING RESPONSE

Figure 4-88, Figure 4-89, and Figure 4-90 show plot of PT force versus lateral drift for the first, second, and third groups of UPT steel, respectively. Nominal yielding limit was shown in each figure by a dashed line. According to these plots, none of the post-tensioned steel groups yielded during the test. The sudden drop of PT forces in those plots which

started from the end of Cycle 35W were due to the shortening of the steel caused by failure of the wall.

4.5.7 SHEAR DEFORMATIONS

Total shear deformations in the wall are shown in Figure 4-95. Shear deformations became significant after the peak load of Cycle 35W. In between the peak load and the end of Cycle 35W, there was a sliding shear occur which indicated by the reduction of wall strength as the lateral drift increased. More pronounced shear deformation occurred between the peak load and the end of Cycle 35E.

4.5.8 FAILURE MODE

Figure 4-91 shows the condition of the wall at the end of Cycle 34E. During this load cycle, new diagonal cracks formed in the web that were flatter than the existing cracks. At the same time, significant gap opening at West end of the base of the wall started to penetrate to the web area. This imposed high tensile strain to the web longitudinal bars at the wall-foundation interface. In addition, initial spalling of web cover was observed.

During Cycle 35W, the wall did not reach the same maximum load as that of Cycle 34W as shown in Figure 4-92. At the peak load of this cycle, at South side of the wall as shown in Figure 4-93, crushing of web concrete cover at the base over a small height occurred (this was accompanied by a reduction of strength). Additionally, there were formations of vertical crack as well as horizontal crack in the web. This was immediately followed by spalling of some concrete cover of Northwest boundary and crushing of web concrete cover at the base over a small height at the North face of the wall as can be seen in Figure 4-94. It is possible that some of the longitudinal bars (West side) in the web buckled during reloading due to tensile plastic deformation from the previous cycle that could not be recovered when these bars subjected to axial compression load. This might cause the shear sliding in the plastic hinge area of the wall.

According to the shear deformation data as shown in Figure 4-95, right after the peak load of Cycle 35W there was an increase in shear deformation of the wall which is an indication of the shear sliding. Comparison of photographs at the peak load and at the end of this cycle, shown in Figure 4-96, shows that in the middle part of the web slightly above the base, there was a misalignment of concrete surface along new diagonal cracks which occurred during the reduction of strength from the peak load. Figure 4-97 shows the condition of web longitudinal bars at South side of the wall after concrete chipping process. It can be seen clearly that these bars buckled.

The condition of wall at the peak load and at the end of Cycle 35E is shown in Figure 4-98. Based on Figure 4-99(a), there was a crack at the end of Cycle 32W which formed inside the concrete cover. As the lateral drift increased, Figure 4-99(b) and Figure 4-99(c), the size of the crack grew. During Cycle 35E, the bond stresses along the web longitudinal bars caused splitting cracks at the bars to propagate and form a splitting plane in the concrete cover along the plane of the bars. Figure 4-100 shows the large sections of web concrete that were separated from the wall along the plane of the vertical web

reinforcement. Following the splitting along this plane, the web longitudinal bars buckled in compression and the sliding shear occurred as the lateral drift increased.

In summary, failure of the Wall 3 was precipitated by splitting of the concrete cover in a plane containing the vertical web reinforcement. The formation of this splitting plane led to a loss of lateral restraint for the vertical web reinforcement, and buckling of the reinforcement upon reversal of load on the wall. Loss of the web concrete and buckling of the vertical bars led to shear failure in the wall. A description of the formation of the splitting plane along the vertical web reinforcement is given below. It is noted here that a construction error caused the web reinforcement to be placed closer to the south face of the wall than was intended. As a result, there was excess concrete cover over the vertical web reinforcement on the north face of the wall, and insufficient concrete cover over the vertical web reinforcement on the south face of the wall.

Several factors contributed to the observed splitting of the concrete cover along a plane containing the vertical web reinforcement. First, compression stress in the web concrete caused transverse strain in the concrete due to the Poisson effect. Because the main flexural reinforcement was either terminated or debonded, the wall exhibited reduced flexural cracking. As a result, large strains develop in the bonded vertical web reinforcement at the gap opening concentrated at the base of the wall. The radial component of the bond stress contributed additional transverse tension in the web concrete in the vicinity of the vertical web reinforcement. As bond failure occurs, concrete along the ribs of the vertical bars crushes, and the radial component of bond stress increases relative to the longitudinal component along the length of the bars. This contributes even more transverse tension to the concrete cover. Bond stresses along the vertical bars on the south face of the wall (where cover was reduced) are likely to split the concrete cover along the length of the bars, and evidence of this was observed during the test. The horizontal web reinforcement would tend to keep these cracks narrow. In contrast, the increased concrete cover on the north face of the wall would resist splitting along the length of the bars, and instead contribute to a splitting failure along the plane of the bars, as was observed in the test. No reinforcement crosses this vertical splitting plane, so once the cover splits, the vertical bars become unrestrained and will easily buckle when in compression upon load reversal. These bars were observed to have buckled near the end of the test. The amount web concrete lost as part of the splitting plane comprised a large percentage of the web concrete, and thus amounted to a large reduction in shear strength. The buckled vertical bars would offer no shear resistance. The end result was a shear failure in the wall.

4.6 DISCUSSION OF EXPERIMENTAL RESULTS

This section of the report presents a brief discussion of the experimental results. A more detailed discussion including comparisons with analytical models and design recommendations is expected in Pakiding (2015).

4.6.1 WALL 1 VS WALL 2

Table 4-2 summarizes the lateral drift of the observed limit states (Srivastava et al. 2013) for each wall. The drifts are given for both Westward and Eastward loadings. Concrete cracking occurred earlier in Wall 1 than Wall 2 for Westward loading and the opposite was

the case for the Eastward loading. For Westward loading, Θ_{ccr} was equal to 0.016% and 0.2% for Wall 1 and Wall 2 respectively. On the other loading direction, Θ_{ccr} was equal to -0.026% and -0.2% for Wall 1 and Wall 2 respectively. Yielding of longitudinal steel and concrete spalling were observed much later in Wall 1 than Wall 2. These indicated that damage in Wall 2 occurred earlier than those in Wall 1. The corresponding drift levels for each limit state for Westward and Eastward loading were the same. Yielding in Wall 1 and Wall 2 occurred at Θ_{msy_n} equaled to 0.57% and 0.21%, respectively. Concrete spalling was observed at Θ_{msy_n} equaled to 1.35% and 0.9% for Wall 1 and Wall 2 respectively. Lateral drifts corresponding to PT yielding for Wall 1 and Wall 2 in the Westward and Eastward loading directions were 3.04%, -2.99%, 3.56%, and -3.3%. As for longitudinal bar fractures, they happened during the third cycle of drift level of 4% and drift level of 3% for Wall 1 and Wall 2, respectively.

Referring to Figure 4-101 and Figure 4-102, which show plots of load deformation for Wall 1 and Wall 2 in the form of hysteresis plot and envelope plot, respectively, the maximum strength of Wall 1 is larger than that of Wall 2. However, at drift level below 0.4%, the two walls show approximately the same strength.

From Figure 4-101, it can be seen that self-centering capacity of Wall 2 is better than that of Wall 1 which is shown by less residual drift in Wall 2 than in Wall 1 for any given equal lateral drift. This difference was pronounced more at larger drift level. In contrary, the energy dissipation in Wall 2 was lower than that in Wall 2.

4.6.2 WALL 2 VS WALL 3

According to Table 4-2, concrete cracking was observed at the same drift levels for both Wall 2 and Wall 3, namely at Θ_{ccr} equaled to 0.2% in both loading directions. However, it is worth to recall that the flexure-shear and flexure cracks on Wall 3 were observed at much larger drift level which was at 0.59% drift (see Figure 4-80 and Figure 4-83). Yielding of longitudinal bar in Wall 3 occurred at much later drift level compared to that in Wall 2. For Wall 3, this limit state was observed at Θ_{msy_n} equaled to 0.9% and for Wall 2, it was at 0.21% drift. Observed concrete spalling happened at the same drift level for Wall 1 and Wall 2, namely at Θ_{sps_n} equaled to 0.9%. Post-tensioned steel in Wall 3 never yielded since the wall failed much earlier than Wall 2. There was also no fracture of longitudinal steel reinforcement observed in Wall 3.

Figure 4-103 and Figure 4-104 show plots of load deformation for Wall 2 and Wall 3 in the form of hysteresis plot and envelope plot respectively. The maximum strength of Wall 2 is larger than that of Wall 3. It can be seen in Figure 4-104 that the stiffness of Wall 2 is also larger than that of Wall 1.

In Figure 4-103, it can be seen that self-centering capacity of Wall 2 is slightly better than that of Wall 3 which indicated by lesser residual drift in Wall 2 than in Wall 3 for any given equal lateral drift. This difference was pronounced more at larger drift level. As for the energy dissipation, Wall 3 dissipated more energy than Wall 2 which shown by larger area under hysteresis curve for Wall 3 than for Wall 2.

4.6.3 EXPERIMENTAL RESULTS VS CLOSED FORM EQUATION (CFE)

Closed form equations (CFE) to predict key response parameters were developed by Srivastava et al. (2013). Figure 4-105 and Figure 4-106 show the comparison of experimental envelopes to the CFE. The comparisons are only available for Wall 1 and Wall 2. In Srivastava et al. (2013), Wall 1 and Wall 2 were assigned as PW1.0.0 and PW2.0.0 respectively. Plots of limit states points in these figures corresponded to the points in Table 4-3 for each wall. For Wall 1, the predicted lateral drift at which yielding of longitudinal bar first occurred was smaller according to CFE than according to that observed in the experiment. The drifts were 0.18% and 0.57% for CFE and experiment, respectively. For Wall 2, the difference of this drift based on CFE and experimental results was small. The drifts were 0.18% for CFE and 0.21% for experiments. In general, for both walls, the yielding of PT steel and fracture of longitudinal bar limit states were underestimated in CFE.

4.6.4 EXPERIMENTAL RESULTS VS DRAIN-2DX

Chapter 2 describes the process of designing Wall 1 and Wall 2 and the kind of modeling that was done for predicting the behavior of this wall. Figure 4-107 and Figure 4-108 show the comparison of the results of finite element analysis (DRAIN-2DX) to those of the experiment. The analytical models predicted the strength of experimental results quite well especially for Westward loading. Energy dissipation based on analytical models was overestimated to a greater extent in Wall 1 than Wall 2. Residual drift was also overestimated by the model. It is noted here that the current model has several limitations, including the inability to model the buckling and fracture of longitudinal steel, as well as nonlinear shear deformations in the concrete.

Current analytical work is being conducted to modify the analytical model to incorporate behavior observed in the tests, including the pull out of longitudinal bar, nonlinear shear deformation and buckling and fracture of longitudinal steel.

Table 4-1 Axial load ratio

Wall ID	Initial prestressing force (kip)			Axial load ratio (f'_c*)
	UPT 1	UPT 2	UPT 3	$P_{pi\ total}$#/A_g+
Wall 1	174.5	176.4	N/A	0.08
Wall 2	239.9	173.5	241.0	0.15
Wall 3	247.0	198.9	255.4	0.16

*Nominal value (6 ksi).
#Total initial prestressing force in the wall.
+Gross section area of the wall (720 in^2).

Table 4-2 Experimental results for selected observed limit states

Wall ID	Loading direction	Concrete cracking Θ_{ccr} (%)	Yielding of longitudinal bar Θ_{msy_n} (%)	Concrete spalling Θ_{sps_n} (%)	PT yielding Θ_{py_n} (%)	Fracture of longitudinal bar Θ_{msf} (%)
Wall 1	Westward	0.016	0.57	1.35	3.04	3.56*
	Eastward	-0.026	-0.57	-1.35	-2.99	N/A
Wall 2	Westward	0.2	0.21	0.9	3.56	3.05*
	Eastward	-0.2	-.21	-0.9	-3.3	2.99*
Wall 3	Westward	0.2	0.9	0.9	N/A	N/A
	Eastward	-0.2	-0.9	-0.9	N/A	N/A

Table 4-3 Analytical results of selected limit states based on Srivastava et al. (2013)

Wall ID	ELL1 Θ_{ELL1} (%)	ELL2 Θ_{ELL2} (%)	ELL3 Θ_{ELL3} (%)	ELL4* Θ_{ELL4} (%)	FMS Θ_{FMS} (%)	LLP Θ_{LLP} (%)	CCC Θ_{CCC} (%)
PW1.0.0	0.25	0.54	0.04	0.18	2.18	2.23	6.43
PW2.0.0	0.29	0.43	0.08	0.18	2.25	2.31	4.40

*Corresponding to yield of longitudinal bar.

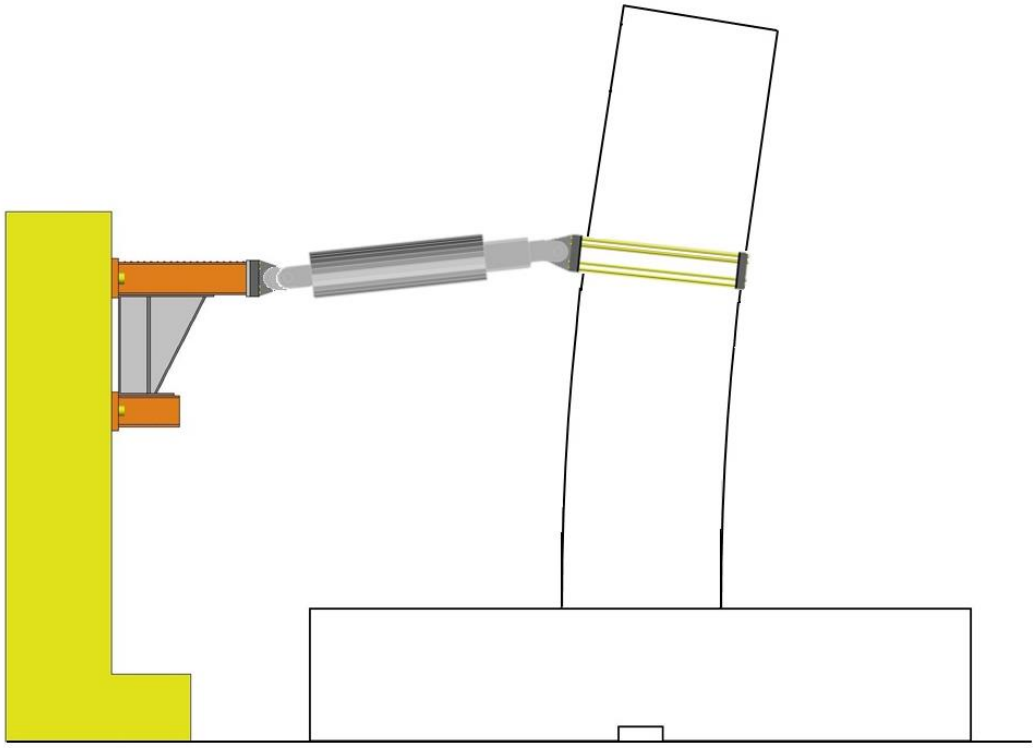

Figure 4-1 Displaced state of test wall loaded East

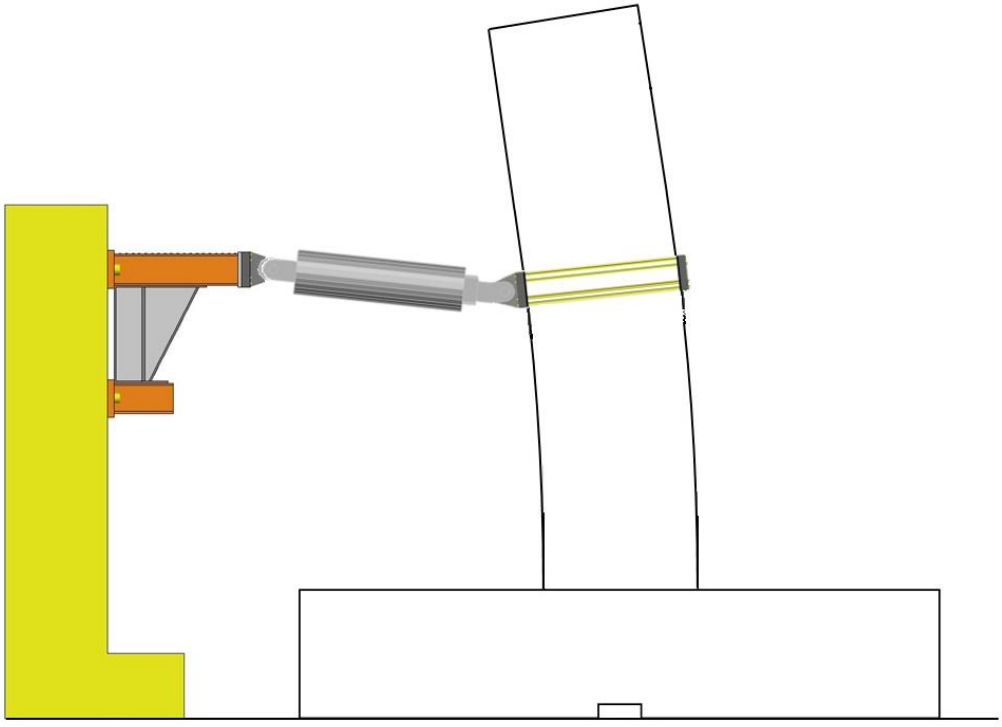

Figure 4-2 Displaced state of test wall loaded West

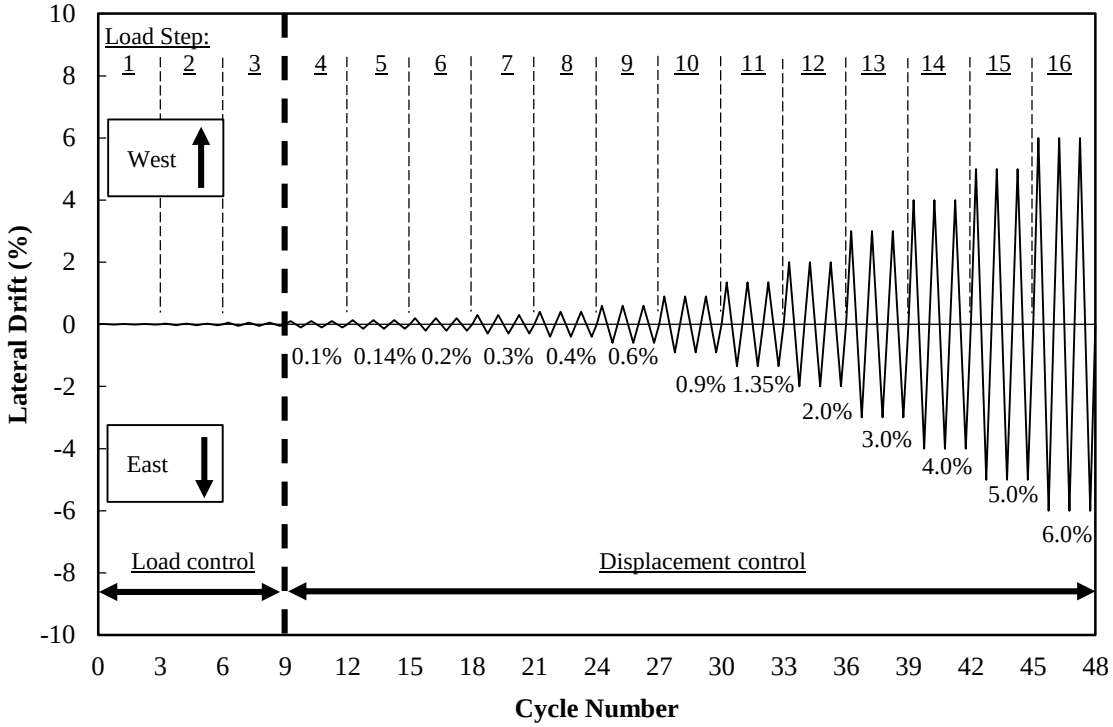

Figure 4-3 Complete planned loading history for Wall 1, Wall 2, and Wall 3

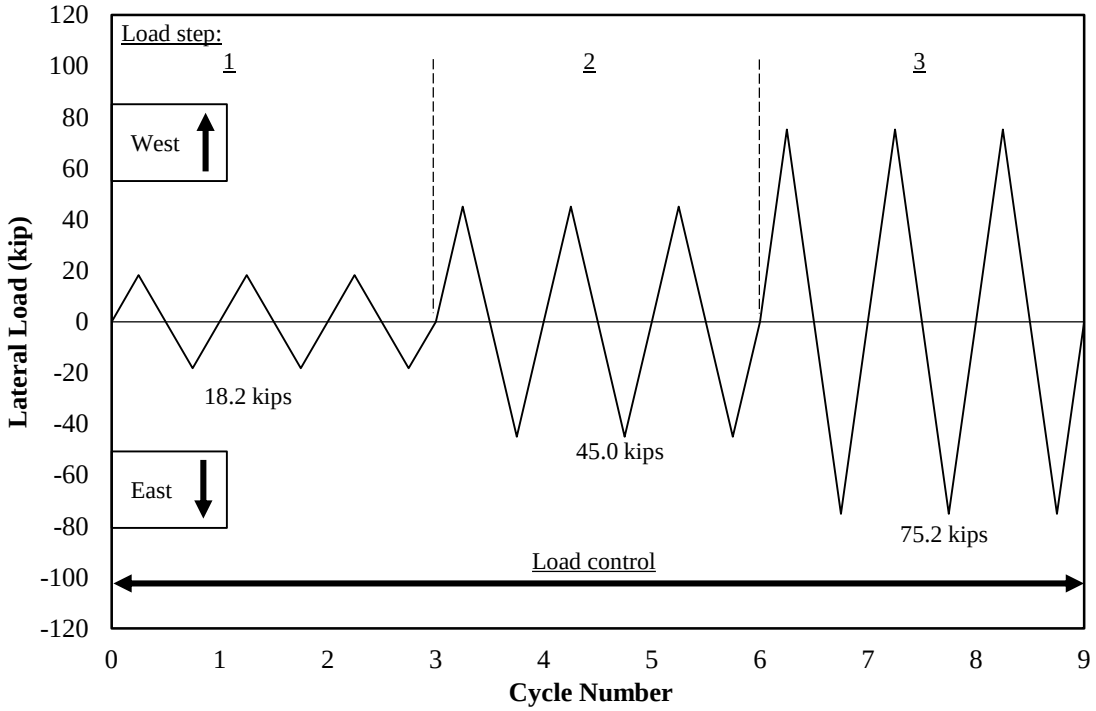

Figure 4-4 Loading history – load control portion Wall 1

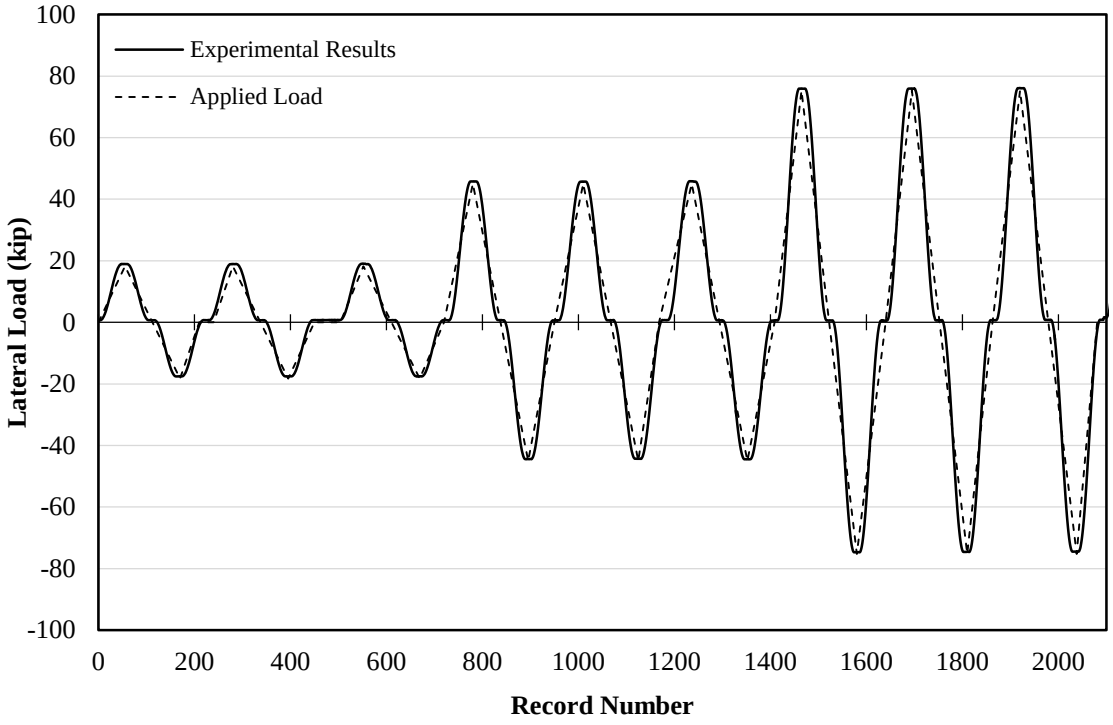

Figure 4-5 Experimental results superposed (load control portion) Wall 1

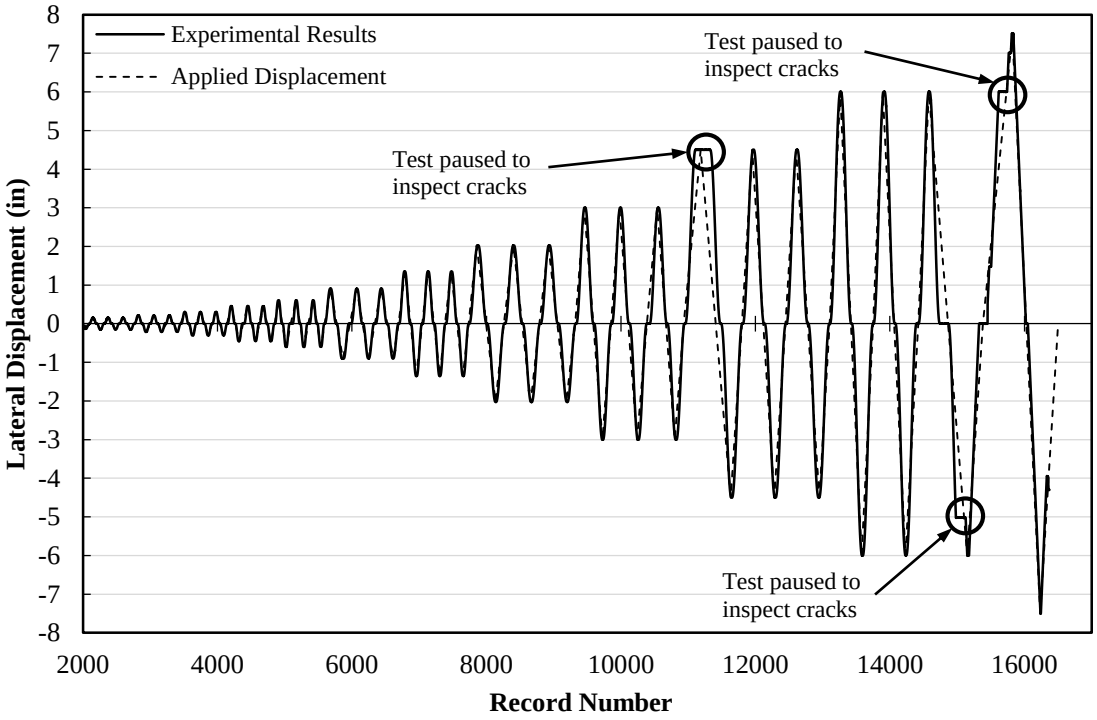

Figure 4-6 Experimental results superposed (displacement control) Wall 1

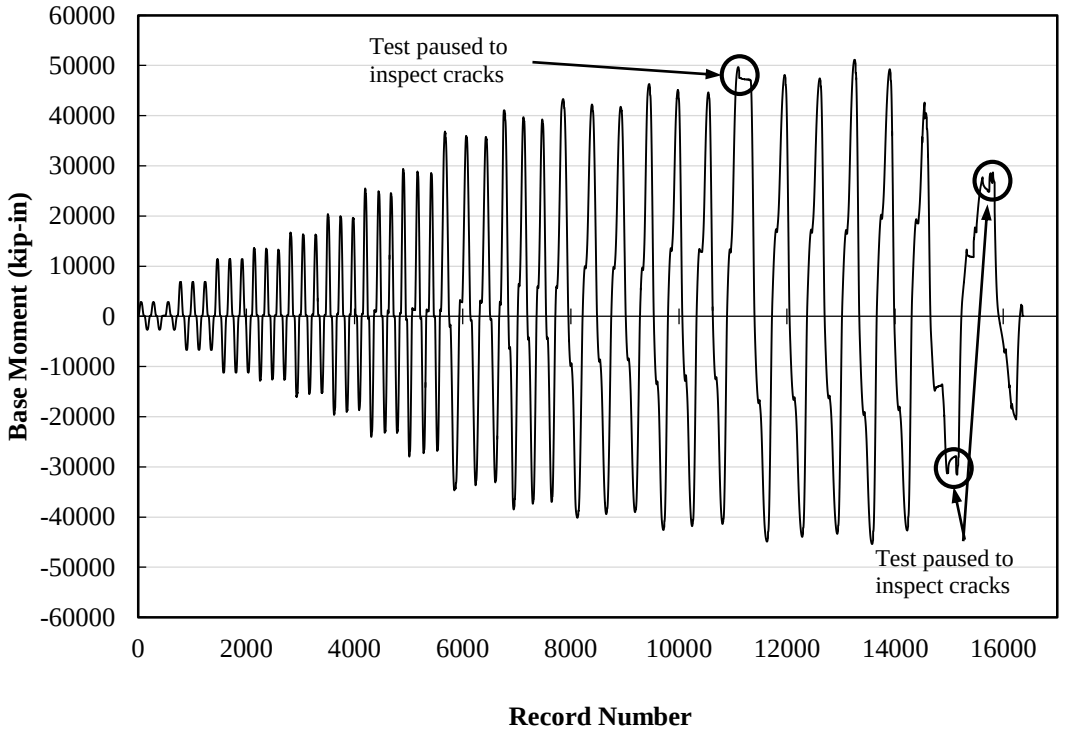

Figure 4-7 Base moment versus record number Wall 1

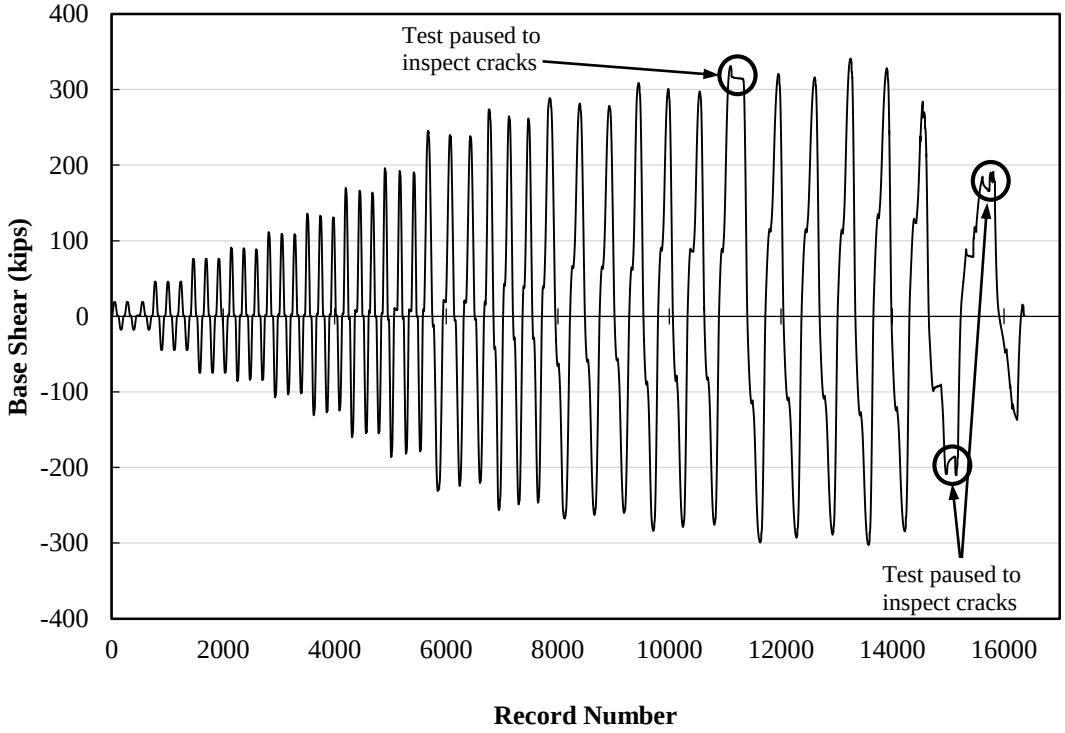

Figure 4-8 Base shear versus record number Wall 1

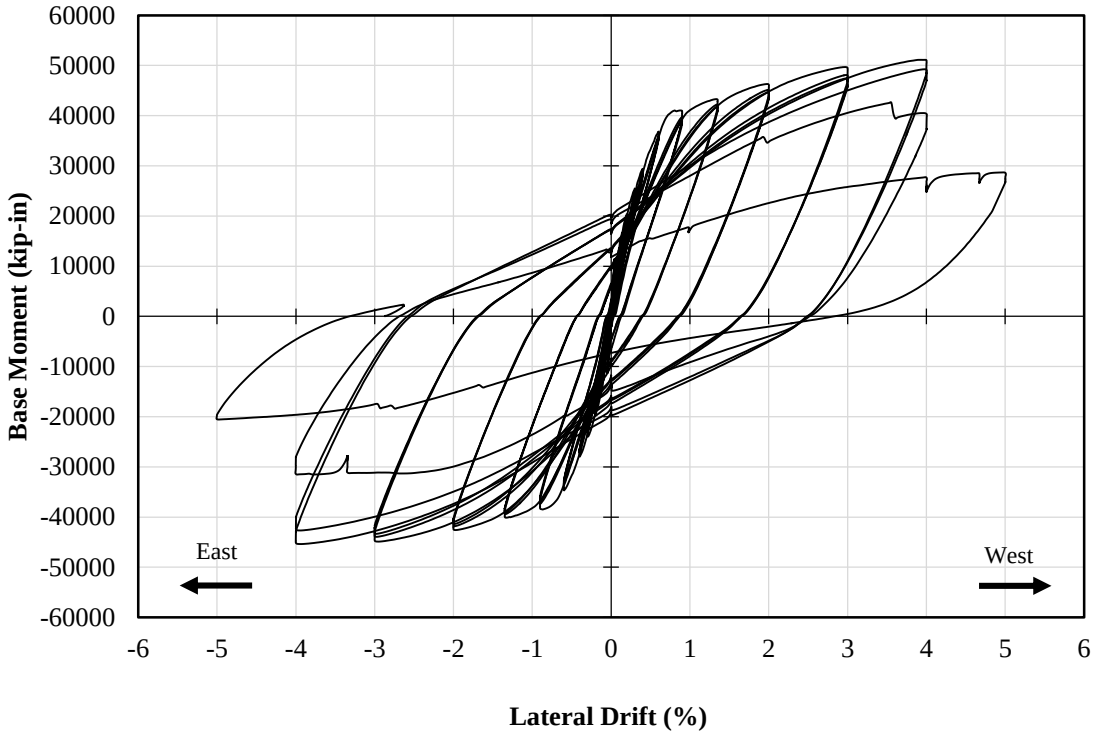

Figure 4-9 Complete experimental response – base moment vs lateral drift Wall 1

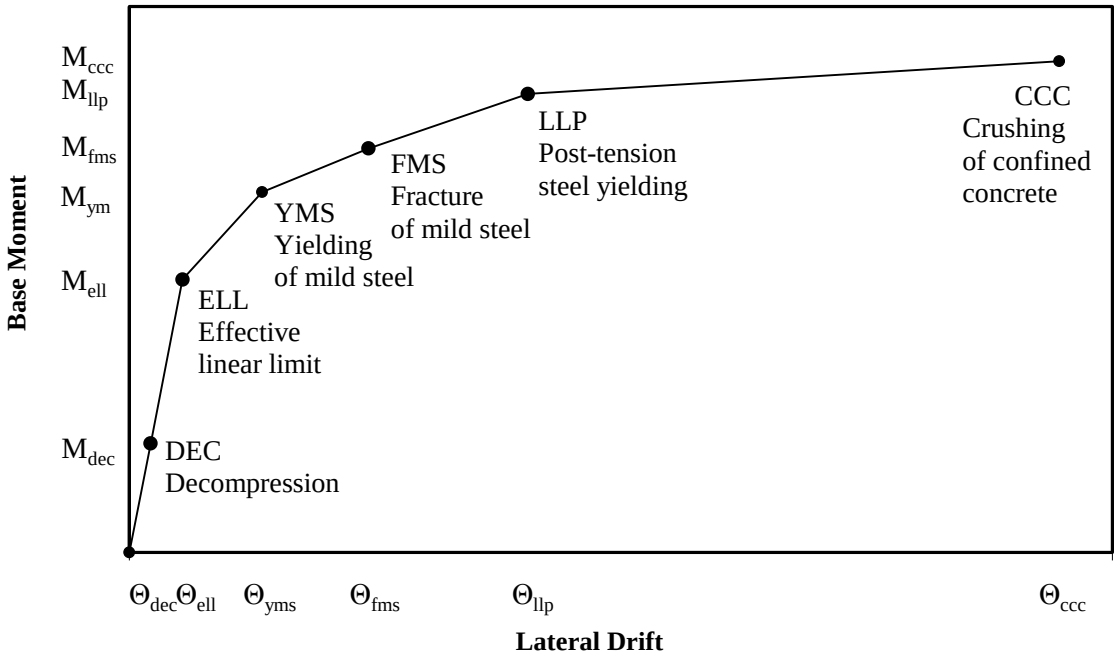

Figure 4-10 Structural limit states (Srivastava et al. 2013)

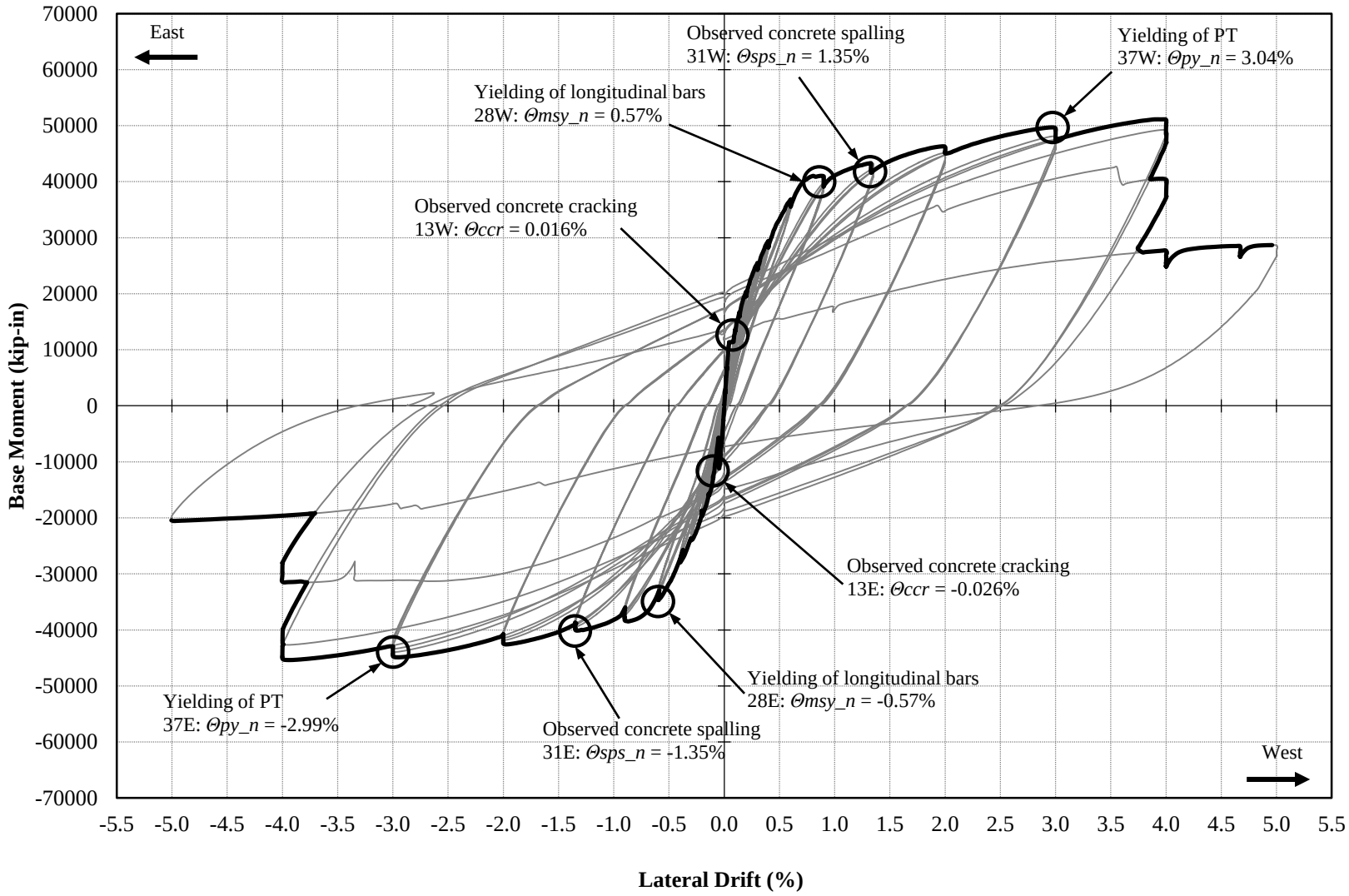

Figure 4-11 Experimental envelope curve and complete hysteresis including observed wall behavior and limit states Wall 1

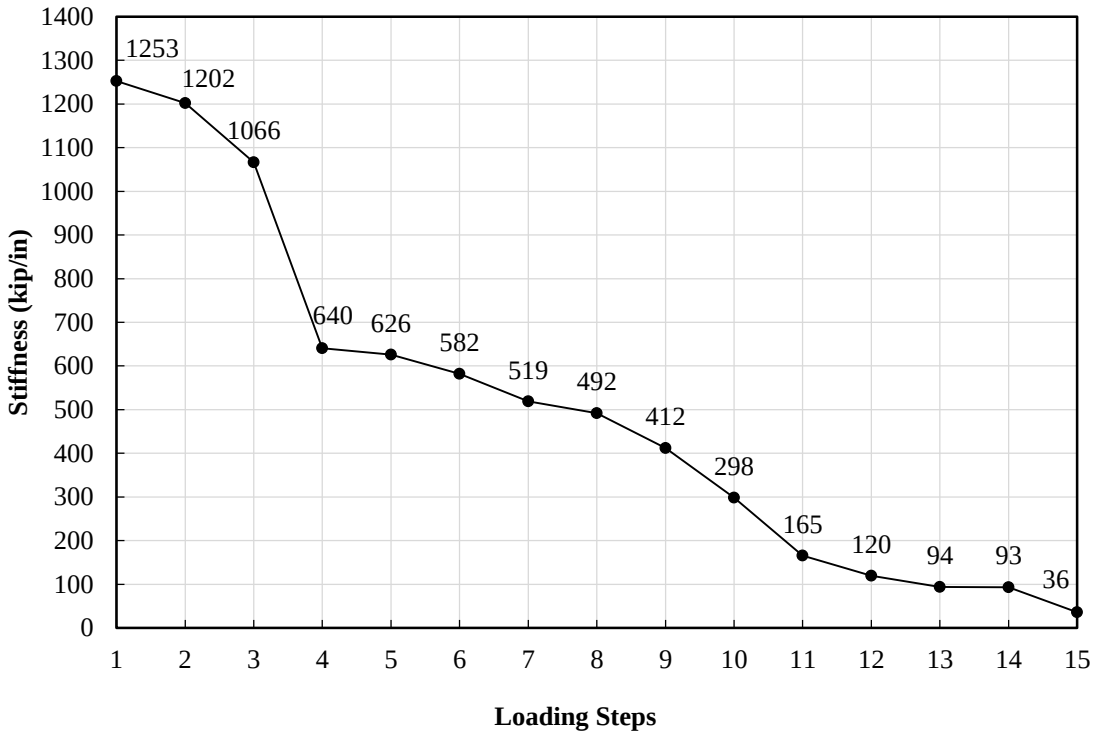

Figure 4-12 Stiffness degradation (per load step increase) versus load steps Wall 1

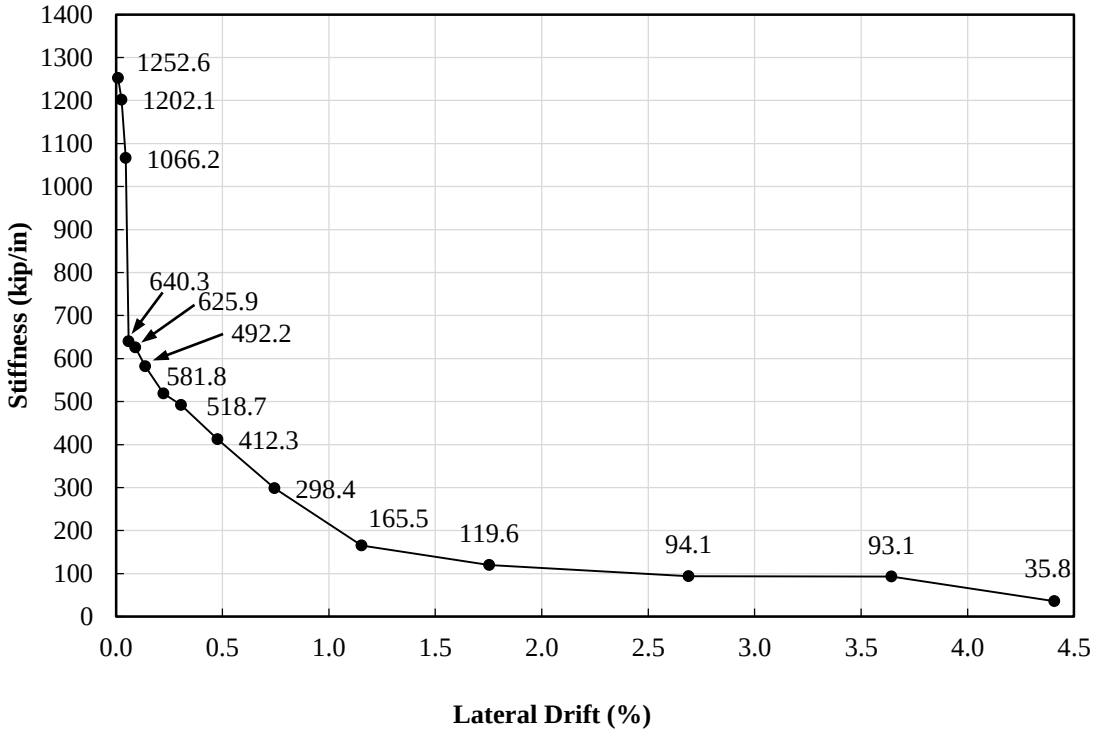

Figure 4-13 Stiffness degradation (per load step) versus lateral drift Wall 1

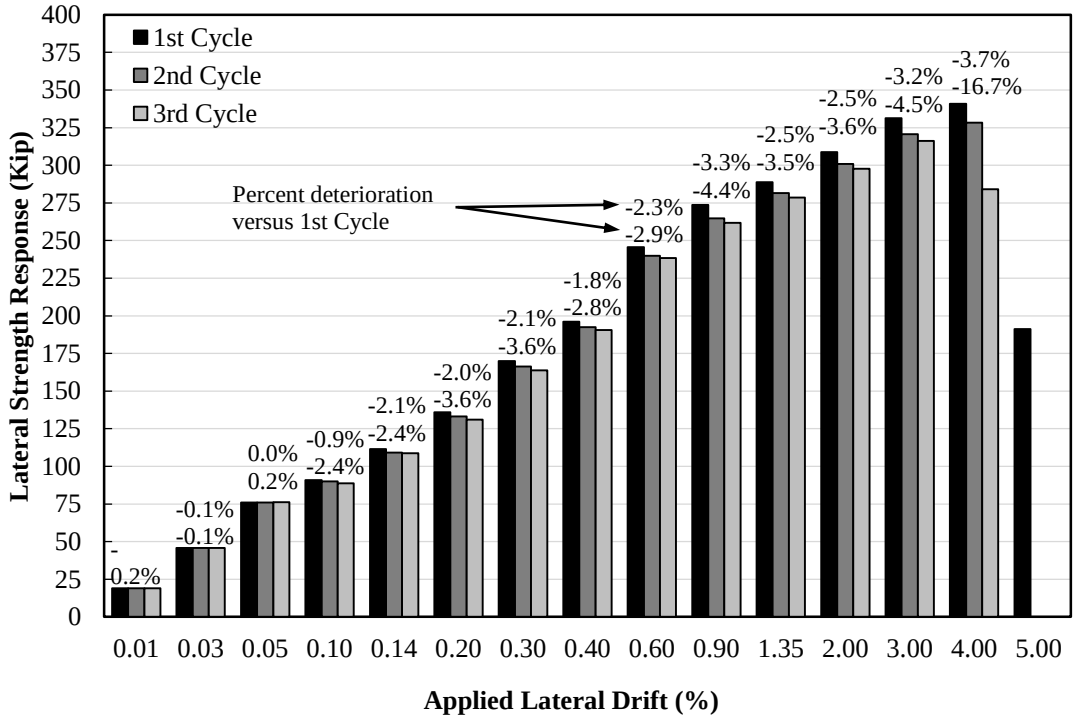

Figure 4-14 Strength deterioration per cycle at applied lateral drift Wall 1

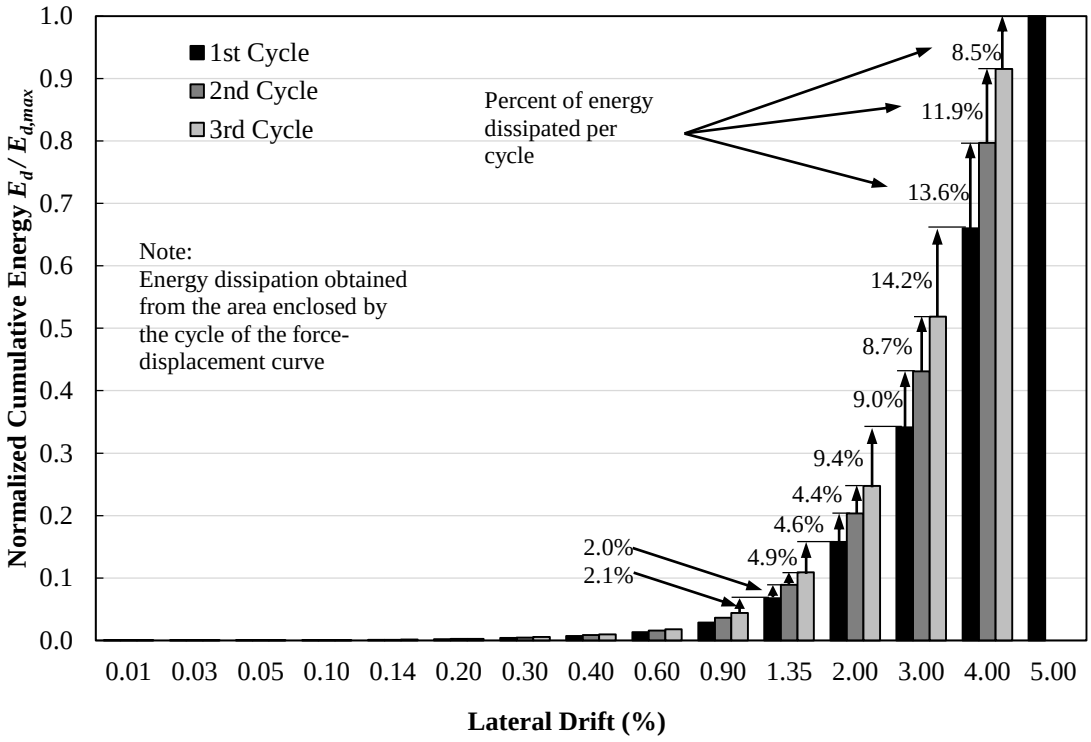

Figure 4-15 Normalized cumulative hysteretic energy dissipation Wall 1

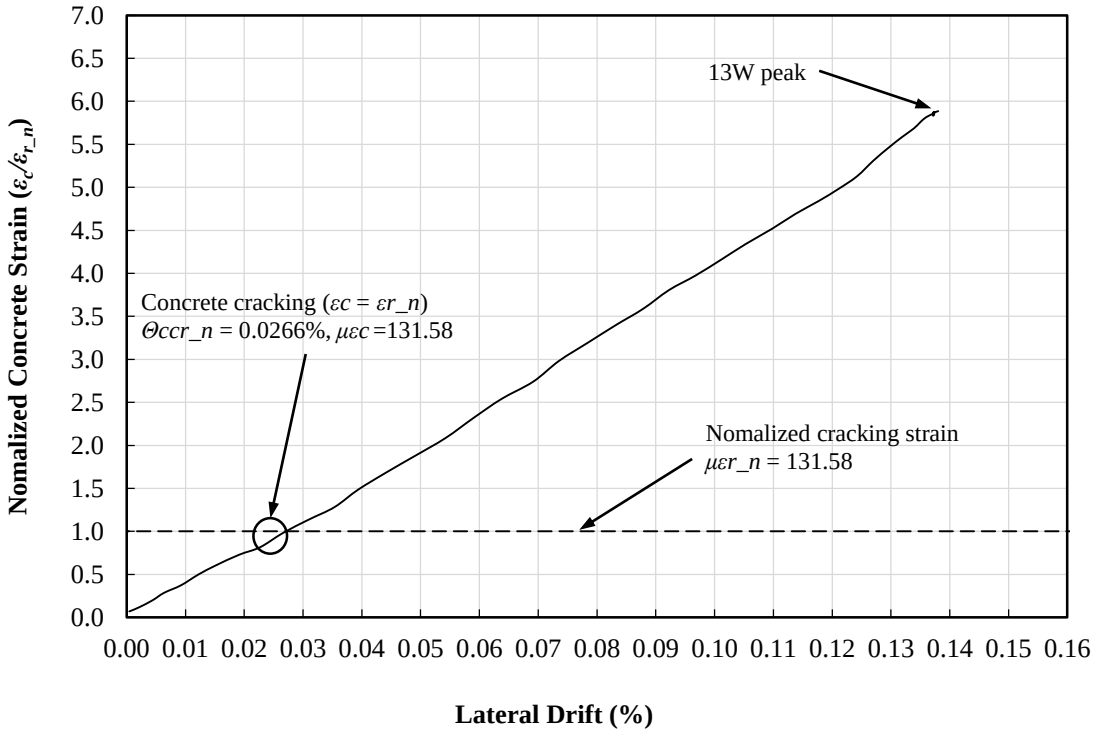

Figure 4-16 Concrete cracking strain versus lateral drift (East side) Wall 1

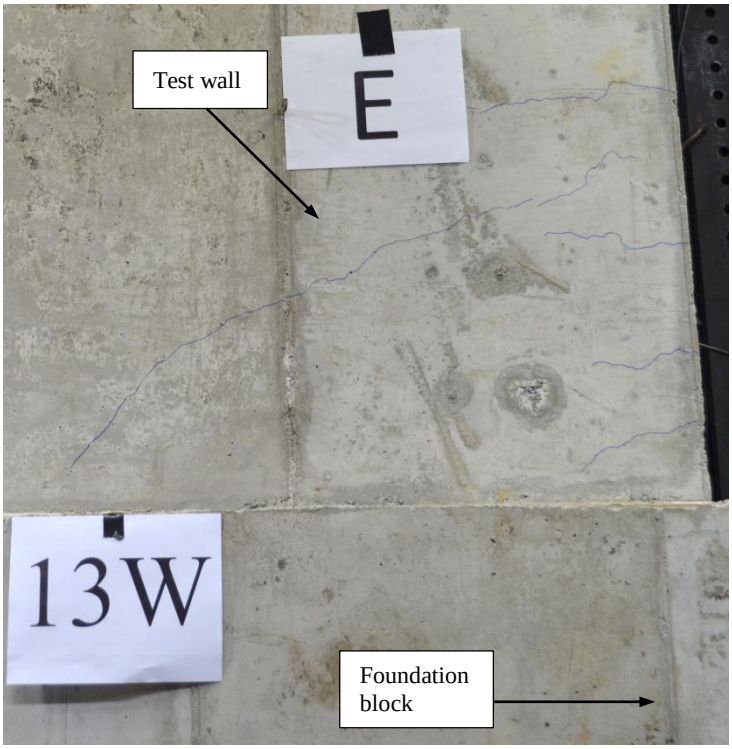

Figure 4-17 Photograph of observed initiation of concrete cracking on the East side Wall 1

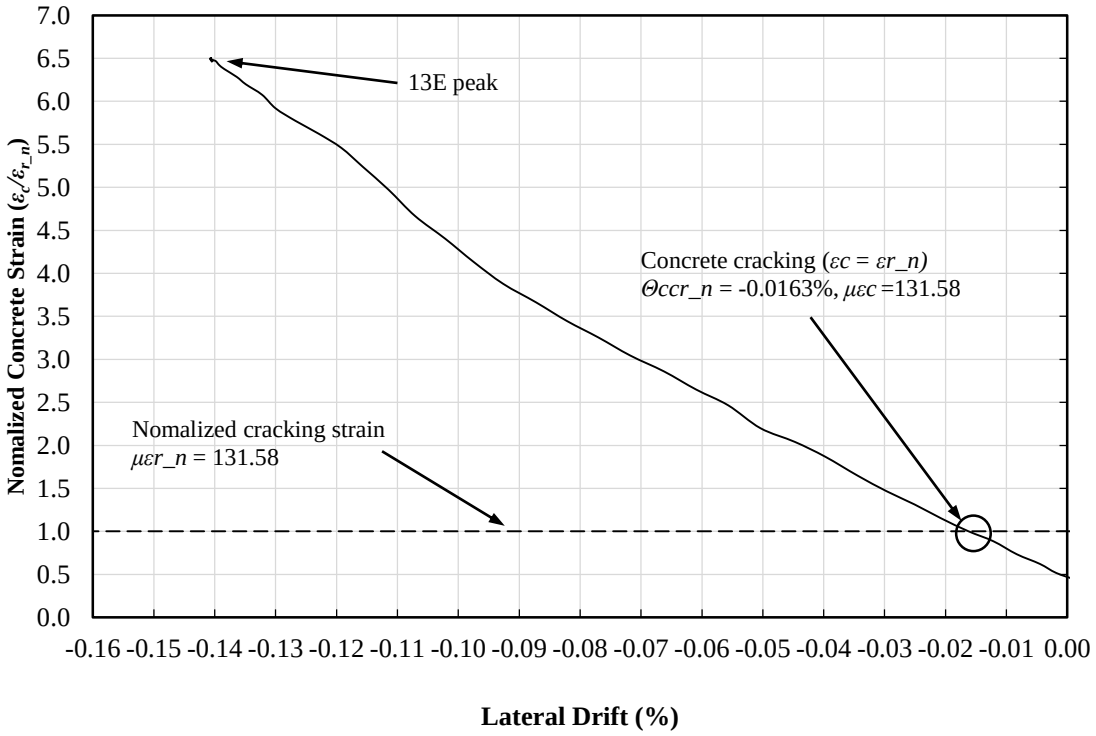

Figure 4-18 concrete cracking strain versus lateral drift (West side) Wall 1

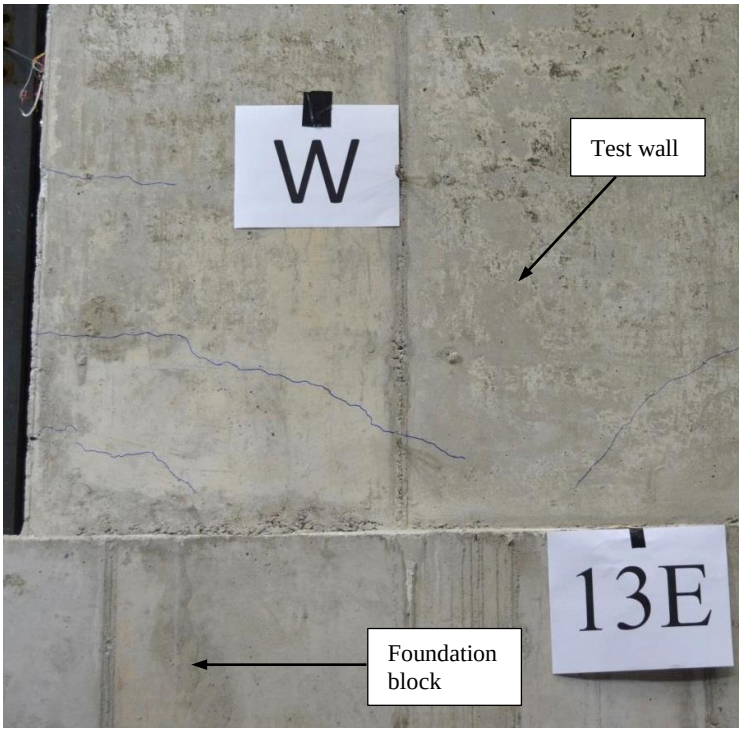

Figure 4-19 Photograph of observed initiation of concrete cracking on the West side Wall 1

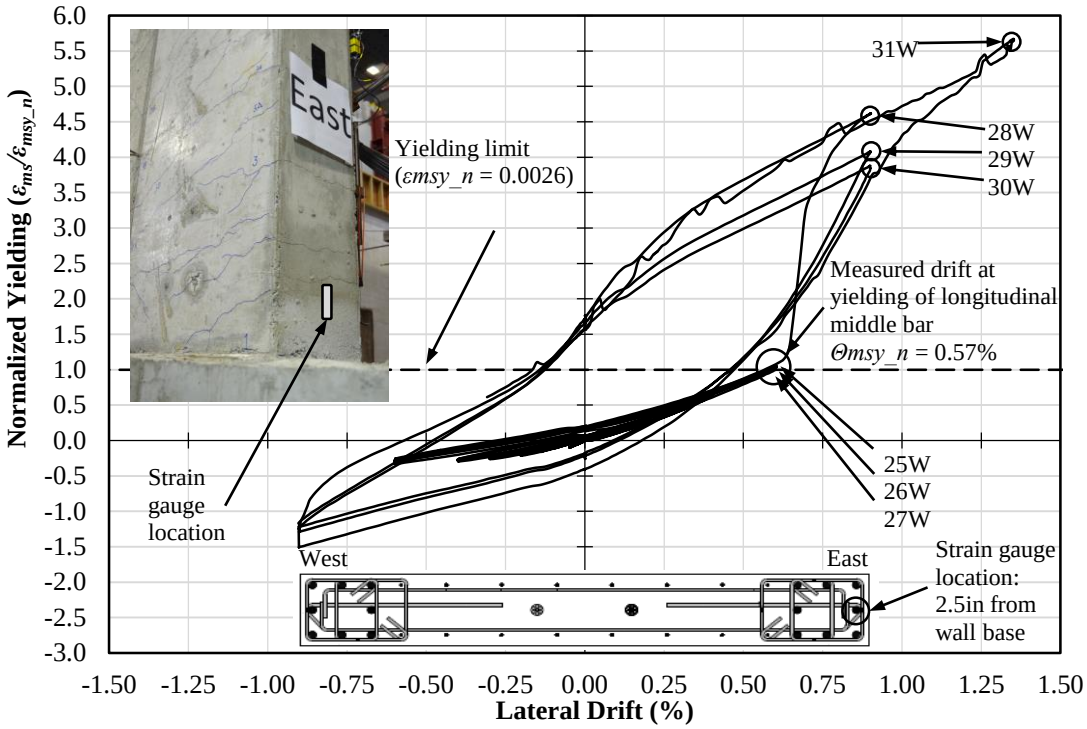

Figure 4-20 Strain of longitudinal middle bar versus lateral drift Wall 1

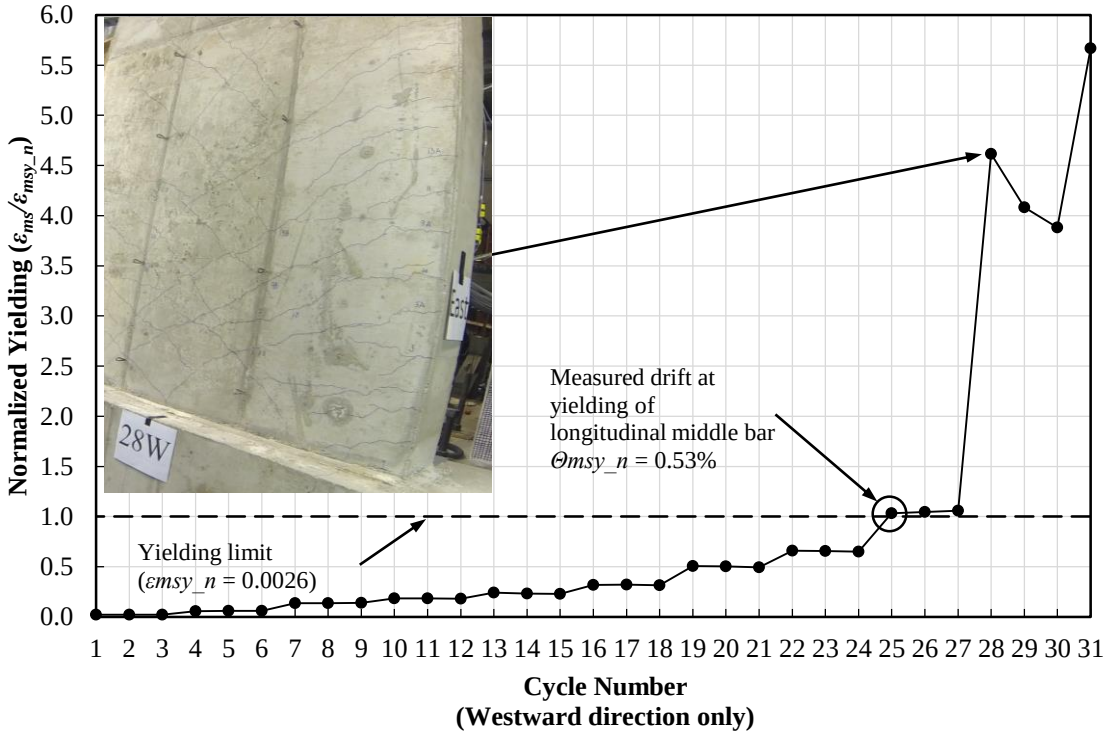

Figure 4-21 Strain of longitudinal middle bar versus cycle number Wall 1

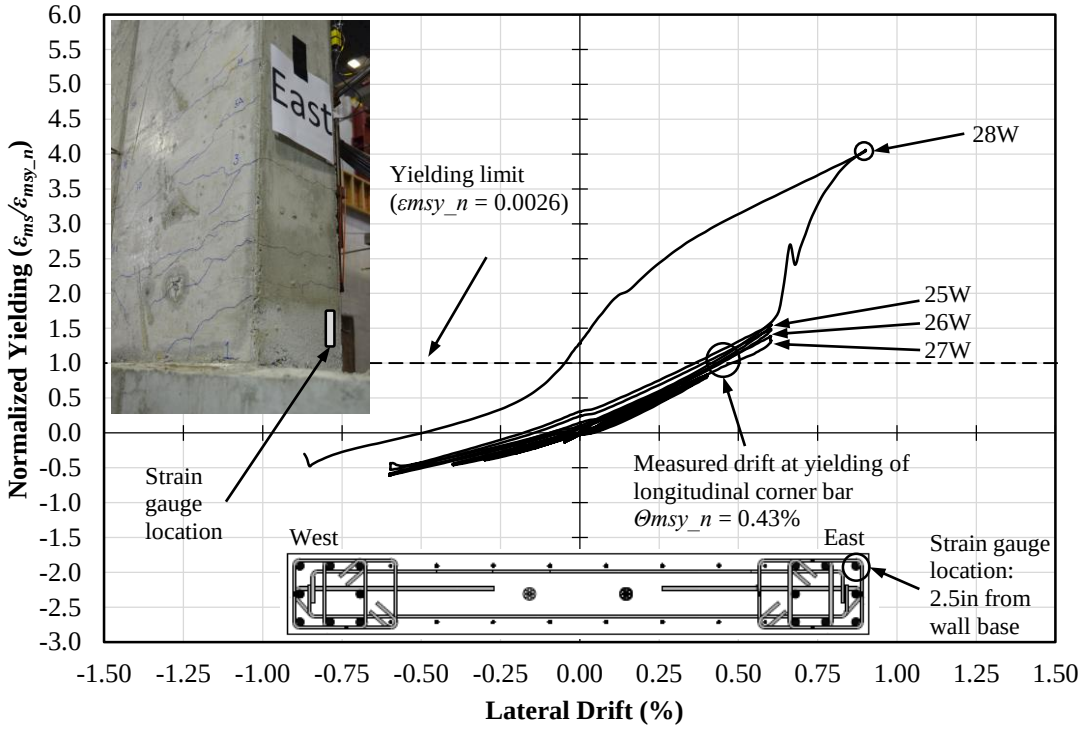

Figure 4-22 Strain of longitudinal corner bar versus lateral drift Wall 1

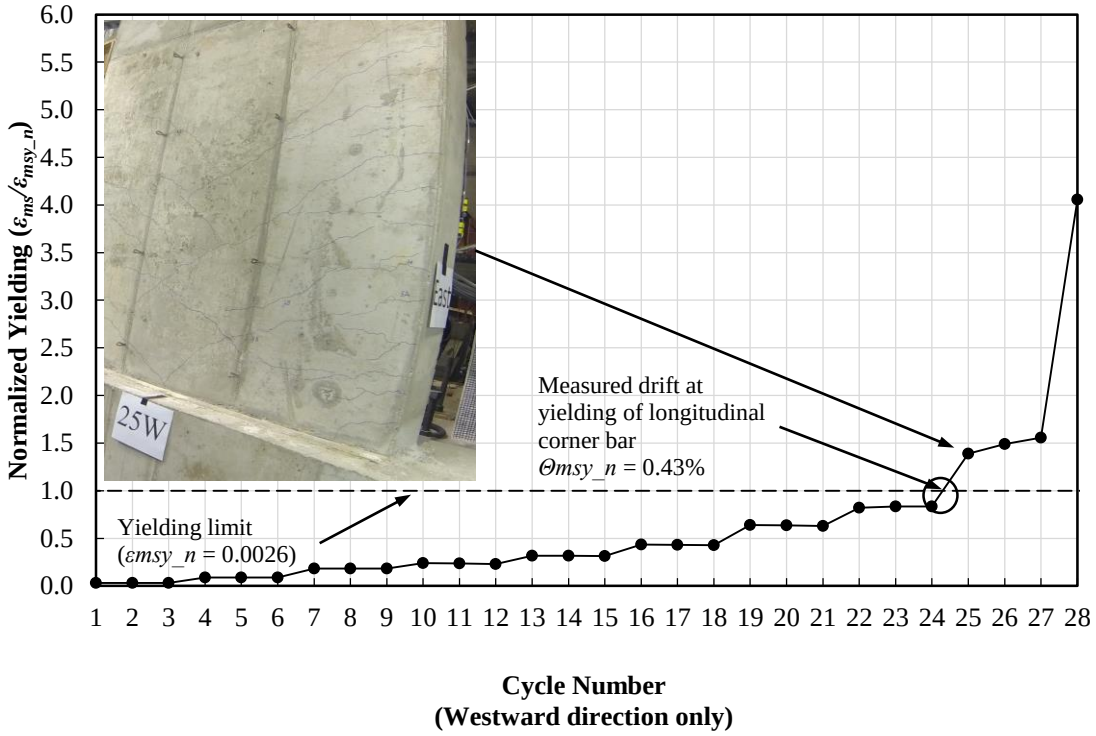

Figure 4-23 Strain of longitudinal corner bar versus cycle number Wall 1

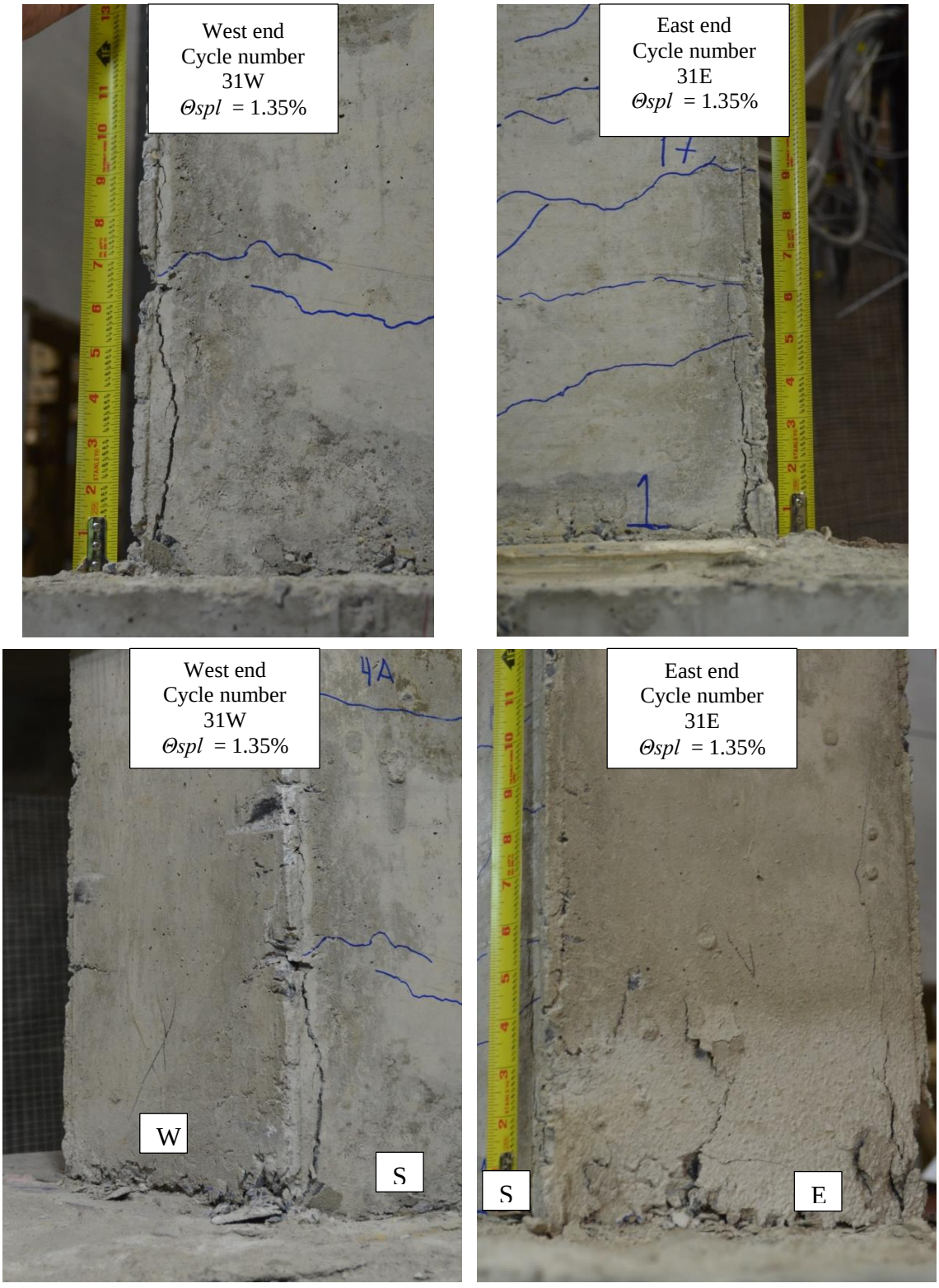

Figure 4-24 Initiation of observed spalling during Load Step 11, Cycle 31 Wall 1

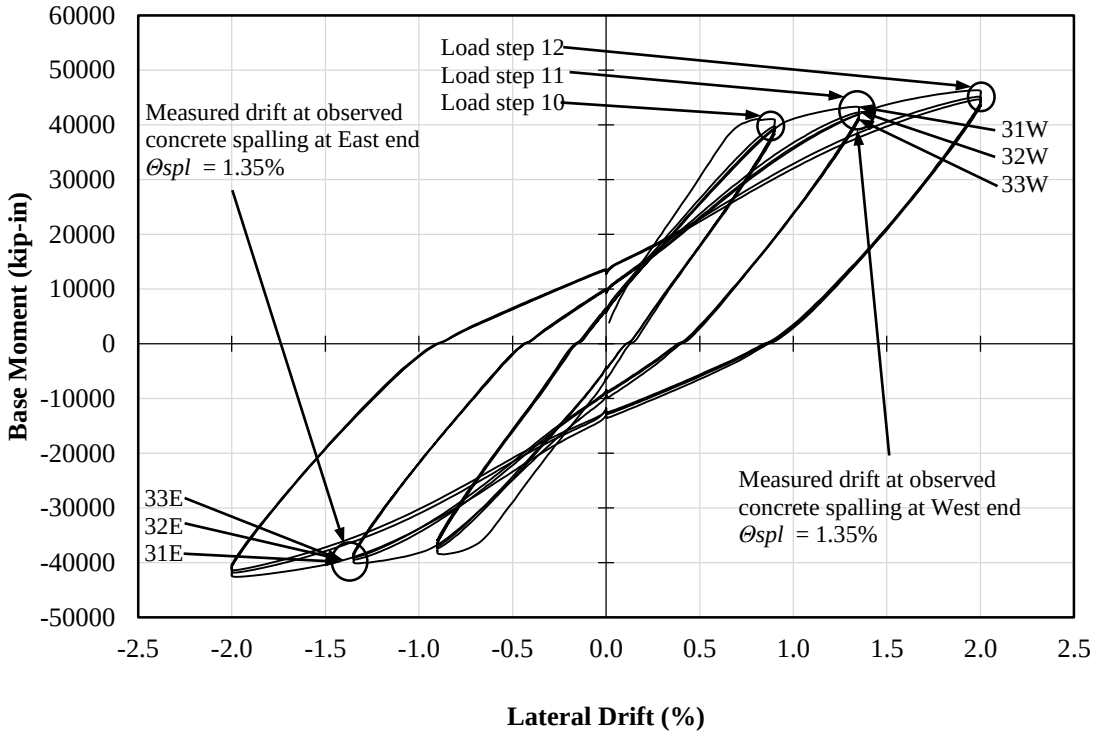

Figure 4-25 Initiation of concrete spalling during Load Step 11, Cycle 31 Wall 1

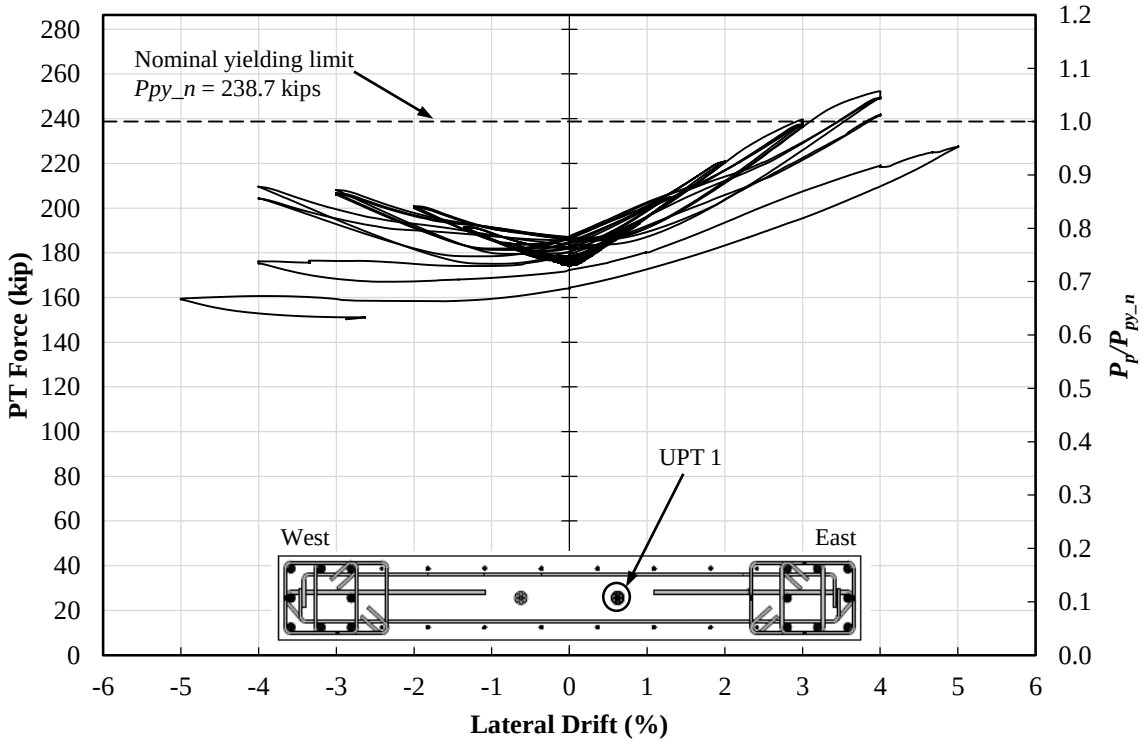

Figure 4-26 Unbonded post-tension complete response – East side Wall 1

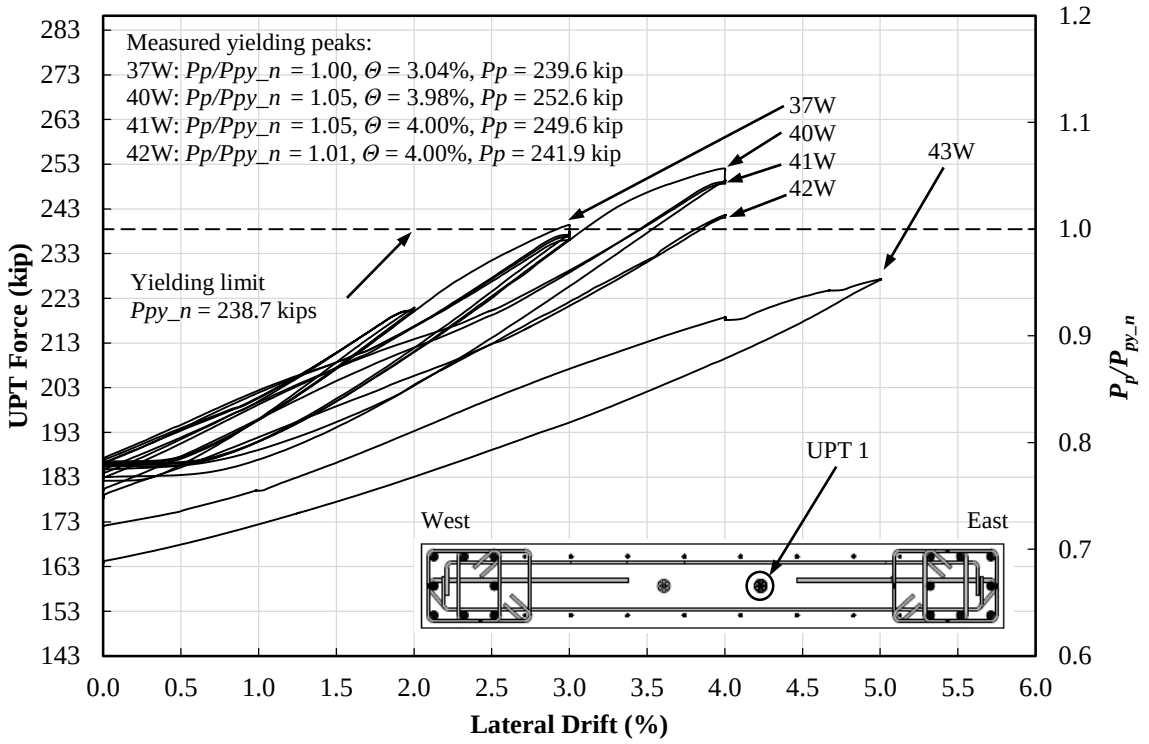

Figure 4-27 UPT normalized yielding peaks – East side Wall 1

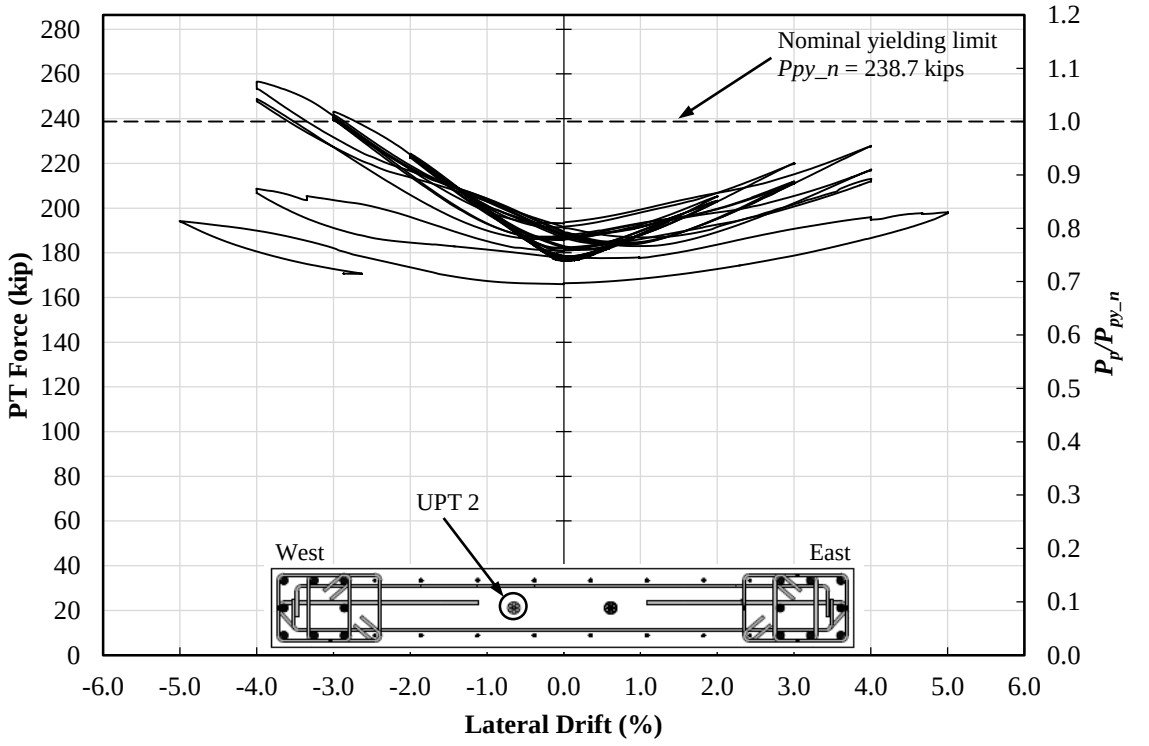

Figure 4-28 Unbonded post-tension complete response – West side Wall 1

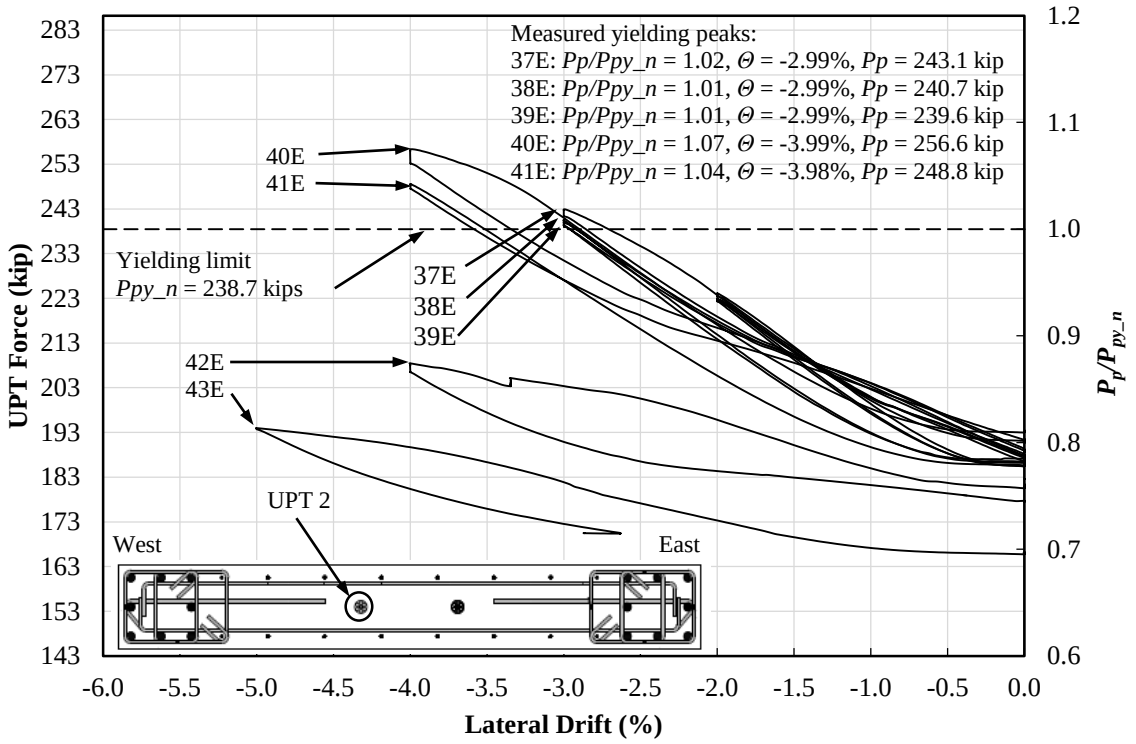

Figure 4-29 UPT normalized yielding peaks – West side Wall 1

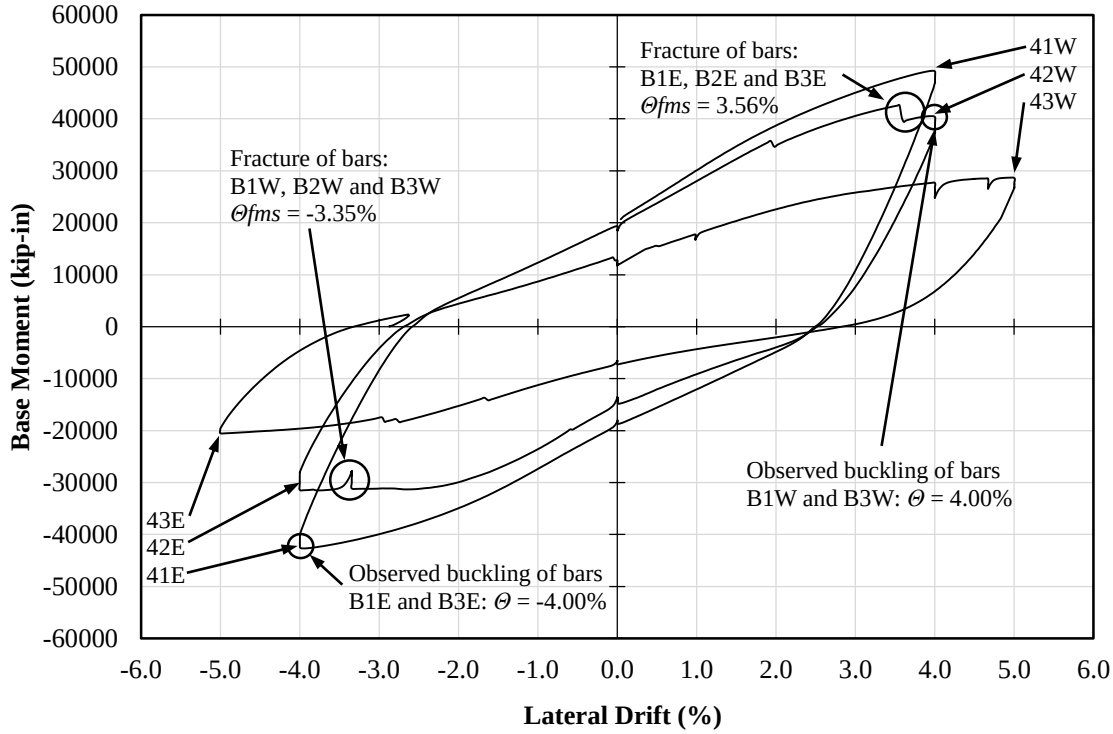

Figure 4-30 Observed fracture of longitudinal reinforcement Wall 1

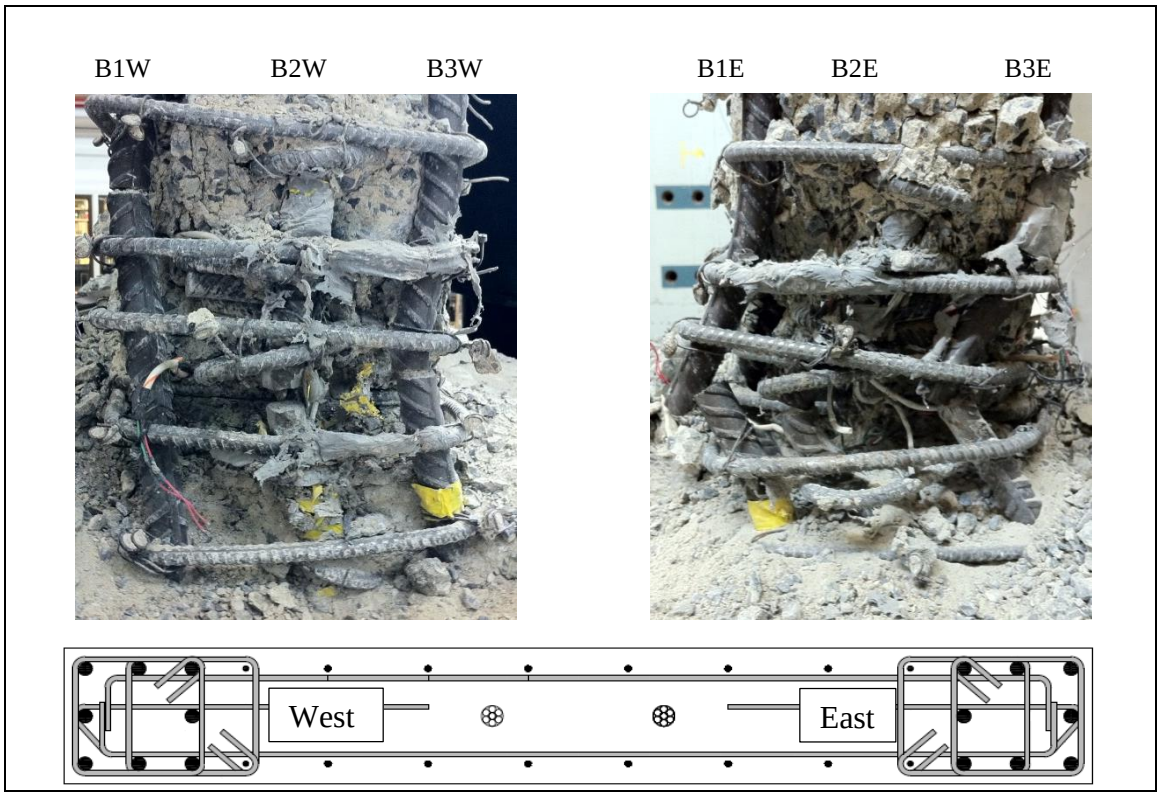

Figure 4-31 Photographs of fractured of longitudinal bars on East and West sides Wall 1

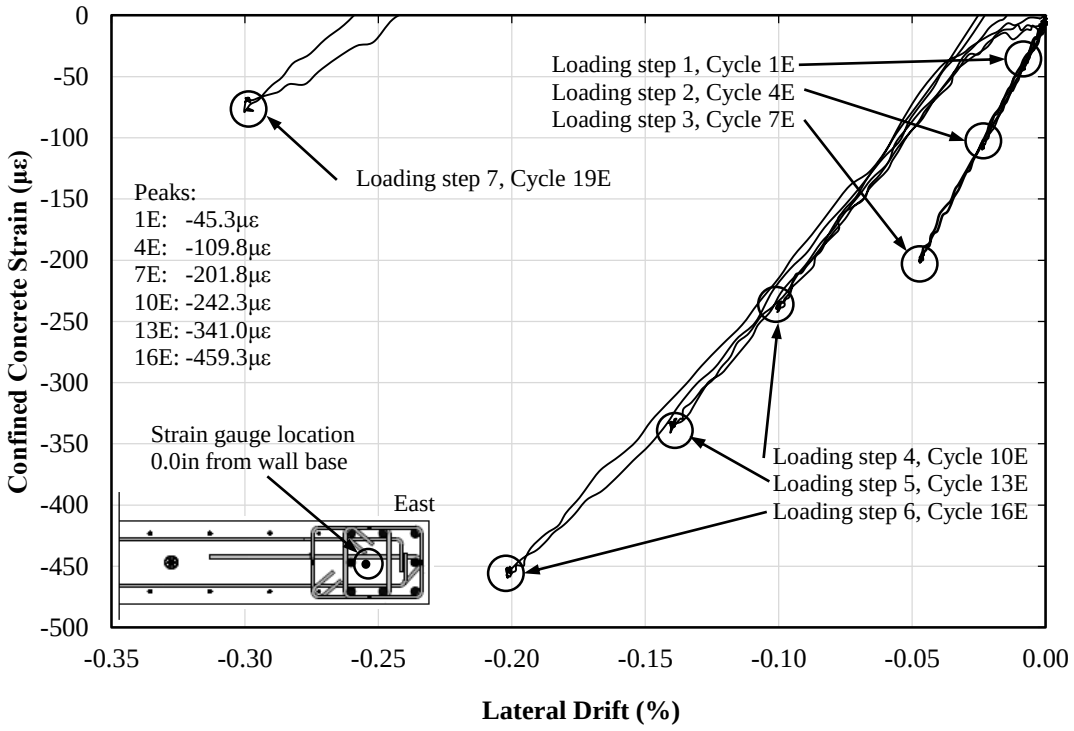

Figure 4-32 Confined concrete strain at East end of Wall 1

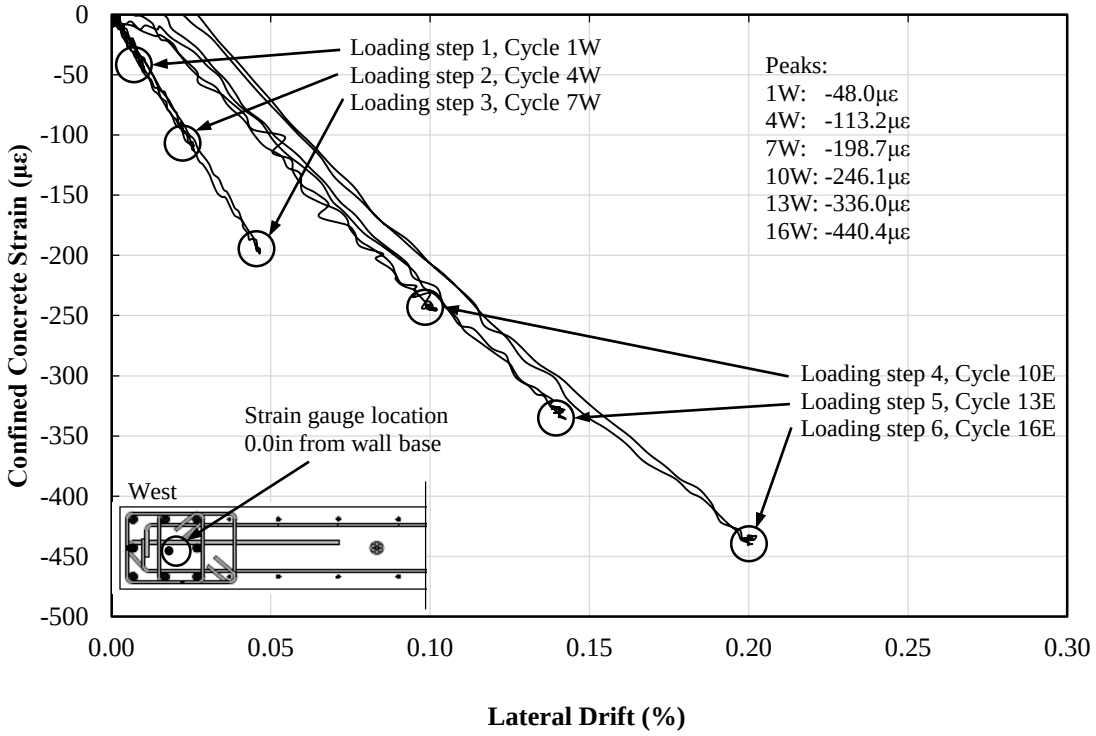

Figure 4-33 Confined concrete strain at West end of Wall 1

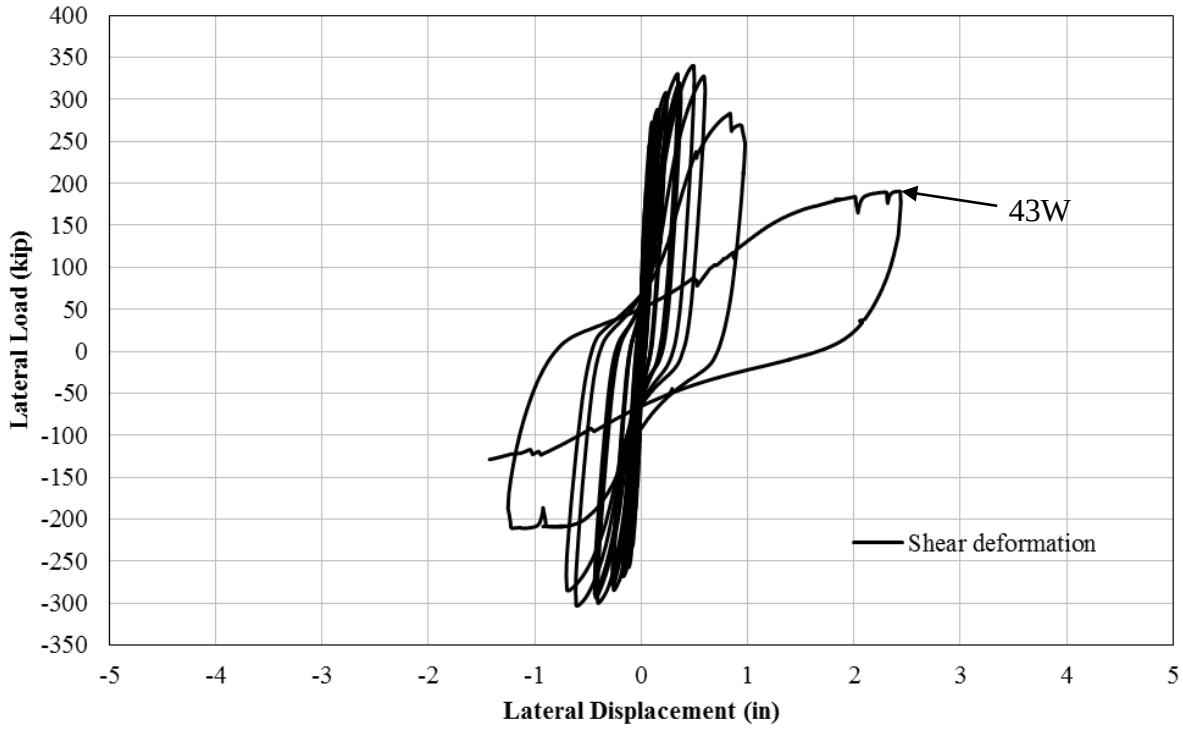

Figure 4-34 Shear deformations in Wall 1

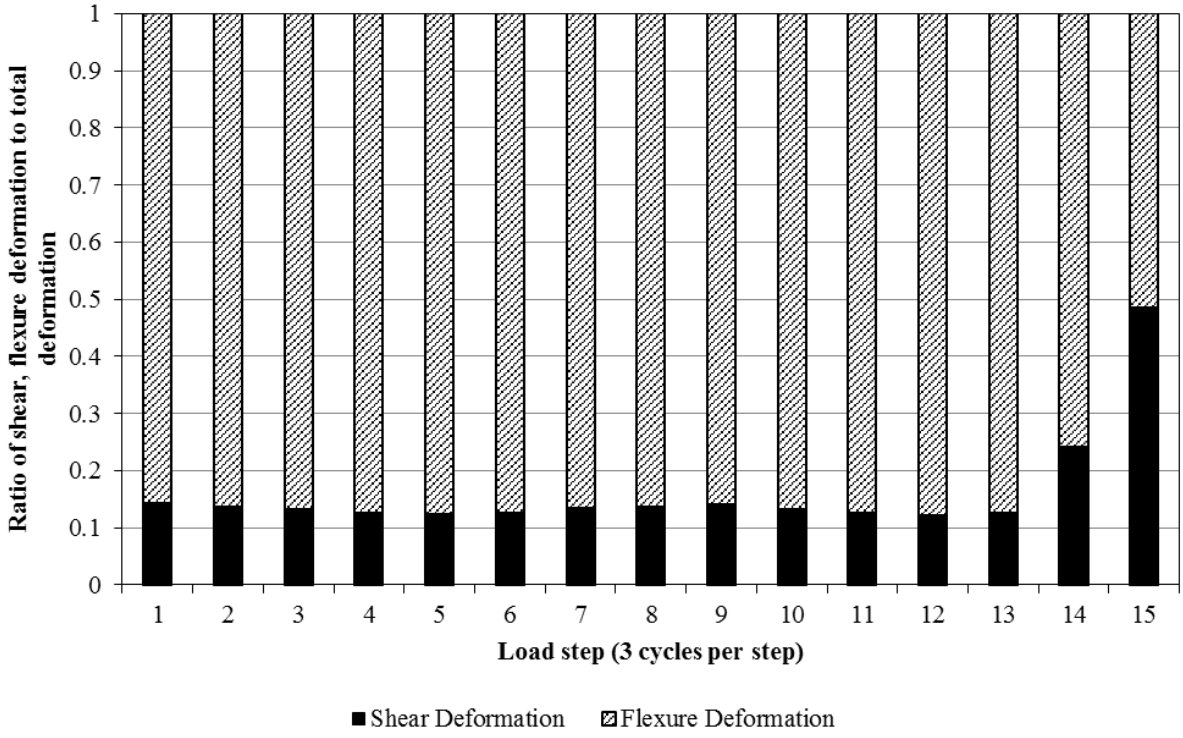

Figure 4-35 Deformation ratios

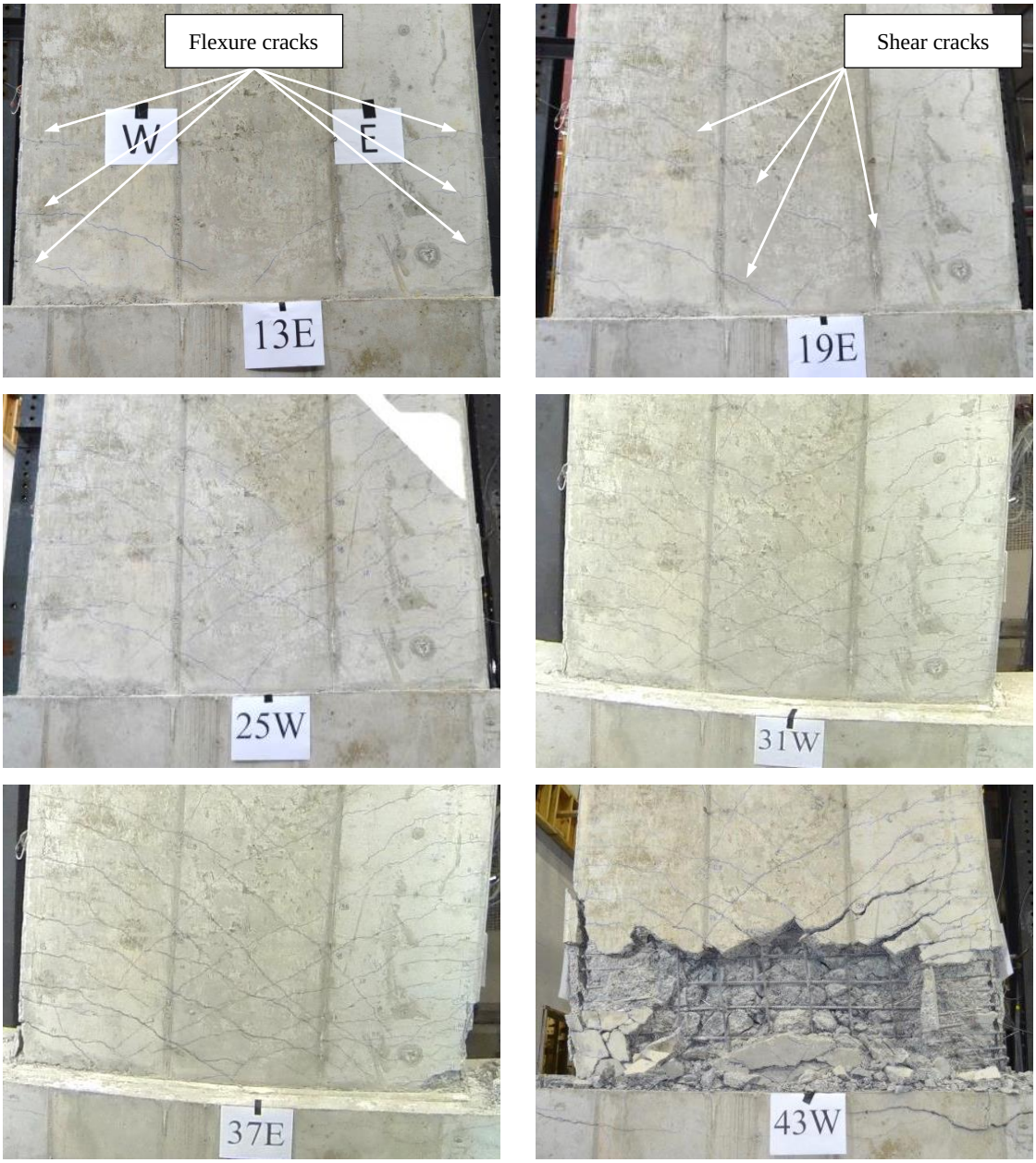

Figure 4-36 Photograph of progression of shear failure Wall 1

Figure 4-37 Confined concrete on the flange sections of Wall 1

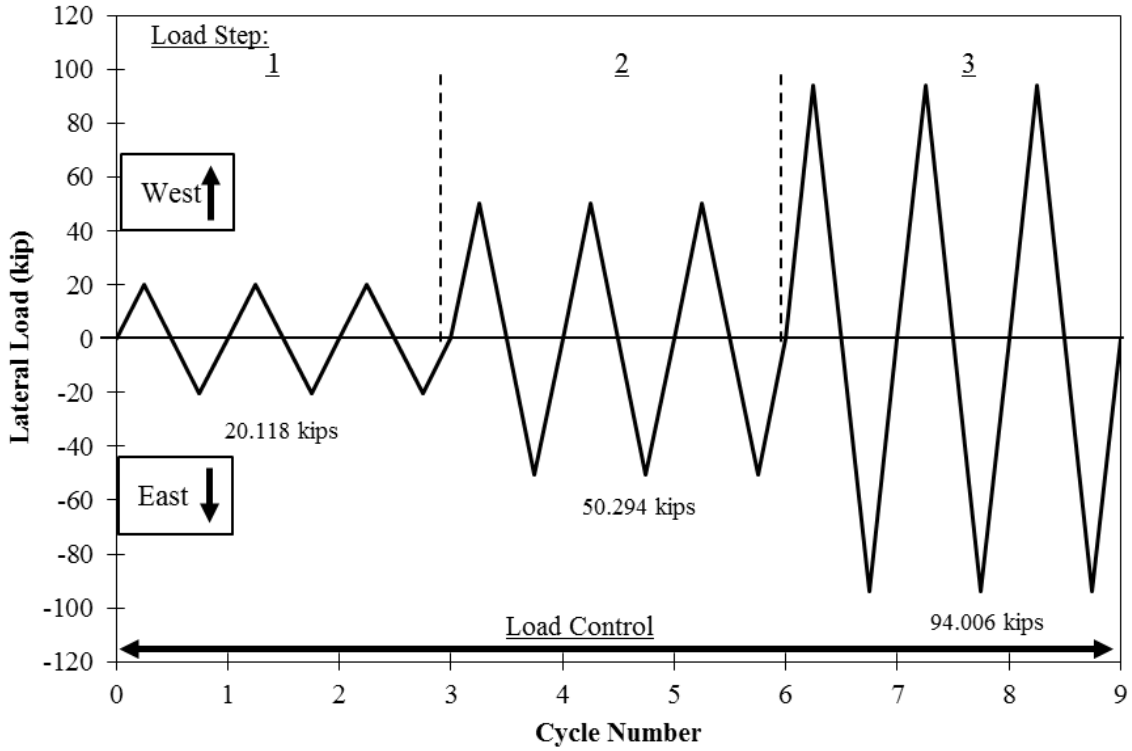

Figure 4-38 Loading history – load control portion Wall 2

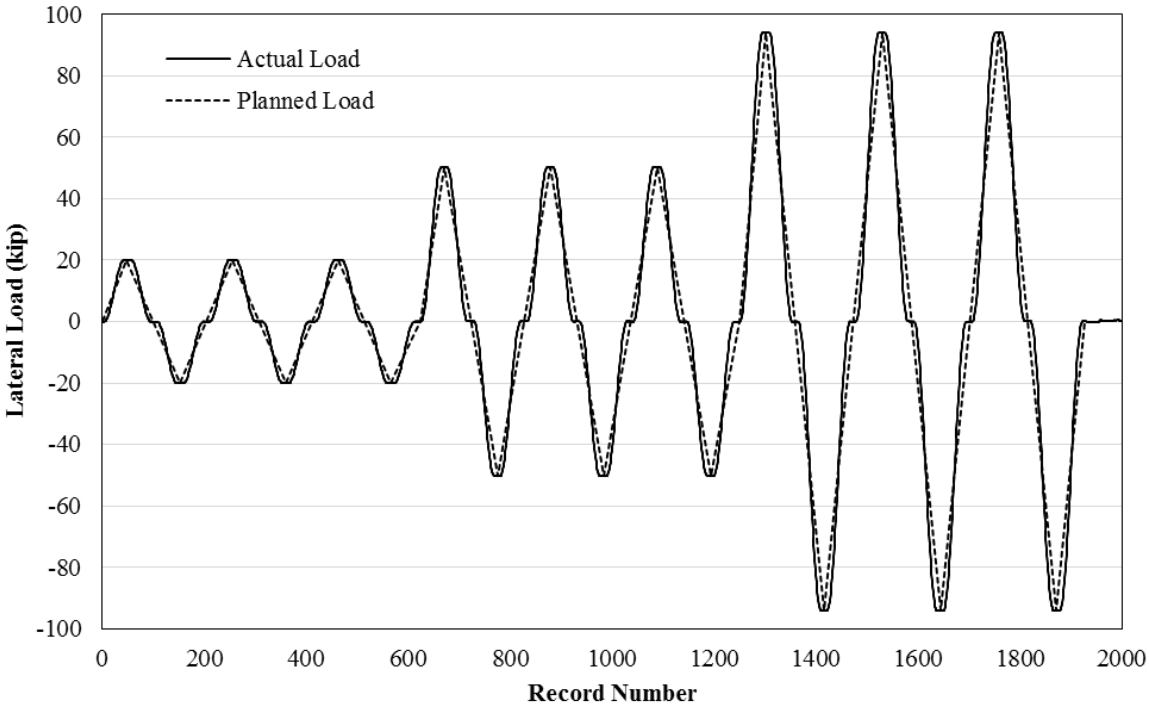

Figure 4-39 Experimental results superposed (load control portion) Wall 2

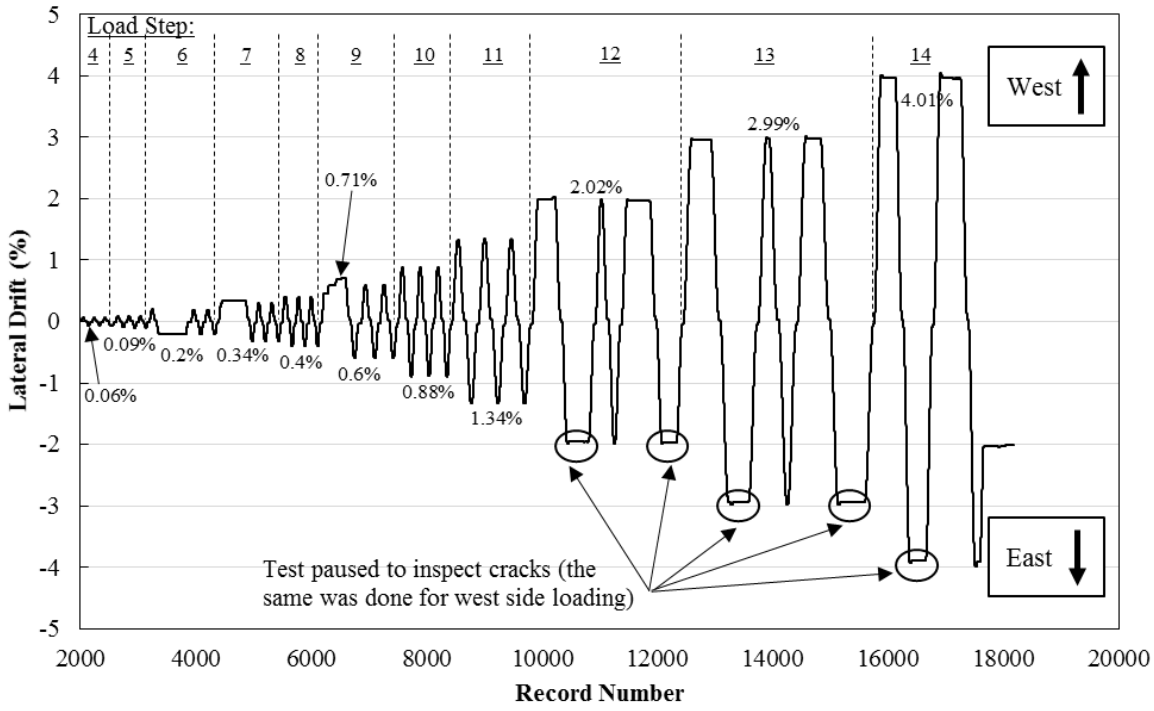

Figure 4-40 Actual loading history (displacement control) Wall 2

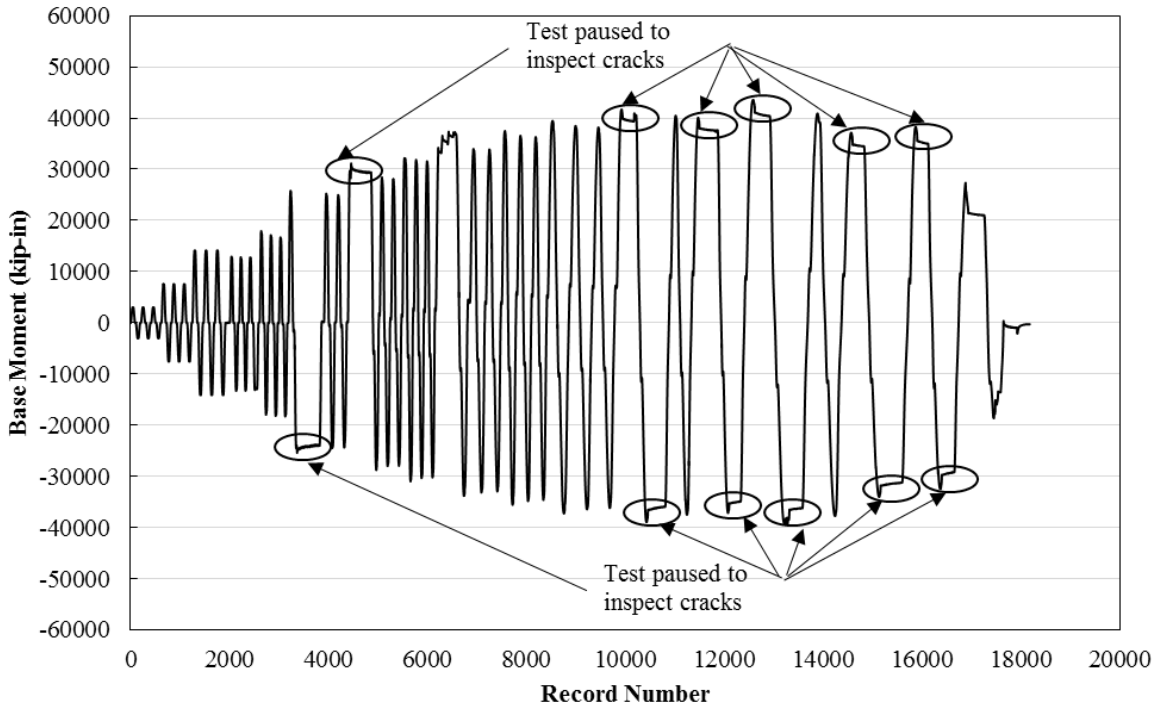

Figure 4-41 Base moment versus record number Wall 2

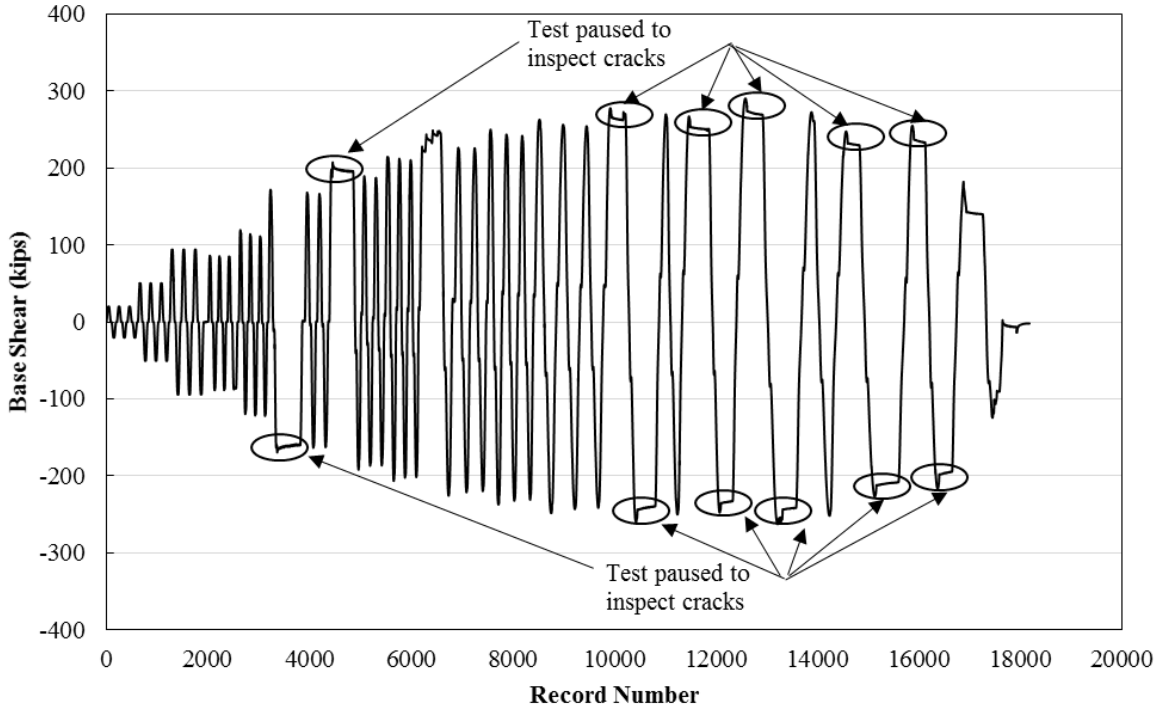

Figure 4-42 Base shear versus record number Wall 2

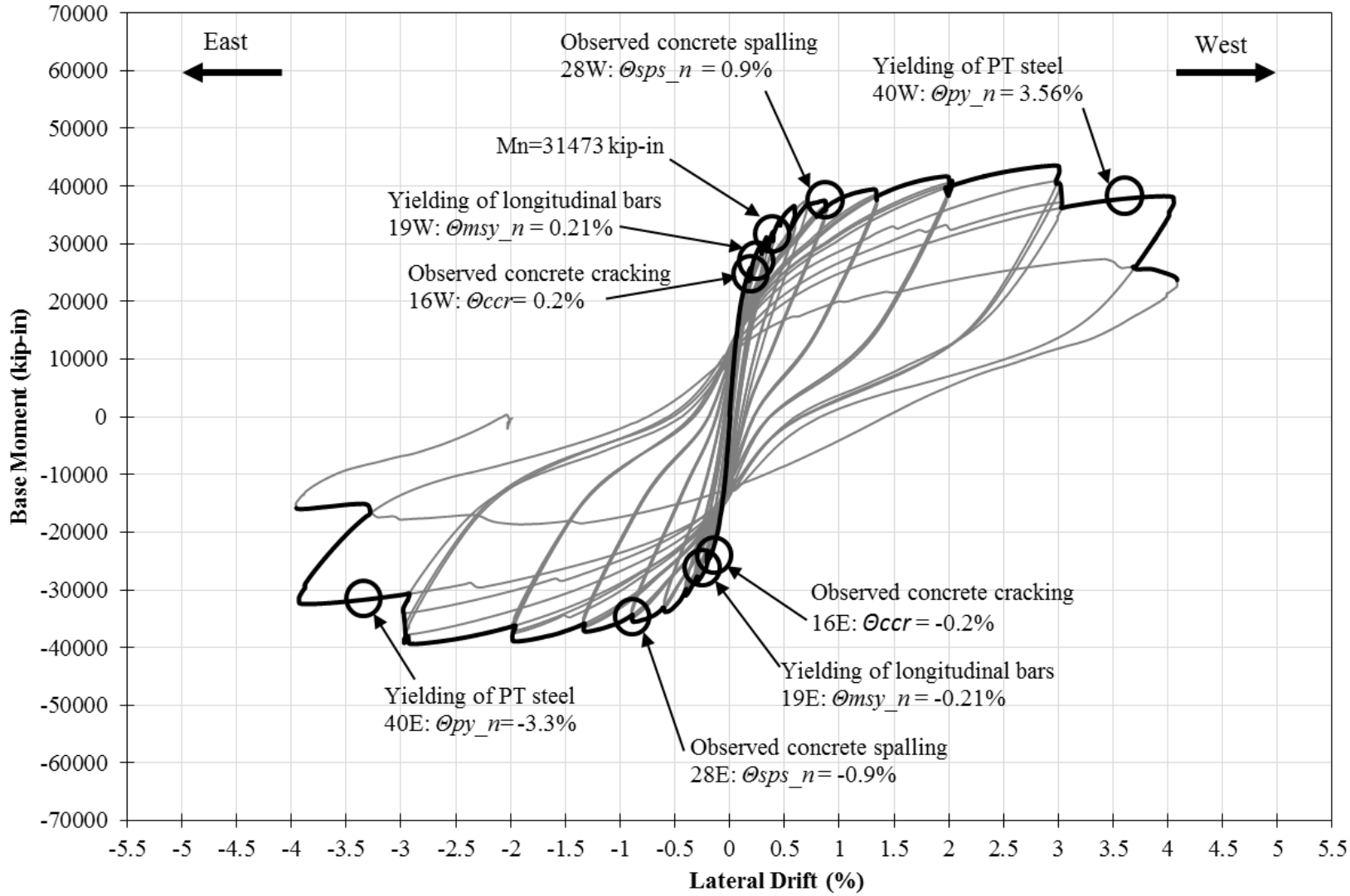

Figure 4-43 Experimental envelope curve and complete hysteresis including observed wall behavior and limit states Wall 2

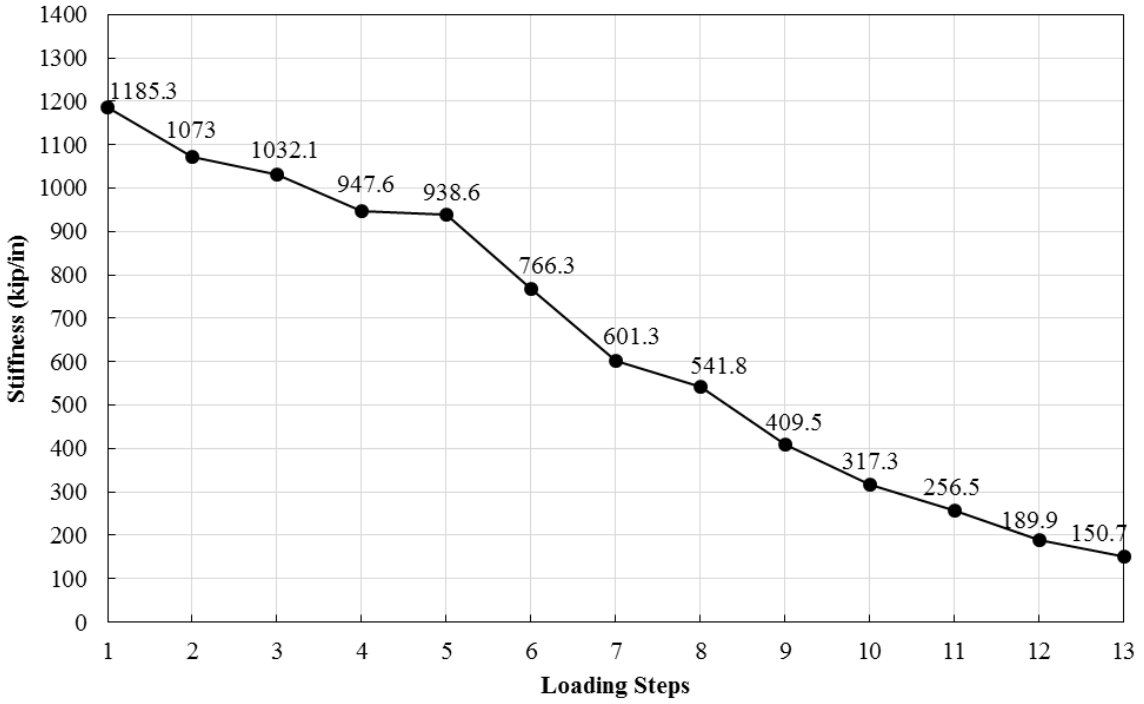

Figure 4-44 Stiffness degradation (per load step increase) versus load steps Wall 2

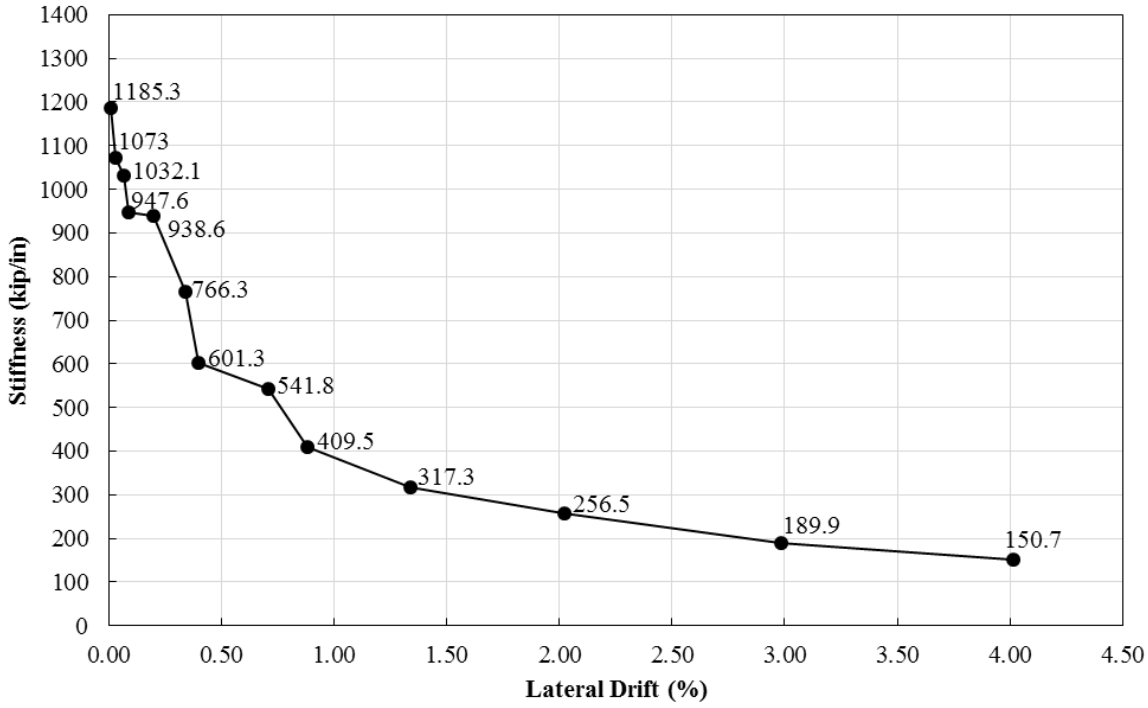

Figure 4-45 Stiffness degradation (per load step) versus lateral drift Wall 2

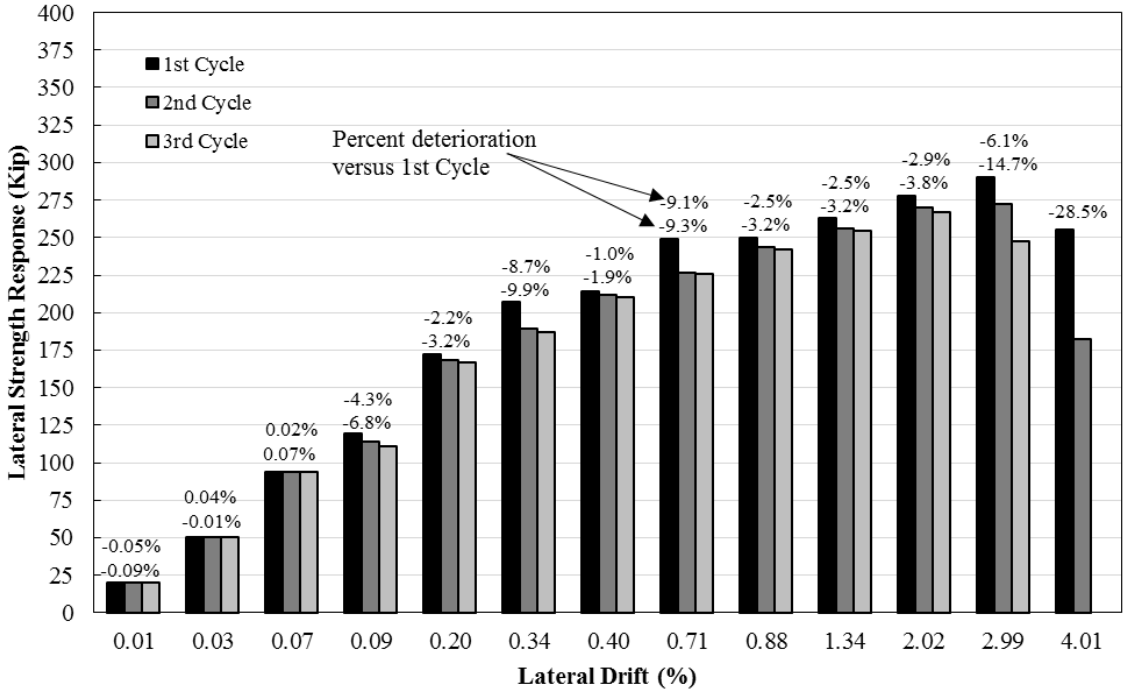

Figure 4-46 Strength deterioration per cycle at applied lateral drift Wall 2

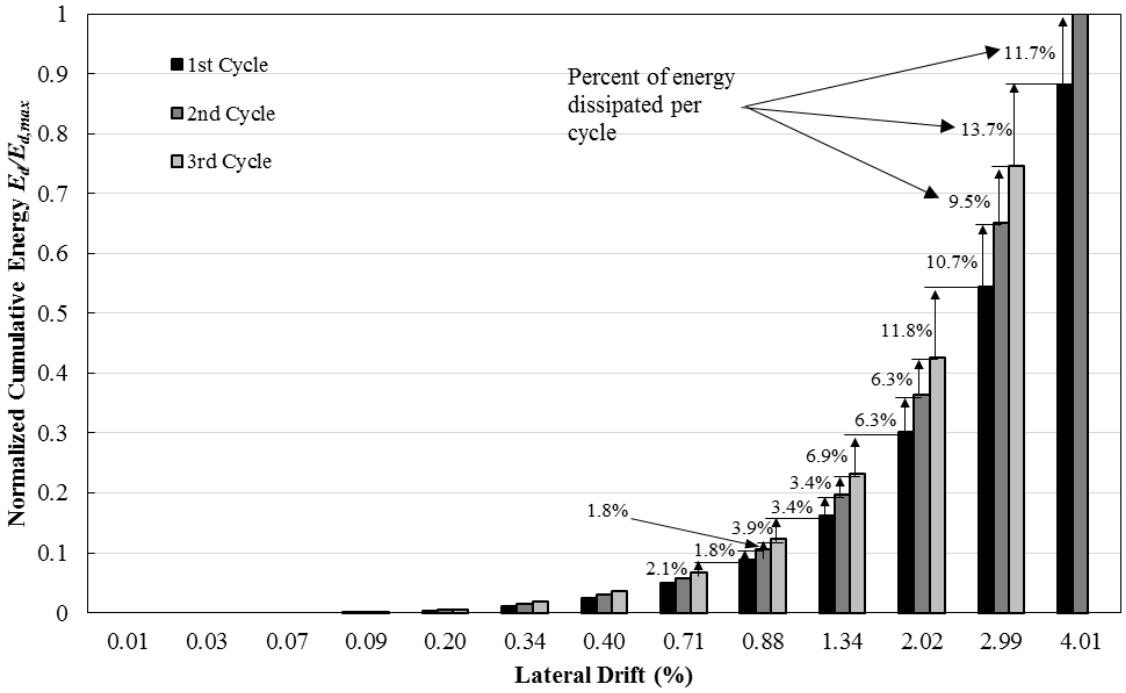

Figure 4-47 Normalized cumulative hysteretic energy dissipation Wall 2

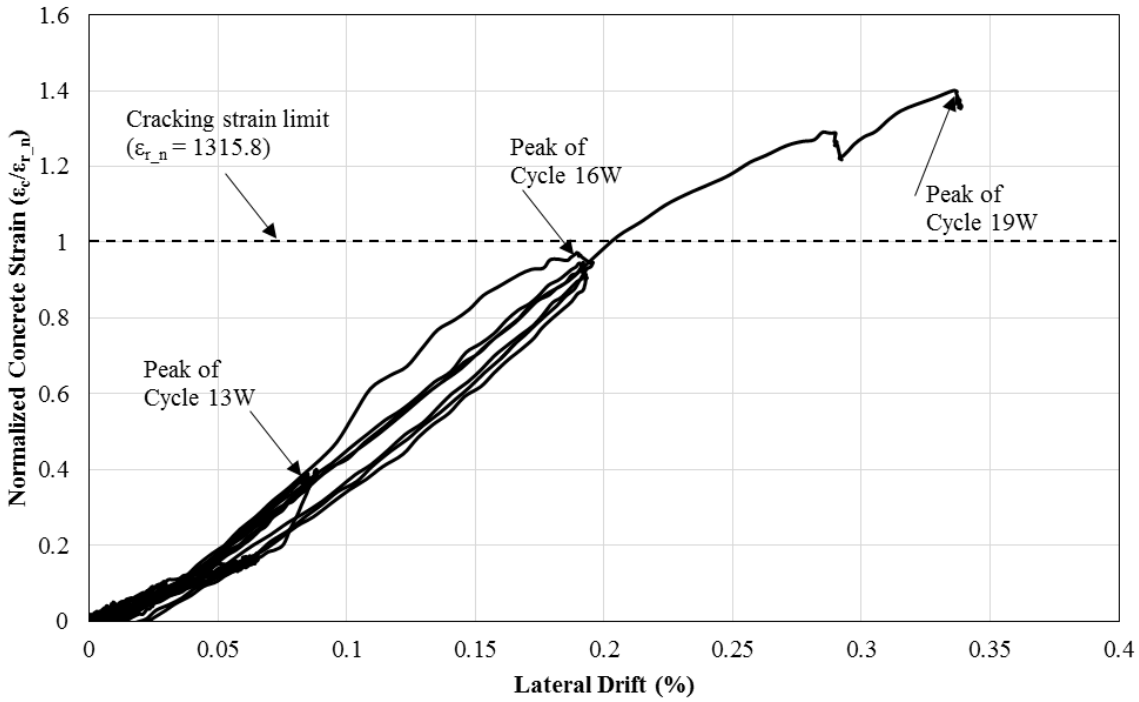

Figure 4-48 Concrete cracking strain versus lateral drift (East side) Wall 2

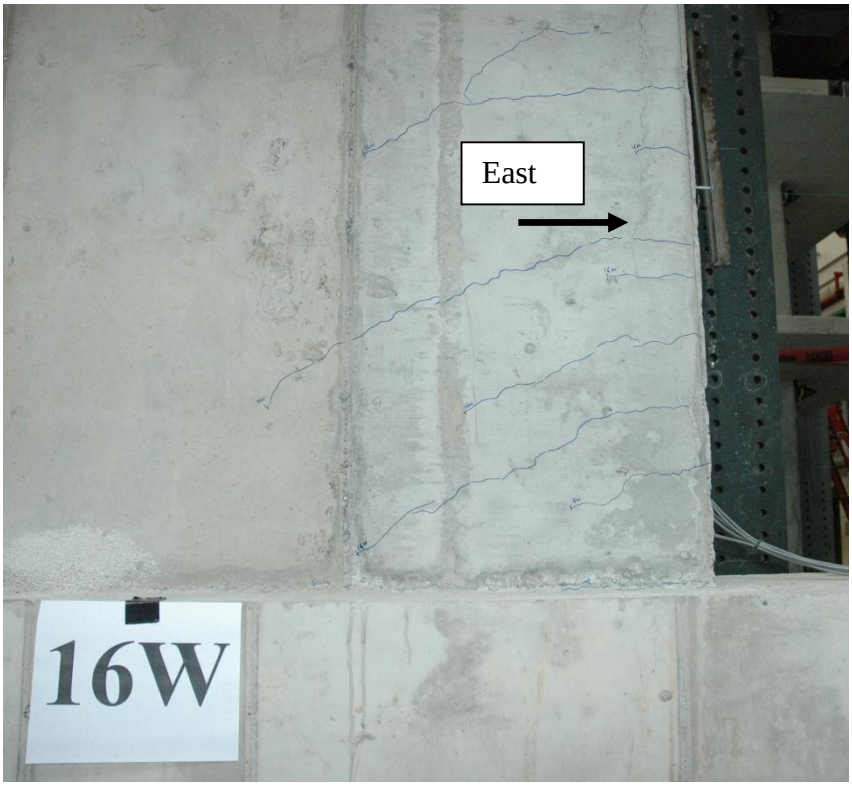

Figure 4-49 Photograph of observed initiation of concrete cracking on the East side Wall 2

Figure 4-50 Photograph of observed initiation of concrete cracking on the West side Wall 2

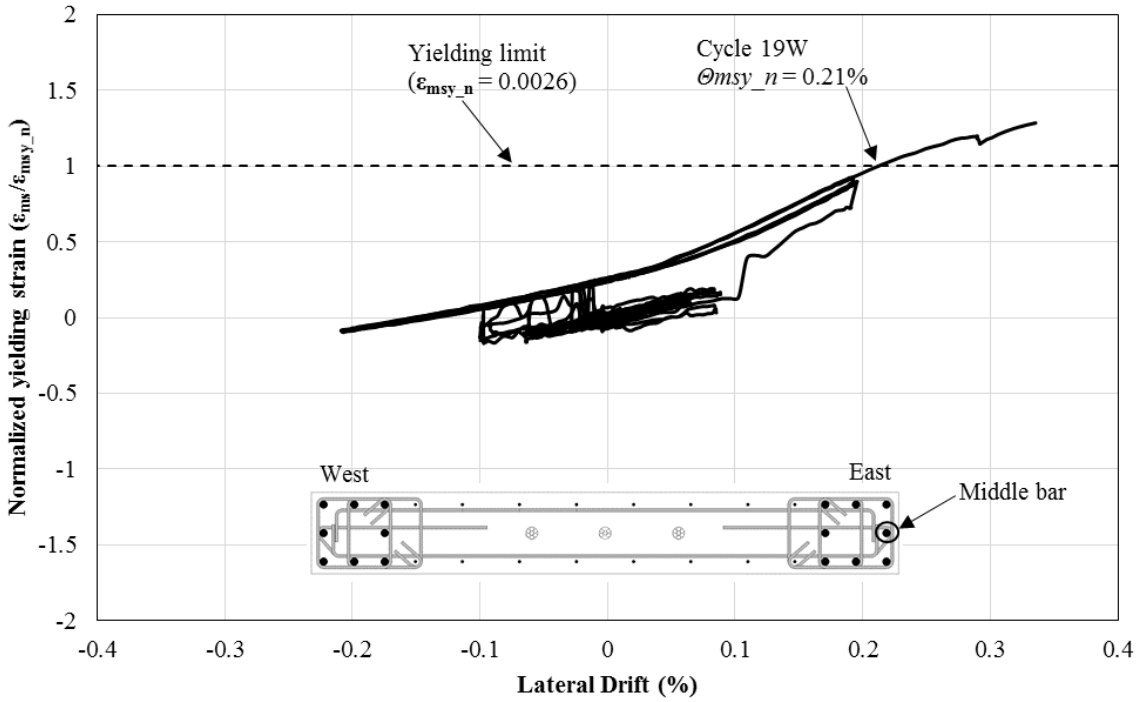

Figure 4-51 Strain of longitudinal middle bar versus lateral drift on the East side Wall 2

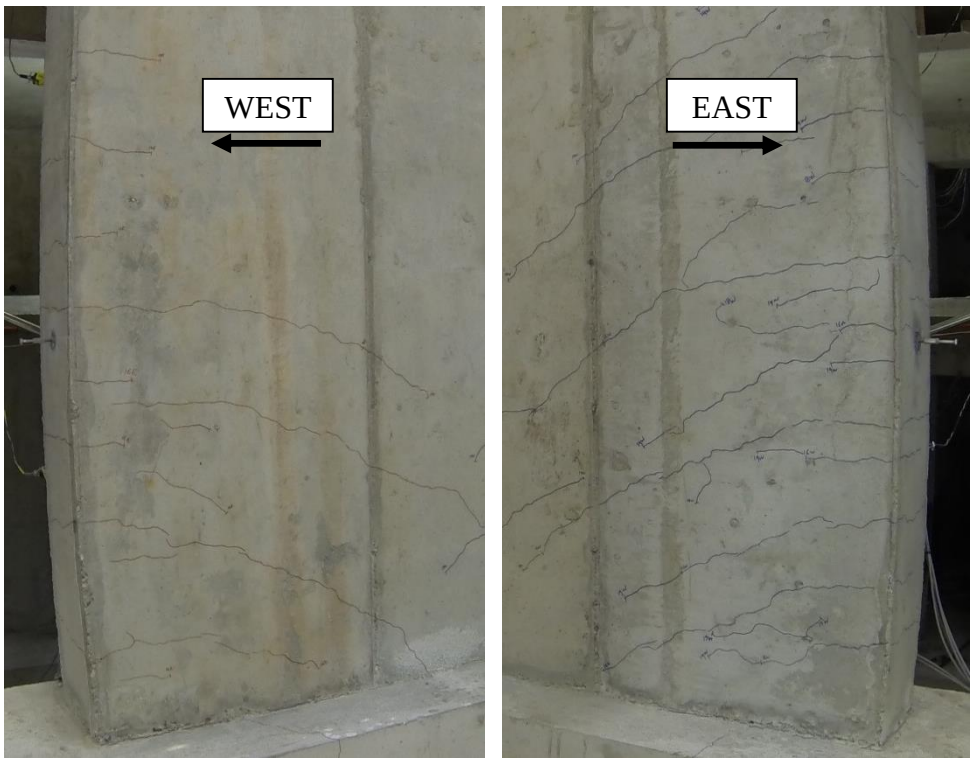

Figure 4-52 Photographs of observed wall conditions at the end of Cycle 19W Wall 2

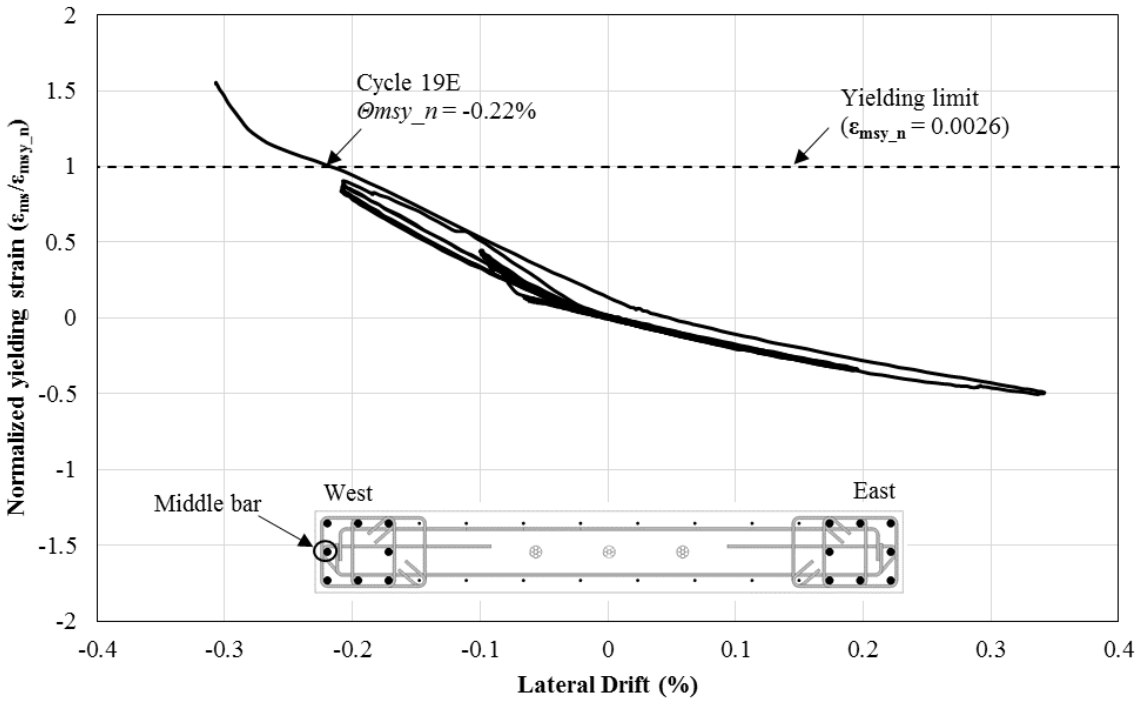

Figure 4-53 Strain of longitudinal middle bar versus lateral drift on the West side Wall 2

Figure 4-54 Photographs of observed wall conditions at the end of Cycle 19E Wall 2

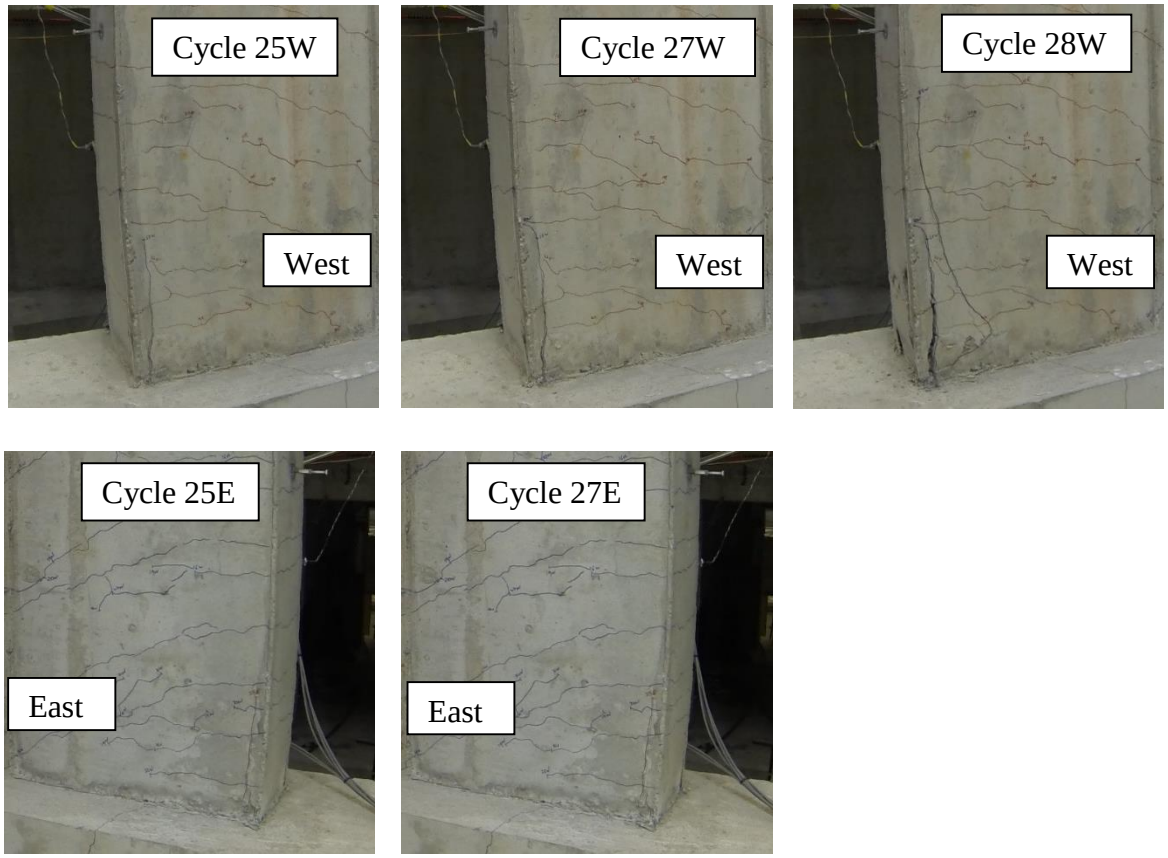

Figure 4-55 Photographs of observed splitting progression Wall 2

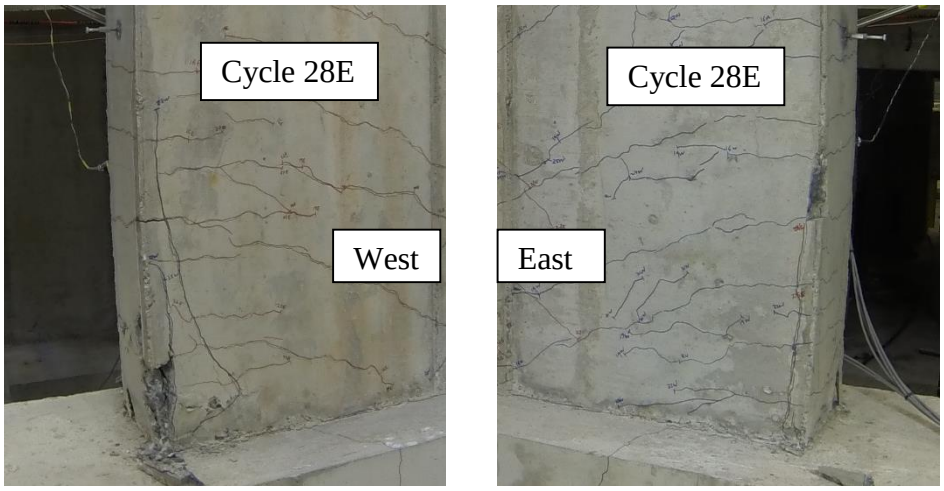

Figure 4-56 Photographs of observed concrete spalling Wall 2

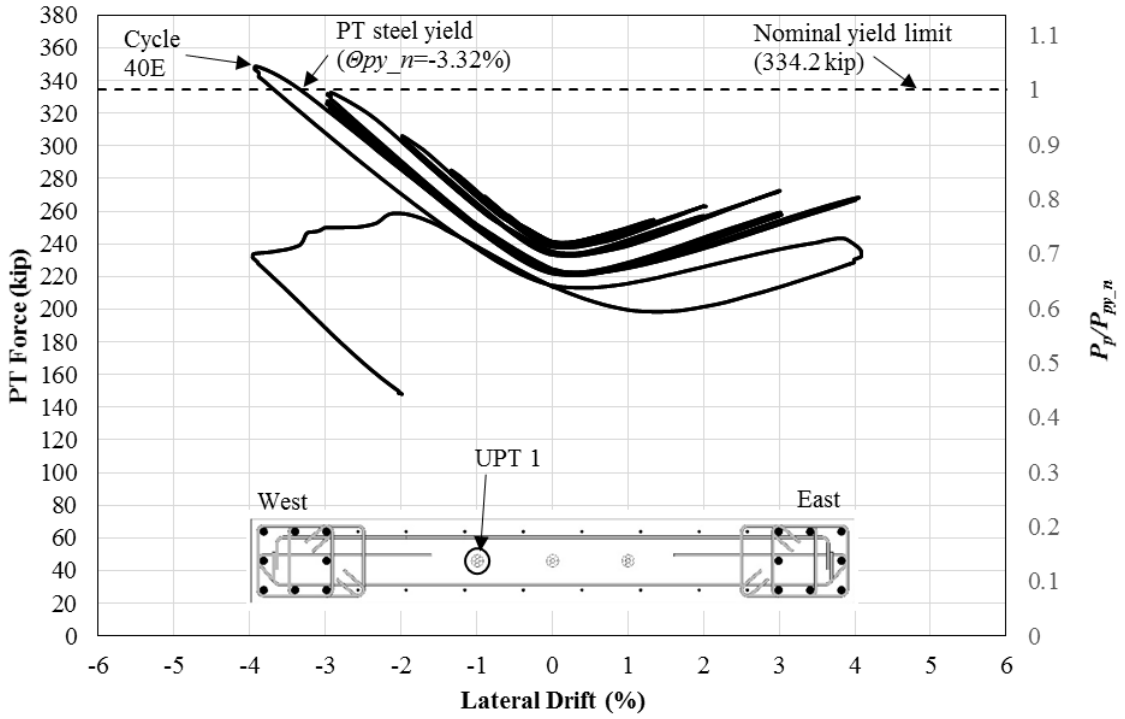

Figure 4-57 Unbonded post-tension complete response and normalized yielding peaks – West side Wall 2

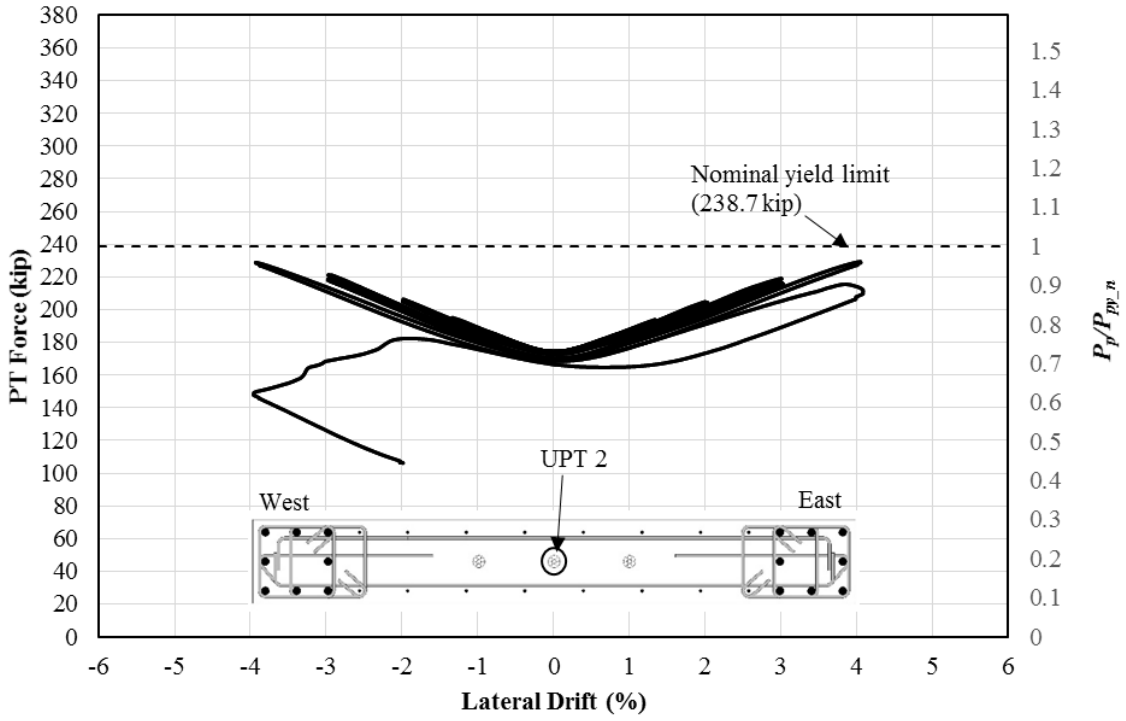

Figure 4-58 Unbonded post-tension complete response and normalized yielding peaks – Middle Wall 2

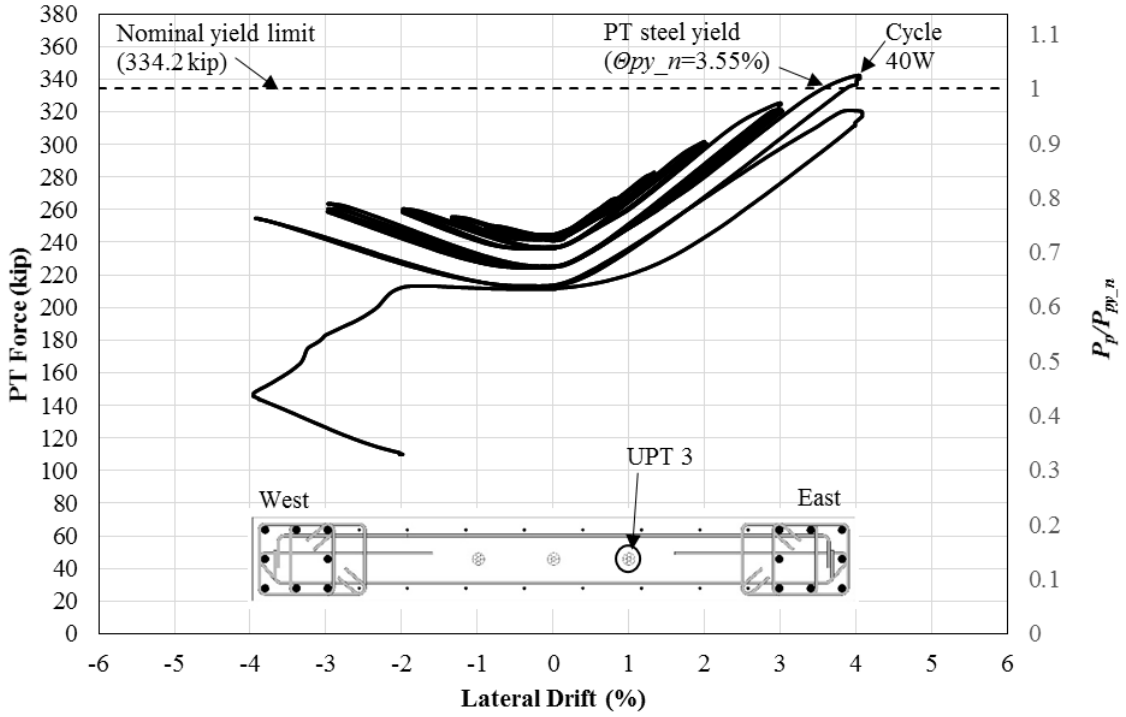

Figure 4-59 Unbonded post-tension complete response and normalized yielding peaks – East side Wall 2

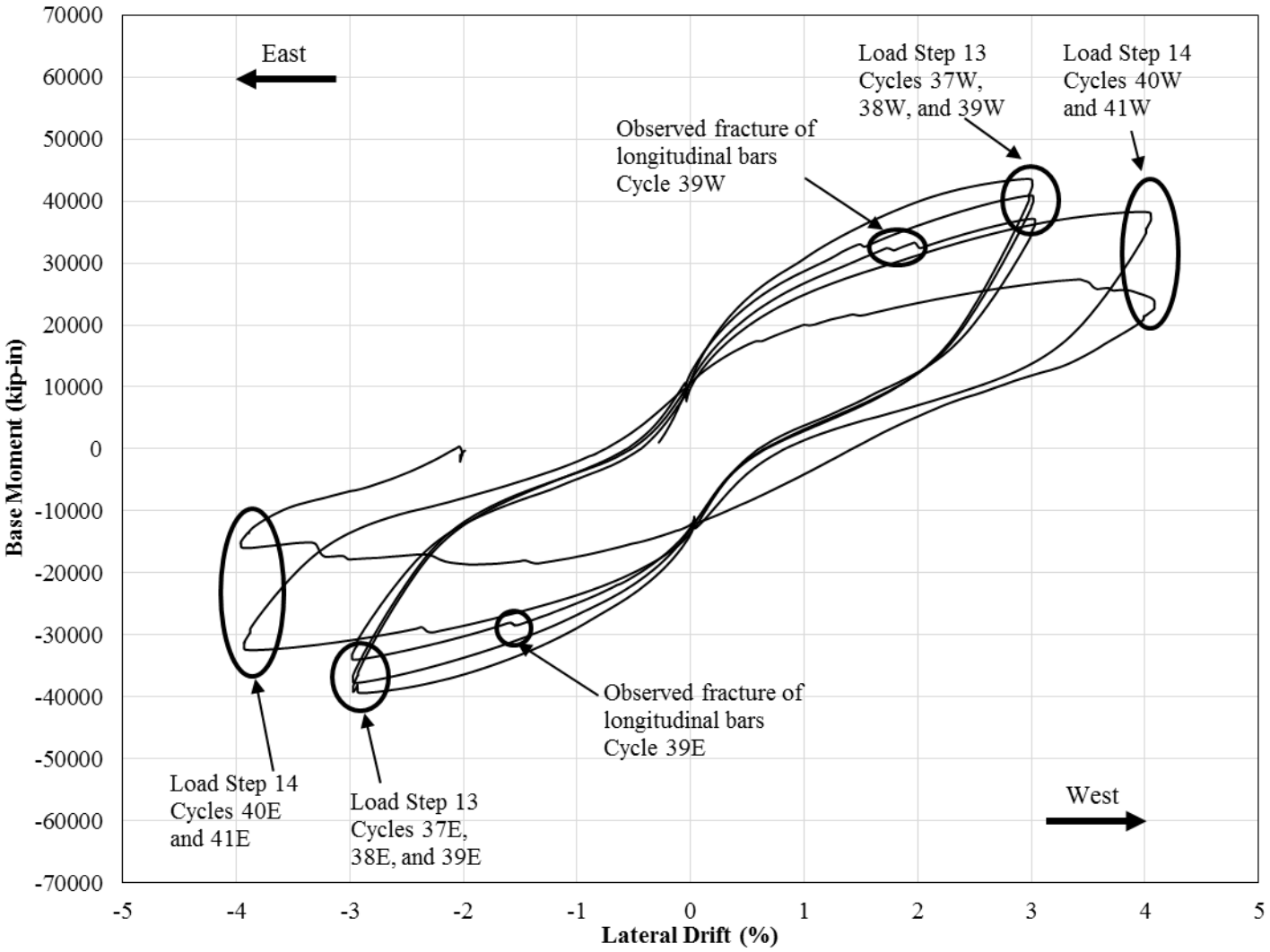

Figure 4-60 Observed fracture of longitudinal reinforcement Wall 2

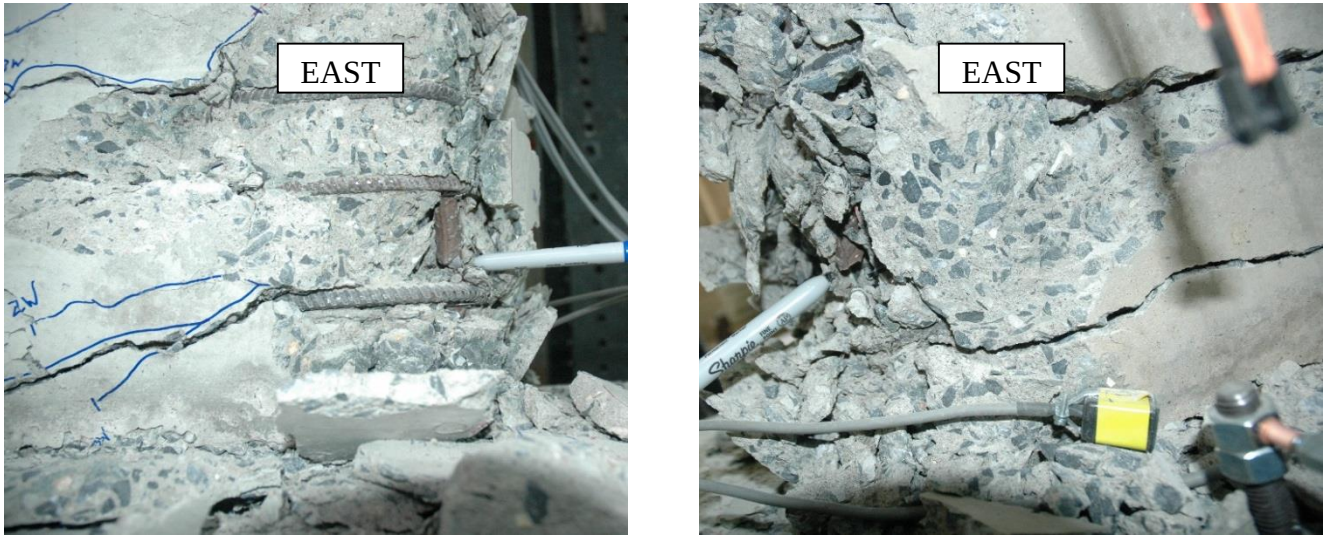

Figure 4-61 Photographs of observed fracture of longitudinal steel reinforcement at Cycle 39W Wall 2

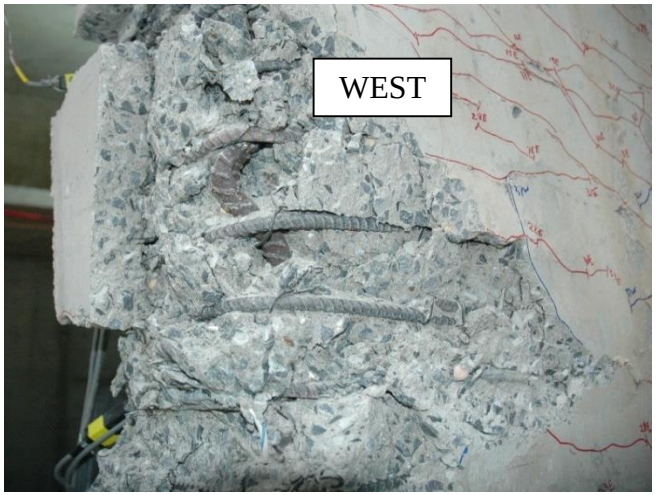

Figure 4-62 Photograph of observed buckling of longitudinal steel reinforcement at Cycle 39W Wall 2

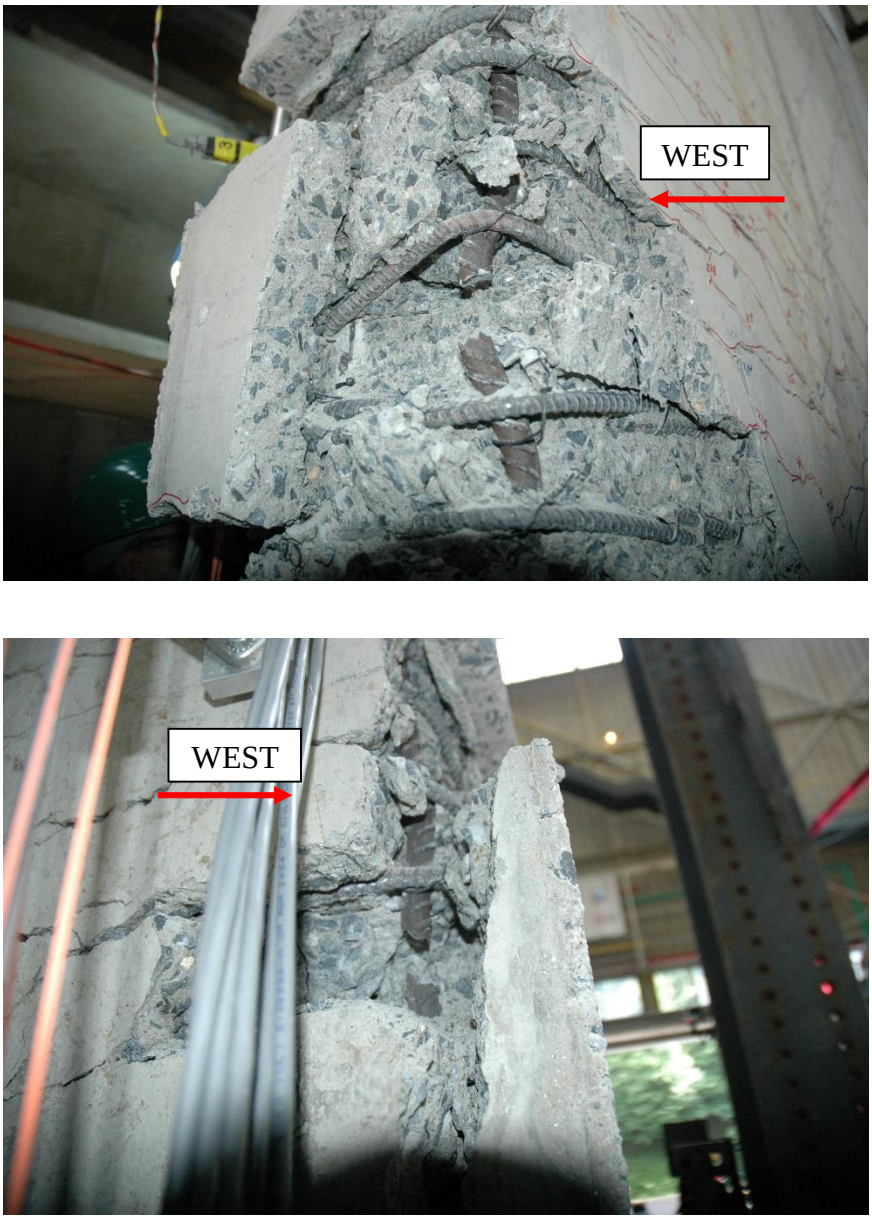

Figure 4-63 Photographs of observed fracture of longitudinal steel reinforcement at Cycle 39E Wall 2

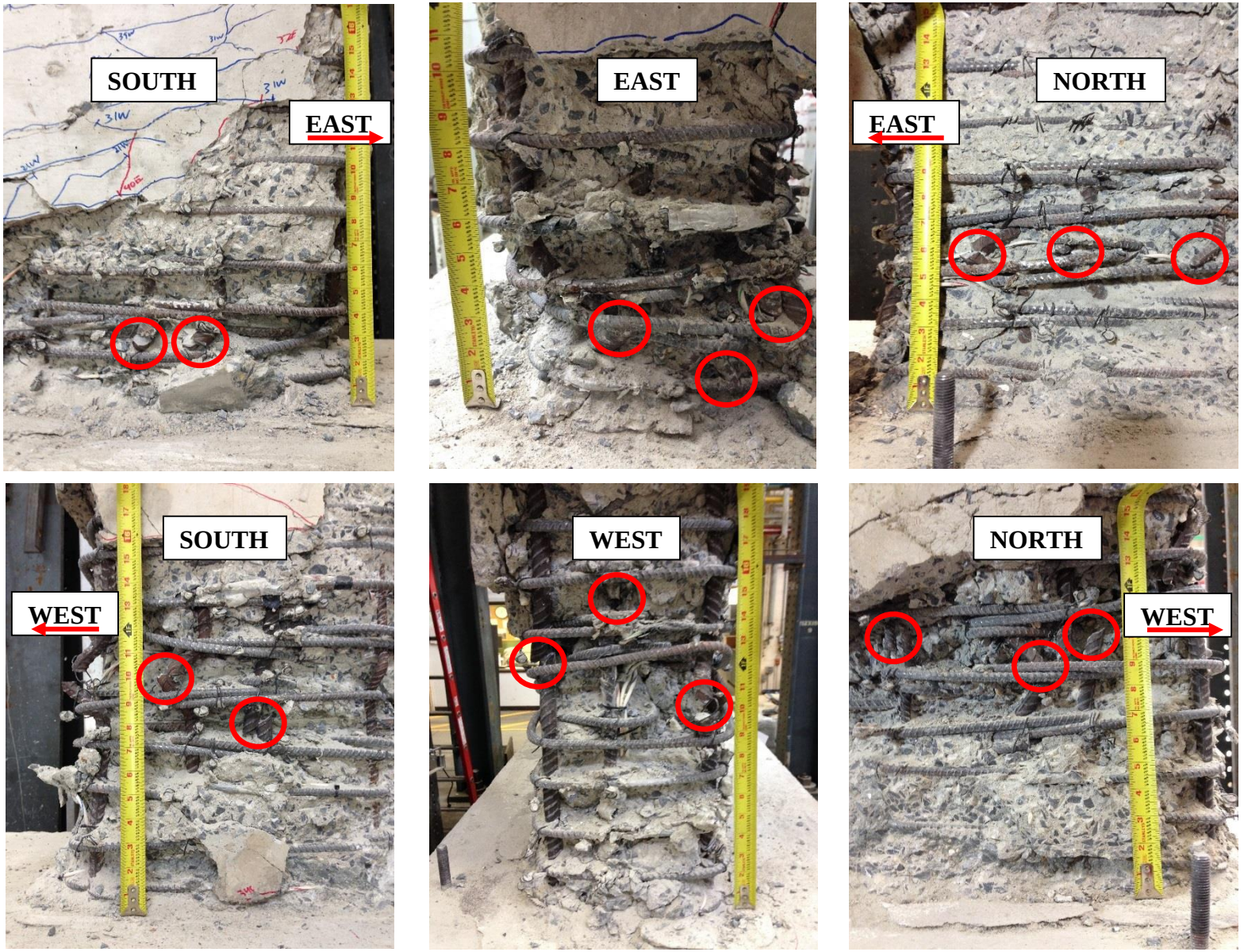

Figure 4-64 Photographs of observed fracture of longitudinal steel reinforcement at the end of the test Wall 2

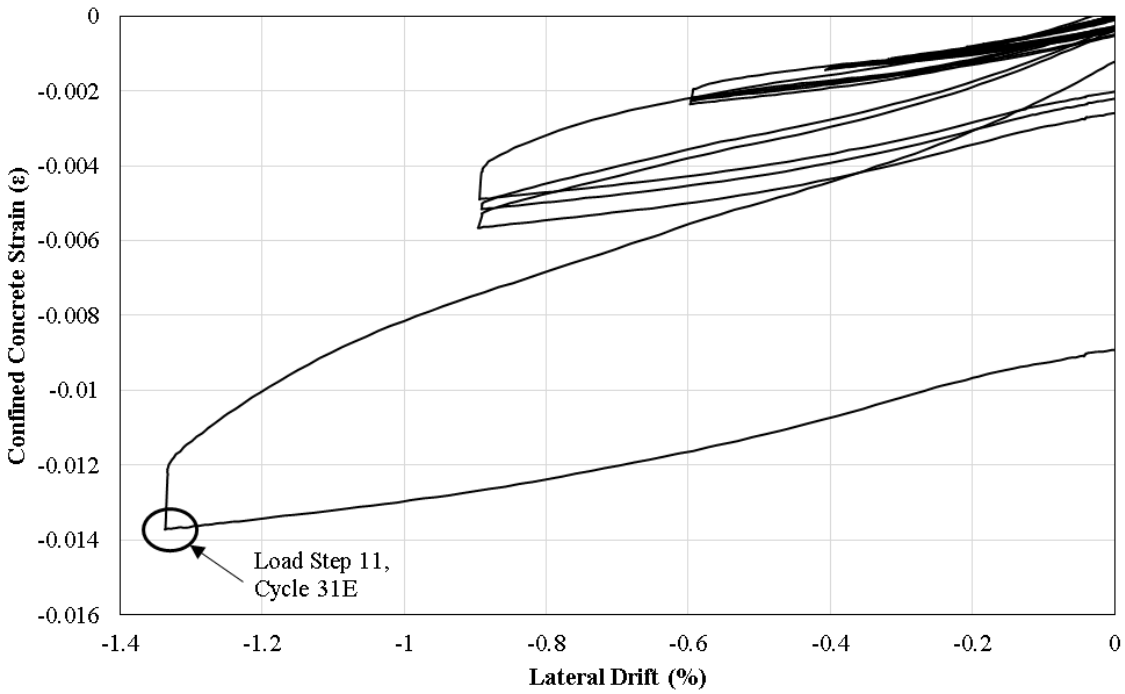

Figure 4-65 Confined concrete strain at East end Wall 2

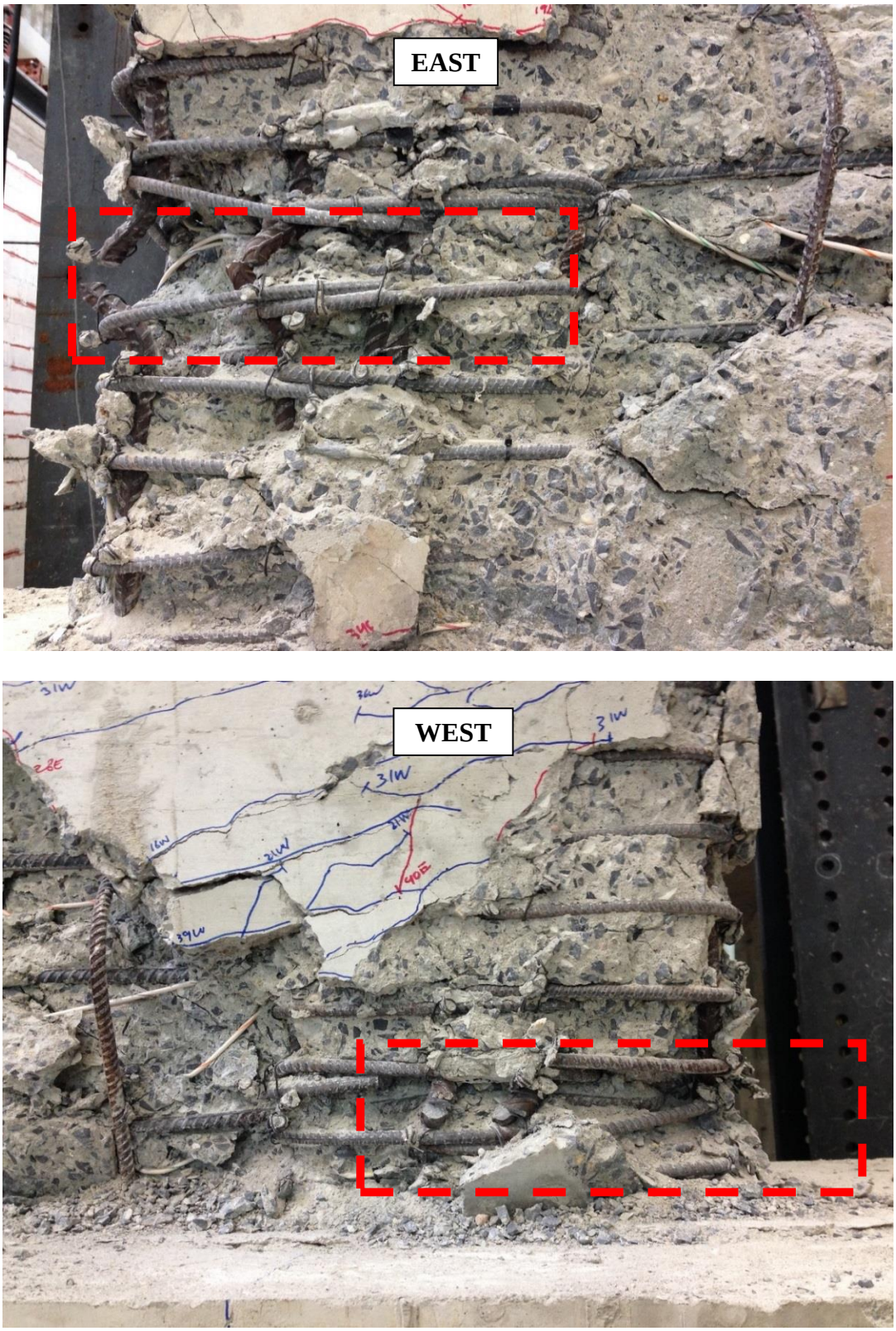

Figure 4-66 Photographs of confined concrete conditions at the end of the test Wall 2

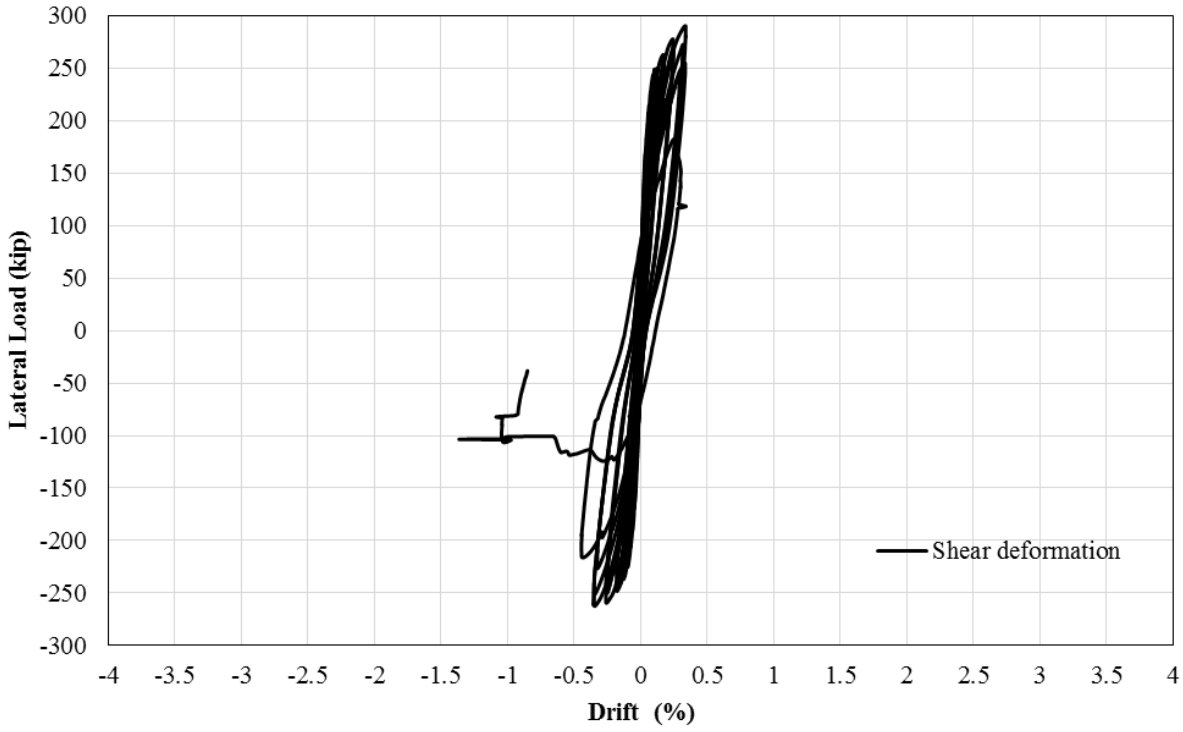

Figure 4-67 Shear deformation Wall 2

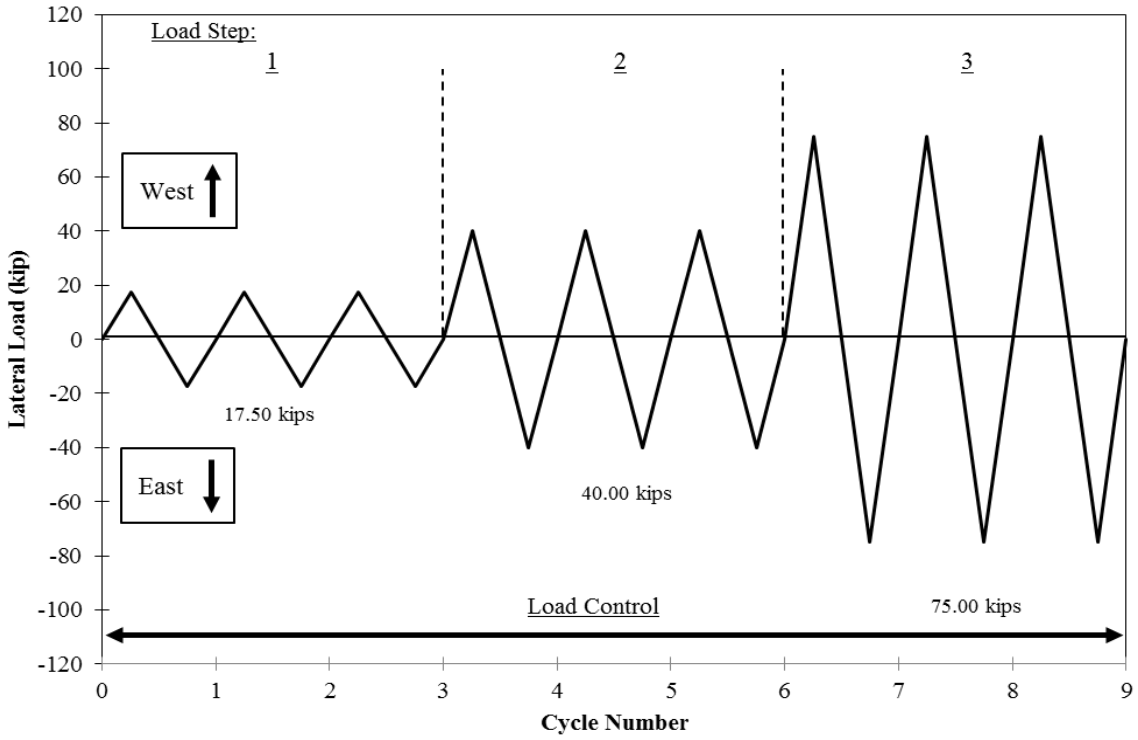

Figure 4-68 Loading history – load control portion Wall 3

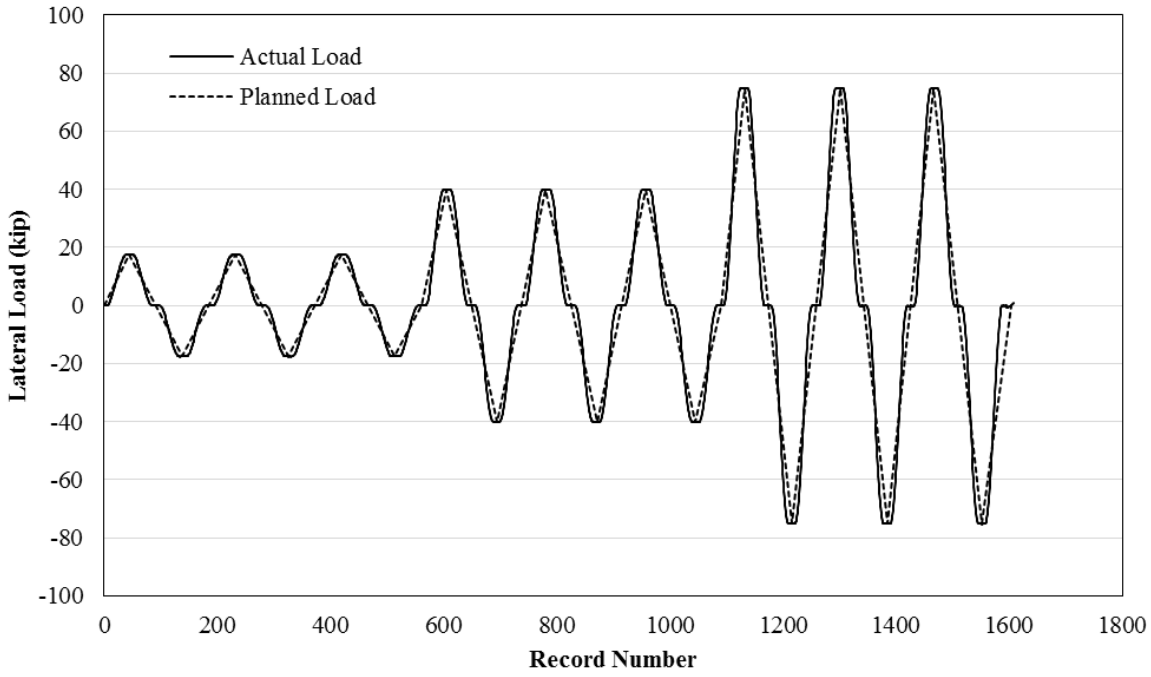

Figure 4-69 Experimental results superposed (load control portion) Wall 3

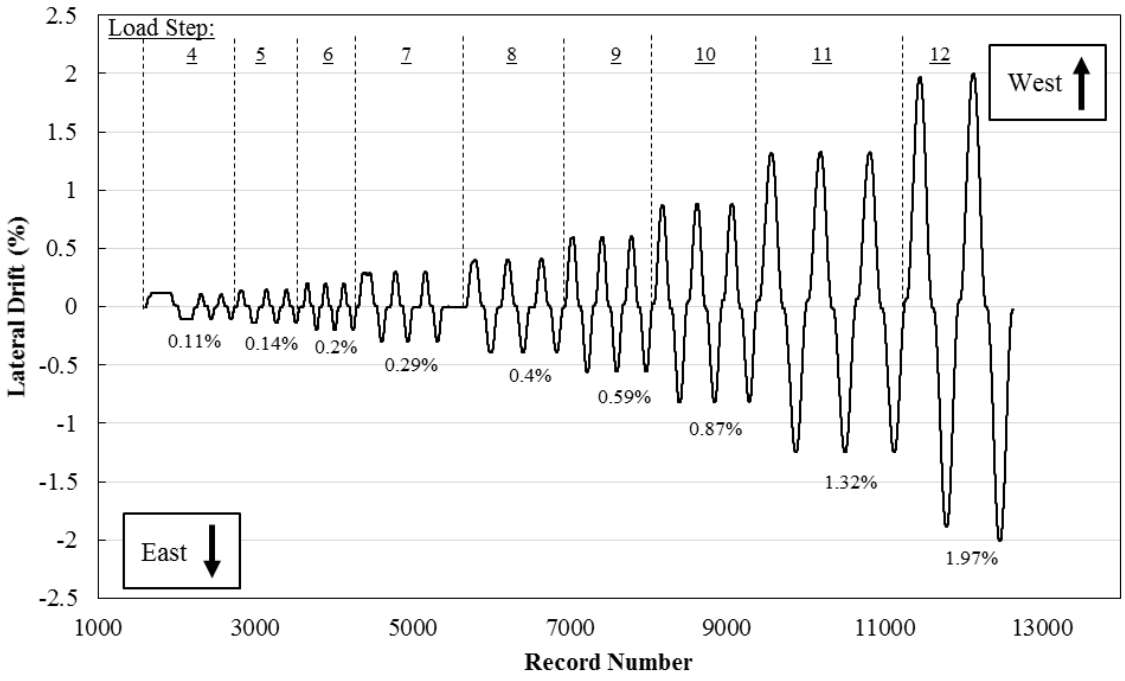

Figure 4-70 Actual loading history (displacement control) Wall 3

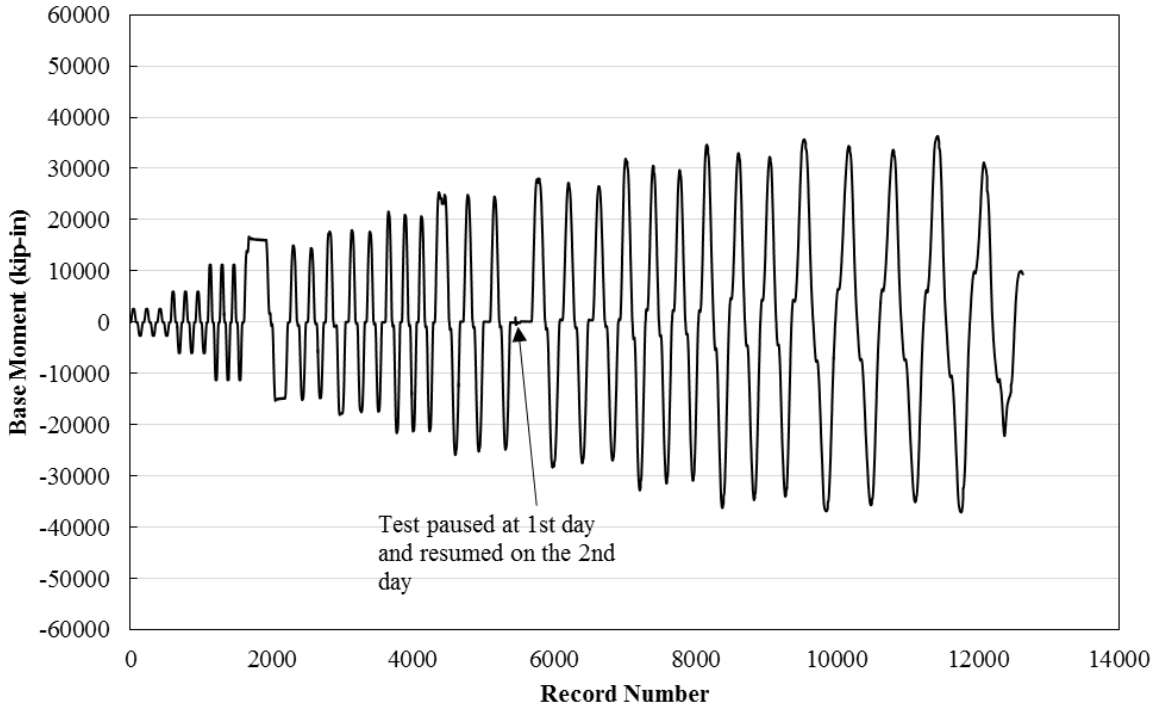

Figure 4-71 Base moment versus record number Wall 3

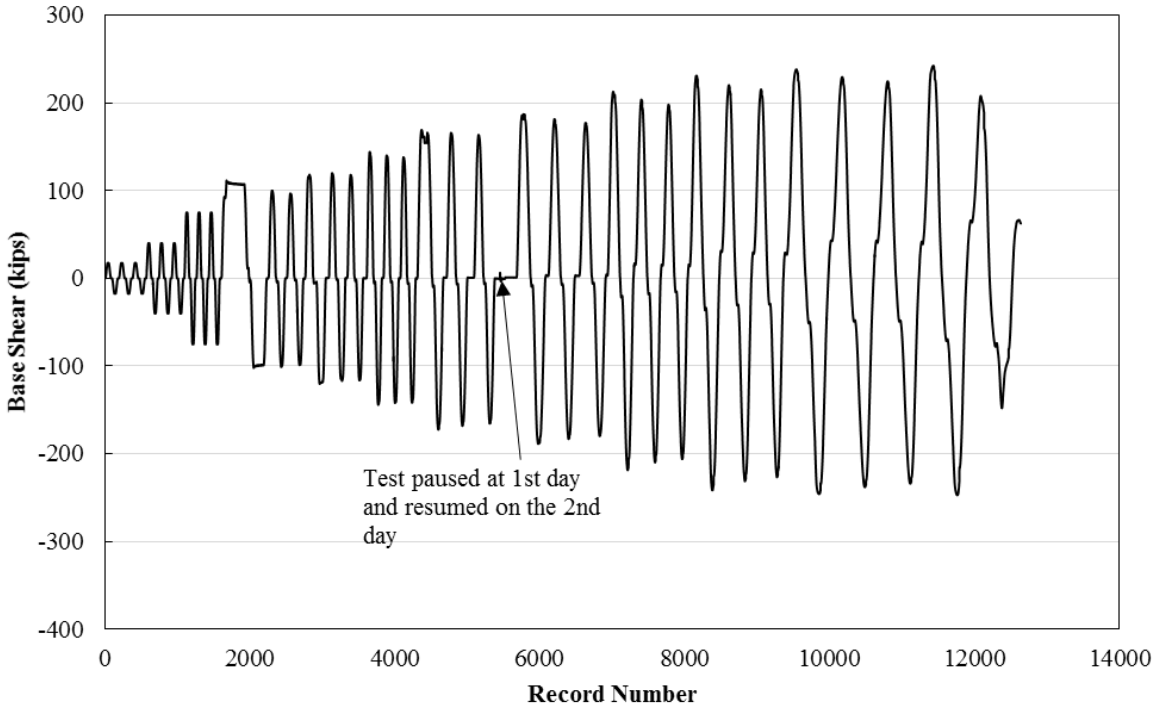

Figure 4-72 Base shear versus record number Wall 3

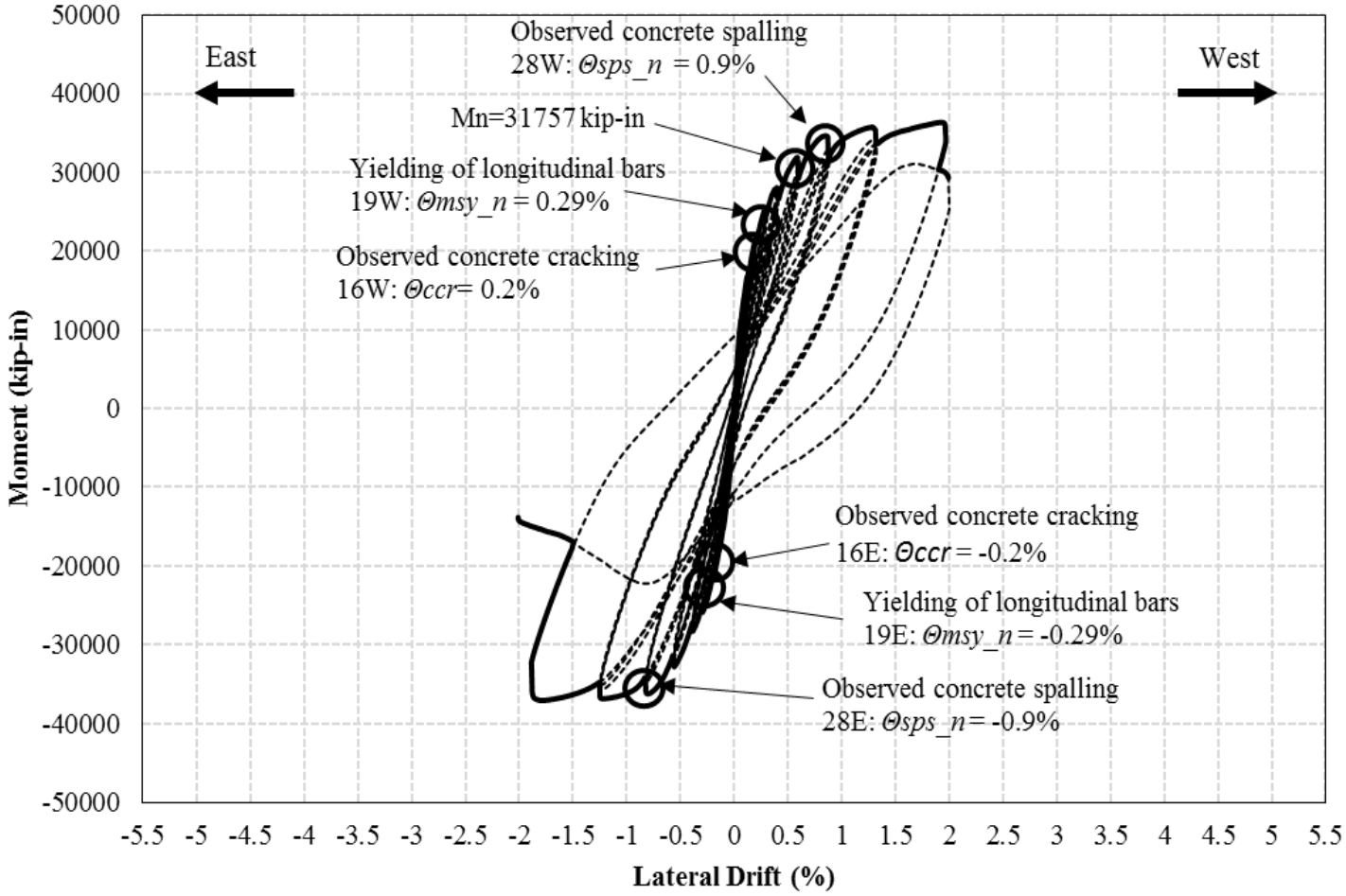

Figure 4-73 Experimental envelope curve and complete hysteresis including observed wall behavior and limit states Wall 3

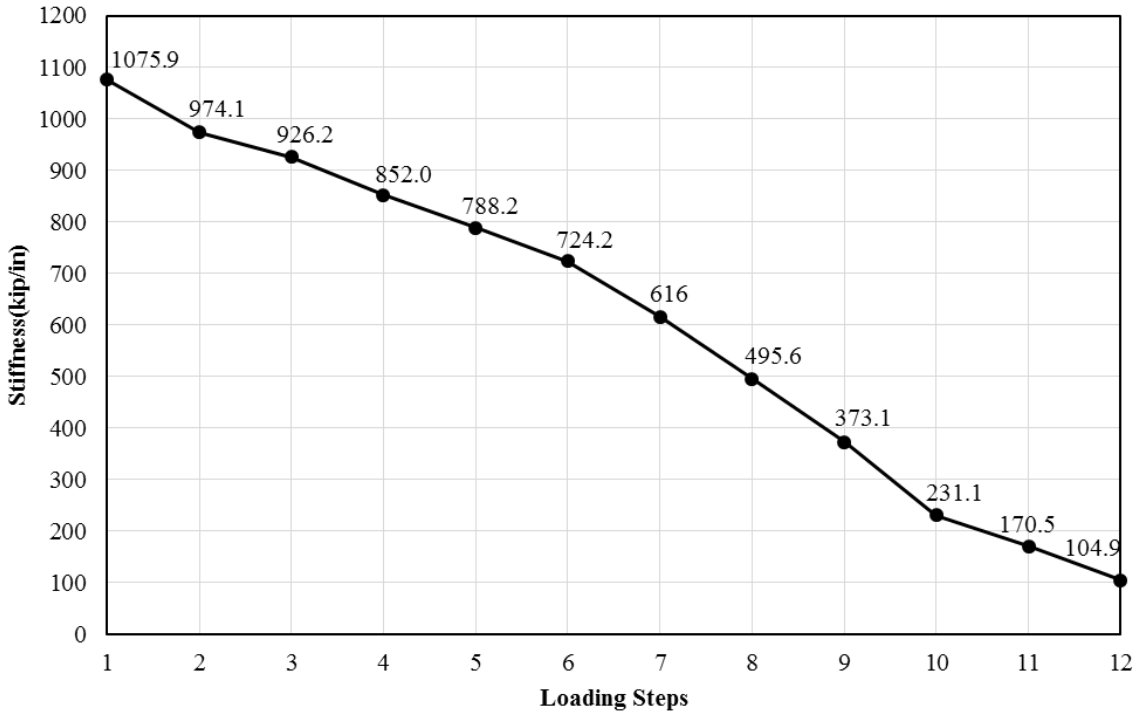

Figure 4-74 Stiffness degradation (per load step increase) versus load steps Wall 3

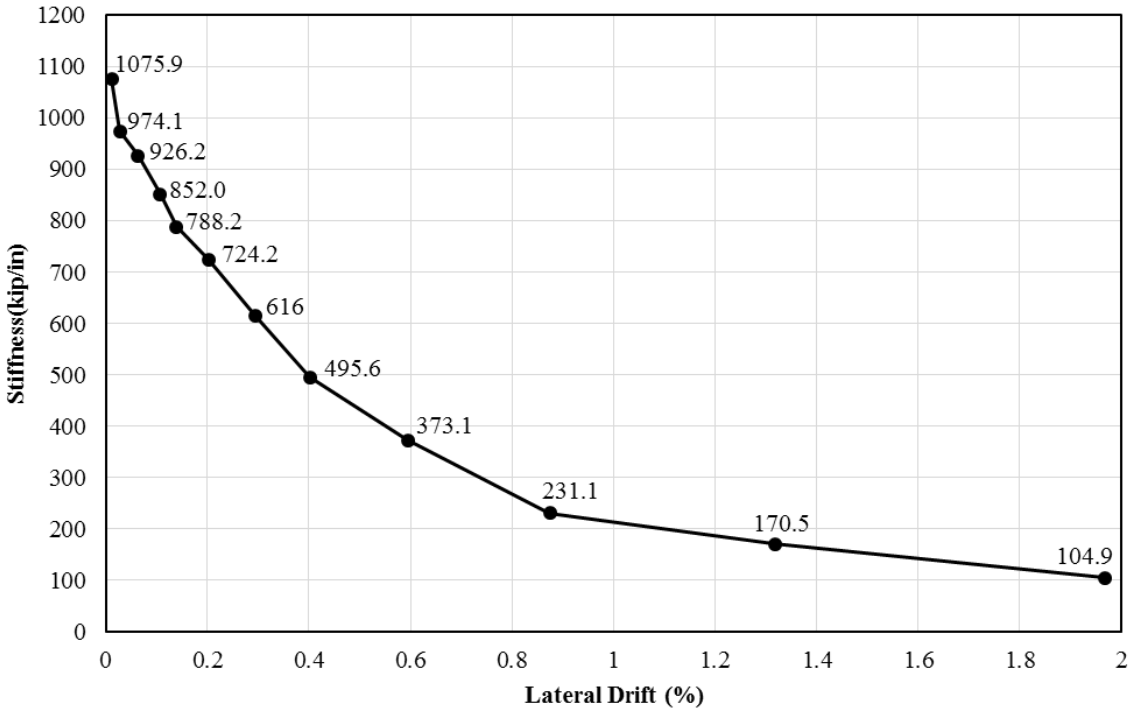

Figure 4-75 Stiffness degradation (per load step) versus lateral drift Wall 3

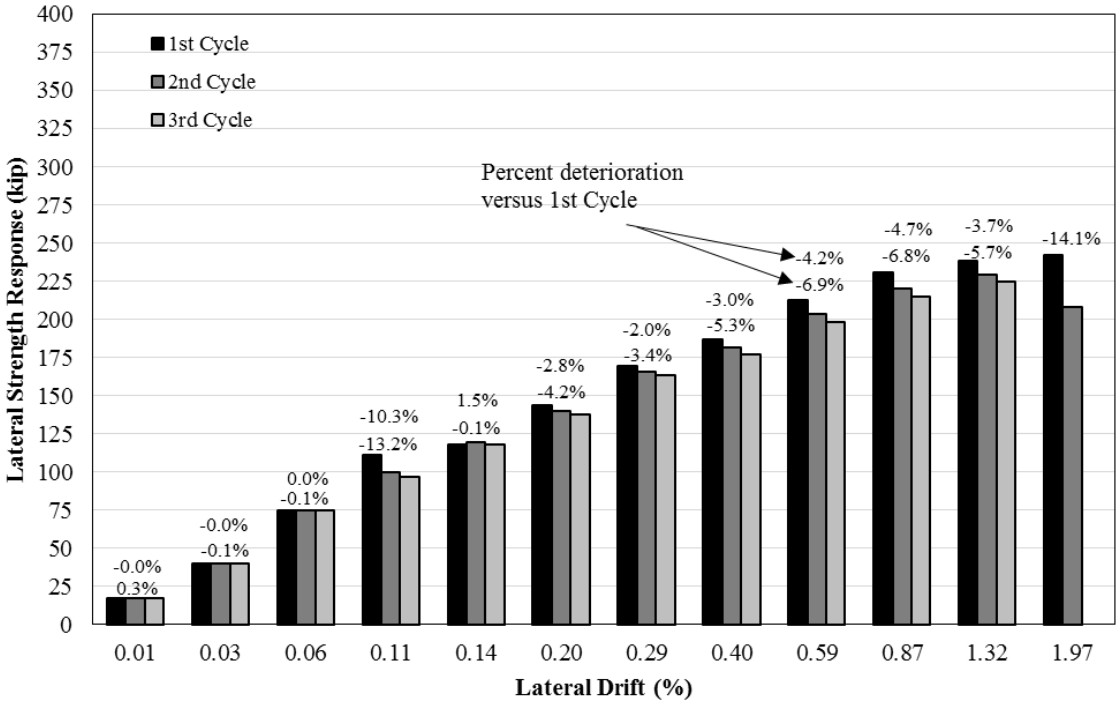

Figure 4-76 Strength deterioration per cycle at applied lateral drift Wall 3

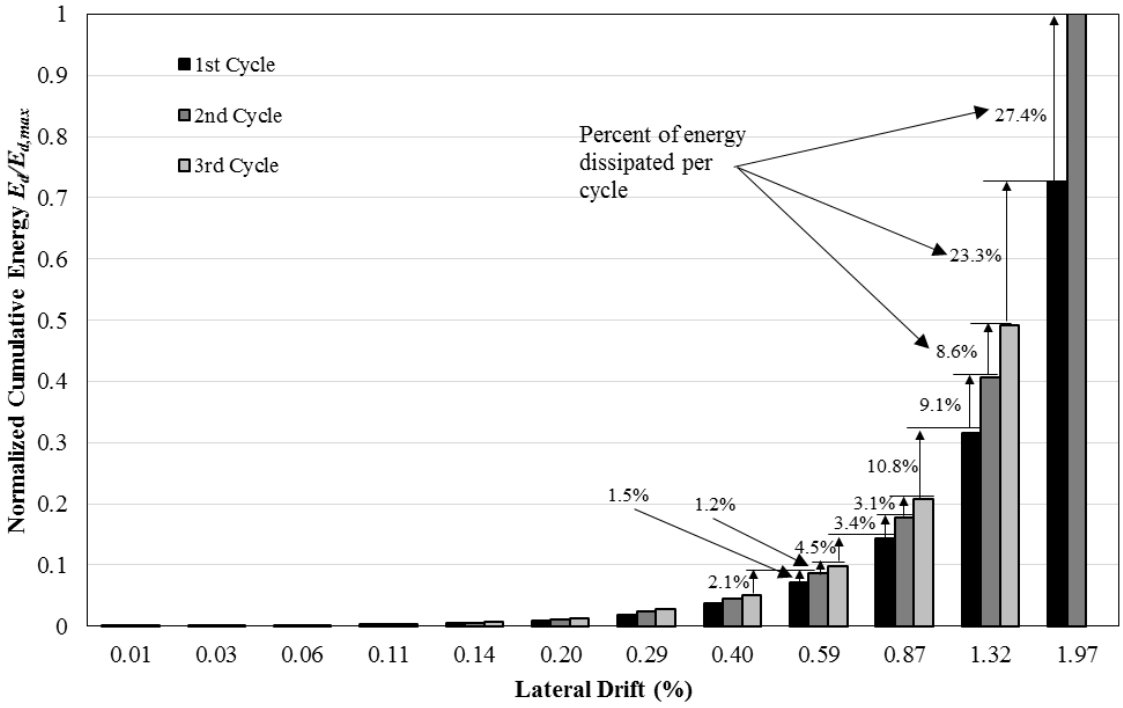

Figure 4-77 Normalized cumulative hysteretic energy dissipation Wall 3

Figure 4-78 Photograph of observed splitting crack at Cycle 16W on the West side Wall 3

Figure 4-79 Photograph of observed splitting crack at Cycle 18E on the East side Wall 3

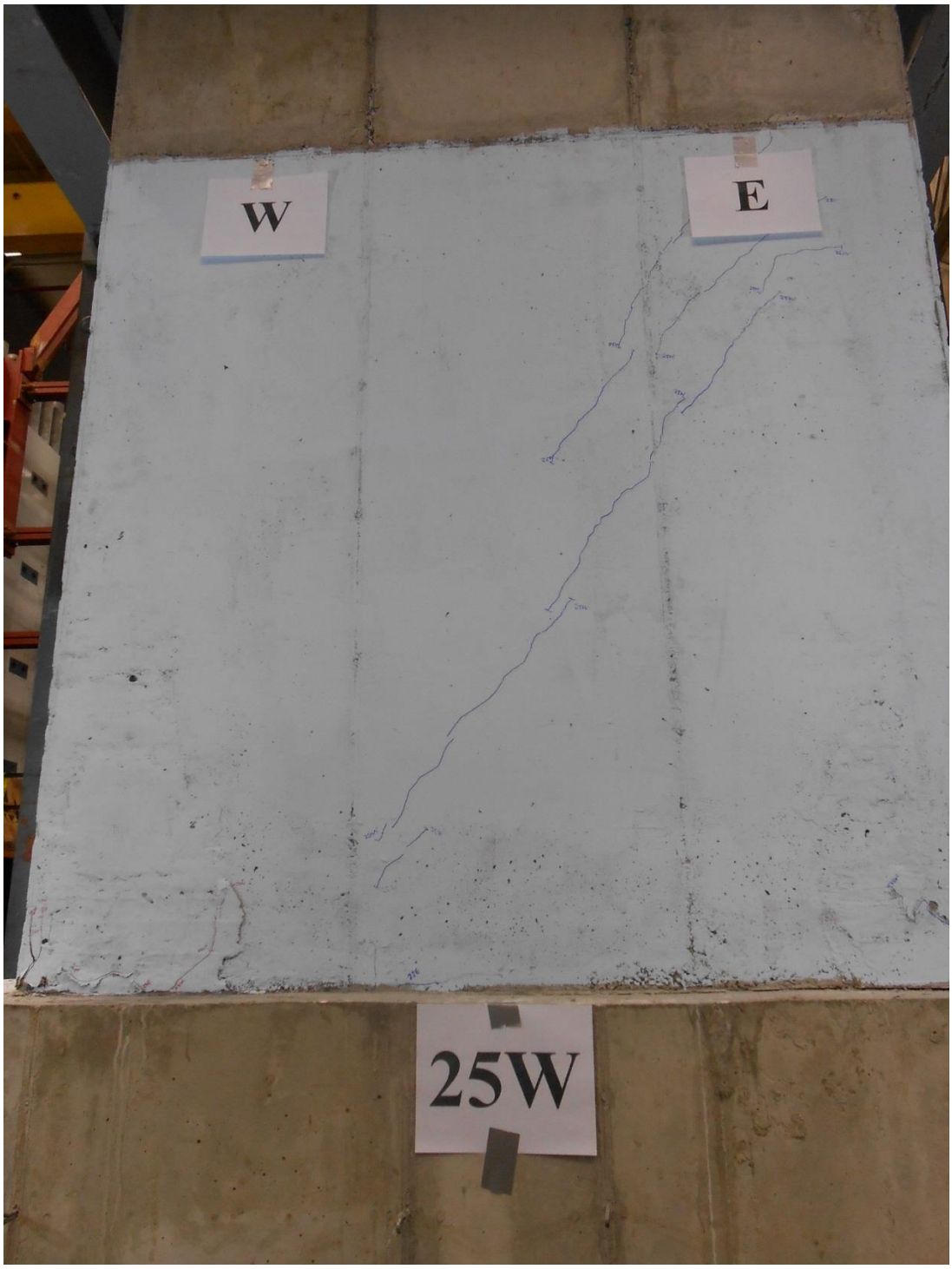

Figure 4-80 Photographs of observed diagonal cracks at Cycle 25W on the East side Wall 3

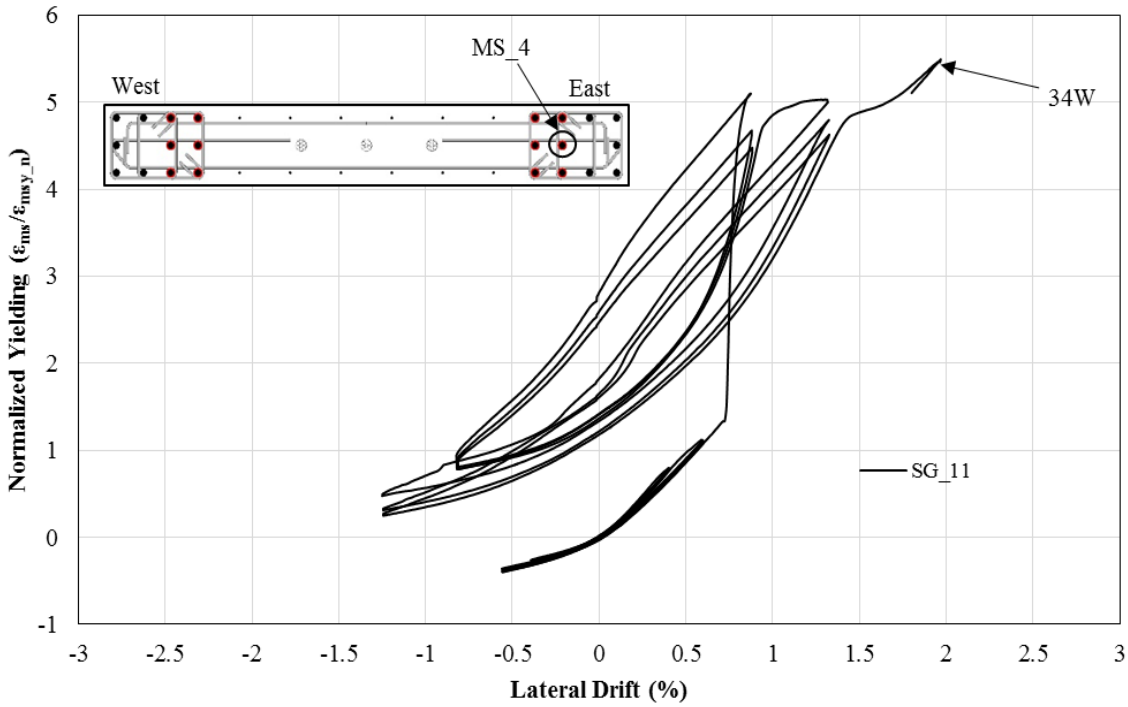

Figure 4-81 Normalized yielding strain of middle bar versus lateral drift on the East side Wall 3

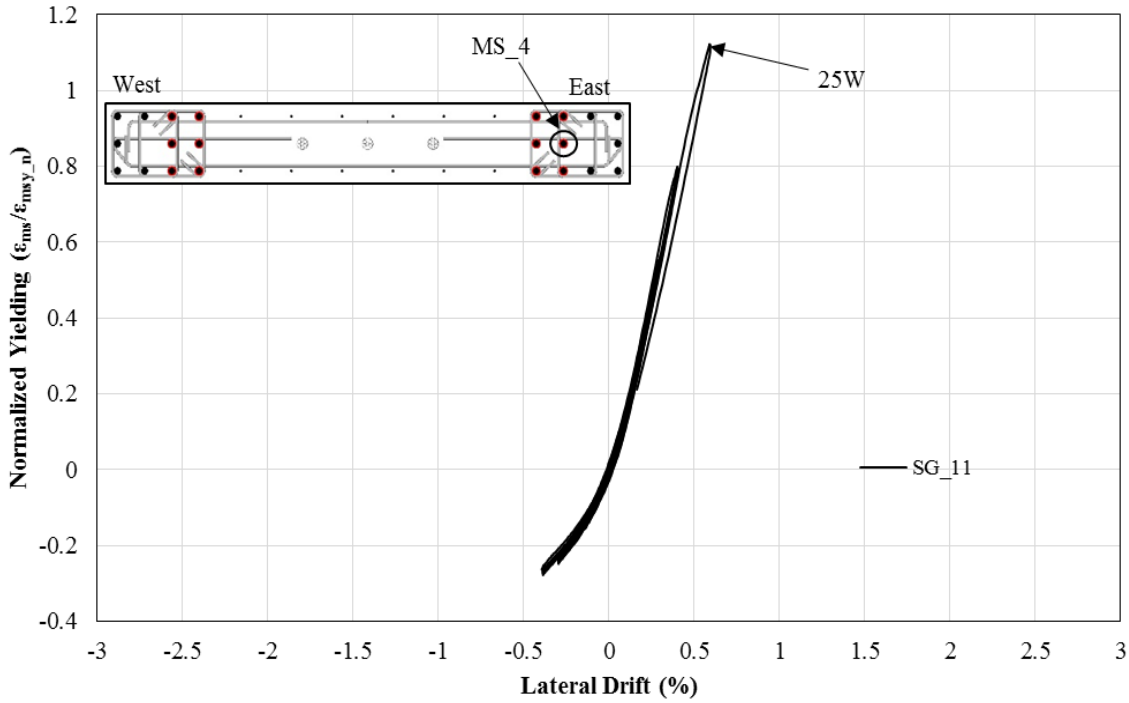

Figure 4-82 First yielding of debonded longitudinal steel reinforcement on the East side Wall 3

Figure 4-83 Photographs of observed diagonal cracks at Cycle 25E on the West side Wall 3

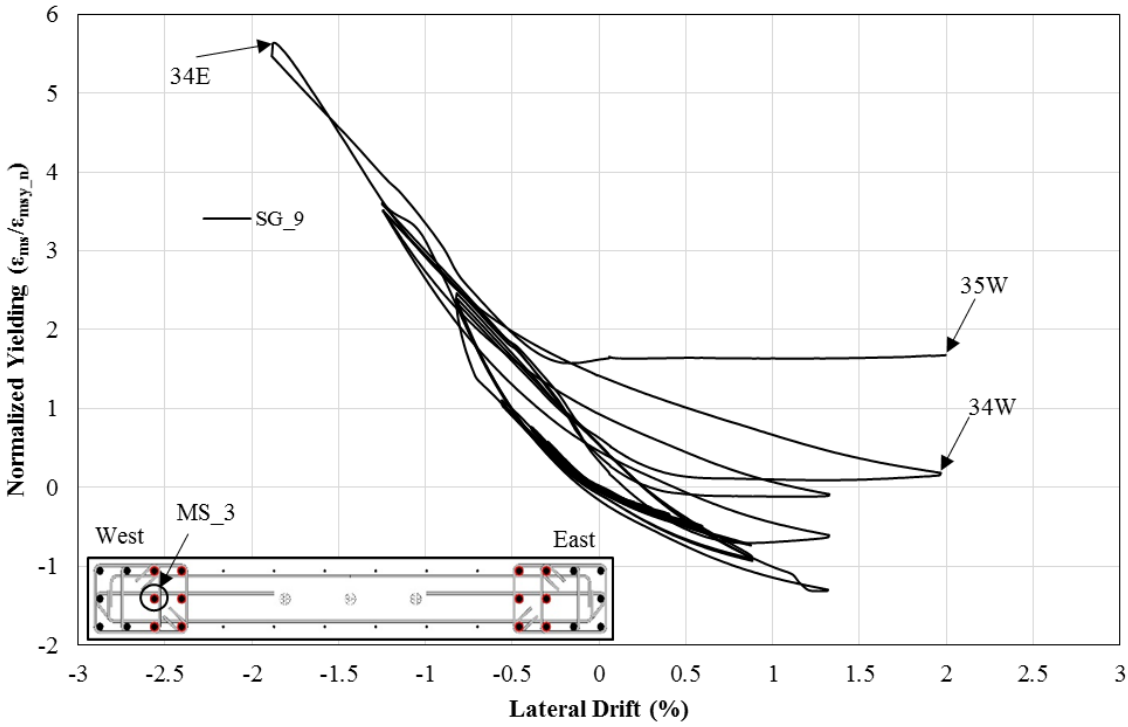

Figure 4-84 Normalized yielding strain of middle bar versus lateral drift on the West side Wall 3

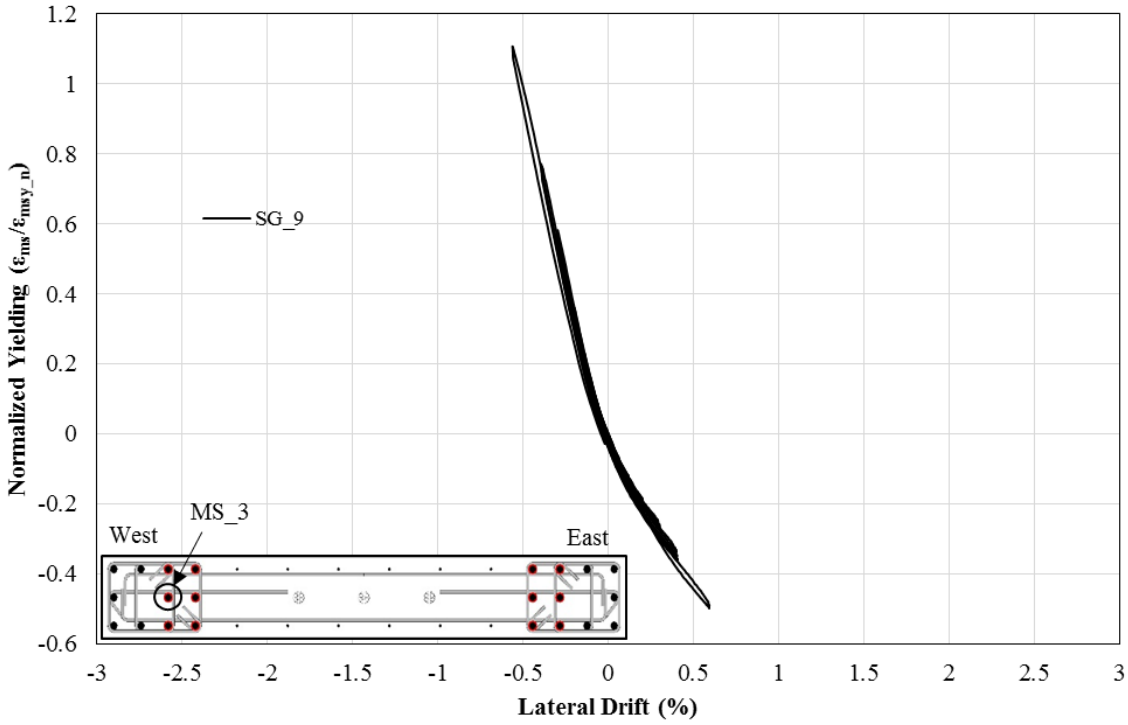

Figure 4-85 First yielding of debonded longitudinal steel reinforcement on the West side Wall 3

Figure 4-86 Photograph of observed cconcrete spalling at Cycle 28W on the West side Wall 3

Figure 4-87 Photograph of observed concrete spalling at Cycle 28E on the West side Wall 3

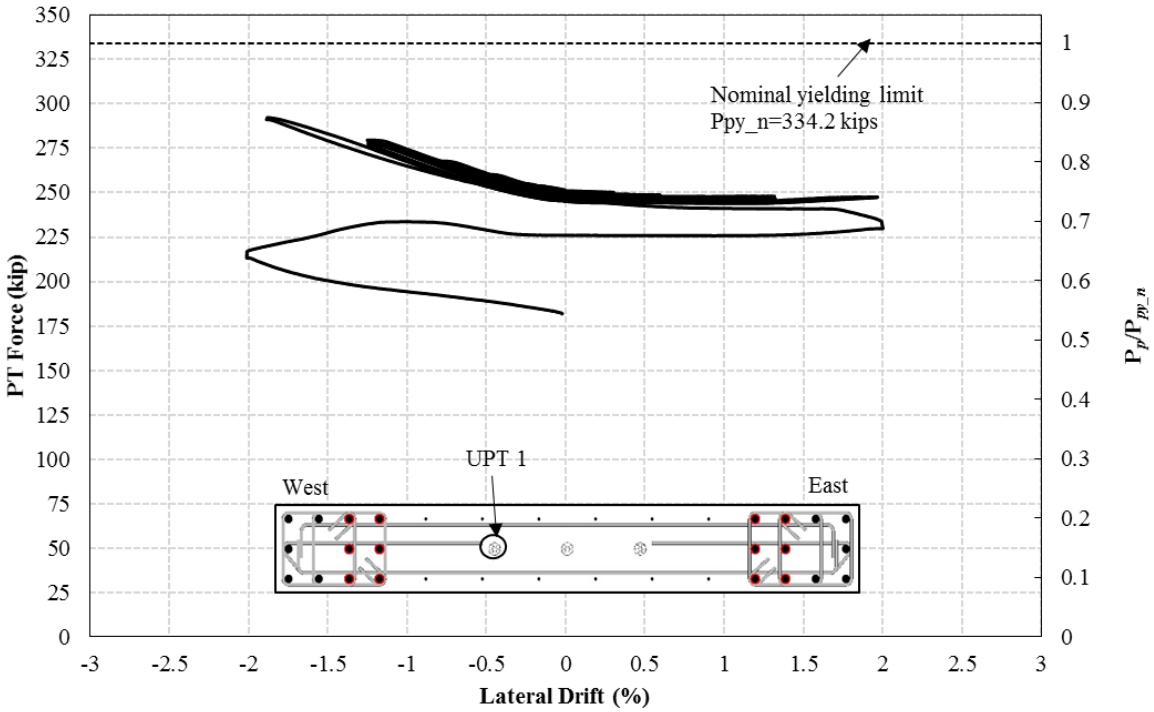

Figure 4-88 Unbonded post-tensioned steel complete response and normalized yielding peaks – West side Wall 3

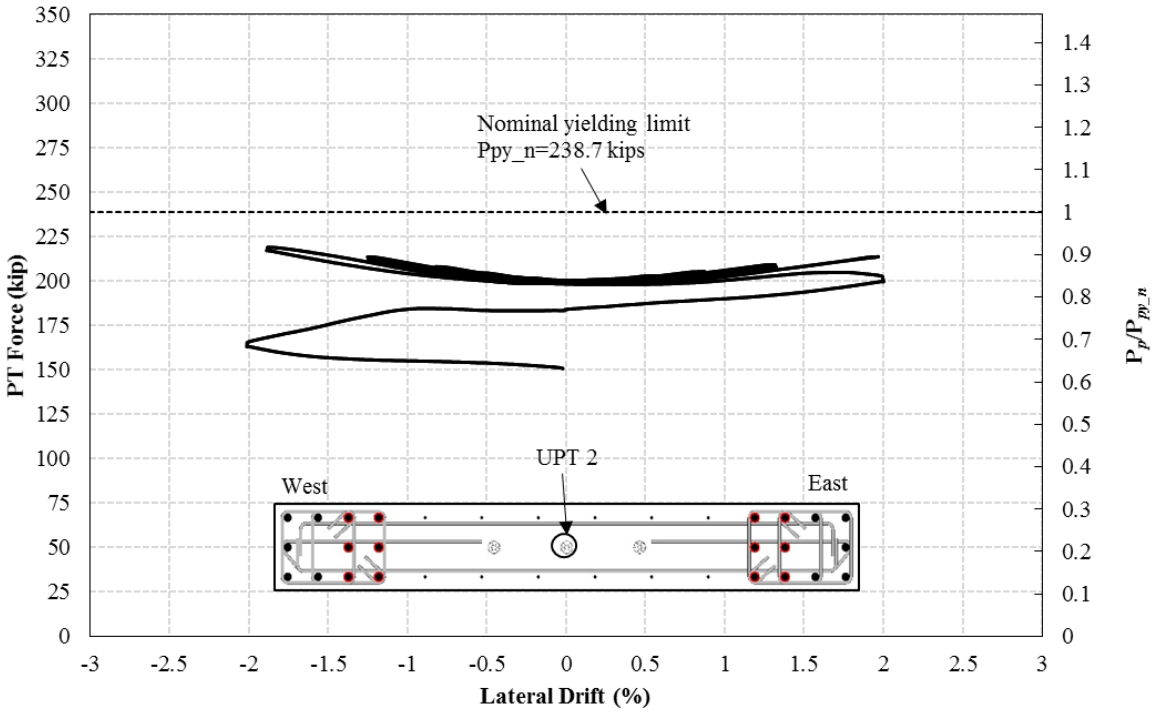

Figure 4-89 Unbonded post-tensioned steel complete response and normalized yielding peaks – Middle Wall 3

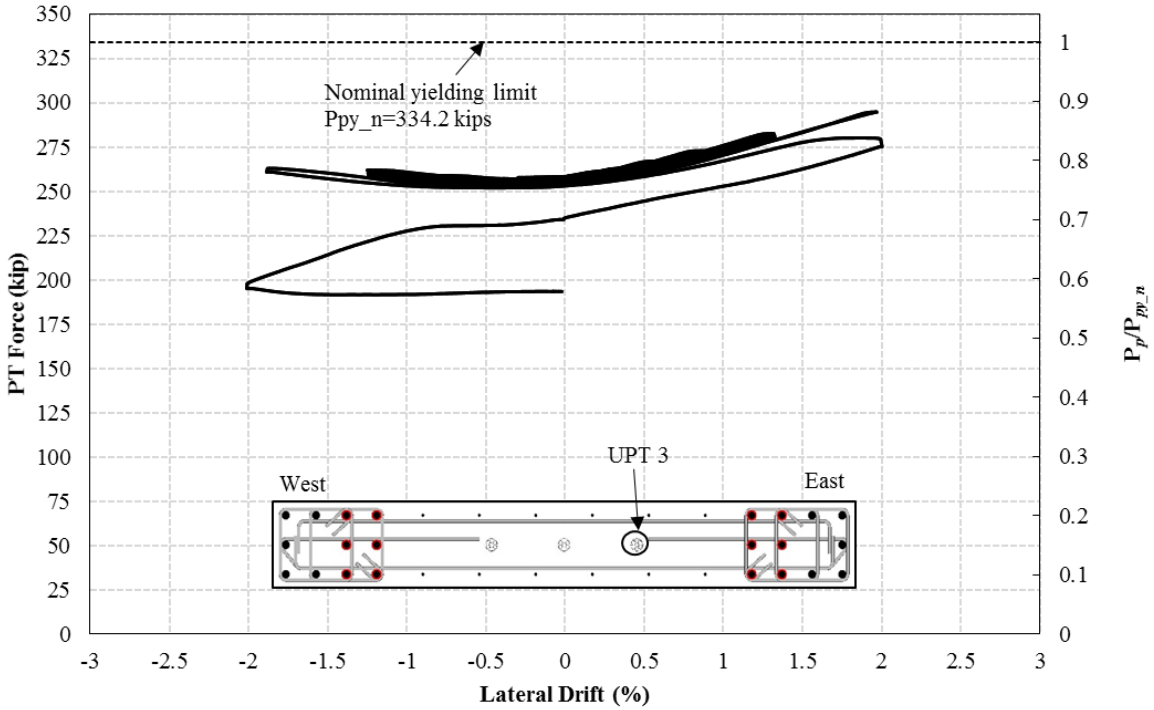

Figure 4-90 Unbonded post-tensioned complete response and normalized yielding peaks – East side Wall 3

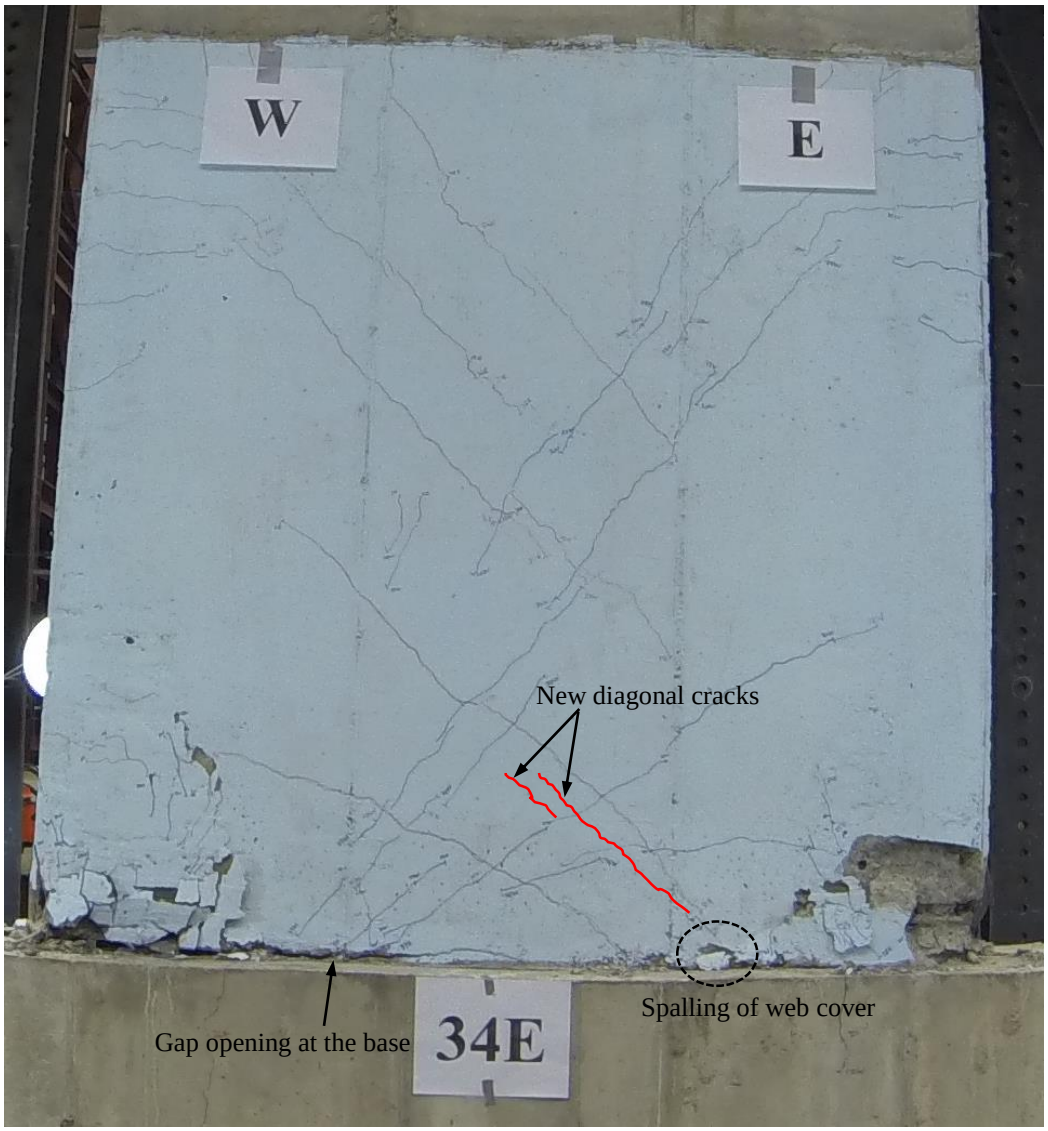

Figure 4-91 Wall condition at the end of Cycle 34E on the South side Wall 3

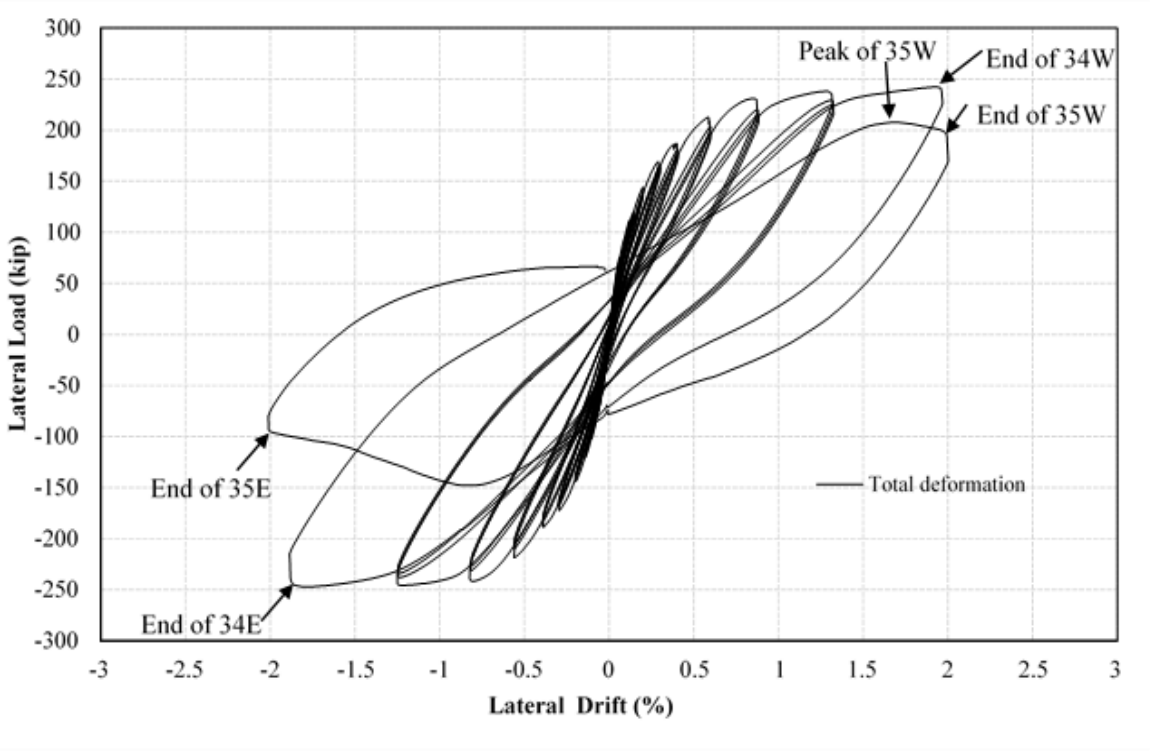

Figure 4-92 Load versus total deformation Wall 3

Figure 4-93 Wall condition at the peak of Cycle 35W on the South side Wall 3

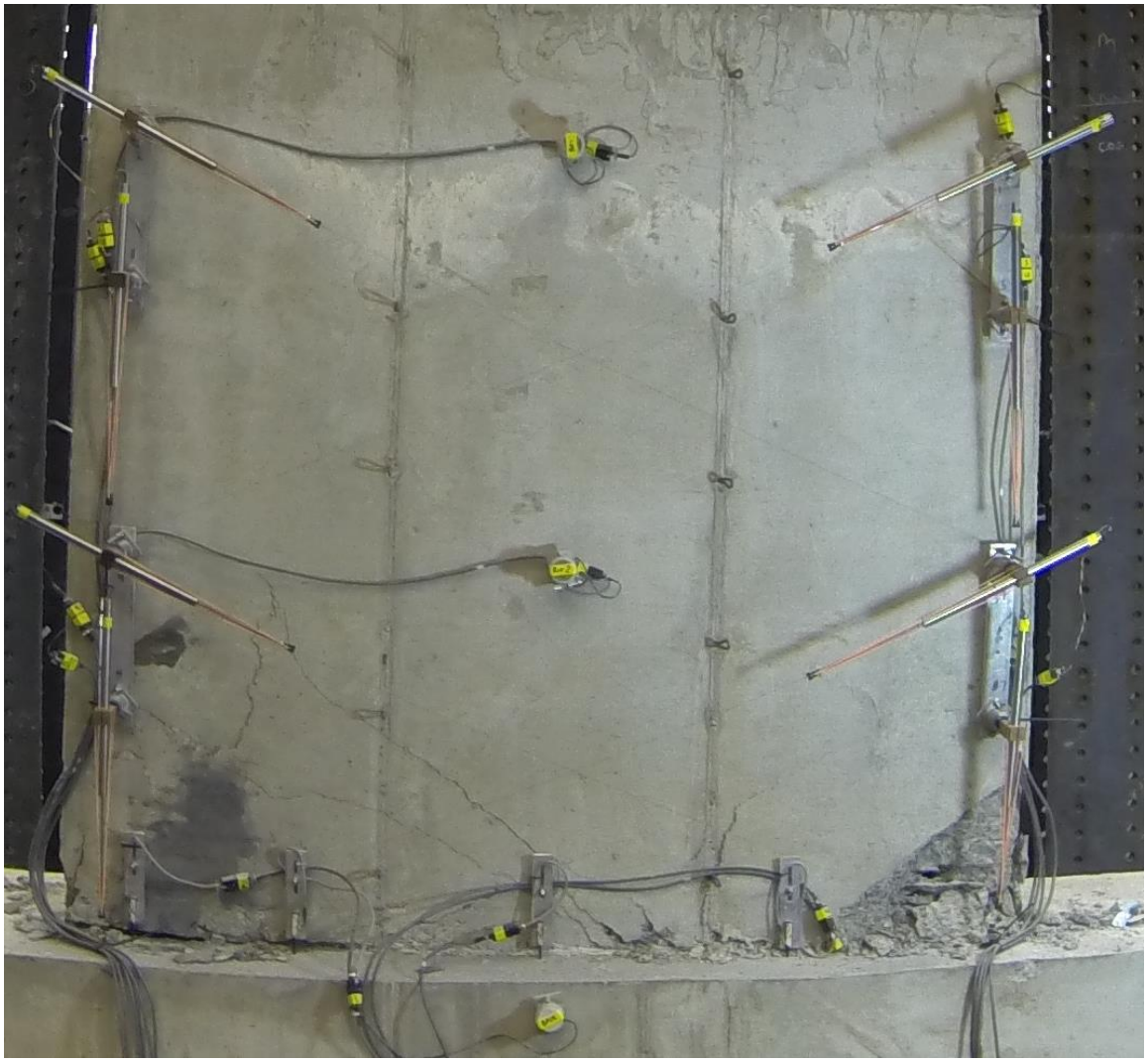

Figure 4-94 Wall condition at the end of Cycle 35W on the North side Wall 3

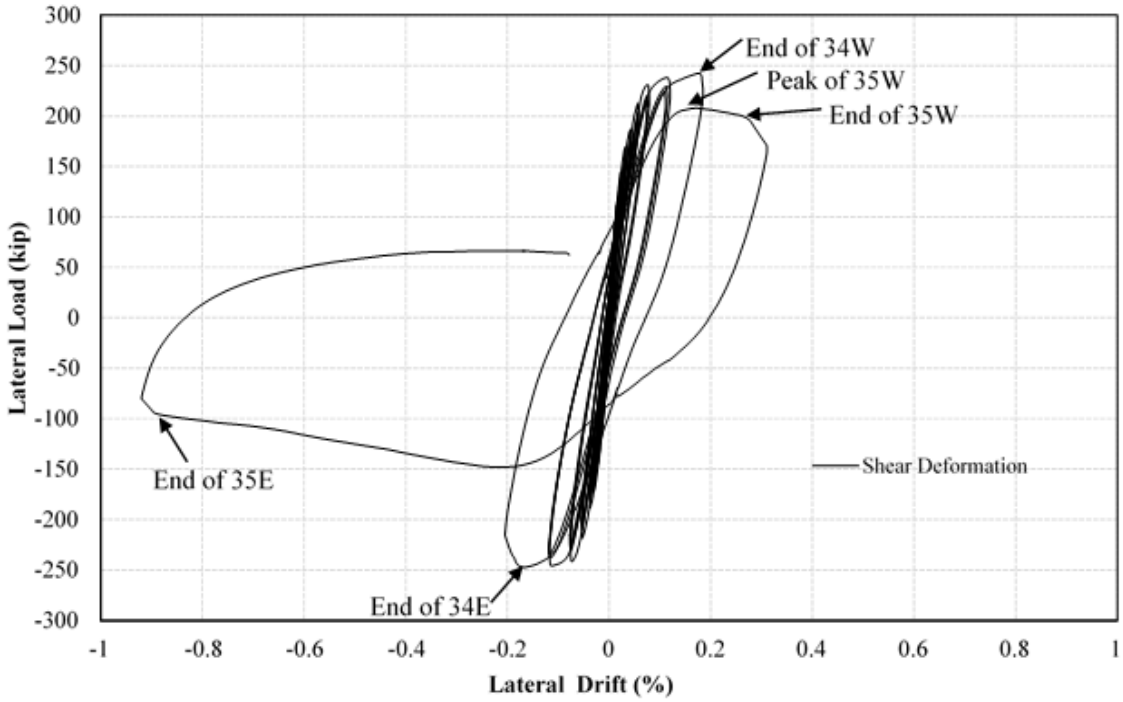

Figure 4-95 Shear deformation Wall 3

(a)

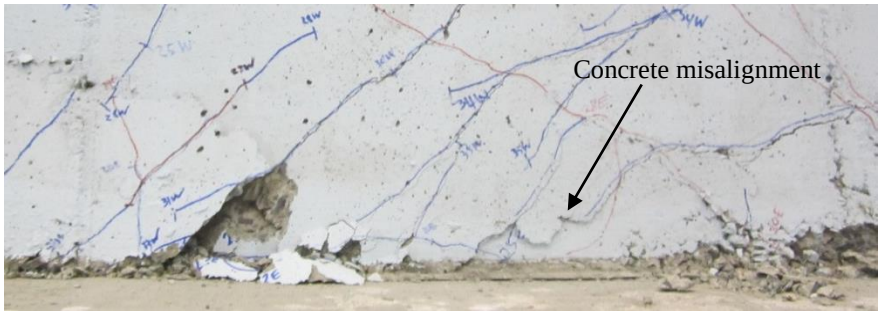

(b)

Figure 4-96 Comparison of the conditions of wall web just above the interface at South side: (a) at the peak load of Cycle 35W, (b) at the end of Cycle 35W

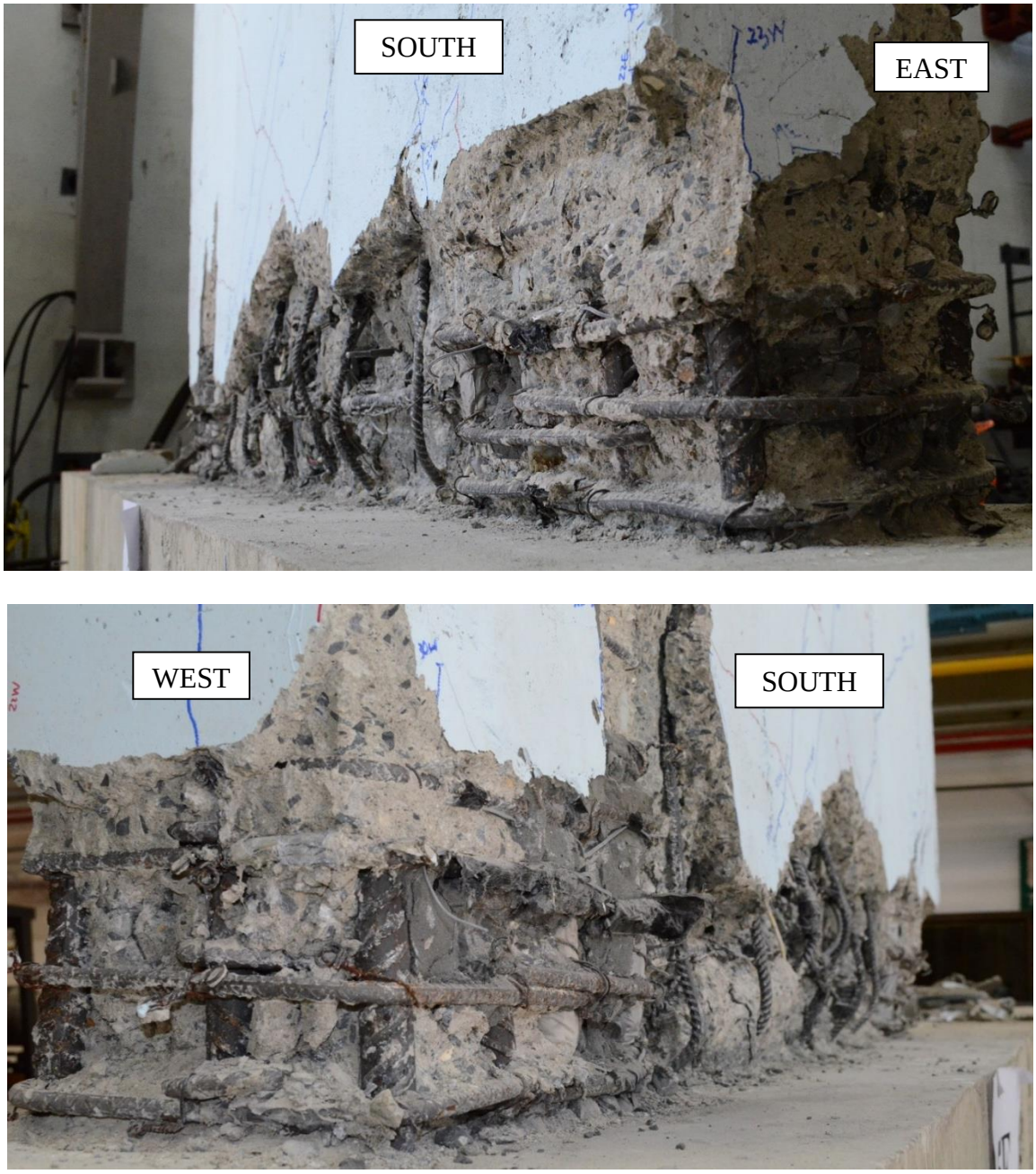

Figure 4-97 Conditions of web longitudinal bars after concrete chipping process

(a)

(b)

Figure 4-98 Wall conditions at Cycle 35E at North side: (a) at the peak load, (b) at the end of load cycle

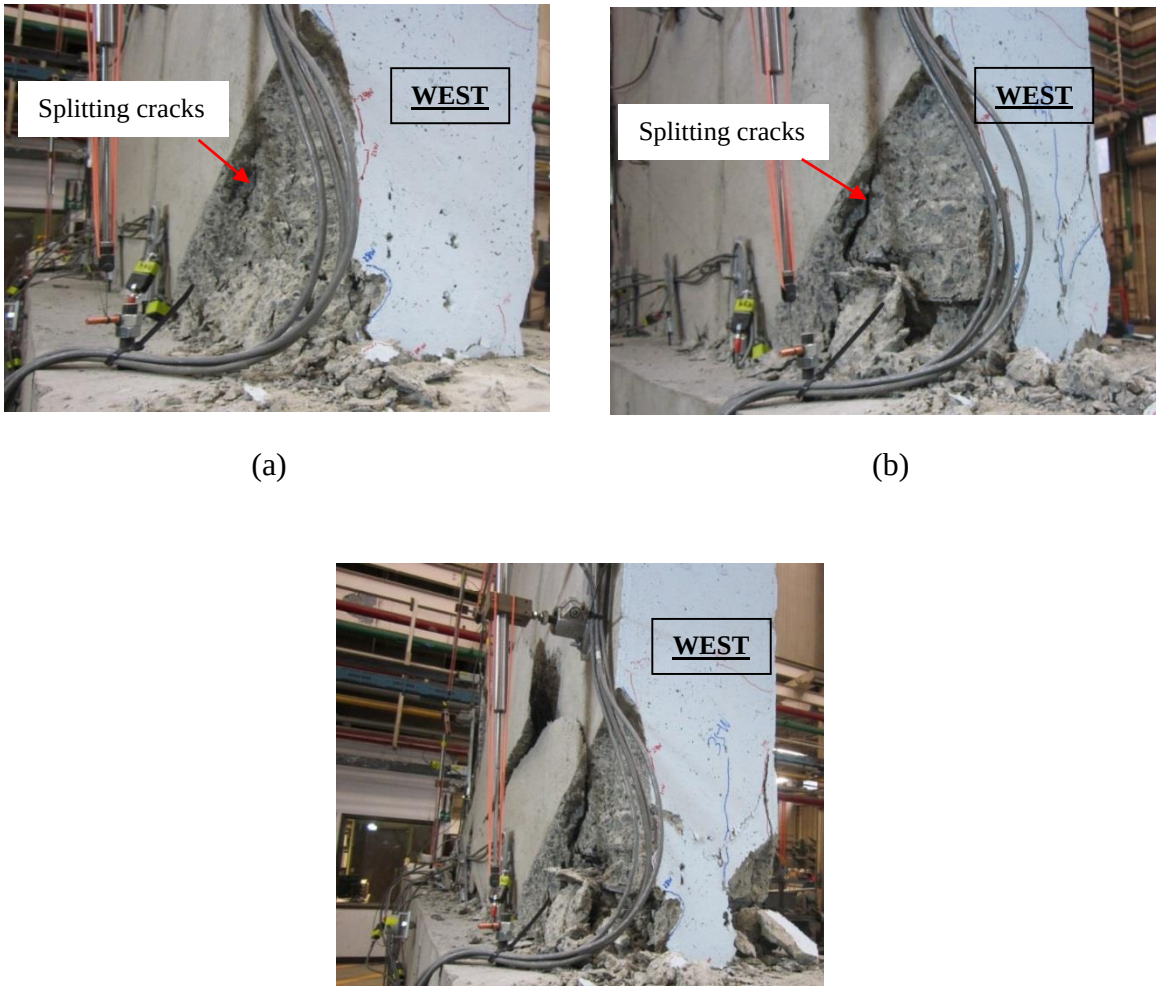

(a) (b)

(c)

Figure 4-99 Progression of splitting crack behind concrete cover at South side: (a) end of Cycle 32W, (b) end of Cycle 35W, (c) end of Cycle 35E

Figure 4-100 Pieces of conrete cover at the South side at the end of the test

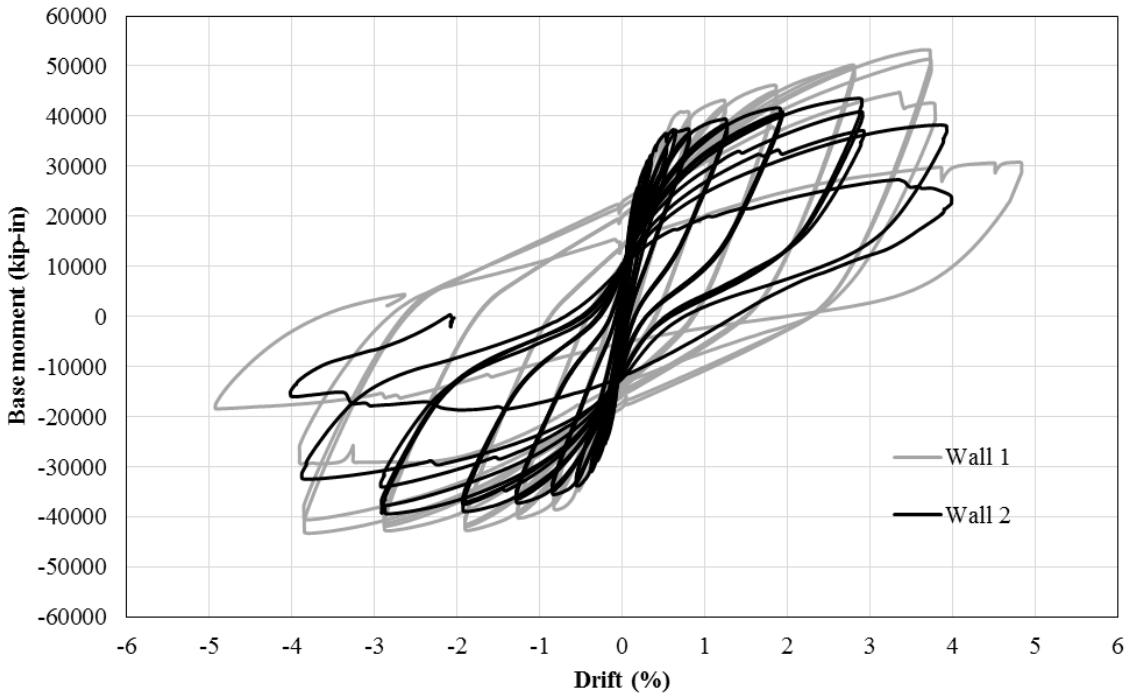

Figure 4-101 Complete responses of Wall 1 and Wall 2

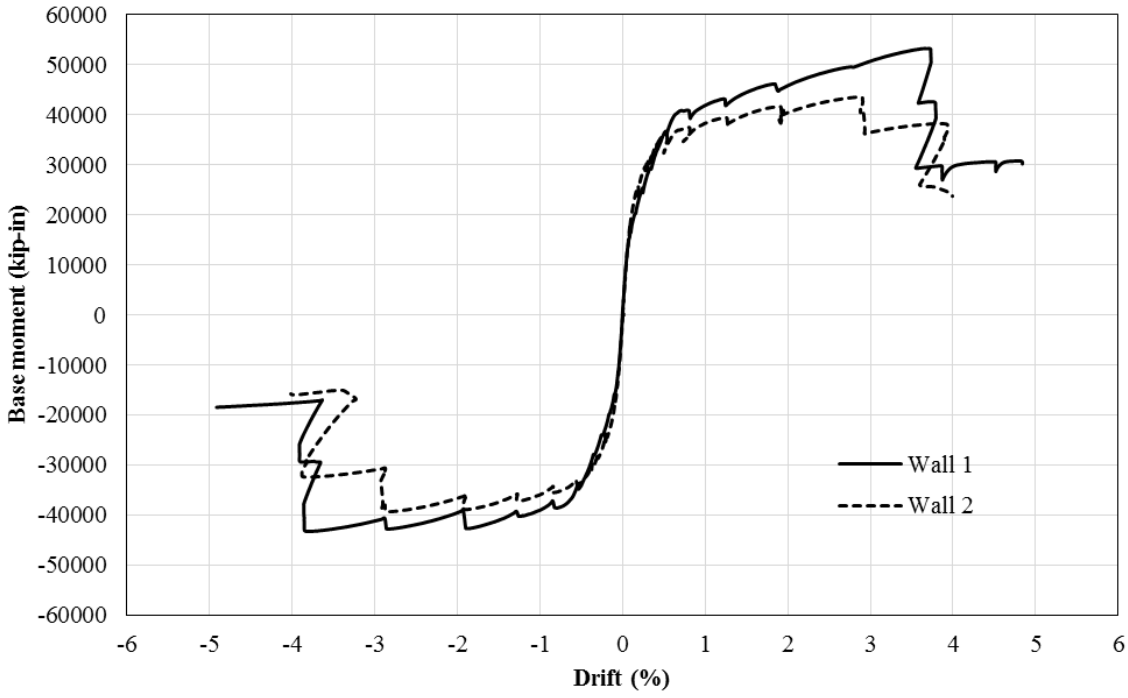

Figure 4-102 Envelope responses of Wall 1 and Wall 2

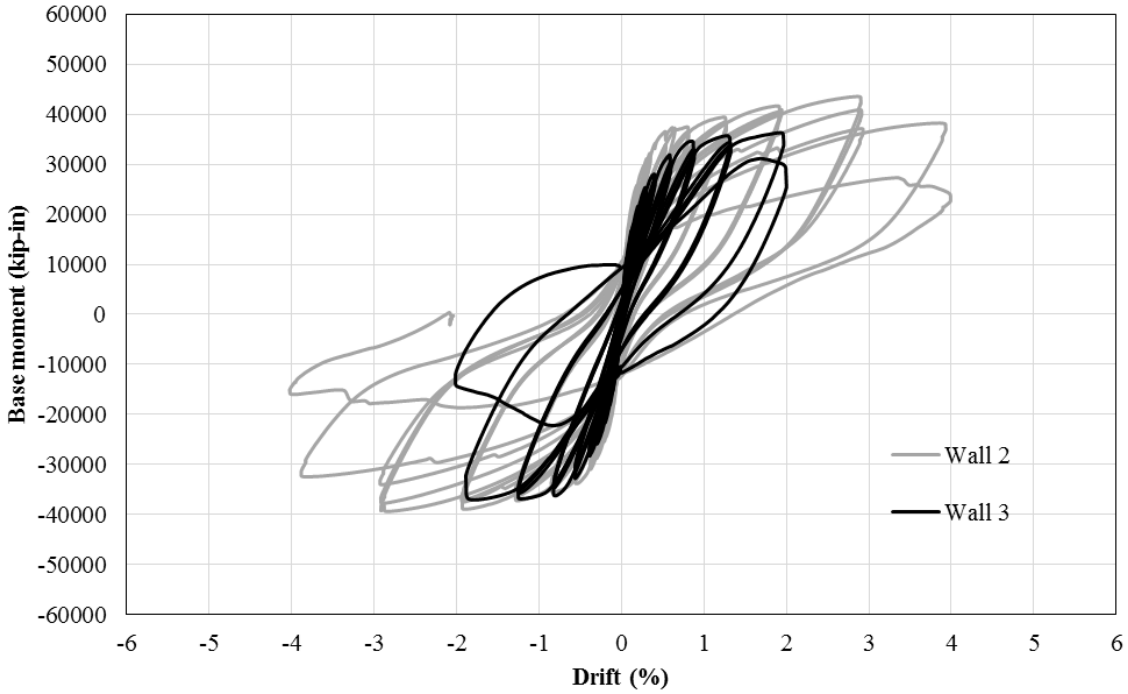

Figure 4-103 Complete responses of Wall 2 and Wall 3

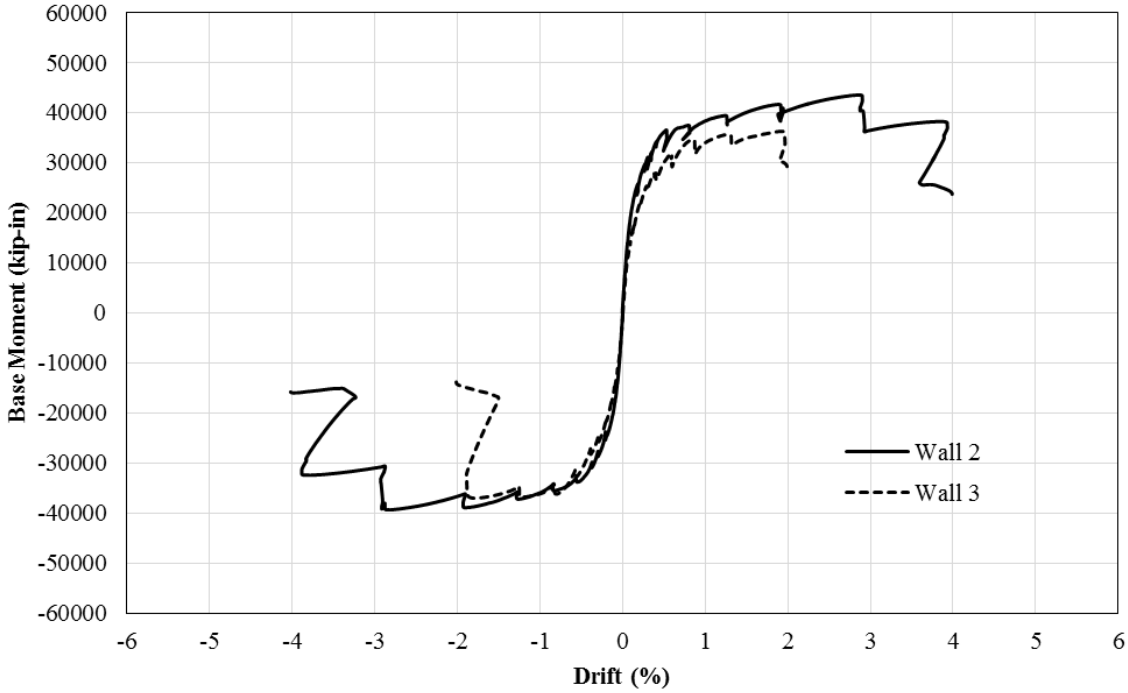

Figure 4-104 Envelope responses of Wall 2 and Wall 3

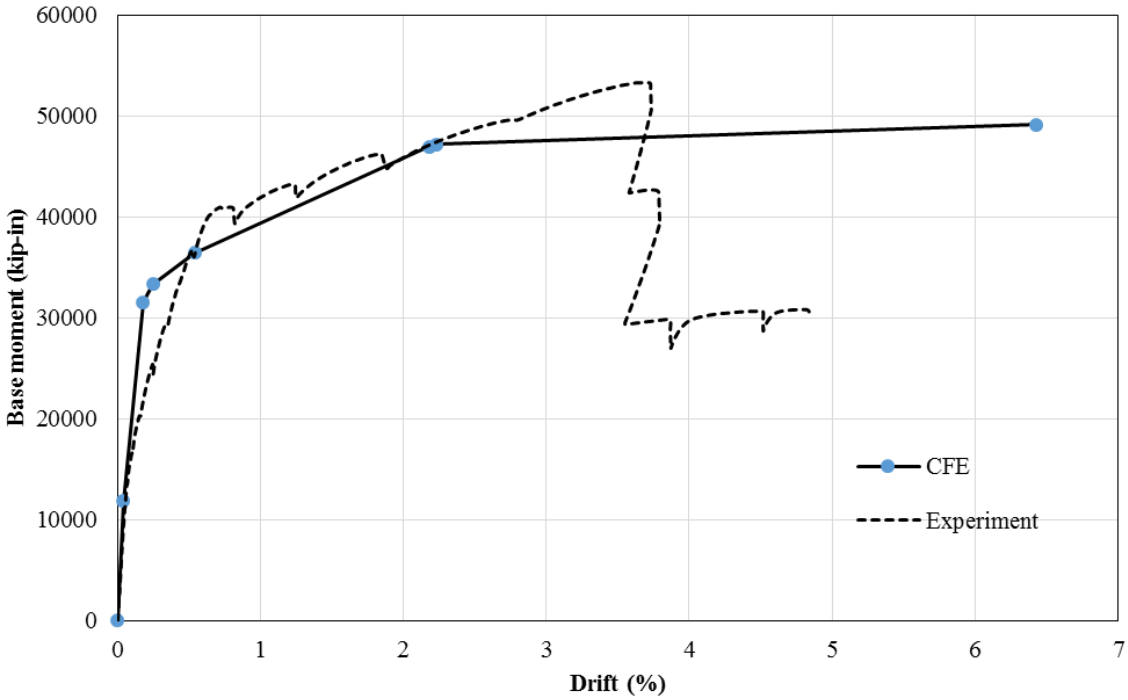

Figure 4-105 Experimental versus CFE for Wall 1

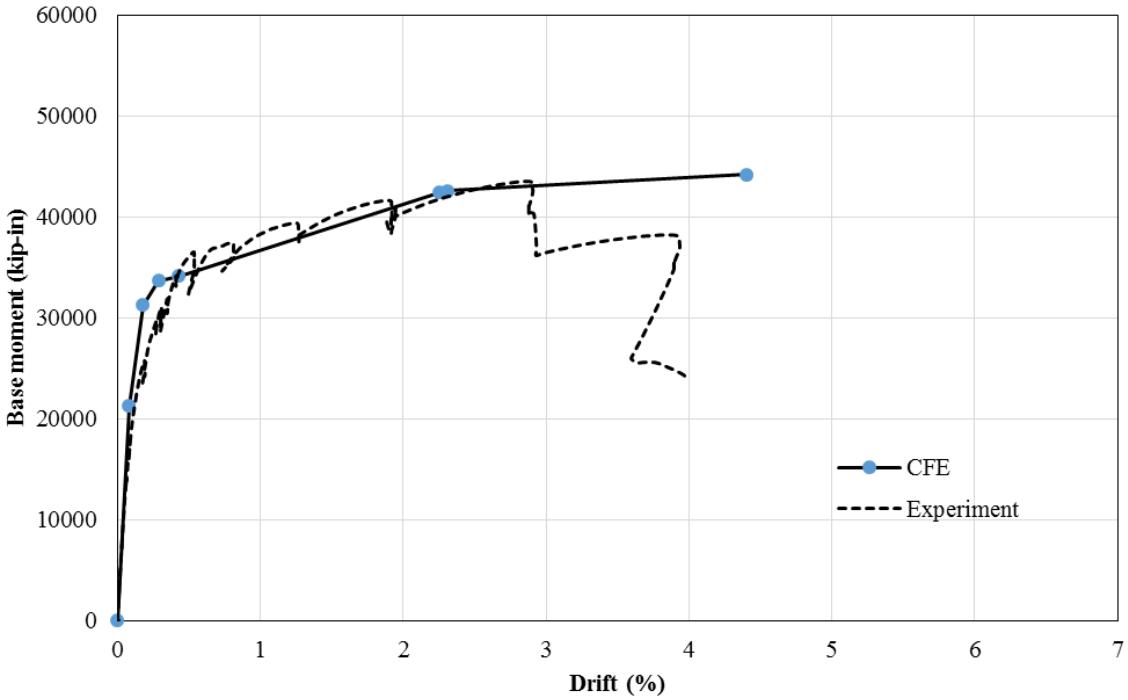

Figure 4-106 Experimental versus CFE for Wall 2

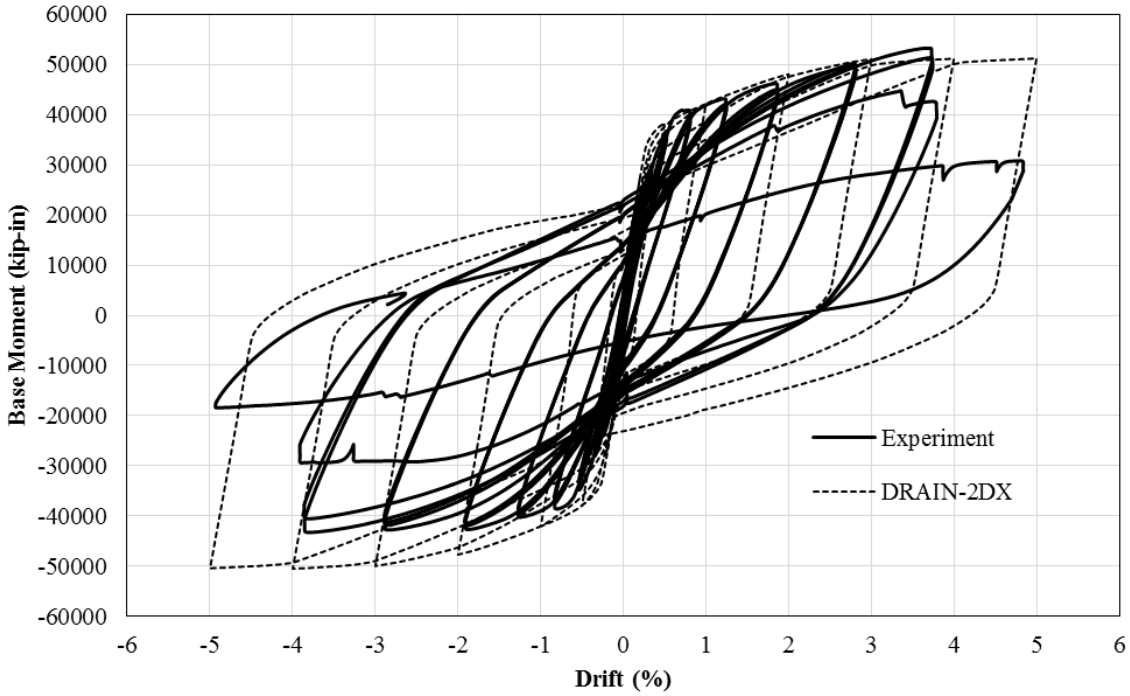

Figure 4-107 Experiment versus DRAIN-2DX Wall 1

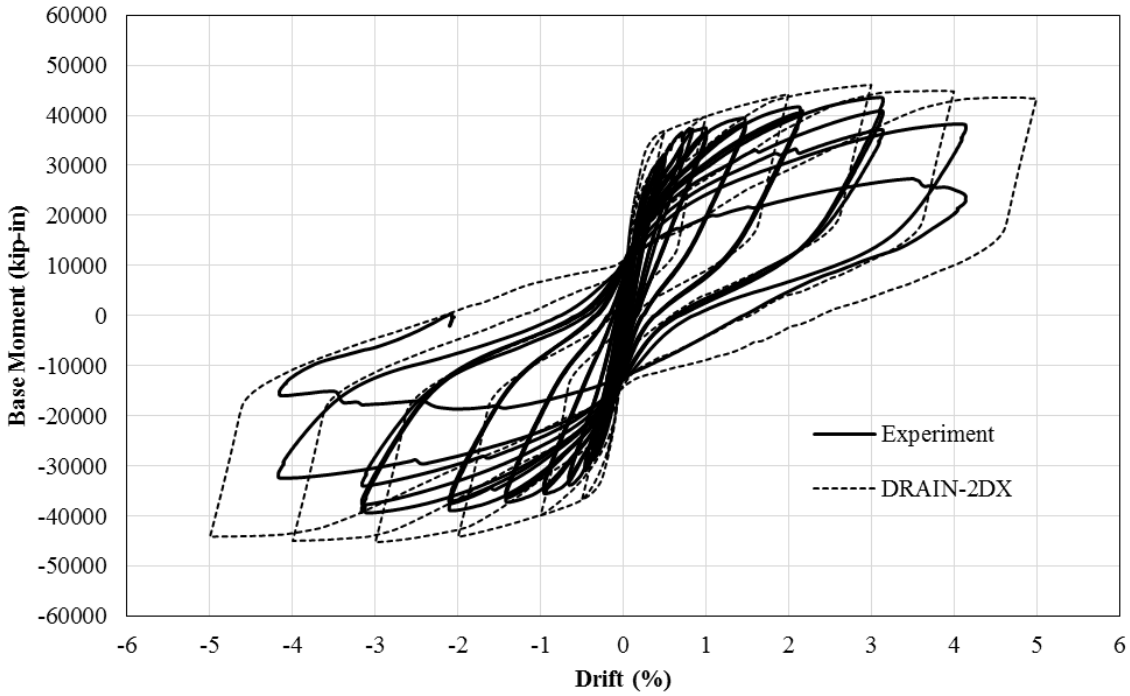

Figure 4-108 Experiment versus DRAIN-2DX Wall 2

CHAPTER 5
CONCLUSIONS

5.1 INTRODUCTION

The work described in this report is part of a project at Lehigh University to develop experimental test data to confirm and codify a design protocol cast-in-place concrete shear walls that incorporate unbonded vertical post-tensioning. The defining feature of the wall system sought by this research is the rocking/flexural response and self-centering capability provided by unbounded vertical post-tensioned tendons coupled with the energy dissipation provided by the reinforcing bars.

The research performed to date, and supported by the Charles Pankow Foundation at Lehigh University, focused on three tasks:

> Task 1 - Development of closed form expression to describe the monotonic lateral load behavior of unbonded post-tensioned cast-in-place special structural walls with bonded or debonded longitudinal mild steel reinforcement.
>
> Task 2 - Experimental evaluation the effects of inelastic tensile cyclic loading of the longitudinal mild steel reinforcement embedded in a confined concrete core on the behavior, strength, and ductility of the confined concrete under compression loading.
>
> Task 3 - Experimental evaluation of large-scale of unbonded post-tensioned cast-in-place special structural walls with bonded or debonded longitudinal mild steel reinforcement. The objectives of this experimental work was to study the behavior of unbonded post-tensioned cast-in-place special concrete walls, and to evaluate different wall details intended to control the response of each test wall.

This report and a companion report (Rivera et al. 2013) Task 3 above. Previous reports present the results of Task 1 (Srivastava et al. 2013) and Task 2 (Noor et al. 2013).

5.2 CONCLUSIONS

The following conclusions are a summarized on the observation and data analysis of the Task 3 experimental work.

1. The behavior of Wall 1 was similar to regular reinforced concrete shear wall where it has a very good energy dissipation capacity by the yielding mechanism in longitudinal steel reinforcement. The influence of axial force in the formed of post-tensioning steel did not play significant role in improving the self-centering capacity by reducing residual drift.

2. The behavior of Wall 2 was more similar to the anticipated behavior of a rocking wall. The energy dissipation in this wall was quite good which is shown by large hysteresis loop of load deformation response. The self-centering capacity of the

wall was improved by the used of higher post-tensioned steel to steel reinforcement ratio.

3. The behavior of Wall 3 was similar to Wall 2 in terms of energy dissipation and self-centering capacity. New detailing of longitudinal steel reinforcement at boundary elements was shown to give significant improvement in reducing damages (cracks) in the concrete and also to prevent fracture of longitudinal steel reinforcement by limiting the tensile strain that can caused buckling which correlate to the fracture of the longitudinal steel reinforcements.

4. Failure mode of Wall 1 was characterized by the formation of shallow diagonal cracks in the web. These cracks corresponded to high shear demand in the wall. The wall eventually failed along these cracks by sliding.

5. Failure mode of Wall 2 was characterized by fractured of longitudinal steel reinforcement at boundaries and web elements. This failure mode corresponded to the dominant flexure deformations in the wall.

6. Failure mode of Wall 3 was sudden and occurred at drift level which was lower than those of the other test walls experienced. This failure was suspected to be precipitated by the formation of a splitting plane along the vertical web reinforcement, followed by buckling of this reinforcement and failure of the wall in shear.

7. Results comparison between the CFE and experimental shows that limit states that occurred at low drift level can be approximated quite good while for limit states that occurred at high drift level the approximations was underestimated.

REFERENCES

ACI Committee 318, "Building Code Requirements for Structural Concrete," American Concrete Institute, Farmington Hills, MI, 2011.

ACI ITG-5.1, "Acceptance Criteria for Special Unbonded Post-Tensioned Precast Structural Walls Based On Validation Testing and Commentary," American Concrete Institute, Farmington Hills, MI, 2007.

ACI ITG-5.2, "Design of Special Unbonded Post-Tensioned Precast Shear Wall Satisfying ACI ITG-5.1 Requirements," American Concrete Institute, Farmington Hills, MI, 2009.

ASCE/SEI 7, "Minimum design loads for buildings and other structures," American Society of Civil Engineers, Washington, D.C, 2010.

El-Sheikh, M., "Seismic Analysis, Behavior, and Design of Unbonded Post-Tensioned Precast Concrete Frames," Ph.D Dissertation, Department of Civil and Environmental Engineering, Lehigh University, Bethlehem, PA, 1997.

International Code Council, "International Building Code," 2011.

Kurama, Y. C., "Seismic Analysis, Behavior, and Design of Unbonded Post-Tensioned Precast Concrete Walls," Ph.D Dissertation, Department of Civil and Environmental Engineering, Lehigh University, Bethlehem, PA, 1997.

Kurama, Y. C., Pessiki, S., Sause, R., Lu, L.W., and El-Sheikh, M., "Analytical Modeling and Lateral Load Behavior of Unbonded Post-Tensioned Precast Concrete Walls," Research Report No. EQ-96-02, Department of Civil and Environmental Engineering, Lehigh University, PA, 1996, 191 pp.

Mander, J., Priestley, M.J.N., and Park, R., "Theoretical stress strain model for confined concrete," J. Struct. Eng., 114(8), 1988b, pp. 1804-1826.

Massone, L. M., and Wallace, J. W., "Load-Deformation Response of Slender Reinforced Concrete Walls," ACI Structural Journal, V. 101(1), 2004, pp. 103-113.

Noor, M., Pessiki, S., Sause, R., "Compression Behavior, Strength, and Ductility of Confined Concrete after Inelastic Tensile Cyclic Loading," ATLSS Report No. 13-04, Lehigh University, Bethlehem, PA, 2013.

Pakiding, L., "Analytical and Experimental Studies of Cast-In-Place Seismic Resistant Unbonded Post-Tensioned Special Reinforced Concrete Wall," Ph.D Dissertation, In preparation, Department of Civil and Environmental Engineering, Lehigh University, Bethlehem, PA, Expected in 2015.

Perez, F. J., "Experimental and Analytical Lateral Load Response of Unbonded Post-Tensioned Precast Concrete Walls," Ph.D Dissertation, Department of Civil and Environmental Engineering, Lehigh University, Bethlehem, PA, 2004.

Perez, F. J., Sause, R., and Pessiki, S., "Analytical and Experimental Lateral Load Behavior of Unbonded Post-Tensioned Precast Concrete Walls," Journal of Structural Engineering, American Society of Civil Engineers, Vol. 133(11), 2007, pp. 1531-1540.

Prakash, V., Powell, G., and Campbell, S., "DRAIN-2DX base program description and user guide," Report No. UCB/SEMM-93/17, Department of Civil Engineering, University of California, Berkeley, CA, 1993.

Rivera, M., Pessiki, S., Sause, R., "Experimental Laboratory Procedures for The Construction and Testing of Seismic Resistant Unbonded Post-tensioned Special Reinforced Concrete Walls," ATLSS Report No. 13-05, Lehigh University, Bethlehem, PA, 2013.

Rivera, M., "Experimental Laboratory Procedures for The Construction and Testing of Seismic Resistant Unbonded Post-tensioned Special Reinforced Concrete Walls," MS Thesis, Department of Civil and Environmental Engineering, Lehigh University, Bethlehem, PA, 2013.

Srivastava, S., Sause, R., Pessiki, S., "Analytical Load Response of Unbonded Post-Tensioned Cast-In-Place Concrete Special Structural Walls with Bonded or Debonded Longitudinal Mild Steel Reinforcement," ATLSS Report No. 13-02, Lehigh University, Bethlehem, PA, 2013.

Srivastava, S., "Analytical Load Response of Unbonded Post-Tensioned Cast-In-Place Concrete Special Structural Walls with Bonded or Debonded Longitudinal Mild Steel Reinforcement," MS Thesis, Department of Civil and Environmental Engineering, Lehigh University, Bethlehem, PA, 2013.

Taucer, F., Spacone, E., and Filippou, F., "A fiber beam-column element for seismic response analysis of reinforced concrete structures," Earthquake Engineering Research Center Rep. No. UCB/EERC-91/17, Univ. of California, Berkeley, CA, 1991.

Tipping Mar, "Unbonded PT-CIP Concrete Walls for Seismic Resistance: Analytical Study of Potential Specimen Designs," 2011.